Cell Disruption Mechanics

by

Andrew Royce KLEINIG

Thesis submitted for the degree of

Doctor of Philosophy

in

The University of Adelaide

Faculty of Engineering

April 1997

Disclaimer

This work contains no material which has been accepted for the award of any other degree or diploma in any University or any other tertiary institution, and to the best of my knowledge and belief, contains no material previously published or written by another person, except where due reference has been made in the text.

I give consent to this copy of my thesis, when deposited in the University Library, being available for photocopying and loan.

SIGNED:

DATE: 16 April 1997

Acknowledgments

Numerous individuals and organisations deserve recognition for their contribution to this thesis. Firstly, I would like to thank my supervisor, Dr Anton Middelberg, for his guidance and encouragement.

I am grateful to Mr Bruce Ide for supplying his practical expertise in the design and manufacture of the custom rigs required to measure homogenizer valve gaps, pressure transients and impinging jet stagnation width. I am thankful to the Department of Mechanical Engineering at the University of Adelaide for providing me with access to the PHOENICS finite volume code and computational facilities. I am particularly indebted to Dr Colin Thomas and Dr Zhibing Zhang of the Micromanipulation group at The University of Birmingham for their collaboration and provision of facilities and expertise for the measurement of the mechanical properties of yeast cells. In particular, I am indebted to Dr Hisham Mashmoushy for conducting most of the micromanipulation experiments presented in this thesis. I would also like to acknowledge the technical support provided by Mr Chris Mansell and secretarial support provided by Mrs Mary Barrow and Mrs Elaine Minerds during my studies.

Financial support for this work was provided by The University of Adelaide (in the form of a postgraduate scholarship), the Cooperative Research Centre for Tissue Growth and Repair (for their provision of a top-up scholarship and their contribution toward the operating expenses occurred) and Adelaide Brighton Cement Ltd (for their provision of a supplementary scholarship in the latter stages of this work). The collaboration with The University of Birmingham was partly funded by The Department of Industry, Science and Tourism through a Bilateral Science and Technology grant.

I would like to thank my fellow postgraduate students within the Department of Chemical Engineering for their camaraderie and philosophical discussion. I would like to thank my family for the support that they have given me throughout my life. Finally, I would like to thank my wife, Angela, for her continued support and encouragment.

Summary

High-pressure homogenization is a key unit operation used to break cells containing intracellular bioproducts. Modeling and optimisation of this process has been restrained by a lack of understanding of the fundamental processes that occur to effect cell breakage during homogenization.

This thesis examines the cell-fluid interactions that occur during homogenization, and combines them with an investigation of the mechanical properties of the cell. This results in a truly predictive model for cell-disruption efficiency during high-pressure homogenization.

An experimental investigation confirmed previous assertions that cell disruption occurs in the valve-inlet and impinging-jet regions of a homogenizer valve. However, experimental disruption data alone does not elucidate the physical processes that cause cell breakage.

To determine how cells and fluid within the homogenizer interact, an investigation of homogenizer fluid mechanics was conducted. The calculated fluid velocities and strain rates within the valve assembly were then used to model the passage of a cell through the valve. The dependence of maximum cell-wall tensions on cell diameter and homogenizer pressure were then calculated. This then provided a homogenizer tension distribution function.

The mechanical properties of individual cells were characterised using a micromanipulation technique. The ultimate cell-wall tension was found to be Gaussian within a population of cells and independent of cell diameter.

Combination of the calculated homogenizer tension distribution function with the measured ultimate cell-wall tension distribution was used to predict cell-disruption efficiency, and homogenate cell-size distributions, for two cultures of yeast cells, after one pass through the valve-inlet region of an APV-Gaulin 15M high-pressure homogenizer.

This result is highly significant, as it is the first time that true *a priori* predictions of cell disruption efficiency (that do not rely in any way on the regression of previous disruption data) have been obtained. Further work is required to extend the approach used in this thesis to different microorganism and homogenizer systems.

Table of Contents

List of Figures

List of Tables

Chapter 1

Introduction and Aims

Microorganisms naturally produce a wide array of useful biochemicals. Commercially important examples include enzymes, antibiotics, vitamins, organic acids, amino acids, ethanol and proteins (Bailey and Ollis, 1986). Most of these products are produced extracellularly and can be separated directly from the fermentation broth.

Since the production of the first recombinant DNA plasmid over 20 years ago (pSC101, Cohen *et al.*, 1973) a rapidly developing "new" field of biotechnology has ensued. Recombinant DNA (or genetic engineering) techniques allow the increased production of intracellular bioactive components and also allow the transfer of mammalian genes to microorganisms. This has resulted in the production of protein products that were either previously not available at all or only available in either limited supply or at prohibitively high costs. Examples of such products include human insulin, growth hormones and growth factors, interferons and other lymphokines, vaccines, blood factors, enzymes and various other biologically active compounds (Khosrovi and Gray, 1985).

The most common hosts currently used for industrial applications are *Escherichia coli*, *Saccharomyces cerevisiae* and Chinese Hamster Ovary (CHO) cells (Cleland and Wang, 1993). *E. coli* is by far the most widely used host (Khosrovi and Gray, 1985). Reasons for this choice are discussed by Shuler and Kargi (1992), with the primary reason being that it has been extensively studied and a good understanding of its molecular biology has evolved. Restriction enzymes, strongly-inducible promoters and cloning techniques are readily available and it can be grown cheaply with high growth rates on simple media. After *E. coli*, the most widely used host is *S. cerevisiae* (Khosrovi and Gray, 1985) which has the advantage that it is a GRAS (generally regarded as safe) microorganism, making it

suitable for the production of food related proteins (Shuler and Kargi, 1992) and use in the tight regulatory environment of Germany. However, expression levels that have been quoted for protein cloned into *S. cerevisiae* are approximately an order of magnitude lower than for *E. coli*.

A major disadvantage of using *E. coli* and *S. cerevisiae* as hosts is that they generally do not excrete high levels of protein into the growth media. This requires an operation to disrupt cells after fermentation, resulting in a suspension containing product mixed with other cellular proteins and cell fragments. This has led to interest in secreting hosts such as *Bacillus subtilis* (Georgiou, 1995) and mammalian cell lines. However, extracellular production also has some inherent disadvantages. Product concentration is likely to be low (requiring a large concentration step) and the product may be degraded by secreted proteases or shearing conditions in the fermenter (Fish and Lilly, 1984). At present, *E. coli* remains the host of choice where its high expression levels and volumetric productivities are required to produce a low-cost and simple product. *S. cerevisiae* and *B. subtilis* are used in specialised applications (*e.g.* where a GRAS organism is required) and mammalian cells are used to produce large complex proteins with important glycosylation or conformational considerations.

Due to the wide use of *E. coli* and *S. cerevisiae*, methods of releasing intracellular products following fermentation are required. Various methods that are available to achieve disruption of the cell wall are reviewed in section 1.1 of this thesis.

In any commercial process, the selection and design of process units to produce a desired product will ultimately be decided by economic considerations. It will be necessary to manufacture the desired product within stringent specifications and at the lowest possible cost. Alternative units will be compared and operating conditions will be specified to optimise the process.

Many biotechnology products are produced for human pharmaceutical markets (Mossinghoff, 1993). For these products, manufacturing costs are generally a low proportion of the product selling price (Hacking, 1986), with initial research and development costs (including costs of clinical trials and regulatory approval) being more significant. High product purities must be consistently achieved. Once a production process is determined, and regulatory approval of the product is underway, the production process cannot be changed (Asenjo *et al.*, 1991). Sales potential is likely to be highly

uncertain (Barnacal, 1995), as is the product's viable life. As a consequence of these product attributes, process units will usually be chosen on the basis of their adaptability, demonstrated efficacy and reliability, even if these objectives are achieved at the expense of economic efficiency for an individual product (Hacking, 1986).

In traditional chemical engineering, the design of an optimal sequence will be conducted mathematically. This is necessary to account for the interaction of unit operations (Fish and Lilly, 1984) However, this approach has limited use in biotechnology because of a lack of useful design equations and databases (Asenjo *et al.*, 1991).

This thesis is concerned with the unit operation used to break cells to release intracellular product. After reviewing the methods available for intracellular product release (section 1.1), the most widely used technique, high-pressure homogenization, is chosen for further examination. The design and operating characteristics of a selection of high-pressure homogenizers are reviewed in section 1.2.1. Previous homogenizer studies are then reviewed in section 1.2.2, with particular emphasis on the variables that affect homogenizer performance and the models developed to describe cell disruption efficiency. This leads to a discussion of some of the key unresolved issues in high-pressure homogenization. Section 1.3 then concludes this chapter by outlining the aims and structure of this thesis.

1.1 Releasing Intracellular Products

Suitable techniques for the release of intracellular products into the culture medium have been extensively reviewed (Middelberg, 1995; Schütte and Kula, 1993; White and Marcus, 1988; Hughes *et al.*, 1971; Wimpenny, 1967) and are summarised in this section. Methods used to break cells open to release intracellular products are chosen based on the characteristics of the microorganism, product being isolated, and scale of operation. The chemical structure of cell walls from different organisms is briefly discussed in section 1.1.1, and is an important consideration in product release techniques. Products that are recovered from cells include enzymes, proteins, cell walls, membrane fragments, intracellular organelles, and polymers. These products may be soluble or insoluble, found within the cytoplasm, periplasm or bound to cell walls, and may be sensitive to protease, shear, temperature, or pH degradation. These factors must also be considered when choosing a product release technique.

At a laboratory scale, an almost unlimited array of techniques may be used to release intracellular products. A subset of these that are suitable for releasing intracellular products at a preparative or production scale are summarised in Fig. 1.1. These techniques are further discussed in sections 1.1.2 to 1.1.4.

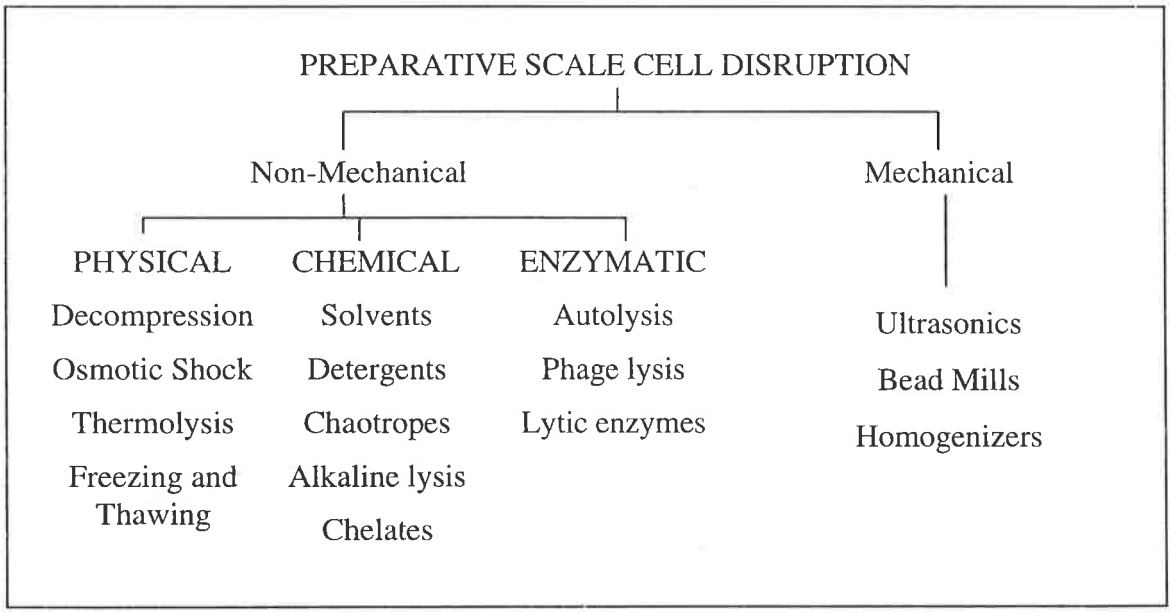

Figure 1.1: Techniques available for the release of intracellular products from microorganisms (after Middelberg, 1995).

1.1.1 Comparison of Microorganisms

A cell is separated from the surrounding media by a complex cell envelope. The cell envelope of microorganisms generally consists of a cytoplasmic membrane and a cell wall. The cytoplasmic membrane maintains concentration gradients between the cell and the surrounding medium. The cell wall is highly elastic and is primarily responsible for cell shape and mechanical strength. An understanding of the composition and structure of the cell envelope is important for an analysis of intracellular product release. The cell wall is mainly composed of various complex polysaccharides that depend on the class of the microorganism. These polysaccharides may be linked by peptides. A schematic illustration of the cell envelope of common classes of microoganisms of commercial importance is given in Fig. 1.2.

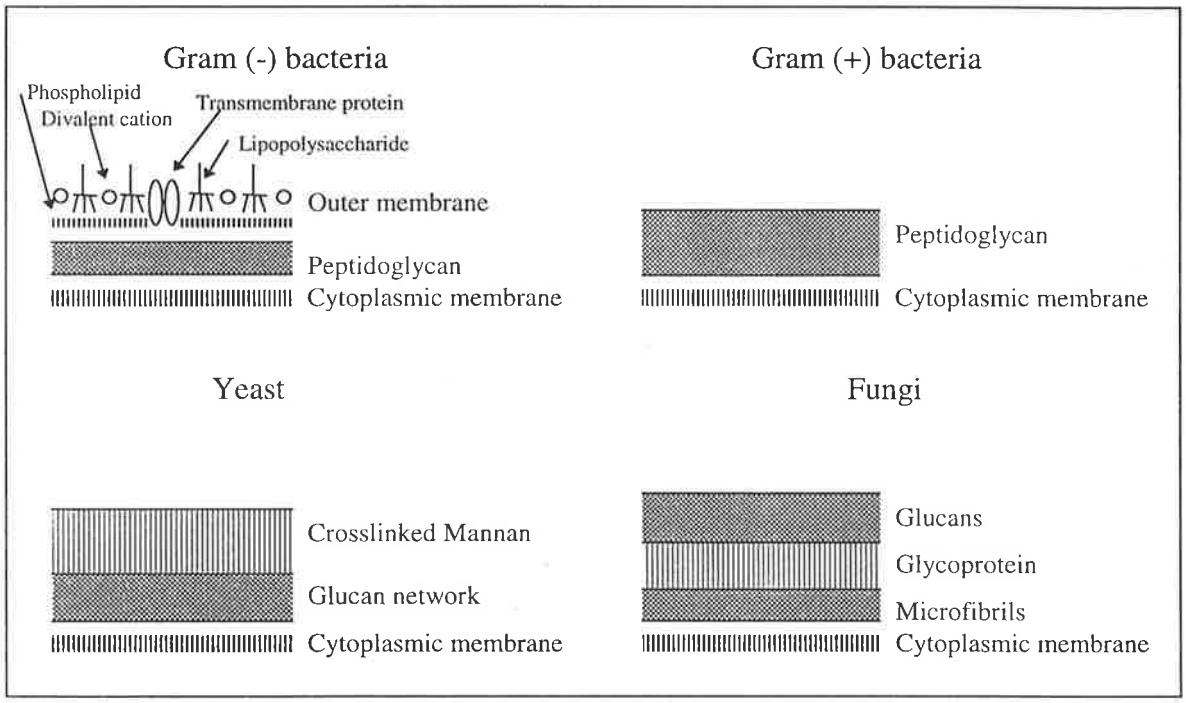

Figure 1.2: Schematic illustration of different classes of microorganisms (after Schütte and Kula, 1993; Middelberg, 1995).

In addition to the gross structural composition differences in the cell envelopes of different classes of microorganisms (Fig. 1.2), the thickness and properties of individual envelope components vary with the growth environment, cell development, and strain of a given species.

For mechanical product release processes, the thickness and degree of crosslinking of the structural components of the cell wall will influence the ease of breakage (Engler, 1985).

The composition of the cell wall determines the way in which its structural integrity can be compromised by chemical or enzymatic methods. Hence, knowledge of the wall structure and composition is particularly important when considering the action of breakage techniques that are reviewed in the following section.

1.1.2 Non-mechanical methods

Non-mechanical methods of cell breakage tend to be gentler than mechanical disruption, and are usually divided into physical, chemical, and enzymatic methods.

Physical Disruption

Physical methods result in breakage of the cell wall without entirely tearing it apart. They are usually only effective for particularly weak wall structures.

Explosive decompression involves mixing a cell suspension with gas (carbon dioxide or nitrous oxide) for a specified time, and then suddenly releasing the applied pressure. This technique has been used for the disruption of *E. coli* (Fraser, 1951) and *S. cerevisiae* (Lin *et al.*, 1991; 1992) cells. The extent of protein release tends to be low and the method is not likely to be of commercial significance in its current form (McLean and Schaschke, 1996).

Osmotic shock involves equilibrating cells in a medium of high osmolarity (*e.g.* 1 M sucrose) and then suddenly diluting the medium. Water rapidly enters the cell, increasing the internal pressure and causing lysis. This technique has limited application as it is not generally able to rupture the strength providing components of the wall (Hughes *et al.*, 1971).

Thermolysis involves heating cells to 50 - 55°C to disrupt the outer membrane and release periplasmic proteins (Katsui *et al.*, 1982; Tsuchido *et al.*, 1985) or up to 90°C to break the cell wall and release cytoplasmic contents (Watson *et al.*, 1987).

Freezing and thawing involves alternate freezing and thawing of cells (Johnson and Hecht, 1994). Freezing and thawing frequently achieves low yields even after a large number of cycles and may denature components that are sensitive to freezing and thawing.

Chemical Disruption

Chemical methods rely on selective interaction of a chemical or mixture of chemicals with components of the cell wall or membrane. Disruption of the inner and outer membranes in gram negative bacteria by chemical means allows product to "seep" through the peptidoglycan layer. In this way, it is not necessary to disrupt the peptidoglycan network to achieve intracellular product release.

Organic solvents probably act by dissolving hydrophobic wall components, such as inner membrane phospholipids in gram-negative bacteria (DeSmet *et al.*, 1978). Suitable organic solvents for bacteria include toluene (Jackson and DeMoss, 1975), chloroform (Ames *et al.*, 1984), acetone (Bhaduri and Demchick, 1983) and ether (Vosberg and Hoffmann-Berling, 1971). Chloroform, toluene and ethanol have also been used to permeabilise yeast (Flores *et al.*, 1994).

Detergents act by binding to membrane lipids, and then forming mixed micelles containing the membrane lipid (Jones, 1992). Detergents available for solubilising cell membranes include anionic (sodium dodecyl sulphate (SDS) and salts of fatty acids), cationic (tetra alkyl ammonium salts) and non-ionic detergents (Triton X and Brij series) (Belter *et al.*, 1988).

Chaotropic agents act by disorganising the bulk structure of water, making it less hydrophilic and able to solubilise hydrophobic compounds (such as integral membrane proteins) from the *E. coli* membrane (Naglak *et al.*, 1990). Suitable chaotropes include guanidine, urea and ethanol.

Alkaline lysis acts by the saponification of lipids in the cell wall (Belter *et al.*, 1988). Although this treatment is cheap and effective, it is also very harsh and subsequently only suitable for products that are not significantly degraded at high pH.

Chelating agents such as ethylenediamine tetra acetic acid (EDTA) act by binding to divalent cations (Mg^{2+}, Ca^{2+}) that cross-bridge adjacent lipopolysaccharide molecules in the outer membrane of gram negative bacteria (see Fig. 1.2). Lipopolysaccharide fragments containing protein and phospholipid are then released from the cell wall (Leive *et al.*, 1968). However, EDTA does not act on the inner membrane or peptidoglycan resulting in periplasmic but not cytoplasmic protein release (Neu and Heppel, 1964).

Enzymatic Disruption

Enzymatic methods generally involve enzymatic attack of the components that provide the cell with its structural integrity (peptidoglycan in bacteria, mannoprotein and glucan in yeast).

Autolysis involves the host producing its own enzymes that degrade the cell wall, increasing its porosity and ultimately causing lysis. The process is affected by a large number of variables, making generalisations difficult (Hughes *et al.*, 1971).

Phage lysis involves the use of a bacteriophage, resulting in lysis. Although the mechanism of lysis is not fully understood, Lubitz *et al.* (1984) suggests that interaction with the host's autolytic system may occur.

Foreign lytic enzymes may also be used to release intracellular products. Enzymes are highly specific with respect to substrate, and hence enzymes that can externally lyse the cell wall must be used. Yeast lytic enzymes contain protease to remove the outer mannan layer, and a β–1,3–glucanase to degrade the inner layer (Hunter and Asenjo, 1988). Bacteria may be lysed using lysozyme (White and Marcus, 1988), which catalyses the hydrolysis of β–1,4–glycosidic bonds.

Combined Methods

As various non-mechanical product release techniques have different modes of action, they may be combined synergistically to give improved product release. This approach is particularly useful for gram-negative bacteria, where the outer lipopolysaccharide membrane protects the cell from some treatments. Combined non-mechanical treatments include EDTA-lysozyme (Dean and Ward, 1992; Novella *et al.*, 1994), polymixin-lysozyme (Dean and Ward, 1992), guanidine HCl-Triton X100 (Hettwer and Wang, 1989), EDTA-guanidine (Novella *et al.*, 1994) and sodium hypochlorite-chloroform (Hahn *et al.*, 1994).

1.1.3 Mechanical Methods

Mechanical methods of cell disruption include sonication, wet milling and high-pressure homogenization. Unlike most non-mechanical methods that are only applicable for a specific organism or class of organisms, mechanical methods tend to be non-specific and are able to disrupt most organisms.

Sonication involves applying ultrasound energy to a cell suspension. This is done by vibrating the tip of a small metal rod (called a 'horn'). The vibrations produce sonic or ultrasonic waves, causing cavitation. Cell breakage is thought to occur as cavitation bubbles collapse in solution. Sonication is widely used on a preparative scale because it is fast and simple to use. However, it has not been successfully used on a process scale (Hughes *et al.*, 1971).

Wet milling involves agitation of a cell suspension mixed with small glass beads. This is usually conducted in bead mills that have been adapted from the paint industry (Hopkins, 1991; Schütte and Kula, 1993). Bead mills consist of a (horizontal) cylindrical chamber surrounded by a cooling jacket. A shaft rotates on the chamber's axis, and is fitted with impellors (various designs exist including discs, rings, and pins) that act to accelerate the mixture of beads and cell suspension in a radial direction. This results in breakage of the cells (Schütte and Kula, 1993). Breakage possibly occurs due to compaction, shear action or energy transfer between beads and cells (Middelberg, 1995). The effectiveness of the technique increases with cell size, and hence is more applicable for disruption of yeasts than bacteria.

A variety of high-pressure flow devices (homogenizers) are used to release intracellular products. These all work by forcing a cell suspension through a valve assembly or orifice with a high pressure drop. Non-specific cell breakage results. Important variables include the operating pressure and the design of the discharge valve. The exact mechanism of cell breakage remains uncertain (Ayazi Shamlou *et al.*, 1995). Repeated passes through a homogenizer are usually needed for complete product release, and also act to decrease the size of cell-wall debris.

1.1.4 Combined methods

Numerous studies have demonstrated that mechanical disruption can be improved by a non-mechanical pre-treatment of the cells that reduces the mechanical strength of the cell wall. *Saccharomyces cerevisiae* cells have been pretreated using an enzyme (Zymolyase, 2 hours) before high pressure homogenization (Microfluidizer, 95 MPa) to increase disruption from 32% after 4 passes without pretreatment, to virtually complete disruption with pretreatment (Baldwin and Robinson, 1990). *Bacillus cereus* has also been enzymatically pretreated (cellosyl, 0.5 mg/g wet cells) before mechanical ball milling and homogenisation. These pretreatments increased disruption from 40% to 98% after one homogenizer pass at 70 MPa (Vogels and Kula, 1992). *E. coli* has been pretreated with EDTA-lysozyme to marginally increase disruption in a Microfluidizer (Lutzer *et al.*, 1994). High temperature or alkaline pH shock prior to homogenization have been shown to be preferred treatments for the extraction of polyhydroxybutyrate (PHB) from *Alcaligenes eutrophus* (Harrison *et al.*, 1991a; Harrison, 1990).

1.1.5 Choice of Method

In general terms, the cell disruption step aims to achieve the following goals (Schütte and Kula, 1993):

- to release the maximum amount of product (at the lowest cost),
- to avoid secondary alteration of product (*e.g.* denaturation, proteolysis, oxidation), and
- to minimise the impact of the disruption step on the performance of subsequent process units.

Whilst a large number of techniques suitable for releasing preparative scale amounts of intracellular products have been reviewed, very few adequately meet the above criteria and are used in industrial practice. Physical methods generally have very low efficiency, and are not used industrially. In general, chemical methods alone result in low levels of protein or product release (except for periplasmic proteins) and are highly dependent on the type and physiological state of the microorganism. The addition of chemicals may be undesirable in subsequent process steps (Hopkins, 1991) and may potentially contaminate

or even inactivate the final product (White and Marcus, 1988). Whilst enzymatic methods do appear promising, the current cost of enzymes tends to be prohibitive for industrial-scale use.

Currently, the mechanical methods of bead milling and high-pressure homogenization are preferred for large scale use, with high-pressure homogenizers most widely used (Schütte and Kula, 1993). These mechanical methods offer advantages of continuous operation, short residence time (to minimise product degradation) and contained operation (Keshavarz *et al.*, 1987). They also have low operating costs compared with chemical or enzymatic addition, and may be readily cleaned and validated.

As high-pressure homogenizers are the preferred method of cell disruption, this unit operation is the logical choice for further examination in this thesis. The following section contains a detailed review of high-pressure homogenizers, the variables that affect their operation, and models used to describe their efficiency.

1.2 High-Pressure Homogenization

High-pressure homogenizers were first used in Europe in the 1890's for processing high fat products such as artificial butter (Pandolfe, 1982). Since that time, homogenizers have been adapted to the process of microbial cell disruption. Although there are several different types of homogenizers available, they all act by passing the cell suspension through a narrow constriction (a valve or orifice) with a high associated pressure drop. Some high-pressure homogenizers that have been reported in the literature are described in section 1.2.1. Previous studies of the operating characteristics and modelling of high-pressure homogenizers are then reviewed (section 1.2.2). This leads into a discussion of the need for further examination of the homogenization process at a fundamental level (section 1.2.3). The aims and scope of this thesis are then outlined at the end of this chapter (section 1.3).

1.2.1 High-Pressure Homogenizers

A high-pressure homogenizer may be considered to be any device that passes a cell suspension through a restriction, under high pressure, to cause cell breakage. Equipment that is consistent with this definition rages from the laboratory scale French Press to industrial scale Manton-Gaulin type homogenizers. Some homogenizers also interact a high velocity jet with either a stationary surface or second jet. The following examples are not exhaustive, nor do they imply that these are the most useful homogenizers available. However, they serve to illustrate that although a range of homogenizers have been produced, with each having a different design, they all share a few essential features.

French Press

The French Press (Milner *et al.*, 1950) is commonly used on a laboratory scale. It consists of a thick walled steel cylinder, with a small orifice and needle valve at its base. A piston with a pressure seal is fitted to the bore of the cylinder and pressure is applied to the cylinder using a hydraulic ram (Fig. 1.3). Approximately 40 mL of cell suspension is homogenized by forcing the cell suspension through the needle valve at pressures of 35 to 270 MPa (typically 100 MPa for common application).

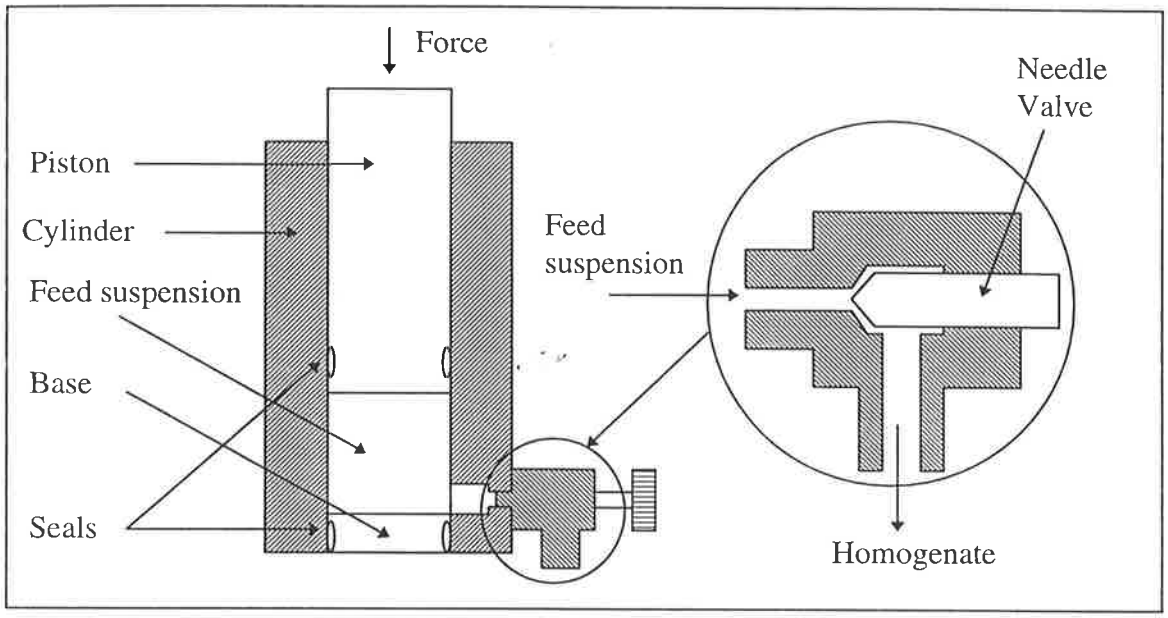

Figure 1.3: Schematic diagram of the French Press.

Stansted Disrupter

The Stansted Disrupter was designed to operate continuously and disrupt larger quantities of material than a French Press. However, it does not appear to have gained widespread usage. A ball valve is used in place of the French Press's needle valve, and continuous operation is achieved through the use of an electric or pneumatic pump capable of delivering pressures up to 270 MPa at a rate of 10 L h^{-1} (Kelemen and Sharpe, 1979).

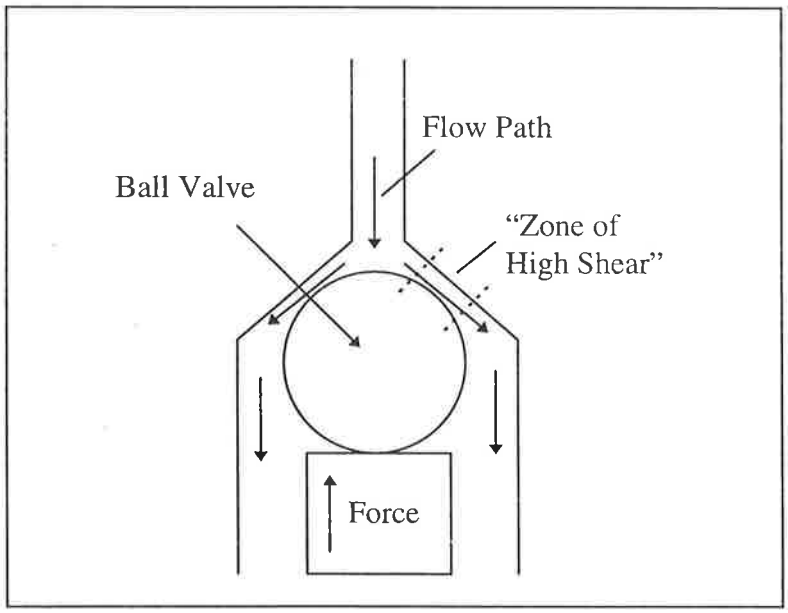

Figure 1.4: Schematic diagram of the disruption valve in the Stansted Cell Disrupter.

CSL Disrupter

The CSL Disrupter uses a hydraulically driven piston to force a cell suspension through a narrow orifice in the same way that a French Press does. Pressure up to 270 MPa may be achieved, with systems available to handle batch volumes of 10 mL or be operated continuously at 200 mL min^{-1}. The suspension is cooled as it impacts onto a target (Collins *et al.*, 1996). The device is relatively new and its commercial importance is yet to be determined.

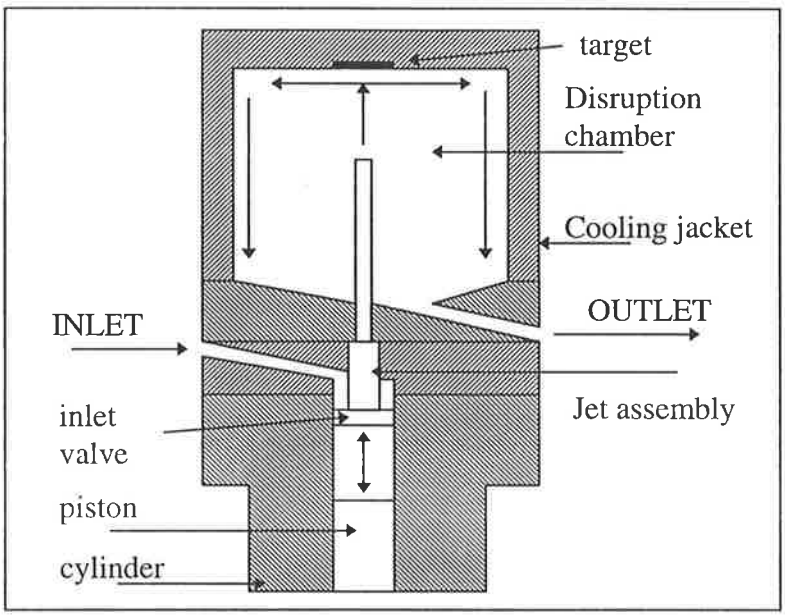

Figure 1.5: Schematic view of the batch version of the CSL Disrupter.

Manton-Gaulin Homogenizer

Manton-Gaulin homogenizers are the most widely used cell breakage unit for industrial applications. The Manton-Gaulin homogenizer consists of a positive displacement pump that forces a cell suspension through a spring loaded (or hydraulically controlled) valve assembly (Fig. 1.6). As the fluid is compressed, the valve is forced away from the valve seat and the suspension is accelerated radially into the small gap between the valve and valve seat. The cell suspension leaves the valve, and forms a radial jet that is stagnated against the impact ring. It then exits the valve assembly at essentially atmospheric pressure. The APV-Gaulin 15M homogenizer is commonly reported in literature (Hetherington *et al.*, 1971; Keshavarz Moore *et al.*, 1990; Middelberg *et al.*, 1991) and would appear to have the status of the "reference" homogenizer. It is a small capacity machine with a nominal flow rate of 56 L h^{-1} and a maximum operating pressure of 70 MPa. In addition to APV-Gaulin (Everett, USA), Manton-Gaulin type homogenizers are

also produced by APV-Rannie (Copenhagen, Denmark), Bran + Luebbe (Darmstadt, Germany) and Niro-Soavi (Parma, Italy). Homogenizers providing pressures up to 1500 bar and flow rates of approximately 70 to 10000 L h^{-1} are readily available from these manufacturers, most with valve designs tailored for cell disruption applications.

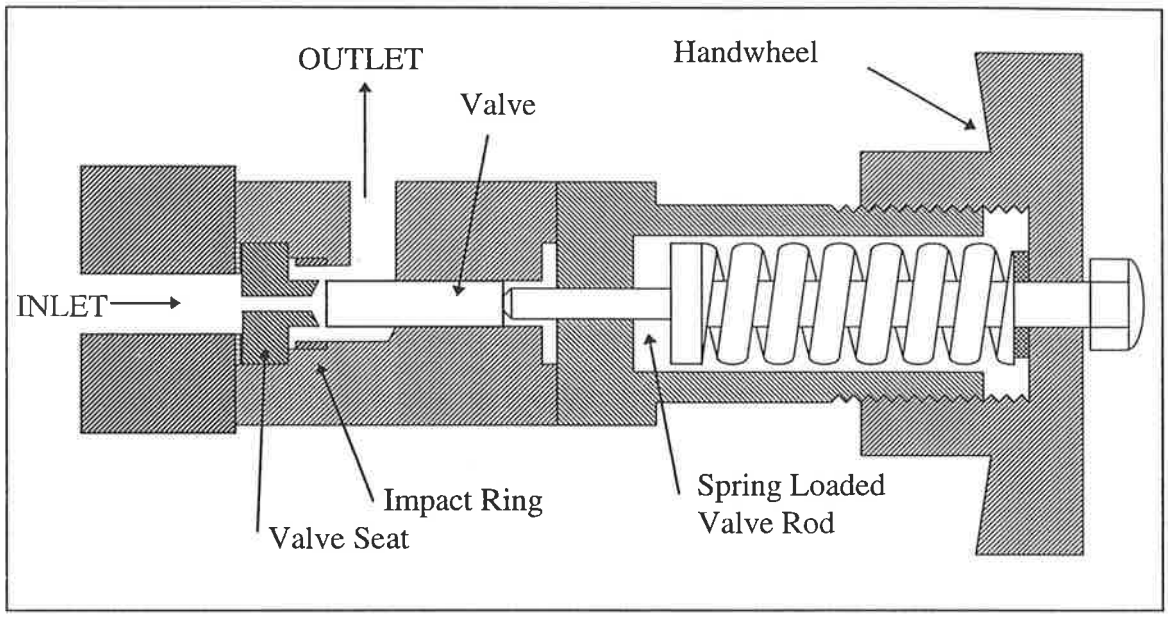

Figure 1.6: Schematic of valve assembly in APV-Gaulin 15M homogenizer.

Microfluidizer®

The Microfluidizer® uses an air driven pump to raise cell suspensions to pressures of up to 140 MPa. The cell suspension is fed into an interaction chamber, which produces two streams that are impacted together at high velocity (Fig 1.7).

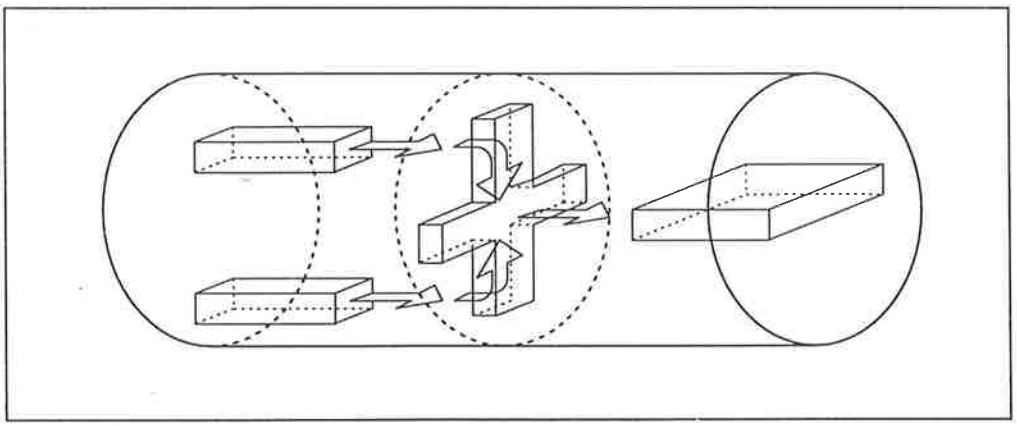

Figure 1.7: Schematic view of disruption chamber in Microfluidizer homogenizer (redrawn from Sauer *et al.*, 1989).

1.2.2 Previous Homogenizer Studies and Modeling

The first application of high-pressure homogenizers to cell-disruption was probably in the early 1930's to release vitamins from beer during fermentation (Lux, 1932), although this process was not widely adopted. Homogenizers subsequently received attention in the 1960's and 1970's for the release of single-cell protein (SCP) used as feed (Tannenbaum and Miller, 1967). Because of the SCP application, many studies have used yeasts as the test organism. With the introduction of intracellular recombinant protein production in the late 1970's, high-pressure homogenization has continued to receive attention in the literature (particularly for the disruption of *Escherichia coli*) and is still an active field of research.

Studies have elucidated the main variables that influence cell disruption efficiency, and have also modelled the disruption process with varying levels of complexity. Disruption efficiency is influenced by both equipment related (*e.g.* design and operating conditions) as well as cell suspension related (*e.g.* microorganism, suspension temperature) variables. The observed effects of these variables and the current numerical models are now reviewed.

Operating Pressure

Disruption efficiency is strongly influenced by pressure, and increases with homogenizer operating pressure drop (Milner *et al.*, 1950; Hetherington *et al.*, 1971; Kelemen and Sharpe, 1979; Sauer *et al.*, 1989; Collins *et al.*, 1996). In some cases, there is little or no cell disruption below a certain critical pressure (Kelemen and Sharpe, 1979; Engler, 1979). At higher pressures, disruption begins to level off and may or may not approach complete cell breakage (Keshavarz *et al.*, 1987; Collins *et al.*, 1996). This results in a sigmoidal disruption versus operating pressure relationship.

Valve Design

Valve design has been examined most extensively using the APV-Gaulin 15M homogenizer, as many valve and seat designs are available for comparison (*e.g.* Fig. 1.8). In general, knife-edge type valve-seats are superior to standard or flat-edged valve-seats (Pandolfe, 1992; Hetherington *et al.*, 1971; Keshavarz Moore *et al.*, 1990) with only one study suggesting the contrary (Madsen and Ibsen, 1987). The jet-impingement phenomenon is also important for cell-disruption (Engler, 1979) and hence valve designs

that incorporate an impact ring are superior for cell-disruption (Madsen and Ibsen, 1987; Keshavarz Moore *et al.*, 1990). Through these observations, Kesahavarz Moore *et al.* (1990) demonstrated that, at a given operating pressure and flow-rate, disruption efficiency increases as impact distance and valve gap decrease. It has been suggested that there are two disruption mechanisms in a homogenizer: one in the valve (related to pressure drop) and one in the impingement region (related to stagnation pressure), with the impingement region responsible for approximately 80% of the overall yeast disruption efficiency (Engler, 1979; Keshavarz Moore *et al.*, 1990).

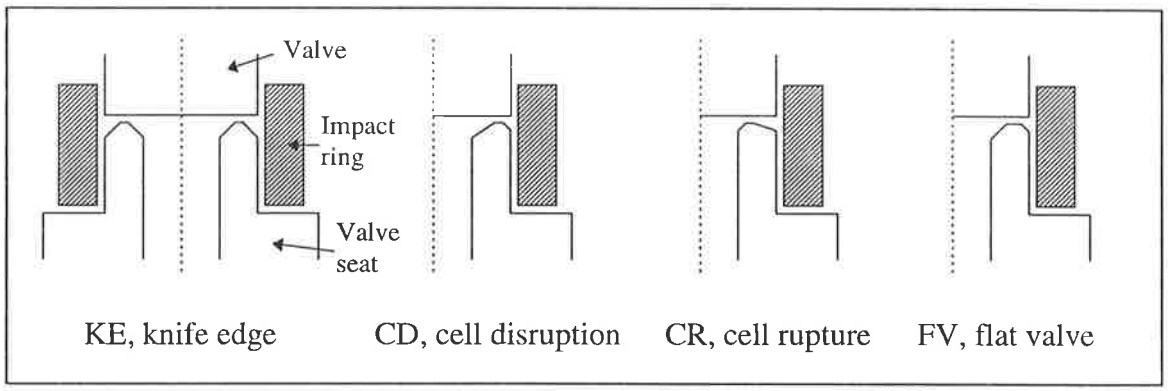

Figure 1.8: Schematic diagram of various APV-Gaulin homogenizer valve and valve seat designs, in decreasing order of effectiveness for yeast disruption from left to right (After Keshavarz Moore *et al.*, 1990).

Homogenizer designs that incorporate a second stage and hence back-pressure are not generally used for cell-disruption applications. Kula and Schütte (1987) report that back-pressure significantly decreases disruption efficiency, whereas Büschelberger (1987) reports that some back-pressure is important to achieve optimal disruption. It is likely that the effect of back-pressure is dependent on other aspects of the homogenizer's valve design. A second stage may, however, be used to break up DNA in the homogenate from the first stage.

Number of Passes

Disruption increases with each homogenizer pass, and is often reported to be first order with respect to the number of homogenizer passes (Hetherington *et al.*, 1971; Augenstein *et al.*, 1974; Engler and Robinson, 1981; Harrison *et al.*, 1991b). However, overall first order kinetics is likely to be a limiting case. Siddiqi and Titchener-Hooker (1994) have shown that the disruption rate per homogenizer pass for cells of a given diameter increases with cell size and homogenizer operating pressure. Hence, overall first-order kinetics will only

apply for a cell population with a sufficiently narrow size distribution. A size dependent disruption rate is also able to explain why other workers have observed a decreased disruption rate after the first homogenizer pass (Brookman and Davies, 1973; Whitworth, 1974; Madsen and Ibsen, 1987; Sauer *et al.*, 1989; Büschelberger and Loncin, 1989; Pittroff *et al.*, 1992, 1993) and the observation that disruption may plateau below 100% (Whitworth, 1974; Büschelberger and Loncin, 1989; Harrison *et al.*, 1991b; Pittroff *et al.*, 1992, 1993). In an extreme case, Kelemen and Sharpe (1979) have reported that after disrupting *Lactobacillus casei* to 50% in a single homogenizer pass, no further disruption could be achieved in subsequent passes unless the initial homogenizing pressure was exceeded.

Suspension Temperature

Disruption efficiency is usually reported to be temperature dependent, with increased disruption efficiencies at higher temperatures for *Saccharomyces cerevisiae* (Hetherington *et al.*, 1971), *Escherichia coli* (Middelberg *et al.*, 1991) and *Alcaligenes eutrophus* (Harrison *et al.*, 1991b). This may be connected to the impact effect present in the APV-Gaulin 15M homogenizer used in these three studies, as Büschelberger and Loncin (1987) report that suspension temperature has no significant effect on disruption.

The maximum temperature that can be used during homogenization is limited to approximately 30°C to prevent protein and nucleic acid denaturation (Hetherington *et al.*, 1971). Suspensions are often homogenized at 0 - 10°C to ensure no thermal denaturation will occur. A suspension temperature rise of approximately 0.24°C MPa^{-1} occurs over the homogenizer valve as pressure energy is ultimately converted to thermal energy in the homogenate. This temperature rise effectively limits the maximum homogenization pressure that can be used to prevent thermal denaturation problems. Also, homogenates must be cooled between subsequent homogenizer passes to offset this temperature increase.

Flow Rate

Flow rate does not appear to have a significant effect on disruption efficiency, as disruption efficiency at a given homogenizing pressure is the same in lab and production scale homogenizers for both *Saccharomyces cerevisiae* and *Escherichia coli.* These homogenizers have different flow rates, but are fitted with the same valve design (Hetherington *et al.*, 1971; Higgins *et al.*, 1978; Schütte and Kula, 1993). Some small

effects of flow rate have been observed. Brookman (1975) reported that disruption efficiency shows a slight decrease as the flow rate through a needle valve increases. Collins *et al.* (1996) report a slight increase in disruption efficiency as orifice diameter (and hence flow rate) are increased at a given pressure drop.

Cell Concentration

Cell concentration is generally reported to have no significant effect on disruption efficiency, except at very high concentrations (Hetherington *et al.*, 1971; Brookman and Davies, 1973; Brookman , 1975; Agerkvist and Enfors, 1990; Pittroff and Schubert, 1990; Harrison *et al.*, 1991b; Milburn and Dunnill, 1994). However, Sauer *et al.* (1989) reports that disruption efficiency increases with cell concentration, whereas Doulah *et al.* (1975) and Middelberg *et al.* (1991) have found that disruption efficiency decreases with cell concentration. With high cell concentrations, the viscosity of the resulting homogenate causes processing difficulties in subsequent units (Agerkvist and Enfors, 1990; Harrison *et al.*, 1991b). Hence, it is viscosity rather than disruption efficiency considerations that influence the upper limit for cell concentration.

Microorganism and Culture Conditions

The cell size, cell shape and strength of the cell wall are important factors that determine the ease of cell disruption (Kelemen and Sharpe, 1979; Engler, 1985). In turn, these factors are influenced by genetics (microorganism, strain), development (growth phase) and environment (carbon source, nutrients). Whilst there is not enough information available to predict *a priori* the relative resistance of various organisms to homogenization (Engler, 1985), some generalisations can be made:

- gram (-) bacteria are easier to disrupt than gram (+) bacteria, which are easier to disrupt than yeasts (Wimpenny, 1967; Kelemen and Sharpe, 1979; Keshavarz *et al.*, 1987),
- rods and bacilli are easier to disrupt than cocci (Wimpenny, 1967; Kelemen and Sharpe, 1979; Pittroff *et al.*, 1992; 1993),
- cells grown at high growth rate (in continuous culture) or in growth phase (batch culture) are easier to disrupt than slow growth rate or stationary phase cells (Engler and Robinson, 1981; Sauer *et al.*, 1989; Harrison *et al.*, 1991b; Middelberg *et al.*, 1992a; Milburn and Dunnill, 1994),

- large cells are more easily disrupted than small cells (Doulah *et al.*, 1975; Kelemen and Sharpe, 1979; Middelberg, 1992; Siddiqi and Titchener-Hooker, 1994; Ayazi Shamlou *et al.*, 1995),
- septated *Escherichia coli* cells are more easily disrupted than non-septated cells (Hull and Middelberg, 1993), and
- cells grown in complex media are more difficult to disrupt than cells grown in simple synthetic media (Gray *et al.*, 1972).

It is difficult to determine the relative importance of each of these effects, as they are often convoluted. For example, growth phase cells may be both larger and have weaker cell walls (Engler and Robinson, 1981). The relative effect of each of these variables has not been studied in detail. However, Middelberg *et al.* (1992b) have shown that the disruptability of *Escherichia coli* can be readily correlated to cell length and degree of peptidoglycan crosslinkage (see *Modeling*, below).

Pretreatments

Pretreatments that are able to modify cell properties have been used to successfully improve disruption efficiency. The most commonly reported example is to pretreat cells with a lytic enzyme (*Micrococus luteus* + lysozyme (Büschelberger, 1987), *Saccharomyces cerevisiae* + Zymolyase (Baldwin and Robinson, 1990), *Bacillus cereus* + cellosyl (Vogels and Kula, 1992) and *Candida utilis* + Zymolyase (Baldwin and Robinson, 1994) all result in significantly improved disruption efficiencies). Chemical pretreatments have also been successfully implemented. These include *Escherichia coli* + EDTA-lysozyme (Lutzer *et al.*, 1994) and the subjecting of *Alcaligenes eutrophus* to high temperatures and alkaline pH shock prior to disruption (Harrison, 1990). These pretreatments, which may not be able to disrupt cells on their own, weaken the cell wall enough to significantly improve the disruption efficiency observed during homogenization.

However, not all pretreatments are favourable. Pretreatments that have resulted in reduced disruption efficiency include increasing the osmotic concentration of the suspending fluid (Büschelberger, 1987), freezing and thawing (Milburn and Dunnill, 1994) and thermal deactivation (Collis *et al.*, 1995). All of these pretreatments act to reduce the size of the cell, making the cell wall "flaccid" (Milburn and Dunnill, 1994). These flaccid cells will have reduced wall tension and will require higher mechanical loadings to achieve cell disruption (Büschelberger, 1987).

Other

Cell disruption is usually determined indirectly from protein release (Hetherington *et al.*, 1971) or from measurements of intact cell volume fractions (Middelberg *et al.*, 1991). The fractional release of specific products is not necessarily equal to the fractional protein release. Follows *et al.* (1971) have shown that periplasmic enzymes are released more quickly than soluble protein, and mitochondrial or plasma-membrane associated enzymes more slowly. Harrison *et al.* (1991b) have reported that DNA release is slower than protein release. This was explained in terms of a two-stage process involving a primary cell rupture followed by disintegration. In addition to product release kinetics, homogenization has been studied to determine the kinetics of:

- Enzyme degradation. Although enzymes are not generally degraded in the homogenizer (Follows *et al.*, 1971), particularly labile enzymes are deactivated (Augenstein *et al.*, 1974). This will occur with high molecular weight or shear sensitive membrane associated enzymes (Keshavarz *et al.*, 1987).

- Cell-wall debris micronisation. Once cells are broken, the homogenizer continues to micronise cell debris with each subsequent pass (Agerkvist and Enfors, 1990; Siddiqi *et al.*, 1995; 1996).

Modeling

The first model for cell disruption was a simple kinetic expression to reflect the first order disruption with homogenizer pass and power law dependence of pressure observed by Hetherington *et al.* (1971) and is given as Eq. (1.1).

$$\log\left(\frac{1}{1-R}\right) = k_1 N P^a \tag{1.1}$$

Values of the pressure exponent, a, between 1.9 and 2.9 have been found for *Saccharomyces cerevisiae* (Follows *et al.*, 1971; Kula *et al.*, 1990), 0.64 to 2.2 for *Escherichia coli* (Gray *et al.*, 1972; Middelberg *et al.*, 1992a) and 1.6 to 3.1 for *Alcaligenes eutrophus* (Harrrison *et al.*, 1991b). Whilst this model is relatively simple, it is only descriptive rather than prescriptive and hence of limited applicability. The rate constant, k_1, varies over two orders of magnitude for different cultures of *E. coli* in an APV-Gaulin 15M homogenizer (Middelberg *et al.*, 1992a). Also, the pressure exponent varies with the

range of operating pressures examined (Dunnill and Lilly, 1975; Engler and Robinson, 1981).

In spite of the deficiencies of simple kinetic models, they are still widely used. Eq. (1.1) has been modified to model non-first order disruption processes (Sauer *et al.*, 1989; Pittroff *et al.*, 1993) (Eq. 1.2).

$$\log\left(\frac{1}{1-R}\right) = k_1 N^{k_2} P^a \tag{1.2}$$

Sauer *et al.* (1989) report values of k_2 between 0.28 and 0.94 for *E. coli.* Pittroff *et al.* (1992) present an alternative kinetic expression to model disruption processes (Eq. 1.3).

$$R = \frac{N}{k_3 + k_4 N} \tag{1.3}$$

In addition to accounting for non-first order disruption processes, Eq. (1.3) also allows for disruption to asymptote below 100%. Pittroff *et al.* (1992) show that for pressures of 50 MPa, complete disruption of yeast and bacterial rods can be achieved within a finite number of homogenizer passes, but the disruption of bacterial cocci will asymptote below 100% ($1/k_4 < 1.0$).

Harrison *et al.* (1991b) used Eq. (1.1) to model soluble protein release from *Alcaligenes eutrophus*, but modified it to model DNA release, which was slower than the release of soluble protein (Eq. 1.4).

$$\log\left(\frac{1}{1-R}\right) = k_5 (N - 0.75) P^a \tag{1.4}$$

Middelberg (1995) has reviewed the proposed physical processes responsible for the disruption of fat globules and microorganisms during homogenization. For microorganisms, proposed processes include the rate and magnitude of the pressure drop (Brookman, 1975; Kelemen and Sharpe, 1979), turbulence (Doulah *et al.*, 1975), cavitation (Save *et al.*, 1994) and jet impingement (Engler, 1979). In an attempt to provide more physically meaningful models for cell-disruption efficiency, various studies have produced models with either a mechanistic or physical basis.

The model proposed by Doulah *et al.* (1975) assumes that cells are buffeted by turbulent eddies, and oscillate. When the kinetic energy of oscillation exceeds an effective cell-surface energy, disruption occurs. The maximum diameter of a cell surviving homogenization was related to operating pressure by Eq. (1.5),

$$d_{\max} \propto \frac{\gamma}{P} \tag{1.5}$$

where γ represents a "wall strength". However, the model is not based on a proven mechanism of disruption, no method for estimating wall strength was suggested, and it does not explain the strong dependence of disruption on impact distance.

Engler (1979) demonstrated that impingement stresses were important for cell disruption, and correlated disruption efficiency with stagnation pressure:

$$P_S = \frac{1}{2}\rho U^2 \tag{1.6}$$

The stress created within a fluid upon impingement is equal to the dynamic pressure of the fluid acting against the plate. A reasonable approximation assumes this stress acts on the cell, justifying the use of stagnation pressure as a correlating variable. Keshavarz Moore *et al.* (1990) subsequently developed an expression to relate homogenizer stagnation pressure (and hence disruption rate) to valve gap and impact distance:

$$P_S \propto \frac{1}{Y^2 h^2} \tag{1.7}$$

Although this expression was developed for a geometrically dissimilar jet, a curvilinear relationship between disruption and the stagnation pressure of Eq. (1.7) was observed for a range of valve seats and impact rings at a fixed operating pressure.

Recently, Ayazi Shamlou *et al.* (1995) have presented their elongational stress model for the disruption of microbial cells during high-pressure homogenization. It was assumed that cell breakage occurs due to viscous extensional shear forces, with a pseudo-Capillary number defining the critical criterion for cell breakage. An expression was presented to correlate the maximum stable cell diameter with homogenizer operating conditions and design variables:

$$d_{\max} = const.\sigma t \left\{ r_V r_i \ln\left(\frac{r_V}{r_i}\right)^{1/3} \right\} \frac{1}{Q^{2/3}\mu^{2/3}\Delta P^{1/3}} \tag{1.8}$$

Qualitatively, the model predicts the effect of homogenizer pressure, impact distance, and cell diameter on disruption efficiency. It contains separate terms to account for valve geometry (term in {}) and cell wall properties (σt). However, Eq. (1.8) suggests that disruption efficiency will show a strong increase with flow rate, which has not been observed in practice. Also, to show that viscous extensional forces are high enough to cause cell disruption, the model assumes that the cell suspension has a Trouton ratio of 1000. This value may be typical for highly non-Newtonian polymer melts, but is unlikely to be representative of a cell suspension, which is more likely to have a Trouton ratio of 3.

The wall-strength model was developed to provide a rational basis for homogenizer modelling (Middelberg *et al.*, 1992a; 1992b). As in the elongational stress model, system and cell properties are separated into separate parameters. Essentially, the wall-strength model proposes that feed cells have a particular strength-distribution, $f_S(S)$, which is a characteristic of the cell determined by their properties (wall structure, size, etc). During homogenization, these cells experience a stress imposed by the homogenizer. The distribution of stresses can be represented by some function $f_D(S)$, which is a characteristic of the homogenizer system. Disruption is calculated using Eq. (1.9).

$$R = 1 - \int_0^\infty \left(1 - f_D(S)\right)^N f_S(S)\, dS \tag{1.9}$$

However, as the strength- and stress-distributions were not actually known, functions were proposed for the two distributions and parameters were determined by regression. The strength-distribution is modelled as a Gaussian distribution,

$$f_S(S) = \frac{1}{\sigma\sqrt{2\pi}} \exp\left[\frac{-(S-\bar{S})^2}{2\sigma^2}\right] \tag{1.10}$$

and an assumed form for the stress distribution is based on the impact of small cylinders against a plane surface:

$$f_D(S) = \frac{\left(mP^n\right)^d}{S^d + \left(mP^n\right)^d} \tag{1.11}$$

Data from the disruption of twenty one different *E. coli* cultures in an APV-Gaulin 15M homogenizer were regressed to determine the parameters in Eqs (1.10) and (1.11). Disruption data could be adequately described when four parameters were kept constant (m = 12.6, n = 0.393, d = 7.85 and σ = 3.82). Variability in the disruption data was accounted for solely by varying the mean effective cell strength, which was different for each culture. This parameter was correlated with the fractional peptidoglycan crosslinkage (measured by high performance liquid chromatography) and the average cell length (measured using image analysis). This correlation was given as Eq. (1.12).

$$\overline{S} = 33X - 8.0L + 48.82 \tag{1.12}$$

However, despite the ability of the wall-strength model's to predict the disruption of *E. coli* independent of culture variability in an APV-Gaulin 15M homogenizer, it still remains dependent on empirical functions. Also, it contains a total of five empirical coefficients; a redundancy analysis (appendix A1) shows that there is high degree of interaction and redundancy if parameters are not predetermined or otherwise constrained. Consequently, simultaneous regression for all model parameters, without prior knowledge of either function, does not give physically meaningful parameter values. As a result, the empirical strength distribution cannot be extrapolated to new homogenizer systems.

1.2.3 Unresolved Issues in Homogenization

As discussed in section 1.1.5, one of the major factors influencing the choice of a cell disruption technique is the need to release the maximum amount of product at the lowest cost. This process of optimisation was discussed in the introduction to this chapter, and the tool of mathematical optimisation was presented.

To conduct a meaningful mathematical optimisation, sound mathematical models of process units are required. The mathematical models that have been developed for high-pressure homogenization were reviewed in section 1.2.2. It is apparent that these mathematical models have key deficiencies. The simple kinetic rate models require

empirical coefficients, which depend on properties of the feed cells and the homogenizer system in an undetermined fashion. Alternative models attempt to separate system and culture specific factors that affect disruption, and are developed with a mechanistic basis for the disruption process. These alternative models include the turbulence model (Eq. (1.5)), the extensional shear model (Eq. (1.8)) and the wall strength model (Eq. (1.9)). Of these models, it is only the wall strength model that has been demonstrated for quantitative disruption modeling. In the development of the wall strength model, Middelberg (1992) concluded that obtaining truly general expressions for the stress and strength distributions within the model was unrealistic and that approximate distributions would suffice. He also deemed that direct and independent measurement of the distributions was impractical, and resorted to empirical approximations. However, the use of empirical approximations resulted in a model that is over-specified and shows parameter redundancy. As a result, the empirical functions are not truly independent, even though they are able to describe and even predict cell disruption efficiency for a specified homogenizer system and microorganism.

Independent characterisation of the strength distribution of cells and the distribution of stresses applied by the homogenizer represents a key challenge for the understanding and modeling of the homogenization process. In developing the wall-strength model, Middelberg (1992) suggested that an independent determination of these distributions was important, but was impractical for *E. coli* for the following reasons:

- The stresses which cause disruption are unknown. It is not clear which experimental measurements are required to determine the stress distribution.
- It is impractical to place "stress" measuring transducers in the closed homogenizer system. Such devices, if they can be defined, will probably alter the actual distribution.
- It is not clear which strength characteristics of the cell provide resistance to disruption, so it is not clear how to measure cell strength.
- The strength of materials often depends on the rate of the applied stress. It is therefore possible that any independent measurement of strength will not be representative of the true resistance to disruption (*e.g.* strength measurements done at low rates of deformation may not be representative of the cell's response to sudden impact or decompression).
- It may not be possible to determine the strength of bacteria considering their size. In some excellent work, Zhang *et al.* (1992) have measured the strength of animal cells

using a micromanipulation technique. These are however, considerably larger than bacteria (ca. 10-15 μm diameter). Furthermore, they lack a crosslinked peptidoglycan layer and may therefore be modelled using a simple isotropic surface tension approach.

Obtaining the answers to these questions requires a better understanding of the fundamental processes that occur during homogenization. These answers are not only important for disruption modeling, but also for the fundamental understanding of the cell disruption process. Hence, finding these answers represents important (but as yet unresolved) issues in cell disruption by high-pressure homogenization. The aim of this thesis is to address these issues, with a view to characterising cell strength and homogenizer stress distributions and hence improving the utility of homogenizer models. These aims and the structure of this thesis are outlined in more detail in the following section.

1.3 Aims and Structure

The aim of this thesis is to independently characterise homogenizer stress- and cell-strength distributions, and to use these distributions to model cell breakage during homogenization. However, to determine these distributions, fundamental knowledge of the homogenization process is required as outlined in section 1.2.3 above. Specifically, this thesis will determine:

- the nature of the stresses that cause cell breakage,
- the magnitude of these breakage stresses,
- the strength of microorganisms,
- the characteristics of the microorganism that resist disruption,
- the dependence of cell strength on the rate of applied stress,

This information will then be used to characterise cell strength- and homogenizer stress-distributions and hence model the cell disruption process.

Initially, chapter 2 presents an experimental study of disruption efficiency. This study confirms previous findings of the effect of valve design on homogenizer efficiency, and provides evidence for the physical processes that result in cell breakage during homogenization.

Chapter 3 provides a comprehensive analysis of homogenizer fluid mechanics. This involves experimental measurement of homogenizer valve gap and pressure profiles and stagnation width. A more complete picture of homogenizer hydrodynamics is provided by the use of analytical and numerical analysis of velocity and pressure fields within a homogenizer valve.

Although the information on homogenizer fluid mechanics does not directly determine the nature of the stresses that cause cell breakage, it is used in chapter 4 to examine the interactions between cells and the homogenizer's flow field. In addition to identifying the likely processes that cause cell breakage, this chapter also estimates the magnitude of the breakage stresses and the characteristics of the microorganism that are likely to provide resistance to cell disruption.

The mechanical or strength properties of cells is examined in chapter 5. Yeast cells are chosen for analysis due to their relatively large size compared with bacteria such as *E. coli*, which allows for direct experimental characterisation. Mechanical properties are obtained

from the analysis of micromanipulation experiments conducted on individual cells which are then analysed to determine fundamental properties of cell strength.

Chapter 6 uses the information provided in chapters 4 and 5 on homogenizer stress and cell strength to characterise cell strength- and homogenizer stress-distributions. Corrections are made to account for the dependence of cell strength on the rate of applied stress. The independent distributions are then substituted into the wall-strength model to predict disruption efficiency. In addition to providing support for the approach used to determine the stress- and strength-distributions, the results also highlight areas where further investigation is required. Simplified approaches to disruption modeling are also outlined, that do not require direct characterisation of cell culture properties, and provide an excellent description of disruption data.

Finally, the results of this study are summarised and discussed in chapter 7.

Although this thesis primarily concentrates on one homogenizer system (APV-Gaulin 15M homogenizer) and one microorganism (non-budding cells of *Saccharomyces cerevisiae*), the methods presented can be readily extrapolated or repeated for different homogenizer systems and microorganisms. Important differences that will exist for different microorganism and homogenizer systems are discussed throughout the thesis.

Chapter 2

Disruption Study*

As stated in section 1.3, determination of the physical mechanism responsible for cell disruption relies on the interpretation of experimental cell disruption data. The two most important variables that determine cell disruption efficiency (and can thus be assumed to reflect the disruption mechanism) were shown to be operating pressure and valve design (section 1.2.2).

To supplement the data provided by previous studies, this chapter examines the effect of homogenizer operating pressure and valve design on the disruption of two microorganisms (*S. cerevisiae* and *E. coli*) in different growth phases. This confirms and extends previous experimental observations and provides data for subsequent analysis.

* The data presented for Experiment A in this chapter was originally part of a research project submitted by the author for the award of B.E. (Chem) and is reproduced in this chapter. However, the analysis of this data presented within this thesis is new, and the original data is also supplemented by additional new data.

2.1 Materials and Methods

A total of three experiments were conducted. Experiment A compared the disruption of yeast (Baker's and Brewer's) over a range of homogenizer pressures and impact rings. Experiment B compared the disruption of *E. coli* over a range of homogenizer pressures and impact rings. These two experiments confirmed the "dual" nature of the homogenization process, with disruption occurring in both the homogenizer valve and at the impact ring. Experiment C then compared the effect of valve seat design on the disruption of Baker's yeast, with the impact ring removed, to study the valve region alone.

2.1.1 Cell Material

Two different organisms were examined - *S. cerevisiae* and *E. coli*.

S. cerevisiae

Baker's yeast (experiments A and C) was prepared by suspending dried Baker's yeast (Fermipan Instant Yeast, Gist-brocades, Delft, The Netherlands) in phosphate buffer (1.4 g L^{-1} DW yeast, 4 mM KH_2PO_4) and storing at 6°C for 24 h prior to disruption. This protocol provided a reproducible suspension of (stationary phase) yeast cells, with a high resistance to homogenization.

Freshly spent Brewer's yeast (Experiment. A) was obtained directly from a local brewery (The South Australian Brewing Company Ltd., Adelaide, Australia). The spent yeast was filtered through a coarse cloth to remove hops and other debris remaining from the brewing process. It was then diluted in 4 mM KH_2PO_4 buffer to provide a suspension of 1.4 g L^{-1} DW. This spent Brewer's yeast was still actively fermenting when obtained.

E. coli

E. coli cells were obtained by fermentation. Two fermentations were conducted, to obtain cells in stationary phase (experiment B1) and growth phase (experiment B2).

Fermentations were conducted in a 20 L (working volume) Chemap CF3000 fermenter. *E. coli* JM101 Ton A (Department of Microbiology, University of Adelaide) was inoculated from a shake flask into 20 L of modified C1 minimal media (composition (g L^{-1}): D-

Glucose, 3.125; NH_4Cl, 2.42; KH_2PO_4, 2.38; Na_2HPO_4, 3.9; K_2SO_4, 1.82; $MgSO_4.7H_2O$, 0.625; $FeSO_4.7H_2O$, 0.02; $MnSO_4.H_2O$, 0.0051; $ZnSO_4.7H_2O$, 0.0086; $CuSO_4.5H_2O$, 0.00076; Trisodium citrate, 0.088; Thiamine, 0.04) to give an initial absorbance (A_{600}) of less than 0.00025. Culture pH was automatically controlled at 6.8 using 25% NH_4OH. Temperature was controlled at 37°C. Dissolved oxygen was automatically controlled above 55% of saturation using cascade control on fermenter pressure (0 - 1 bar gauge), agitation (200 - 1000 rpm) and aeration rate (). Due to the low cell densities obtained, no chemical antifoam or mechanical foam breakage was required.

Experiment B1's cells were allowed to proceed to glucose exhaustion (noted by a sudden increase in oxygen concentration), and were then held at fermentation conditions for a further 3.5 hours to allow the cells to strengthen (Middelberg *et al.*, 1992b). Dissolved oxygen control was then terminated, and the broth was cooled to 7°C in the fermenter. The final fermentation optical density (A_{600}) was 3.80±0.05. This broth was maintained at 7°C for twenty hours before homogenization.

For experiment B2, the initial media composition was altered by increasing the D-Glucose concentration to 6.7 g L^{-1}. When the broth reached an optical density (A_{600}) of 3.9, the temperature setpoint of the fermenter was altered to 5°C. Additional growth occurred while the broth was cooling to give a final optical density of 5.3. Cells were fixed to prevent any further growth by the addition of formaldehyde (0.02% v/v). Reverse osmosis water was added to dilute the broth (final A_{600} of 3.9±0.05, approximately 1.4 g L^{-1} DW), which was then homogenized within four hours.

2.1.2 Homogenization

Cell suspensions were homogenized in an APV-Gaulin 15MR-8TBA high-pressure homogenizer. Homogenizer pressure measurement using the fitted gauge was supplemented with accurate pressure transients for all tests, obtained using a pressure transducer (Keller PA-22/8465I-1000, 0-1000 bar) fitted to the homogenizer's upper cap plug. The reported pressure for all data is the maximum average pressure calculated over 0.1 seconds from the measured pressure transients. The homogenizer feed temperature for all samples was 20°C.

For experiments A and B, the homogenizer was fitted with a ceramic cell-disruption (CD) valve and valve seat. Impact rings with internal diameters ranging from 9.98 to 16.95 mm were fabricated from heat treated alloy steel (ASSAB 7210M, Assab Steels, Adelaide, Australia) to supplement the standard 11 mm ceramic impact ring. A total of eight impact rings were tested, including the standard impact ring. Following the convention of Keshavarz Moore *et al.* (1990), the impact distance, *Y*, is defined as the distance between the valve and the impact ring (see Fig. 3.1)

For experiment C, disruption was conducted with the impact ring removed. A total of six valve seats were compared for disruption efficiency. Two valve seats (the APV standard and cell-disruptions seats) had chamfered inlets, and four were machined with square inlet profiles. Dimensions of these valve seats are given in Table 3.1.

2.1.3 Disruption Analysis

Two methods of disruption analysis were employed: a direct technique (analytical disk centrifuge) and an indirect technique (soluble protein release). Feed and homogenate samples were treated with formaldehyde (0.02% v/v) and stored on melting ice prior to disruption analysis (within 2 hours for soluble protein and 18 hours for analytical disk centrifuge analysis).

Direct Technique

The direct technique used was only suitable for the analysis of *E. coli*, as a reproducible protocol for the analysis of yeast could not be developed. The analytical disk centrifuge operation protocol used in this study was modified to be considerably faster and simpler than that reported previously (Middelberg *et al.*, 1991) by mixing spin and buffer fluids prior to injection, eliminating requirement for boost operation. The modified protocol is presented in Table 2.1. This modification gives a higher technique reproducibility error (approximately 3%, compared with 1.4% (Middelberg, 1992)). However, this error results in only slight increases in the final disruption error estimate, particularly at high disruption levels.

Table 2.1: Operating conditions for the analytical disc centrifuge.

Spin Fluid (SF)	15 mL 10% w/w glycerol-water
Buffer Fluid (BF)	1.0 mL water
Sample Volume and Suspension	0.5 mL phosphate buffer*
Disc Speed	8000 rpm
Gain	6
Time = 0 s	inject SF and BF
Time = 90 s	inject sample
Time = 200 s	end

*Phosphate buffer used was 20 mM Na_2HPO_4, 30 mM NaCl.

Indirect Technique

The indirect technique is suitable for the analysis of yeast and *E. coli* disruption efficiency. Soluble protein content of the supernatant was determined using the Bio-Rad Protein Assay (Bio-Rad Laboratories, Sydney, Australia). Calibration of the assay over the range of measured protein concentrations was conducted with a sample of homogenate supernatant. Samples were initially centrifuged (20 min, 14000 g) before supernatant was withdrawn. Fractional soluble protein release is calculated using Eq. (2.1).

$$R = \frac{A_h - A_f}{A_{\max} - A_f} \tag{2.1}$$

Due to the low cell concentrations used, no correction was made for solids volume fraction. Maximum soluble protein release was determined from multiple homogenizer passes at 46 or 56 MPa, using the standard impact ring and cell disruption valve seat.

2.2 Results

The effect of operating pressure and impact distance (Y, Fig. 3.1) is shown for Baker's yeast (experiment A1) in Fig. 2.1 and for Brewer's yeast (experiment A2) in Fig. 2.2.

The effect of operating pressure and impact distance is shown for glucose-exhausted *E. coli* (experiment B1) in Fig. 2.3 and for growth-phase *E. coli* (experiment B2) in Fig. 2.4.

The effect of valve seat geometry and valve inner radius (r_i, Fig. 3.1) on disruption efficiency of Baker's yeast (experiment C) is shown in Fig. 2.5.

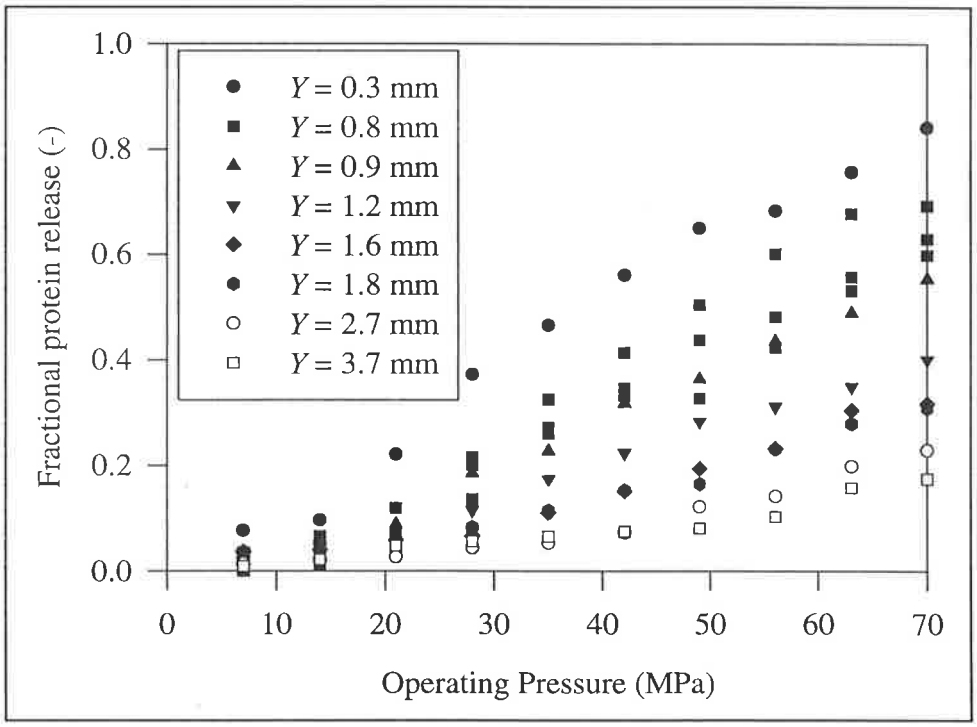

Figure 2.1: Dependence of Baker's-yeast disruption efficiency on homogenizer operating pressure for a range of impact distances.

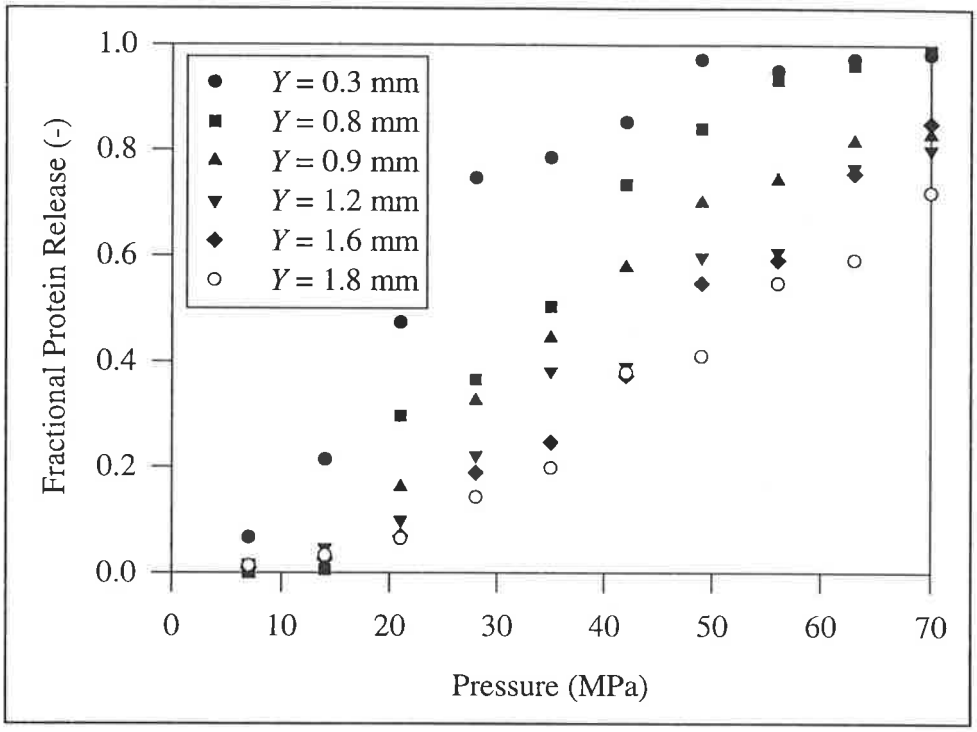

Figure 2.2: Dependence of Brewer's yeast disruption efficiency on homogenizer operating pressure for a range of impact distances (*Y*).

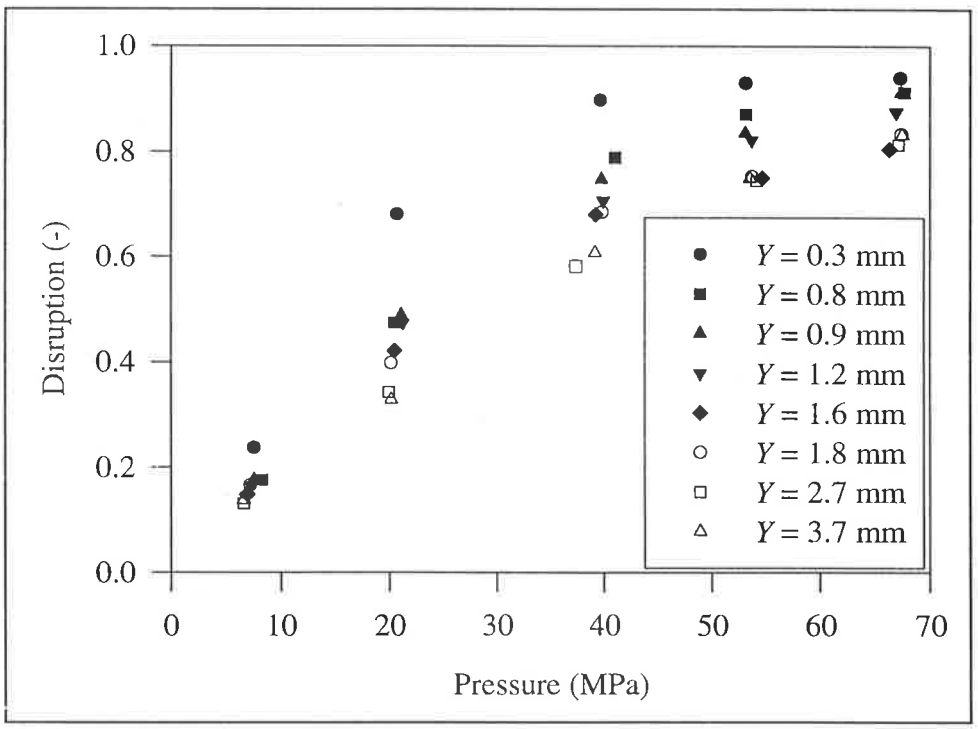

Figure 2.3: Dependence of stationary-phase *E. coli* disruption efficiency on homogenizer operating pressure for a range of impact distances (*Y*).

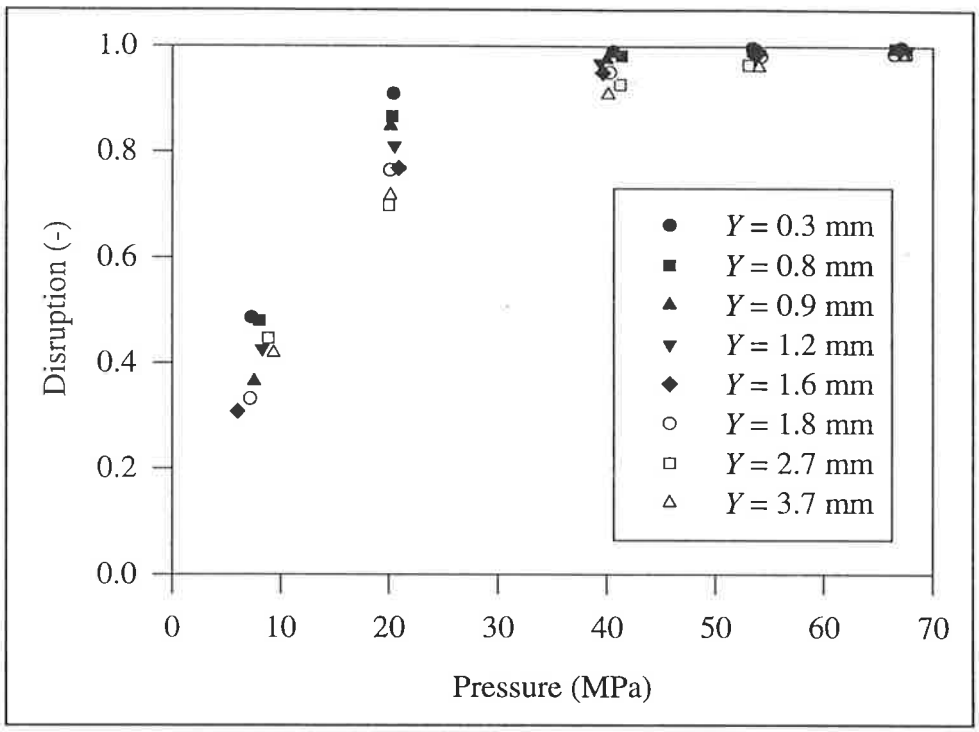

Figure 2.4: Dependence of growth phase *E. coli* disruption efficiency on homogenizer operating pressure for a range of impact distances (*Y*).

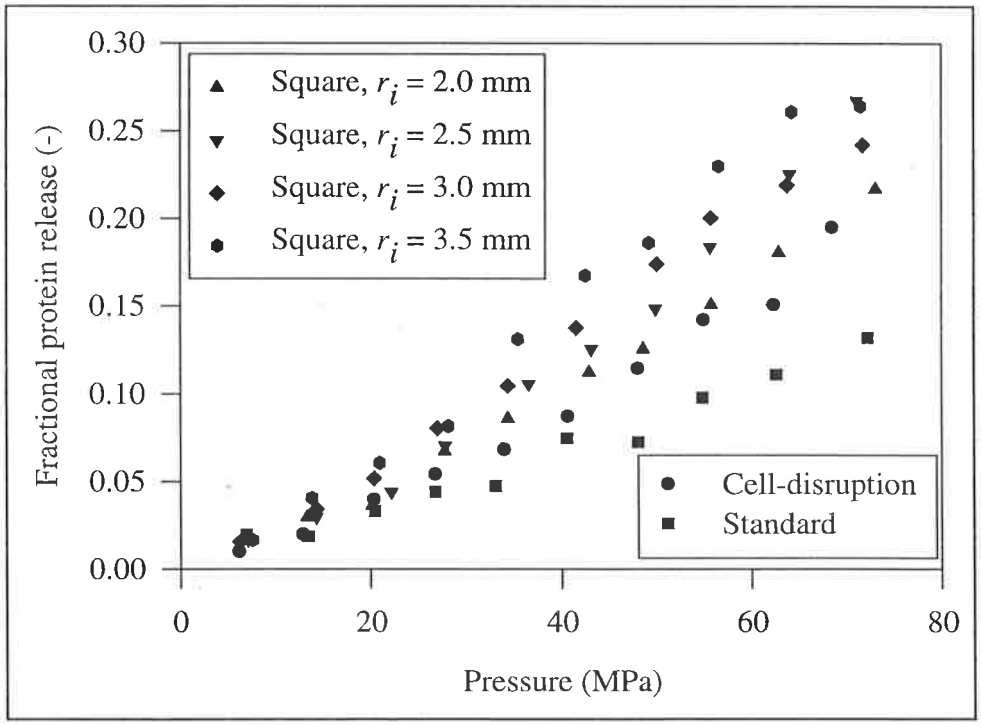

Figure 2.5: Dependence of Bakers yeast disruption efficiency on homogenizer operating pressure for a range of valve seats (differentiated by valve seat inner radius, r_i, and design).

2.3 Discussion

For each of experiments A, B and C it is apparent that disruption increases with operating pressure. For experiments A and B, growth phase cells proved much easier to disrupt than stationary phase cells, and gram (-) rods were much easier to disrupt than yeasts as expected from the review in section 1.2.2.

Experiment A confirmed the observed dependence of impact distance on the disruption of yeast as observed by Keshavarz Moore *et al.* (1990) and extends their data to a range of homogenizer pressures. Experiment B shows that impact distance is also important for the disruption of *E. coli*, but apparently not as important as it is for yeast, as high levels of cell disruption still occur at the largest impact distance.

To examine this quantitative difference in more detail, data were regressed to a modified form of Eq. (1.1):

$$\log\left(\frac{1}{1-R}\right) = k_6\left(k_7 P\right)^a \tag{2.2}$$

This form was chosen to effectively "map" each data set at different impact distance to an equivalent pressure with the standard impact ring. This was done by fixing k_7 to 1.0 for the standard impact ring, and then regressing the data by allowing a separate k_7 value for each non-standard impact ring, but a fixed k_6 and a for the given data set (non-weighted, non-linear regression). Regressed values of k_6 and a are given in Table 2.2, and the dependence of k_7 on impact distance is shown in Fig. 2.6.

Table 2.2: Regressed values of k_6 and a for experiments A and B.

Experiment	k_6 (MPa^{-a})	a (-)
A - Baker's yeast	0.00036	1.68
A - Brewer's yeast	0.00015	2.18
B1 - stationary E. coli	0.010	1.12
B2 - exponential E. coli	0.027	1.15

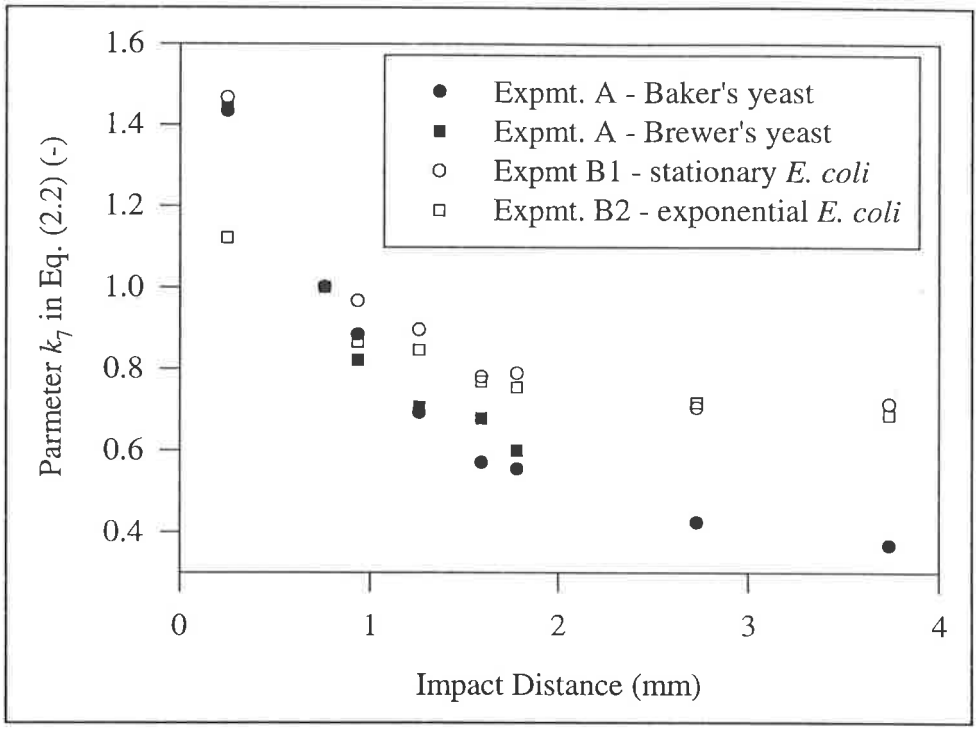

Figure 2.6: The dependence of regressed parameter k_7 in Eq. (2.2) on homogenizer impact distance.

Figure 2.6 shows a good correlation between parameter k_7 and impact distance for a given cell type. The value of k_7 of approximately 0.4 for Baker's yeast at large impact distances confirms the conclusion of Engler and Robinson (1981) that without jet impingement, pressures 2.5 times higher than those with jet impingement are required to achieve the same level of disruption. For yeast, the shortest impact distance is equivalent to a disruption pressure that is 3.5 times greater than that with the longest impact distance. However, the effect for *E. coli* is not so great, with a maximum difference of only 1.8 times. Possible causes for this difference are addressed in chapter 4.

Figure 2.5 shows the effect of valve seat design (with the impact ring removed) on the disruption efficiency for Baker's yeast. Without impact, it is apparent that square edged inlet valve seats are more effective than seats with a chamfered inlet. Also, seats with decreased land distance (distance between inner and outer valve seat radii) results in more efficient cell disruption. Explanations of these observations in terms of disruption mechanism are discussed in chapter 4.

2.4 Summary

This chapter investigated the effects of homogenization variables on cell disruption efficiency. Disruption efficiency increases with operating pressure, is higher for growth phase than stationary phase cells, and is higher for gram (-) bacteria (*E. coli*) than yeast (*S. cerevisiae*) as regularly reported in literature.

The effect of impingement on the disruption of yeast was confirmed, and was also demonstrated for *E. coli*. However, it is apparent that impingement is more important for yeast than for *E. coli*.

In the absence of jet impingement, square-edged valve seats perform better than chamfered valve seats and disruption efficiency also increases as land distance decreases.

Chapter 3

Homogenizer Fluid Mechanics

As outlined in section 1.3, examination of experimental disruption data (such as the data of chapter 2) is not sufficient to determine the mechanisms that are likely to cause cell breakage. Instead, the interactions between cells and the homogenizer, and the resulting forces applied to cells must be examined. A key requirement for such an analysis is a detailed picture of fluid mechanics within a homogenizer valve assembly.

In this chapter, homogenizer fluid mechanics are investigated experimentally, analytically and numerically. The results obtained from these investigations are used in the following chapter to investigate the interaction of cells and the homogenizer flow field, and the likely mechanism of cell breakage during homogenization.

3.1 Introduction

The APV-Gaulin 15MR-8TBA high-pressure homogenizer used in this study consists of a high-pressure positive-displacement piston-pump that forces a cell suspension through a valve unit. As shown in Fig. 3.1, the suspension is fed axially into the valve seat, and then accelerated radially into a small gap between the valve and seat. The valve gap is small for low capacity homogenizers, typically of order 10 μm at high pressures. Fluid velocities of 200-300 m s^{-1} occur in the valve gap. Once the suspension leaves the gap at high velocity, it becomes a radial jet that stagnates on an impact ring before leaving the homogenizer at atmospheric pressure.

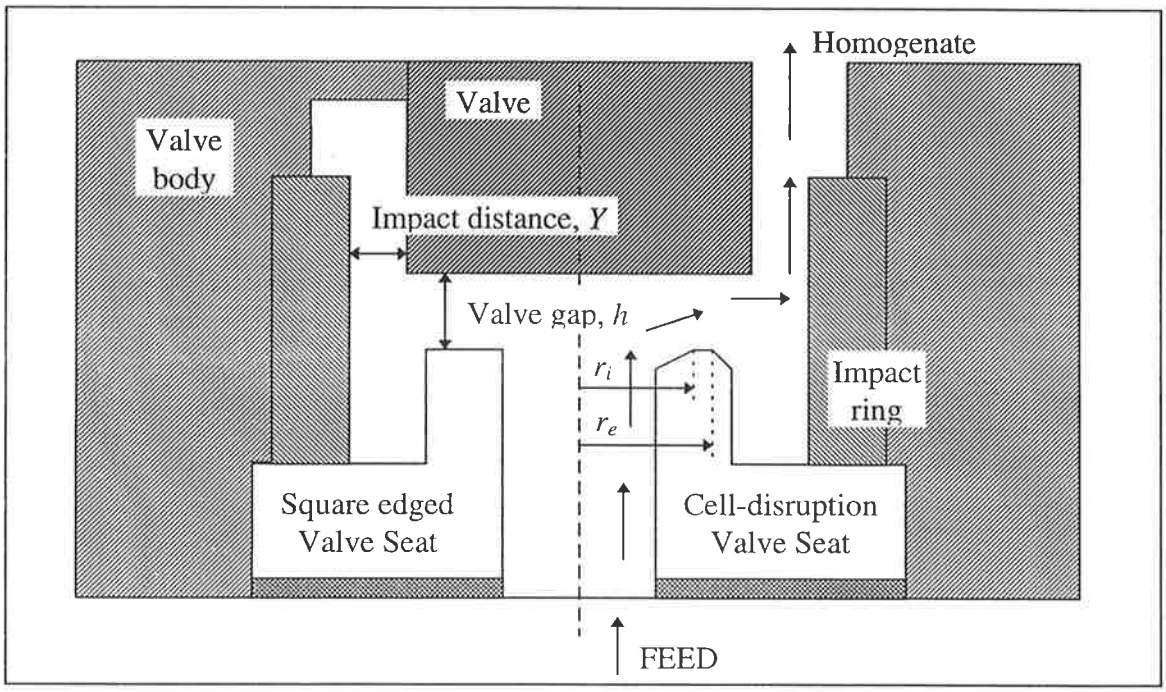

Figure 3.1: Schematic diagram of homogenizer valve assembly. A square edged inlet profile (LHS) is compared with a chamfered inlet profile on the cell-disruption valve (RHS).

For further analysis, the homogenizer flow is divided into two distinct regions: the "valve-inlet" region, where fluid is accelerated radially into (and passes through) the gap between the valve and seat, and the "impinging-jet" region, where the suspension behaves as a radial jet with a subsequent stagnation point. It is expected that there is only minimal feedback between the impinging jet and valve inlet regions. Cell disruption occurs in both the valve inlet and the impinging jet regions (Keshavarz Moore *et al.*, 1990; Ayazi Shamlou *et al.*, 1995), with the relative importance of each region dependent on valve design (Keshavarz Moore *et al.*, 1990).

In the following two sections, the valve inlet and impinging jet regions are investigated. Within these sections, expressions are developed to allow calculation of key variables that are important in determining the forces that act to disrupt cells. These expressions remove the need for numerical simulation for each new set of homogenizer operating conditions.

3.2 Valve Inlet Region

As described above, the valve inlet region consists of the developing flow of fluid issuing from a central orifice and flowing radially outwards between two parallel discs. Previous examinations of this flow geometry in homogenizer valves and other similar geometries are reviewed, highlighting the need for further information. Further information is obtained through experimental (section 3.2.2), analytical (section 3.2.4) and numerical (section 3.2.3) investigations of a homogenizer.

3.2.1 Previous studies

Numerous investigators have examined the hydrodynamics of homogenizer valves, to attempt to develop a mechanistic explanation for the dispersion of oil emulsions.

Loo *et al.* (1950) used dial gauge measurements and a hydraulic analysis to conclude that cavitation occurs during homogenizer operation. Loo and Carleton (1953) subsequently demonstrated that pressure dropped to atmospheric near the valve entrance, and that the effect of back pressure on valve gap and flow rate supported the occurrence of cavitation. McKillop *et al.* (1955) measured the homogenizer valve gap for a Manton-Gaulin homogenizer and found that valve gap decreased from 200 to 80 μm as pressure increased from 3.5 to 17.5 MPa. Kurzhals (1977) also investigated homogenizer fluid mechanics, and found that valve gap decreases with operating pressure. He concluded that cavitation occurs under normal operating conditions, and is a primary cause of milk fat globule dispersion.

Phipps (1974a, 1974b, 1975) conducted a series of studies into homogenizer valve mechanics. Visualisation experiments (Phipps, 1974a) showed that flow separated with possible cavitation at lower pressures only and that rounding of the valve inlet decreased separation effects. Pressure tappings (Phipps, 1974b) revealed that separation could be eliminated by increasing homogenizer pressure or fluid viscosity, or by decreasing flow rate. A semi-empirical expression was developed (Phipps, 1975) to relate homogenizer valve design and operating pressure to valve gap:

$$\Delta P = \frac{\rho}{4}\left[\frac{Q}{2\pi r_i h}\right]^2 + \frac{5\rho\nu^{3/5}}{h^3}\left[\frac{Q}{2\pi}\right]^{7/5}\left[\frac{1}{r_i^{2/5}} - \frac{1}{r_e^{2/5}}\right] + \frac{\rho}{2}\left[\frac{Q}{2\pi r_e h}\right]^2 \qquad (3.1)$$

Using a displacement transducer, measured valve gaps were found to be in good agreement with this expression, except at high flow rates where flow separation took place across the whole valve face and measured valve gaps were higher than the calculated valve gaps from Eq. (3.1).

In general, emulsion dispersion homogenizers used in the above studies operate with lower pressures and higher valve gaps than cell-disruption homogenizers. For a cell-disruption homogenizer, Brookman (1974) found that valve gap increased from 20 to 180 μm as pressure increased from 20 to 120 MPa. However, the validity of these results have subsequently been questioned (Engler, 1979), as they violate a momentum balance.

Other studies that characterise the homogenizer valve inlet region investigate pressure drop during radial flows between parallel discs with an inlet region. The total pressure loss for this simplified homogenizer geometry depends on inlet losses as fluid accelerates into the gap between the two discs, friction losses as fluid flows through the gap, and expansion losses as fluid exits the gap. Radial pressure distributions between parallel discs (for laminar and turbulent flows) could be predicted with good accuracy downstream of entry conditions, but flow near the inlet was dominated by separation and subsequent reattachment, making analytical solutions for the total pressure drop impractical (Moller, 1963). Experimental studies have approximated the effect of this inlet region by using an inlet loss coefficient to calculate the total pressure drop for flow between parallel discs. For laminar flow, Eq. (3.2) describes the relationship between total pressure drop and disc spacing (Nakayama, 1964).

$$\Delta P_L = f_L \frac{\rho}{2}\left[\frac{Q}{2\pi r_i h}\right]^2 + \frac{6\mu Q}{\pi h^3}\ln\left[\frac{r_e}{r_i}\right] + \frac{54\rho}{70}\left[\frac{Q}{2\pi r_e h}\right]^2 \qquad (3.2)$$

For turbulent flow between parallel discs, Kawaguchi (1971) used Eq. (3.3) to describe the dependence of pressure drop on disc spacing.

$$\Delta P_T = f_T \frac{\rho}{2}\left[\frac{Q}{2\pi r_i h}\right]^2 + \frac{0.00336\rho\nu^{1/4}}{h^3}\left[\frac{Q}{\pi}\right]^{7/8}\left[\frac{1}{r_i^{3/4}} - \frac{1}{r_e^{3/4}}\right] + \frac{64\rho}{126}\left[\frac{Q}{2\pi r_e h}\right]^2 \qquad (3.3)$$

For both laminar and turbulent flows, the inlet loss coefficient, f, approaches 0.18 in the limiting case of small valve gaps.

Although considerable information regarding homogenizer fluid mechanics has been obtained, further work is required. Experimental measurement of high-pressure, low-valve-gap homogenizers is obtained (section 3.2.2) to ascertain the applicability of Eqs (3.1) to (3.3) to describe cell-disruption homogenizer valve gaps.

However, pressure drop and valve gap information alone do not provide any information on the velocity and pressure fields within a homogenizer valve. It is not possible to apply the qualitative results of Phipps (1974a, 1974b) to cell-disruption applications. It is unlikely that detailed measurements of pressures and velocities within a high-pressure homogenizer can be obtained experimentally, due to the presence of large changes in both velocity and pressure that occur over small distances. An alternative approach is to obtain pressure and velocity fields numerically, using computational fluid dynamics. Numerical investigations of similar flow geometries have been conducted (Chatterjee and White, 1989), but cannot be applied to homogenizer valves. Specific numerical studies are conducted for the valve-inlet region of a homogenizer in this thesis (section 3.2.3). These results are summarised in the form of simplified expressions (section 3.2.4) that are used in the following chapters to calculate cell-disruption efficiency.

3.2.2 Experimental

Experimental measurements of the dependence of homogenizer valve gap on operating pressure were required for comparison with published semi-analytical expressions (Eqs (3.1) to (3.3)) and for comparison with numerical predictions (section 3.2.3). These valve gaps were measured on an APV-Gaulin 15MR-8TBA single-stage high-pressure homogenizer. In addition to the APV standard and APV cell-disruption valve seats with chamfered inlets, four machined valve seats, with sharp-edged inlets were also studied. Dimensions for all of these seats are shown in Table 3.1.

Modifications were made to the homogenizer to allow accurate measurements of homogenizer valve gap and pressure transients. The upper cap plug of the homogenizer was replaced with an insert that connected to a pressure transducer (Keller PA-22-1000, 0 to 1000 bar, TSE Pty Ltd., Melbourne) to provide pressure transient measurements. Valve

gaps were measured using a highly sensitive dc/dc linear variable displacement transducer (LVDT) (Lucas-Schaevitz, 75 V/mm) connected to an amplifier (Lucas-Schaevitz, ATA-101 Analog Transducer Amplifier). Signals were collected on a PC (486DX 33 MHz) via a CIO-DAS08-PGA data acquisition card and a signal processor (Intellecta Technologies, Technology Park, Adelaide, Australia). A modified valve rod (with a hollow centre) was designed and manufactured to replace the valve rod supplied with the homogenizer. This permits insertion of a push rod (machined from 316L SS) that rests directly against the homogenizer valve on one end and holds the LVDT core at the other end (Fig 3.2). This arrangement eliminates any requirement to correct for valve rod compression during valve gap measurement. Modified valve seat gaskets (annealed copper) were used during operation to minimise valve seat movement within the valve body. A support for the LVDT body was fixed directly onto the valve body, to prevent movement of the LVDT body relative to the valve body.

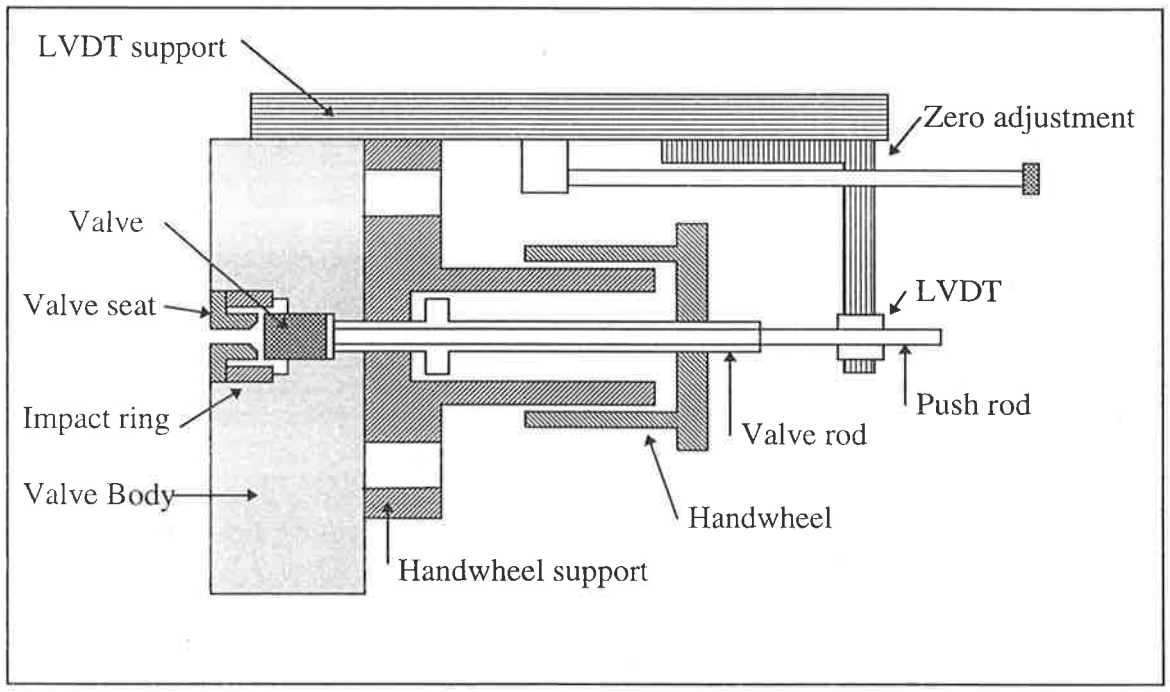

Figure 3.2: Schematic diagram of modified homogenizer design incorporating LVDT to measure homogenizer valve gap transients.

Homogenizer valve gaps were measured using water at 20°C as the homogenizer operating fluid. This provides a Newtonian fluid with known density (1000 kg m^{-3}) and kinematic viscosity (1×10^{-6} m^2 s^{-1}).

3.2.3 Numerical Simulation

As shown in Fig. 3.1, the valve-inlet region is characterised by axial flow in the centre of the valve seat, followed by radial flow between the valve and seat. The flow is in cylindrical coordinates and is axisymmetric. The resulting computational domain is two dimensional as shown schematically for the chamfered cell-disruption valve geometry in Fig 3.3. The chamfer on the cell-disruption seat was modelled as a series of small steps. Although the single-stage homogenizer used in this study operates in a cyclic mode, with the flow rate and hence valve gap and operating pressure changing over each piston stroke, the flow was modelled at steady state and the mean flow rate. The steady-state assumption greatly simplifies the computational procedure and ensures that a tractable problem is solved. Whilst this simplification occurs at the expense of transient effects (appendix A2), it is expected that the steady-state analysis still retains the important aspects of the homogenizer flow field.

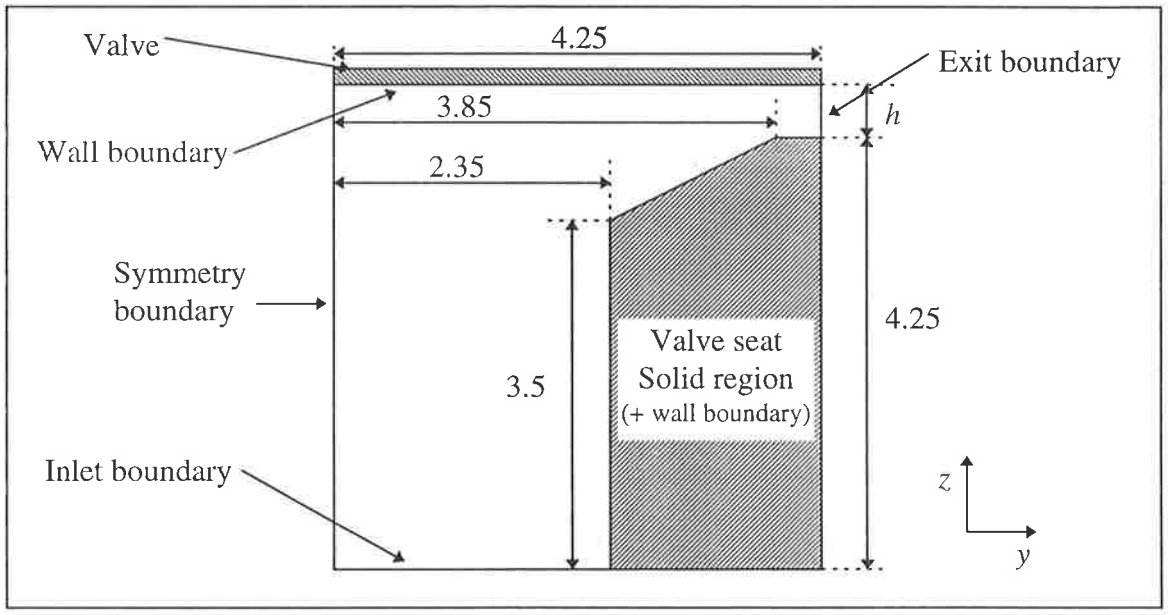

Figure 3.3: Representation of computational domain used for the valve inlet region of the cell-disruption valve seat (not to scale: all dimensions are mm).

In addition to the chamfered cell-disruption valve seat, simulations were conducted for a square edged seat (r_i = 0.0025 m, r_e = 0.0045 m). Valve gaps were chosen based on experimental results (section 3.2.5), and ranged from 7.6 to 24.0 μm for the cell-disruption seat and 10.8 to 30.0 μm for the square edged seat examined. These gaps resulted in total simulated pressure drops over the valve of 5 to 65 MPa, which is typical of the operating pressure range for the homogenizer being studied.

The fluid was assumed to be Newtonian, isothermal, incompressible, and homogeneous. Fluid density (1000 kg m^{-3}) and kinematic viscosity (1×10^{-6} m^2 s^{-1}) were fixed to allow comparison with experimental valve gap measurements obtained with water at 20°C.

Flow was simulated assuming that it was laminar throughout the computational domain. For flow between parallel discs, the transition of flow from laminar to turbulent is dependent on disc spacing and Reynolds number (Kawaguchi, 1971). A reduced Reynolds number was defined,

$$\mathrm{Re} = \frac{hQ}{4\pi r_i^2 \nu} \tag{3.4}$$

and flow was found to be laminar for a reduced Reynolds number less than 10. For the cell-disruption valve, reduced Reynolds number decreases from 6 for a 24 μm valve gap to 2 for an 8 μm valve gap, suggesting that flow in the valve gap is laminar. Even if flow is turbulent within the valve gap, the region of most interest where fluid accelerates into the gap is a highly convergent flow and is still likely to be laminar.

Governing Equations

The fundamental partial differential equations for laminar flow in cylindrical coordinates are the conservation equations for mass and momentum and can be written in tensor notation as follows:

$$\frac{\partial U_i}{\partial x_i} = 0 \tag{3.5}$$

and

$$U_j \frac{\partial U_i}{\partial x_j} = -\frac{1}{\rho}\frac{\partial P}{\partial x_i} + \frac{\partial}{\partial x_j}\left(\nu \frac{\partial U_i}{\partial x_j}\right) \tag{3.6}$$

Boundary Conditions

1. At the inlet to the computational domain, mass flow was fixed to an average value in the homogenizer valve of 4.6×10^{-5} m^3 s^{-1} (appendix A2). Although there is some variation in homogenizer flow rate with operating pressure, the flow rate is constant to

within approximately ± 2% over most of the range of operating pressures used (Appendix A2). The inlet velocity profile was square and had no radial velocity component.

$$V = 0 \tag{3.7}$$

$$W = \frac{0.00046}{\pi r^2} \tag{3.8}$$

2. The flow exit boundary between the valve and valve seat was given a fixed pressure boundary condition.

$$P_e = 0 \text{ Pa} \tag{3.9}$$

3. The axis of the valve seat was a symmetry boundary.

$$\frac{\partial W}{\partial y} = 0 \tag{3.10}$$

$$V = 0 \tag{3.11}$$

4. Solid walls were given laminar flow boundary conditions.

$$V = W = 0 \tag{3.12}$$

Solution Procedure

The governing equations (Eqs (3.5) and (3.6)) were solved subject to the conditions of Eqs (3.7) to (3.12) using a commercially-available finite-volume fluid dynamics code (PHOENICS 2.1, CHAM, Wimbledon, London, UK). The computational domain was divided into a total of 77 radial by 46 axial unevenly sized grid cells for the cell-disruption valve seat, and 80 radial by 49 axial unevenly sized grid cells for the square-edged-inlet valve seat. Solutions were checked for grid independence in a typical case by doubling the number of grid cells in the radial and axial directions. It was found that the total pressure drop in the two cases differed by less than 2%.

3.2.4 Theoretical Considerations

Numerical simulation provides an extremely large quantity of homogenizer fluid mechanics information. However, it is likely that only a small fraction of the vast amount of information generated will be required in the prediction of cell disruption efficiency. As an example, Ayazi Shamlou *et al.* (1995) suggest that the fluid's strain rate in regions of hyperbolic flow is likely to be an important variable. Whilst Ayazi Shamlou *et al.* (1995) assert that this region is likely to be near the valve on the axis of symmetry of the valve assembly, Loo and Carleton (1953) and Phipps (1974b) have found that fat globules are disrupted close to the inlet of the valve gap. It is possible that the fluid strain rate in this region is an important variable. For the case of a chamfered inlet (Fig. 3.4), the average strain rate at the inlet to the valve gap is given by:

$$\alpha = \frac{1}{w}\frac{dw}{dt} - \frac{1}{y}\frac{dy}{dt} \tag{3.13}$$

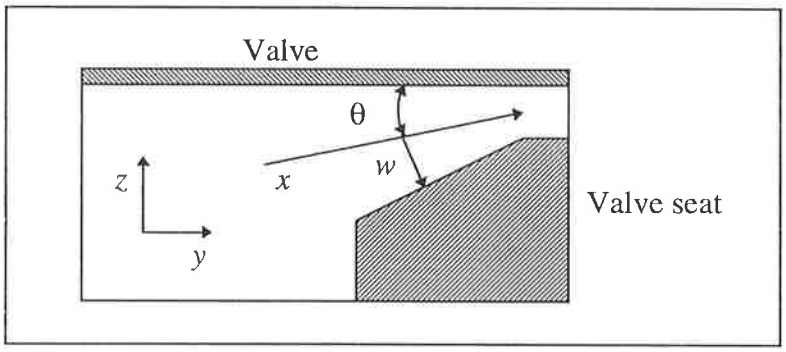

Figure 3.4: Geometry of converging flow in valve inlet region.

By defining the primary flow direction as x, the following quantities are defined:

$$\frac{dy}{dx} = \sin\left(\frac{\pi}{2} - \theta\right) \tag{3.14}$$

$$\frac{dy}{dt} = \frac{dx}{dt}\sin\left(\frac{\pi}{2} - \theta\right) = V \tag{3.15}$$

$$\frac{dw}{dx} = \tan(\theta) \tag{3.16}$$

$$\frac{dw}{dt} = V\sin(\theta) \tag{3.17}$$

$$w = z\cos(\theta) \tag{3.18}$$

Substituting Eqs (3.15) and (3.17) into Eq. (3.13) defines the average strain rate:

$$\alpha = V\left(\frac{1}{z}\tan(\theta) - \frac{1}{y}\right) \tag{3.19}$$

For the case of a typical homogenizer valve with low gap, at the entrance to the valve gap $z = h$ and $y = r_i$. As $r_i >> h$, Eq. (3.19) simplifies to:

$$\alpha = \frac{V}{h}\tan(\theta) \tag{3.20}$$

This strain rate will be greatest at the entrance to the gap between the valve and valve seat, where the mean radial velocity is:

$$V = \frac{Q}{2\pi r_i h} \tag{3.21}$$

Substituting Eq. (3.21) into Eq. (3.20) gives the maximum strain rate in the valve inlet region:

$$\alpha = \frac{Q\tan(\theta)}{2\pi r_i h^2} \tag{3.22}$$

However, Eq. (3.22) is only likely to be applicable for chamfered valve seats, as a square edged valve seat is not likely to show a smooth flow convergence in the same way that a chamfered seat will. An alternative approach is based on the assertions of Brookman (1975), who proposed that cell-disruption is dependent on the "rate and magnitude of pressure drop" - or pressure gradient - in the homogenizer valve. The maximum pressure gradient in the valve inlet region will occur as fluid accelerates into the valve gap, where pressure is rapidly converted into kinetic energy. The pressure drop in this region will approximately equal the fluid's kinetic energy after acceleration:

$$\Delta P = \frac{1}{2}\rho V^2 = \frac{\rho Q^2}{8\pi^2 r_i^2 h^2} \tag{3.23}$$

Nearly all of this pressure drop will occur over a small region, with a length scale proportional to the valve gap:

$$L_I = \beta_I h \tag{3.24}$$

This length scale is unknown, but will depend on valve seat geometry and also fluid properties (viscosity and density). The pressure gradient will then be:

$$\frac{dP}{dy} = \frac{\rho Q^2}{8\beta_I \pi^2 r_i^2 h^3} \tag{3.25}$$

Whilst this pressure-gradient approach has the disadvantage that the value of the length scale proportionality constant is unknown *a priori*, and must be evaluated from numerical results for the valve inlet region, it has the advantages that it is applicable for both chamfered inlet and square edged valve seats and also accounts for viscous effects on the convergence.

There is a direct link between strain rate and pressure gradient. At a fixed position within the flow field:

$$\frac{dP}{dy} = \rho V \alpha \tag{3.26}$$

Substitution of Eqs (3.21), (3.22) and (3.25) into Eq. (3.26) gives;

$$\frac{\rho Q^2}{8\beta_I \pi^2 r_i^2 h^3} = \frac{\rho Q^2 \tan(\theta)}{4\pi^2 r_i^2 h^3} \tag{3.27}$$

and hence

$$\beta_I = \frac{1}{2\tan(\theta)} \tag{3.28}$$

As these two variables (strain rate and pressure gradient) are connected by velocity (Eq. (3.26)), the two variables may be readily interchanged.

3.2.5 Results and Discussion

Results from experimental measurement of homogenizer valve gap and numerical results for the flow field within a homogenizer valve are presented here.

Experimental Valve Gap and Pressure Measurement

Measured homogenizer valve gap and operating pressure transients are shown for the cell-disruption valve in Figs 3.5 and 3.6. The pressure and valve gap profiles follow each other closely at both low and high operating pressures. The pressure transient is "squarer" at the low operating pressure. Fig. 3.6 shows a relatively large amount of noise on the valve gap transient measurement. It is uncertain if this noise was due to experimental errors or if it reflects noise in the valve transient. The transients justify the assumption used in numerical modelling that the valve is open for approximately 1/3 of the total operating cycle (0.21 seconds/cycle).

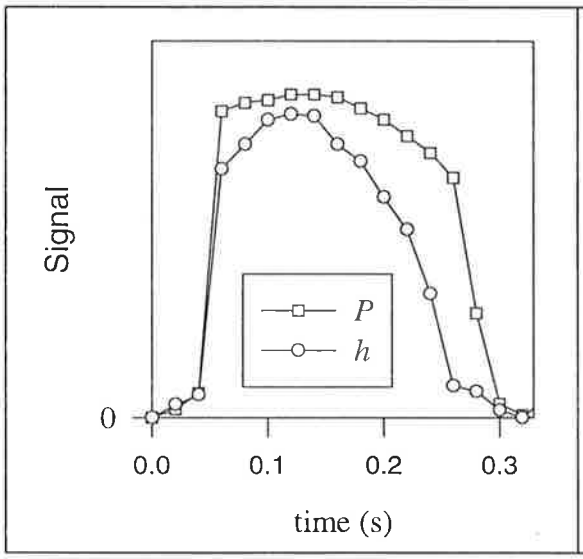

Figure 3.5: Pressure and valve gap transients for the cell-disruption valve with a peak pressure of 5.3 MPa.

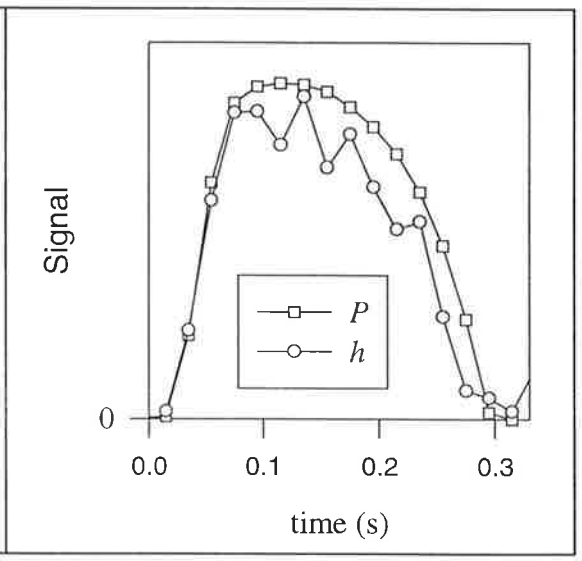

Figure 3.6: Pressure and valve gap transients for the cell-disruption valve with a peak pressure of 66.1 MPa.

The homogenizer operates at an instantaneous steady state when valve gap and operating pressures are at their peak values during a pump cycle. The valve gap at this instantaneous steady-state position was determined for a wide range of operating pressures. At the steady-state position, the instantaneous homogenizer flow rate is slightly higher than at the average homogenizer flow rate (Appendix A2). Steady-state homogenizer valve gaps,

corrected to the average homogenizer flow rate, are shown in Fig. 3.7, together with predicted valve gaps obtained from the literature correlations of Eqs (3.1), (3.2) and (3.3).

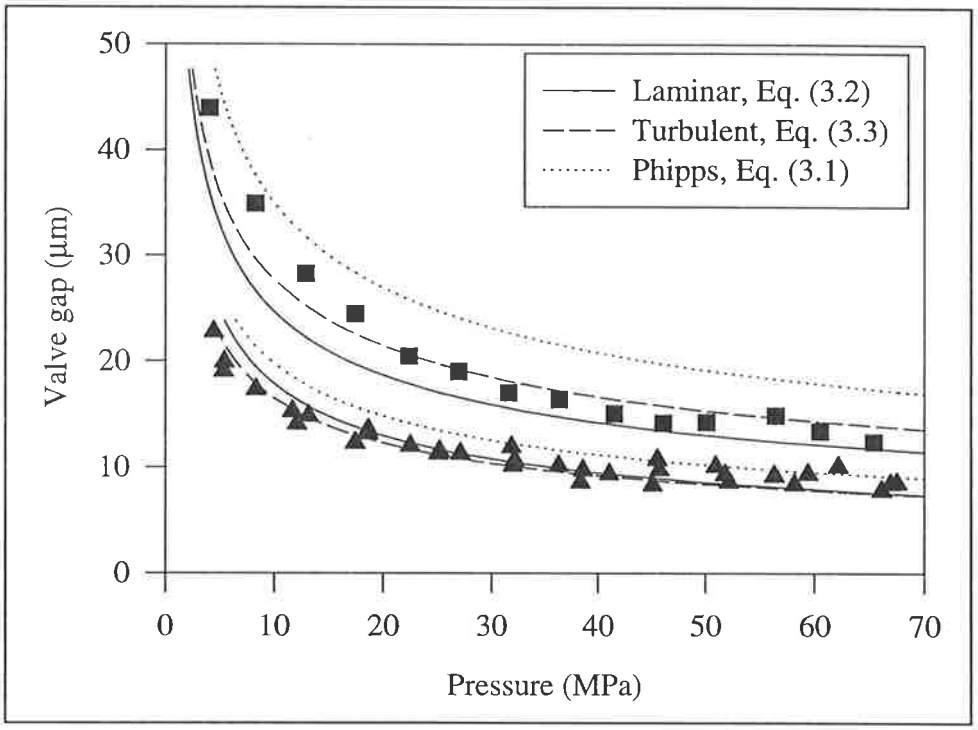

Figure 3.7: Dependence of homogenizer valve gap on operating pressure for the cell-disruption valve seat and a square-edged-inlet valve seat (r_i = 0.0025 m, r_e = 0.0045 m) with water as the operating fluid.

The cell-disruption seat produces much lower valve gaps than the square-edged seat at the same operating pressure. This is primarily due to the much lower land distance (difference between the inner and outer radii) of 0.4 mm on the cell-disruption seat and 2.0 mm on the particular square-edged seat, which results in lower frictional losses. The chamfered inlet of the cell-disruption seat also reduces frictional losses. For the cell-disruption seat, Phipps' (1975) correlation (Eq. (3.1)) over-predicts pressure drop. For the square edged seat, pressure drop matches Phipps' (1975) correlation at higher valve gaps (low operating pressures). Pressure drop is better matched with the laminar flow prediction for the cell-disruption seat and the square edged seat at higher operating pressures, although it is difficult to differentiate conclusively between the laminar and turbulent correlations. The scatter in experimental measurements, particularly at high operating pressure, can be attributed to the noise observed in Fig. 3.6, and also to difficulties experienced in preventing movement of the homogenizer valve seat in the valve body at high pressure. Any movement of the valve seat will significantly influence results, particularly at the lower valve gaps of approximately 8 µm. As such, the experimental measurements were

found to be reproducible within a range of ± 1.5 μm. This also makes it impossible to select laminar, turbulent or Phipps' empirical correlations as most suitable for these homogenizer operating conditions.

For all valve seats examined, the dependence of the valve gap on homogenizer pressure (at mean homogenizer flow rate) were obtained experimentally (as shown for two seats in Fig. 3.7) and described empirically using a power-law expression. The dimensions of each of the valve seats and the observed dependence of valve gap on operating pressure is given in Table 3.1.

Table 3.1: Dimensions of valve seats together with the measured dependence of valve gap (at mean homogenizer flow rate) on operating pressure (P in MPa, h in μm).

Description	Inlet Profile	Inlet Radius	Exit Radius	Valve Gap
APV Cell-disruption	chamfered	0.00385	0.00425	$37P^{-0.35}$
APV Standard	chamfered	0.0032	0.00425	$62P^{-0.42}$
Machined	square	0.0020	0.0045	$120P^{-0.52}$
Machined	square	0.0025	0.0045	$85P^{-0.45}$
Machined	square	0.0030	0.0045	$65P^{-0.43}$
Machined	square	0.0035	0.0045	$56P^{-0.42}$

Numerical Simulation

The measurements of valve gap do not provide detailed information on flow within the homogenizer valve. For example only limited information is obtained regarding the presence or absence of cavitation or separated flow. This information is supplied by numerical simulation. Typical streamline patterns in the region where fluid enters the valve gap are compared for the cell-disruption and square-edged seats in Figs (3.8) and (3.9) respectively for low operating pressures. No flow separation is predicted to occur in the cell-disruption seat over the range of valve gaps examined (24.0 to 7.6 μm, corresponding to pressure drops of 5 to 65 MPa). Some separation is predicted to occur in the square valve, but only at higher valve gaps (Fig. 3.9).

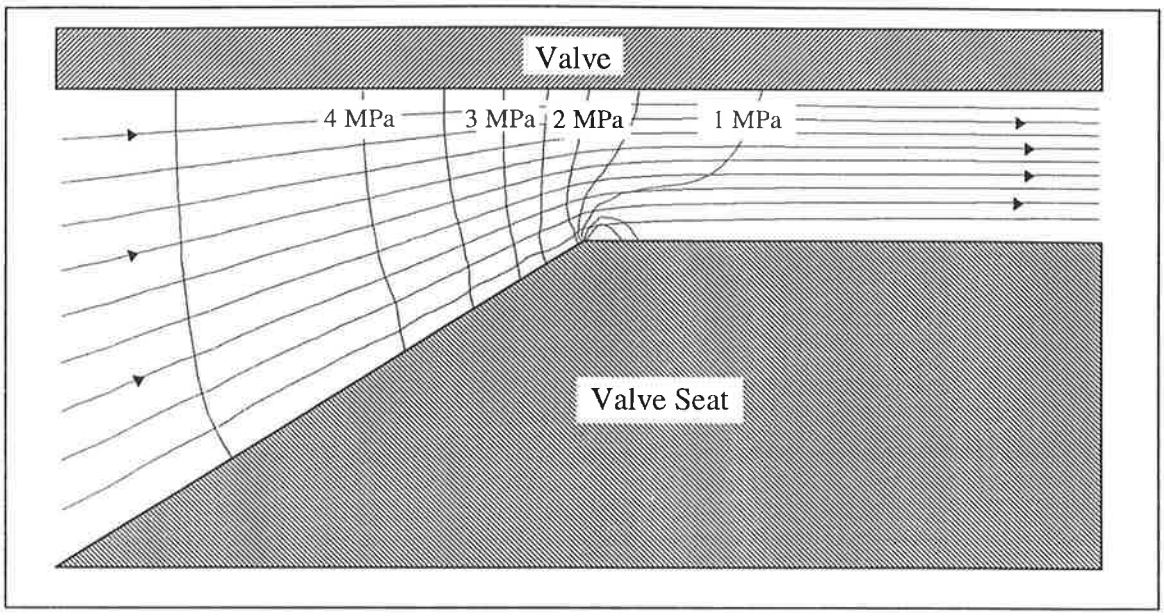

Figure 3.8: Numerical simulation results for streamlines and pressure contours in the valve inlet region of the cell-disruption valve seat (24.0 μm valve gap, 5 MPa total pressure drop).

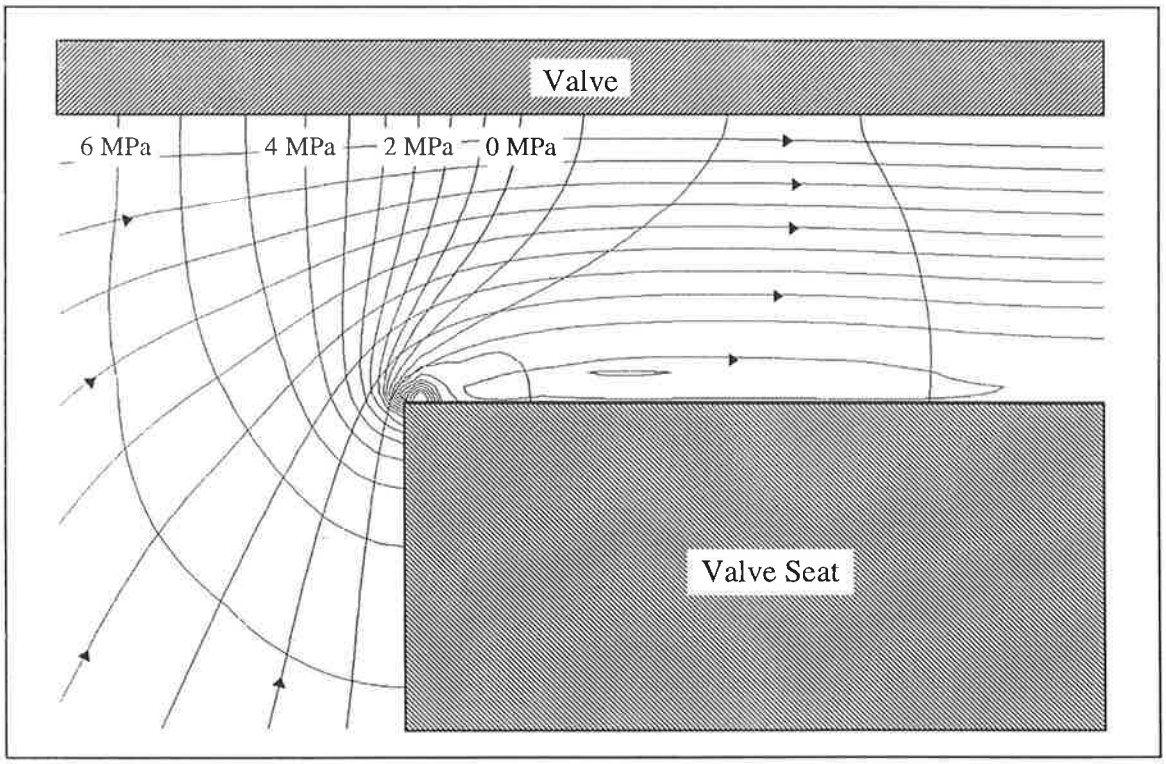

Figure 3.9: Numerical simulation results for streamlines and pressure contours in the valve inlet region of a square edged inlet valve seat (30.0 μm valve gap, 7 MPa total pressure drop).

Figs (3.10) and (3.11) show calculated pressure contours in the inlet to the valve gap. Even though flow separation does not occur in the cell-disruption valve, a small region of low pressure (directly behind the valve inlet, against the valve seat) is predicted, indicating that some cavitation may occur in this region. The low pressure region disappears as the valve gap decreases and total pressure drop increases. This is due to higher frictional losses across the face of the valve and hence higher static pressure near the inlet. Normalised pressure profiles for the cell-disruption seat (at the centre of the valve gap) show that a positive pressure is maintained in the valve gap under normal operating conditions (Fig. 3.10). The high pressure acts to suppress cavitation in the valve gap. However, normalised pressure profiles for the square edged seat (Fig. 3.11) show that negative pressures are predicted in the valve gap at lower operating pressures (< 30 MPa). The presence of negative pressures indicates that the square-edged valve will cavitate during operation at low pressures.

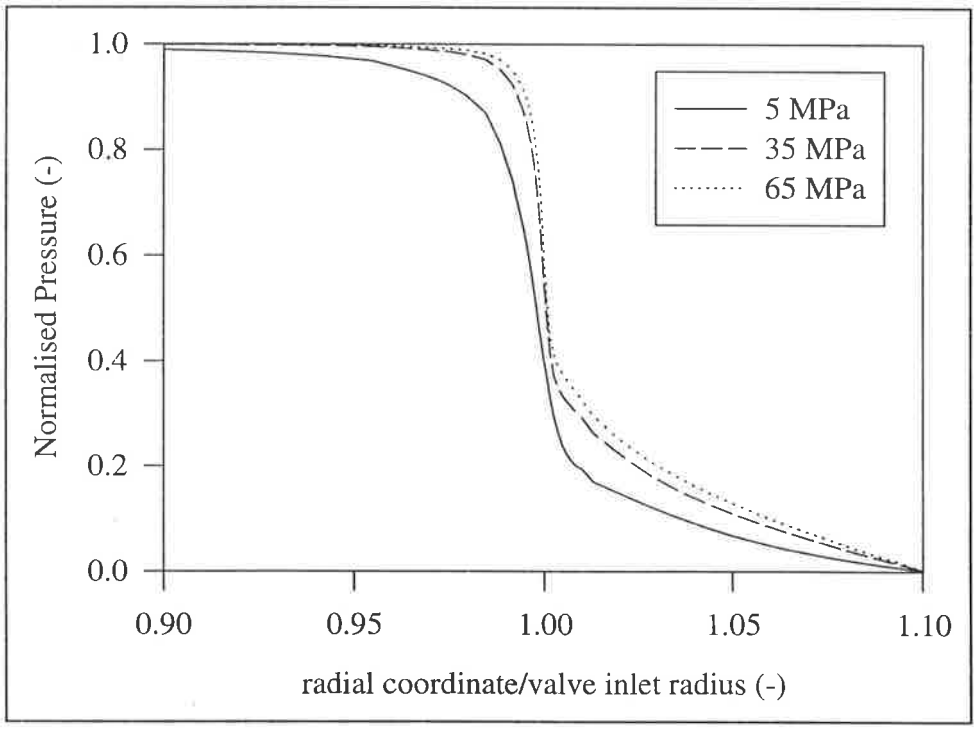

Figure 3.10: Normalised pressure profile across the centre plane of the valve gap for the cell-disruption valve seat.

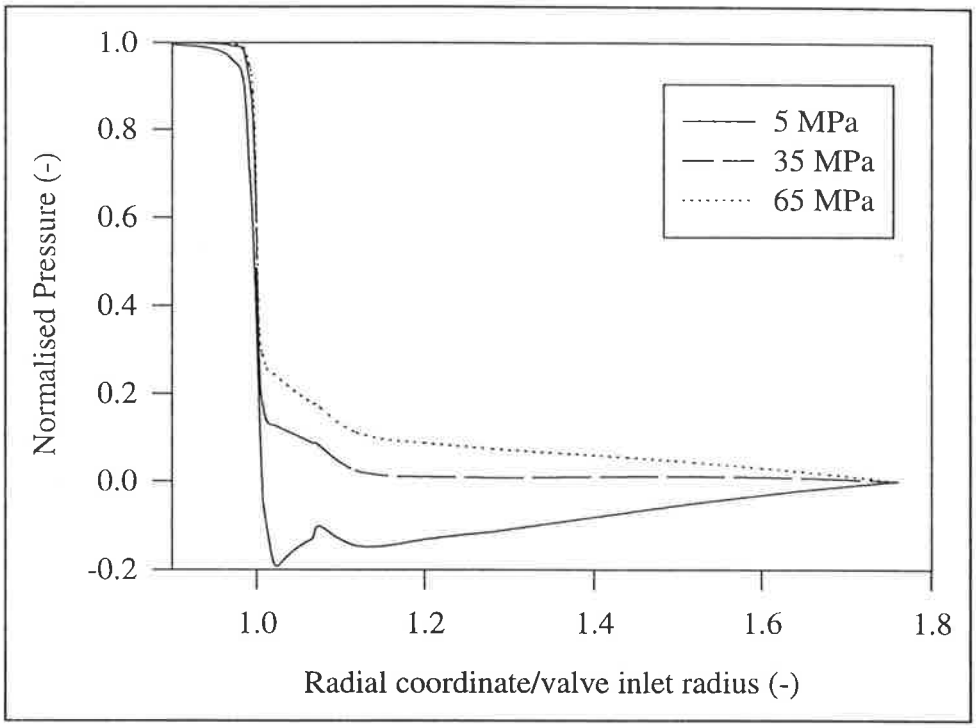

Figure 3.11: Normalised pressure profile across the centre plane of the valve gap for a square-edged valve seat.

Fig. 3.11 shows an interesting change in pressure with radial distance for the square edged inlet. For the 5 MPa total pressure drop, pressure initially decreases due to the conversion of pressure to kinetic energy. The reduction is followed by a sudden increase in pressure, that occurs as the mean fluid velocity decreases when the gap width available to flow increases past the separation region. Pressure then decreases again, due to frictional losses. Before exiting the valve gap, the pressure again increases due to inertial effects (as the radial distance increases, the flow velocity decreases, causing a rise in pressure).

The expectation that the square valve cavitates at low operating pressure provides a plausible explanation for the deviation of valve gap from the laminar flow prediction seen experimentally in Fig. 3.7. Valve gap is expected to increase due to the presence of cavitating flow. It is probable that Phipps' (1975) correlation (Eq. (3.1)) was developed with, and is applicable for, cavitating valves.

Qualitatively, these observations of separation and cavitation are in agreement with the experimental observations of Phipps (1974a) that flow in homogenizer valves will only separate with associated cavitation at low operating pressure, and is more likely to occur for a square-edged seat than for a seat with a rounded inlet. It is apparent that separation and cavitation do not influence flow in the valve inlet region under normal homogenizer operating conditions (> 50 MPa).

The total pressure drop calculated from these numerical results is in excellent agreement (within 1%) with independent laminar predictions (Eq. (3.2)). Numerical results show the same deviation from experimental valve gap measurements as the laminar semi-analytical prediction (Fig. 3.7).

For the cell-disruption seat, the calculated radial velocity profile as fluid exits the gap between the valve and valve seat is compared with a parabolic profile in Fig. 3.12. For the lowest valve gap examined, the valve gap is long enough to develop a nearly parabolic velocity profile. Higher valve gaps show increasing levels of asymmetry, with higher velocities closer to the valve than valve seat.

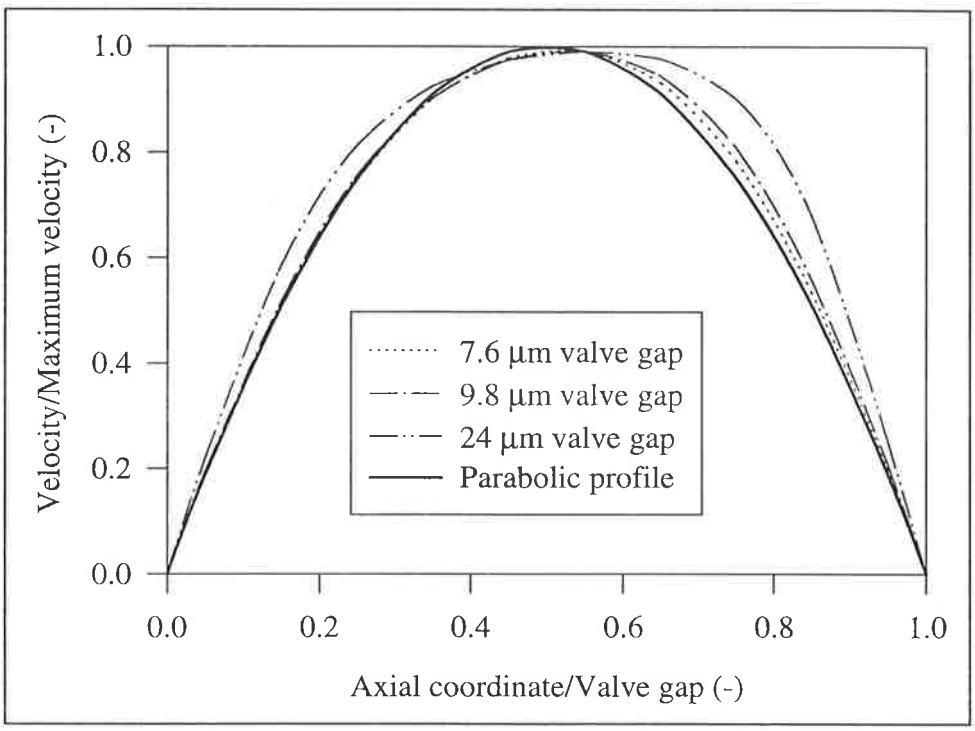

Figure 3.12: Calculated radial velocity profile as fluid exits the valve gap for the cell-disruption valve seat.

Pressure Gradients

As shown graphically in Figs (3.10) and (3.11), approximately 2/3 of the total pressure drop over the homogenizer valve occurs in a small region as fluid accelerates into the valve gap. In this small region, extremely high pressure gradients are present. For the cell-disruption valve, the radial pressure gradient in the centre of the valve gap increases from 6 $\times 10^{10}$ Pa m^{-1} at a 5 MPa simulated pressure drop to 2 $\times 10^{12}$ Pa m^{-1} at 65 MPa.

Radial pressure gradients in the centre of the valve gap, obtained from radial pressure profiles determined by computational fluid dynamics, were then used to evaluate the constant β in Eq. (3.24). For the cell-disruption seat, β_I was found to have a mean value of 2.1 over the range of valve gaps examined. For the square-edged seat, β_I was found to have a mean value of 1.2. A parity plot comparing the calculated pressure gradient from Eq. (3.25) with mean β_I values and the pressure gradient from numerical results is shown in Fig. 3.13. The excellent parity plot confirms the validity of this approach, and allows calculation of pressure gradients (Eq. (3.25)) or strain rates within a homogenizer valve without the need for computational fluid dynamics analysis for each valve gap. The lower value of β_I seen for the square-edged seat is expected, as the absence of a chamfer causes fluid acceleration to occur over a shorter distance for the same mean fluid velocity.

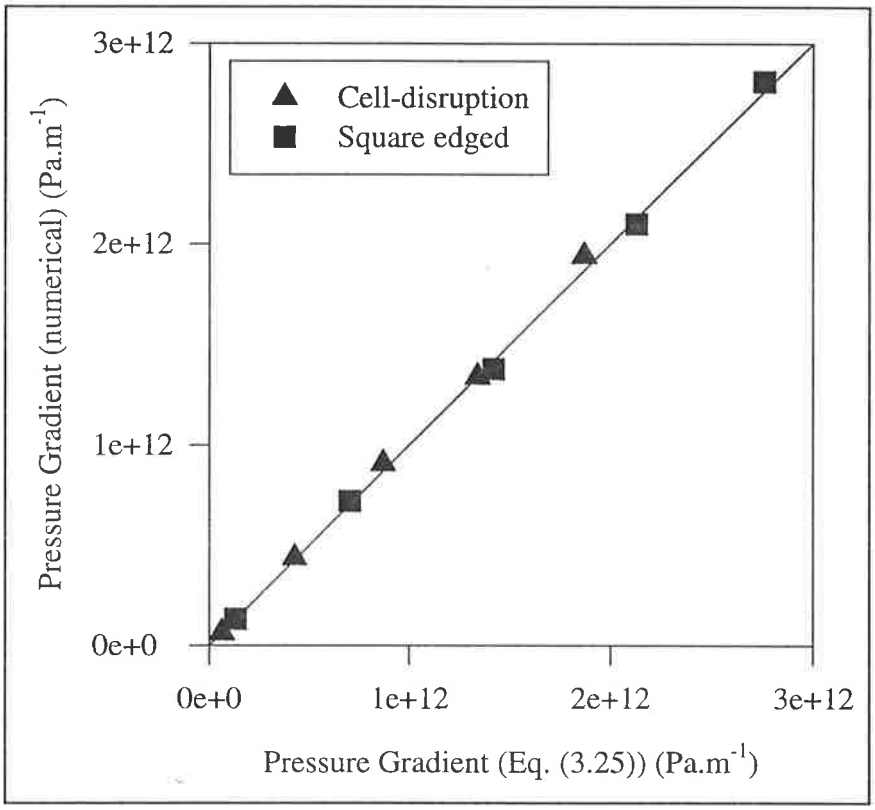

Figure 3.13: Parity plot for pressure gradient in the valve inlet region obtained from numerical results and using the expression of Eq. (3.25).

Using the β_I values found above, Eq. (3.28) allows calculation of the "apparent" inlet half-angle, θ, for the square and chamfered valves. A β_I value of 2.1 corresponds to an inlet half-angle of 13°, which is close to the actual half angle of 15° in the cell-disruption valve. The small difference can be attributed to viscous effects at the valve and valve seat surface, that act to reduce the effective chamfer. A β_I value of 1.2 corresponds to an inlet half-

angle of 22.6°, which is somewhat different to the actual half-angle of 45° in the square-edged valve. This demonstrates the inadequacy of the simple expression of Eq. (3.22) to describe the more complex flow path as fluid enters the valve gap with a square-edged valve seat, where a large part of the geometry does not contribute to the development of the inlet flow profile. It also highlights the need for numerical simulation to characterise the flow within homogenizer valves.

3.3 Impinging Jet Region

As the cell suspension emerges from the ring-shaped gap formed by the outer edges of the homogenizer valve and seat (Fig. 3.1), a radial fan jet is produced. The radial jet subsequently stagnates at the homogenizer impact ring, before leaving the valve unit at atmospheric pressure. Previous examinations of this flow geometry in homogenizer valves and other similar geometries are reviewed, highlighting the need for further information. This is obtained through a combination of experimental (section 3.3.2) and numerical (section 3.3.3) investigations.

3.3.1 Previous studies

The homogenizer impinging jet has received relatively little attention. Engler (1979) constructed purpose-built equipment to examine the effect of impingement on cell disruption efficiency. He correlated disruption efficiency with the calculated maximum stagnation pressure of the impinging jet,

$$P_S = \frac{1}{2}\rho U^2 \tag{3.29}$$

where the velocity was evaluated as the mean jet velocity exiting the impingement nozzle. Effectively, this assumes no velocity decay between the nozzle exit and the impingement plate. Although no experiments were conducted to test this assumption, it was justified by previous results for high-pressure cutting jets (Mohaupt and Burns, 1974).

Keshavarz Moore *et al.* (1990) developed an expression to calculate homogenizer impinging jet stagnation pressure from valve gap and impact distance:

$$P_S \propto \frac{1}{Y^2 h^2} \tag{3.30}$$

This expression was based on similarity results obtained for a turbulent, axisymmetric impinging air jet (Beltaos and Rajaratnam, 1974). However, there are differences in geometry between the jet studied by Beltaos and Rajaratnam (1974) and a homogenizer jet

(axisymmetric and radial, respectively), and there is a complete lack of evidence to determine whether a homogenizer impinging jet is laminar or turbulent. As such, the result of Eq. (3.30) requires further justification.

Radial jets have also been examined as a fundamental fluid flow geometry. Turbulent radial jets have been studied experimentally (Heskestad, 1976; Witze and Dwyer, 1976; Tanaka and Tanaka, 1976; Patel, 1979) and numerically (Wood and Chen, 1985; Malin, 1989). The turbulent radial jet attains self-similarity after a certain development region, when the velocity half width increases linearly with distance, and the maximum jet velocity on the symmetry plane decays with distance.

A study of small, impinging circular water jets found jets to be laminar for hydraulic Reynolds numbers less than 6000 (Elison and Webb, 1994). As the jet in this homogenizer has a Reynolds number less than 6000 (based on $Q = 4.6 \times 10^{-5}$ m^3 s^{-1}, $r_e = 0.0045$ m, $\nu = 1 \times 10^{-6}$ m^2 s^{-1}, $\mathrm{Re} = Q/\pi r_e \nu = 3200$), it is probable that it is laminar. Laminar radial jets have been examined theoretically (Squire, 1955; Schwartz, 1963) and numerically (Laschefski *et al.*, 1994). At higher Reynolds numbers, a laminar jet has a lower velocity decay rate than the corresponding turbulent jet (Deshpande and Vaishnav, 1982; Elison and Webb, 1994).

It is the stagnation point that is of interest for cell-disruption (Engler, 1979). No studies have been reported for an impinging jet with the same geometry as a high-pressure homogenizer (radial jet impingement on a surface perpendicular to the jet's plane of symmetry). However, impinging jet flows of different geometry occur in a wide variety of practical situations and have been extensively examined. Experimental measurements of velocities and pressures in turbulent plane and circular impinging jets have been reported (Beltaos and Rajaratnam, 1973; 1974). Numerical studies of stagnating turbulent (Champion and Libby, 1994) and laminar (Deshpande and Vaishnav, 1982; Law and Masllyah, 1984) axisymmetric jets have also been reported.

It is not possible to obtain detailed measurements of pressures and velocities within a high-pressure homogenizer's impinging jet experimentally, due to the presence of large changes in both velocity and pressure that occur over small distances. Previous studies have not been conducted for similar geometries and are of limited application to the high-pressure homogenizer. Specific numerical studies are required for the impinging jet region of a

homogenizer (section 3.3.3). Experimental measurements are also required to determine if the jet is laminar or turbulent (section 3.3.4). Results are presented in section 3.3.5.

3.3.2 Experimental

Due to the small size of the impinging jet, it is not possible to obtain direct measures of, for example, flow velocities or stagnation pressure profiles. This study does, however, provide a measurement of the width of the jet stagnation region.

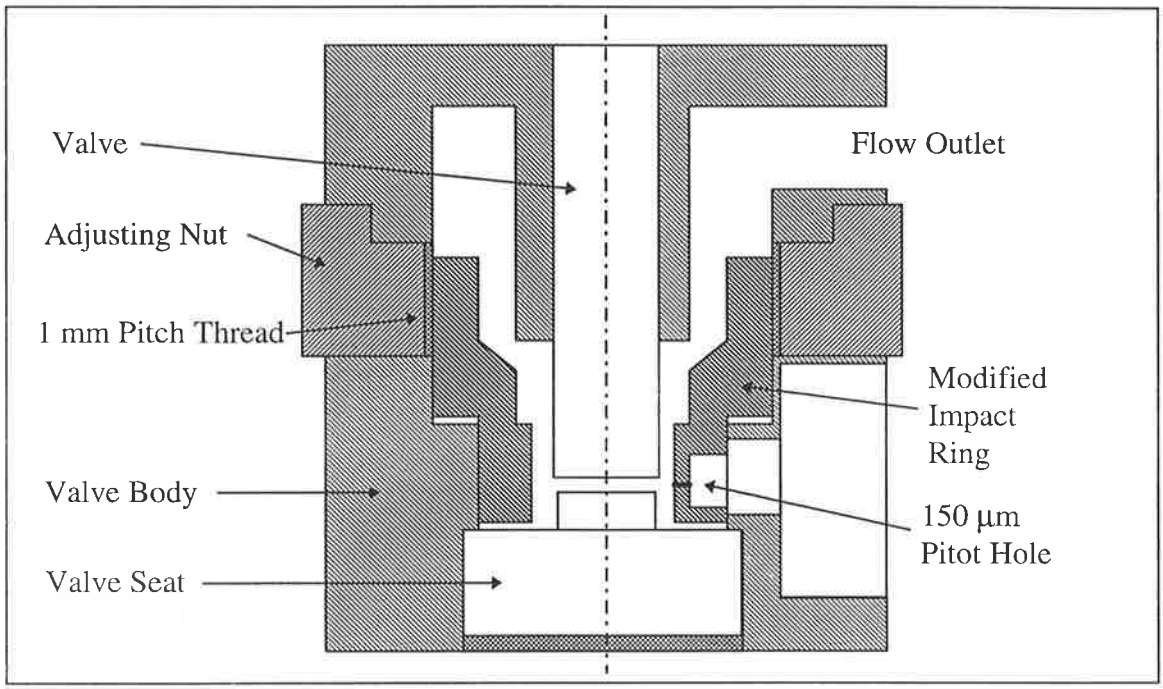

Figure 3.14: Experimental arrangement used to measure jet width at stagnation point.

To measure the impinging-jet width, the homogenizer was extensively modified. An impact ring was produced that contained a 150 µm radial bleeding hole. This modified impact ring was threaded (1 mm pitch thread) to allow axial movement of the bleeding hole, using an adjusting nut. The modified impact ring and adjusting nut were housed in a two-part valve-body, which also housed the valve and valve seat. This arrangement allowed accurate axial positioning of the bleeding hole in the impact ring, and is shown in Fig. 3.14. The experimental arrangement was not able to give quantitative information on the actual stagnation pressure at the bleeding hole, as the bleeding hole is large compared to the dimensions of the stagnation region. The measured stagnation pressure is therefore averaged over a large area. However, axial movement of the bleeding hole provided an

estimate of the width of the stagnation region at the impact ring. This was determined by the presence or absence of a jet issuing from the bleeding hole as the hole was translated axially.

3.3.3 Numerical Simulation

The homogenizer radial jet exits the gap between the valve and valve seat. Initially, a radial wall jet (along the valve face) is formed that becomes a free radial jet as it leaves the valve face. The jet then stagnates at the impact ring. A recirculation zone will exist in the annular space bounded by the jet, valve seat and impact ring. Fluid exits the valve assembly by passing through the annular gap between the valve and impact ring. To simplify this flow geometry, the radial jet was approximated as a plane-symmetric radial jet (neglecting effects of the recirculation zone), starting at a radial coordinate which is the average of the valve radius and valve seat exit radius (neglecting effects of the radial wall jet). The resulting two dimensional computational domain is shown in Figure 3.15. Based on experimental measurements of valve gap (section 3.2.5), the jet was simulated for valve gaps of 8 to 24 μm.

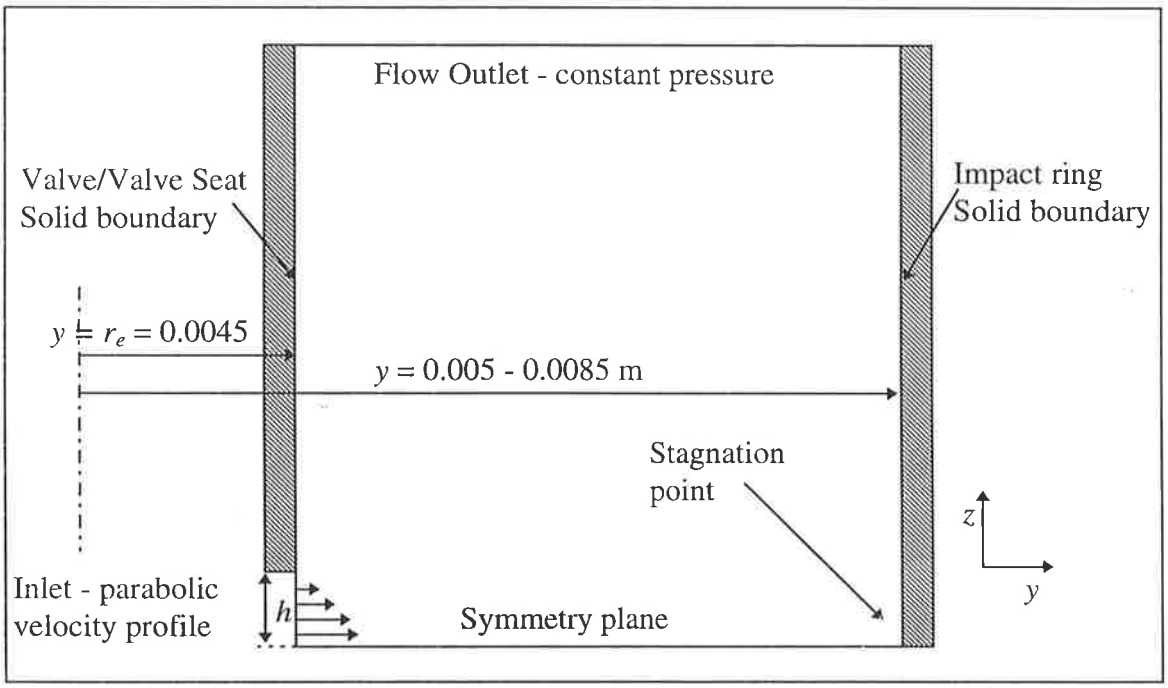

Figure 3.15: Schematic diagram of the computational domain used for the impinging jet region.

The fluid was assumed to be Newtonian, isothermal, incompressible, and homogeneous, with constant density and viscosity throughout the domain. The assumption of isothermal and hence constant density and viscosity was only an approximation. A significant temperature rise ($0.24°C \cdot MPa^{-1}$) occurs over the homogeniser. At high operating pressure, this temperature rise significantly affects fluid viscosity. However, it was estimated that most of this temperature increase occurs after the stagnation point where pressure and kinetic energy are converted to thermal energy. Thus, whilst an error was introduced by assuming isothermal conditions, it was expected to be less than 10% at the highest operating pressures and does not change the conclusions of this study. Gravity effects were considered negligible and not included in calculations.

Governing Equations

The transport equations for laminar fluid flow in axisymmetric coordinates are given as Eqs (3.5) and (3.6). Turbulence modeling was conducted by using the high-Reynolds-number Harlow and Nakayama (1968) form of the k-ε turbulence model, built into the PHOENICS 2.1 code. For the simulation of turbulent flow, the momentum equations are modified to include the turbulent shear stresses:

$$U_j \frac{\partial U_i}{\partial x_j} = -\frac{1}{\rho}\frac{\partial P}{\partial x_i} + \frac{\partial}{\partial x_j}\left(\nu \frac{\partial U_i}{\partial x_j} - \overline{u_i u_j}\right) \tag{3.31}$$

The k-ε model determines the Reynolds stresses through the use of the Boussinesq eddy viscosity concept, as represented by Eq. (3.32),

$$-\overline{u_i u_j} = \nu_T \left(\frac{\partial U_i}{\partial x_j} + \frac{\partial U_j}{\partial x_i}\right) - \frac{2}{3} k \delta_{ij} \tag{3.32}$$

where the kinematic eddy viscosity is found from:

$$\nu_T = C_\mu \frac{k^2}{\varepsilon} \tag{3.33}$$

Two further transport equations are required for the solution of k and ε,

$$\rho U_i \frac{\partial k}{\partial x_i} = \frac{\partial}{\partial x_i}\left(\frac{\mu_T}{\sigma_k}\frac{\partial k}{\partial x_i}\right) + \rho\left(P_k - \varepsilon\right) \tag{3.34}$$

$$\rho U_i \frac{\partial \varepsilon}{\partial x_i} = \frac{\partial}{\partial x_i}\left(\frac{\mu_T}{\sigma_\varepsilon}\frac{\partial \varepsilon}{\partial x_i}\right) + \rho\frac{\varepsilon}{k}\left(C_{1\varepsilon}P_k - C_{2\varepsilon}\varepsilon\right) \tag{3.35}$$

where

$$P_k = -\overline{u_i u_j}\frac{\partial U_i}{\partial x_j} \tag{3.36}$$

is the rate of production of turbulent kinetic energy, and the standard value of the empirical constants are given in Table 3.2.

Table 3.2: Values of the *k*-ε turbulence model coefficients.

C_μ	$C_{1\varepsilon}$	$C_{2\varepsilon}$	σ_k	σ_ε
0.09	1.44	1.92	1.0	1.314

Boundary Conditions

1. Jet inlet mass flow was fixed to the average homogenizer flow rate of 4.6×10^{-5} $m^3\ s^{-1}$. The length of the valve gap is 20-50 times larger than the valve gap itself, which develops a velocity profile that is adequately represented by the parabolic velocity profile given by Eq. (3.37) with no axial velocity component.

$$V = \frac{3Q}{4\pi r_e h}\left[1-\left(\frac{2z}{h}\right)^2\right] \tag{3.37}$$

$$W = 0 \tag{3.38}$$

Inlet values of k and ε were set by assuming a nominal turbulence intensity of 3% for the inlet flow in the case of a turbulent jet. Although 3% was chosen arbitrarily, the results obtained were insensitive to the actual value used. This is because the radial jet distance is much larger than the initial jet width (> 40 times) and the initial turbulence intensity is rapidly balanced by shear production and dissipation of turbulent kinetic energy within the jet.

2. The flow exit boundary (between the valve and impact ring) was given a fixed pressure boundary condition.

$$P = 0 \text{ Pa} \tag{3.39}$$

3. The symmetry plane of the radial jet was a symmetry boundary.

$$\frac{\partial V}{\partial z} = 0 \tag{3.40}$$

$$W = 0 \tag{3.41}$$

4. Solid walls (the valve/valve seat and impact ring) had velocity components fixed to zero at the wall.

$$V = W = 0 \tag{3.42}$$

Solution Procedure

The computational domain was divided into 59 axial grid cells and 45 to 85 radial grid cells (depending on the distance to the impact ring). The grid was clustered to give greatest grid refinement at the jet stagnation point. Solutions were checked for grid independence for a typical case by doubling the number of grid cells in the radial and axial directions. Maximum stagnation pressure was found to differ by less than 1% for the two cases.

3.3.4 Theoretical Considerations

Free Radial Jet

Schwarz (1963) provided the following analytical solution for a laminar free radial jet:

$$V_{\max} = \left[\frac{9}{32}\frac{M^2}{\nu}\right]^{1/3}\left[r^3 - l^3\right]^{-1/3} \tag{3.43}$$

where M is a measure of the jet strength, and is defined as:

$$M = \int_{-\infty}^{\infty} yV^2 dz \tag{3.44}$$

Substituting the fully developed parabolic velocity profile of Eq. (3.37) into Eq. (3.44), M is evaluated as:

$$M = \frac{3Q^2}{10\pi^2 h r_e} \tag{3.45}$$

The constant l in Eq. (3.43) is denoted as the "virtual origin" of the jet, and can be evaluated by determining the jet's centreline velocity from Eq. (3.37),

$$V_{e,\max} = \frac{3Q}{4\pi r_e h} \tag{3.46}$$

and equating this to the left hand side of Eq. (3.46) and solving for l:

$$l^3 = y^3 - \frac{3Q r_e h}{50\pi\nu} \tag{3.47}$$

By substituting Eqs (3.45) and (3.47) into Eq. (3.43), the laminar radial-free-jet centreline velocity is obtained as Eq. (3.48).

$$V_{\max} = \left[\frac{81}{3200}\frac{Q^4}{\pi^4 \nu h^2 r_e^2}\right]^{1/3}\left[y^3 - r_e^3 + \frac{3Q r_e h}{50\pi\nu}\right]^{-1/3} \tag{3.48}$$

Similarly, for a turbulent radial-free-jet, Witze and Dwyer (1976) presented the following semi-analytical expression for the jet's centreline velocity (valid for the case of $r_e >> h$):

$$V_{\max} = V_e\left[\frac{1.32 r_e h}{my(y - r_e)}\right]^{1/2} \tag{3.49}$$

Substituting the jet's mean exit velocity in Eq. (3.21) gives the centreline velocity for a turbulent radial free jet:

$$V_{\max} = \frac{Q}{2\pi r_e h}\left[\frac{1.32 r_e h}{my(y - r_e)}\right]^{1/2} \tag{3.50}$$

Published experimental spreading rates (parameter m in Eq. (3.50)) range from 0.098 to 0.110, whilst the standard k-ε turbulence model predicts a spreading rate of 0.090, which is somewhat lower (Malin, 1989).

Stagnation Region

In the impinging jet's stagnation region, the fluid also attains high strain rate and velocity combinations. Pressure gradient in this region will depend on a pressure divided by a length scale. The logical choice for pressure is the maximum pressure in the region, the stagnation pressure. A suitable length scale will be proportional to an equivalent jet width at stagnation, z_J,

$$L_J = \beta_J z_J \tag{3.51}$$

which is defined as Eq. (3.52) from the jet's flow rate, geometry, and mean velocity.

$$z_j = \frac{Q(r)}{2\pi r U_J} \tag{3.52}$$

Flow rate is represented as a function of radial distance due to the increase in jet volume with distance due to fluid entrainment by the jet. The equivalent jet velocity is calculated from the jet's stagnation pressure.

$$U_J = \sqrt{\frac{2P_S}{\rho}} \tag{3.53}$$

Equations (3.51), (3.52) and (3.53) are combined to calculate the pressure gradient in the stagnation region:

$$\frac{dP}{dx} = \frac{P_s}{L_J} = \frac{\sqrt{8}P_S^{1.5}\pi r}{Q(r)\sqrt{\rho}\beta_J} \tag{3.54}$$

Use of Eq. (3.54) to calculate pressure gradient in the impinging jet region requires the dependence of stagnation pressure and jet flow rate on impact distance and valve gap. These are obtained numerically. The length-scale proportionality constant, β_J, is also evaluated from numerical results.

3.3.5 Results and Discussion

As described above, calculations were conducted for the case of both laminar and turbulent impinging jets. Results obtained are compared, and contrasted with the experimental jet width measurement to suggest that the jet is laminar. To provide further evidence to elucidate if the jet is laminar or turbulent, experimental measurements of disruption efficiency (Chapter 2) are plotted against numerically determined stagnation pressures. The results support the presence of a laminar homogenizer jet.

Numerical Results

Initially, calculations were conducted for free radial jets. The free radial jet's centreline velocity is of most interest, as it will have a direct influence on the jet stagnation pressure which is likely to be important for cell disruption (Engler, 1979). Centreline jet velocities from Eqs (3.48) and (3.50) are compared with numerical results in Fig. 3.16.

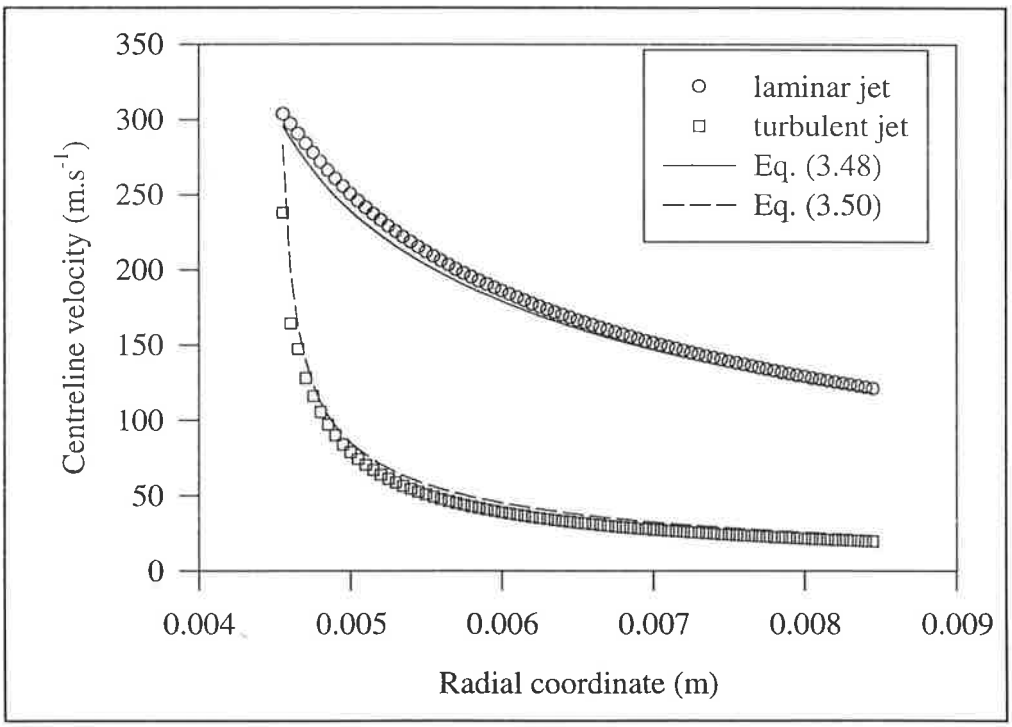

Figure 3.16: Comparison of calculated laminar and turbulent free jet axial centreline velocity profile for an 8 μm valve gap.

It is apparent from Fig. 3.16 that the turbulent jet has a considerably greater rate of velocity decay with radius than the corresponding laminar jet. Also, the numerical results are in good agreement with the available analytical and semi-analytical solutions for radial free jets.

Subsequently, numerical results were obtained for impinging jets. For the case of an 8 μm valve gap, and the standard impact ring (y = 5.5 mm), laminar and turbulent impinging jet streamlines are compared in Figs 3.17 and 3.18, respectively. Due to the lower spreading rate of the laminar jet in comparison with the turbulent jet, the laminar impinging jet has a very small stagnation region. The difference is seen more clearly by comparing the calculated stagnation region pressure profiles for the laminar and turbulent jets (Fig. 3.20). The stagnation pressure of the laminar jet is significantly higher than for the turbulent jet, and focussed over a considerably smaller axial distance.

As the turbulent jet has a lower stagnation pressure than the laminar jet over a wider region, pressure gradients in the turbulent jet stagnation region are approximately two orders of magnitude lower than those found in a laminar stagnation region. However, high turbulent kinetic energy dissipation rates occur in the mixing region of the turbulent jet (where the jet leaves the valve gap and entrains the surrounding fluid). The maximum turbulent energy dissipation rate found numerically in this study is in the order of 10^{10} W kg^{-1} in this region (Fig. 3.19, 8 μm valve gap). As seen in Fig 3.19, the maximum energy dissipation rate is close to the valve, and is independent of impact distance, even down to the lowest distance of 0.5 mm used in this study. A turbulent radial jet is thus unable to describe the effect of impact distance on cell disruption efficiency.

Although these numerical results highlight the large quantitative differences between a laminar and turbulent impinging jet, they do not answer the question of which type of flow occurs in practice. The flow type is determined by measuring the stagnation region width at the impact ring, and by correlation of experimental disruption data.

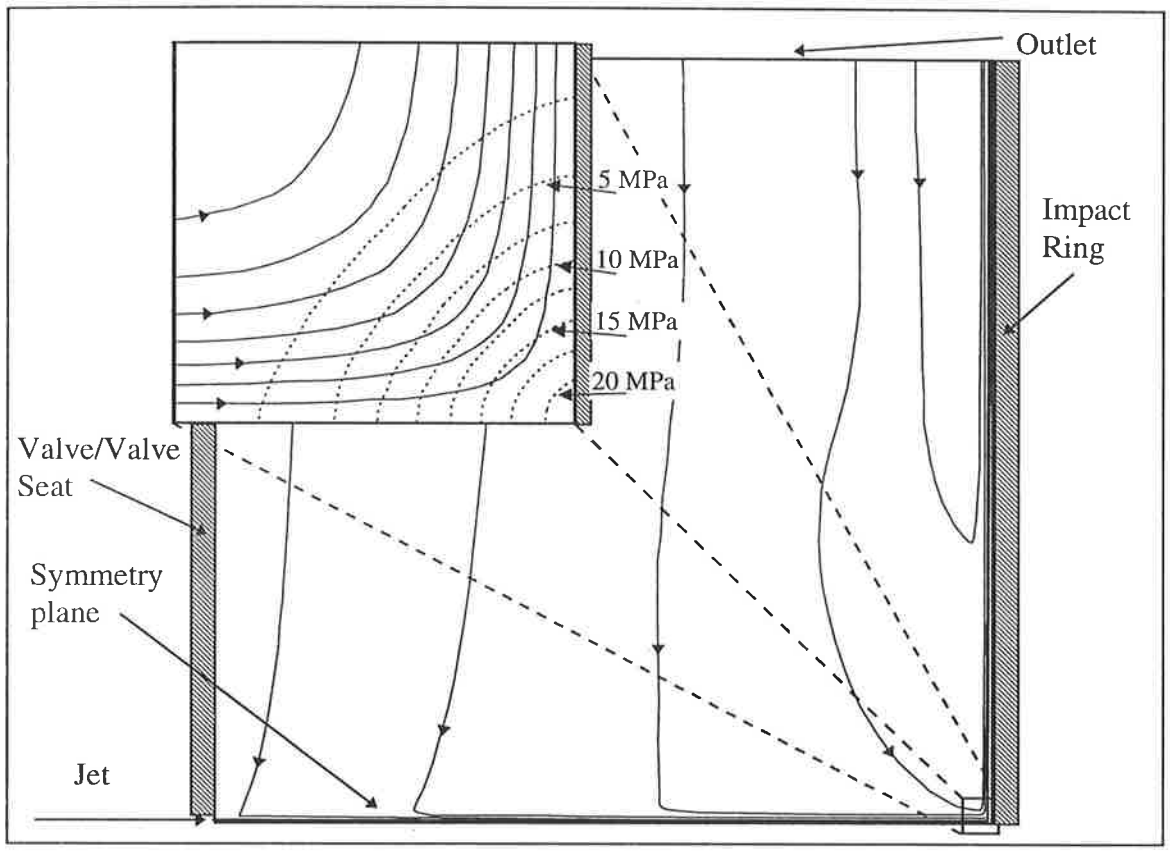

Figure 3.17: Streamlines and pressure contours in the impinging jet region for a laminar impinging jet (8 μm valve gap, 11 mm diameter impact ring).

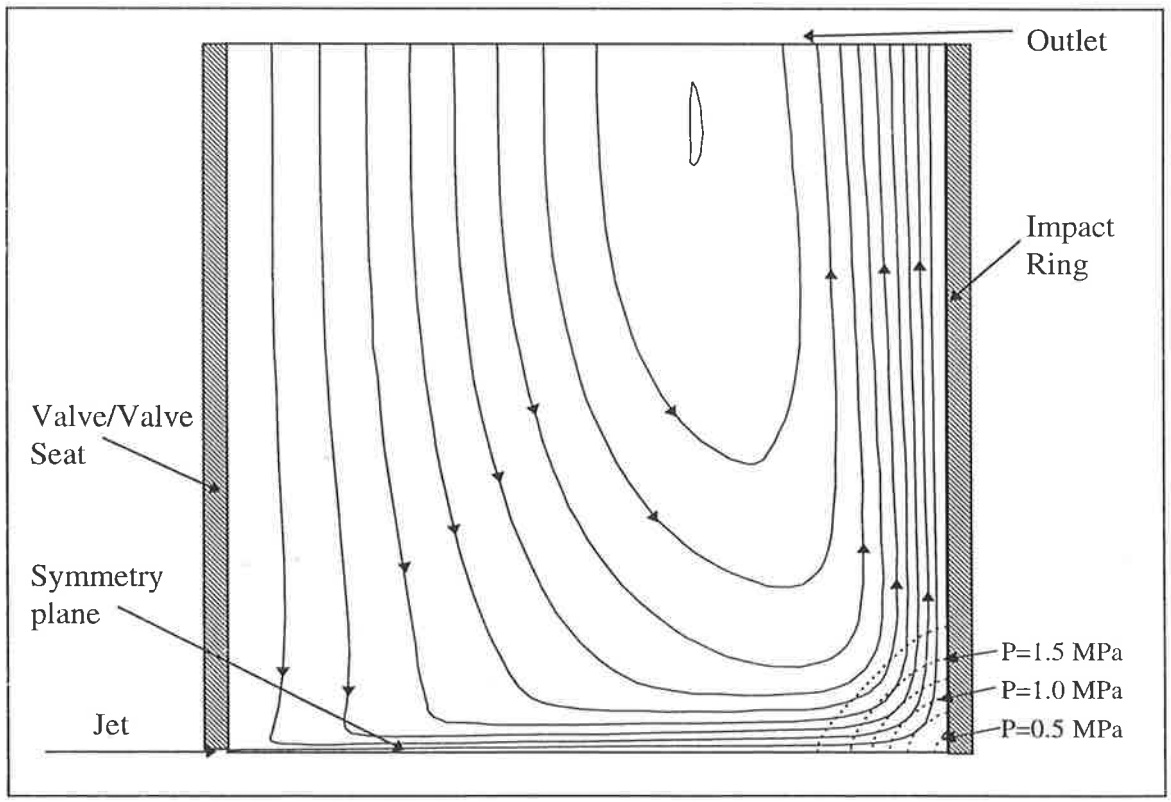

Figure 3.18: Streamlines and pressure contours in the impinging jet region for a turbulent impinging jet (8 μm valve gap, 11 mm diameter impact ring).

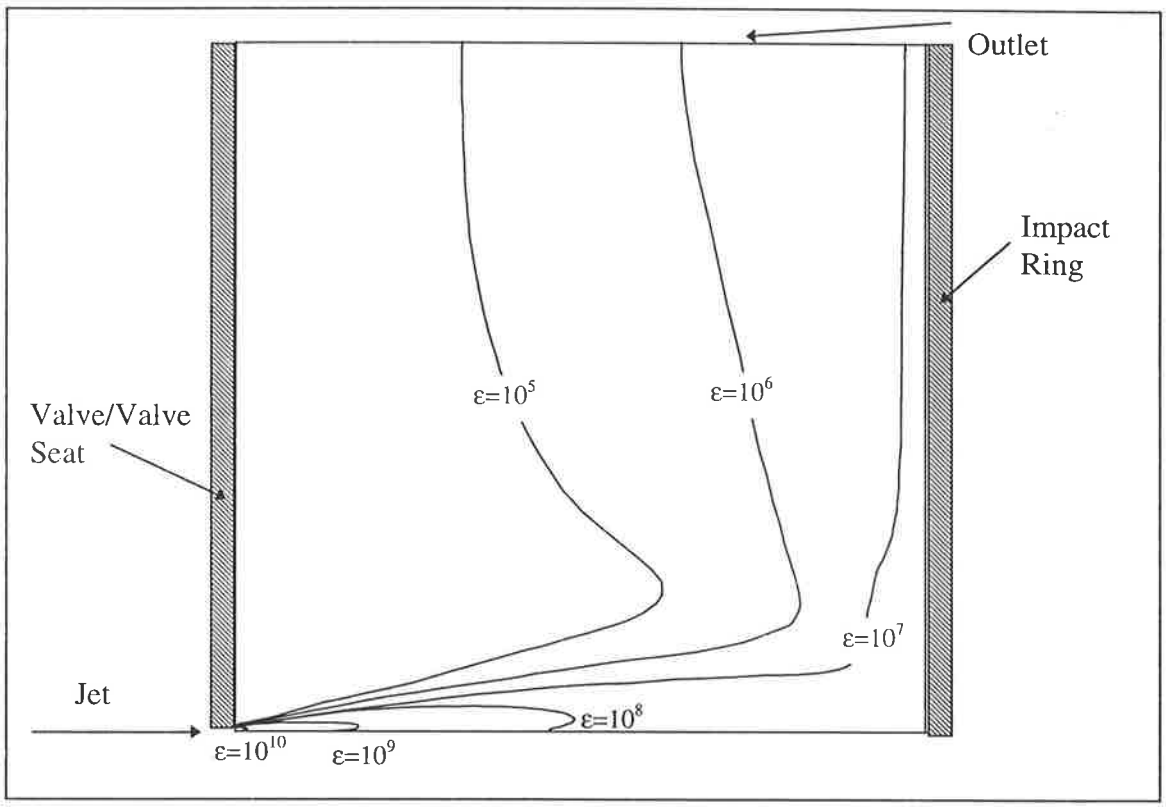

Figure 3.19: Turbulent kinetic energy dissipation contours in the impinging jet region for a turbulent impinging jet (8 μm valve gap, 11 mm diameter impact ring).

Homogenizer Jet Width Measurement

The laminar jet width at stagnation is expected to be approximately 40 μm for the standard impact ring and cell-disruption valve at 60 MPa, compared with over 400 μm for the corresponding turbulent jet (Fig. 3.20). Experimentally, the width of the stagnation region was found to be 30 ± 30 μm, a range that includes the expected stagnation width of a laminar jet but is much lower than that expected for a turbulent jet. This stagnation width was obtained as a jet was found to issue from the bleeding hole in the modified impact ring over an axial distance of 180 ± 30 μm. After correcting for the diameter of the bleeding hole, the stagnation region width given above is obtained. The narrow stagnation region suggests that the impinging jet in this high-pressure homogenizer is probably laminar under standard operating conditions.

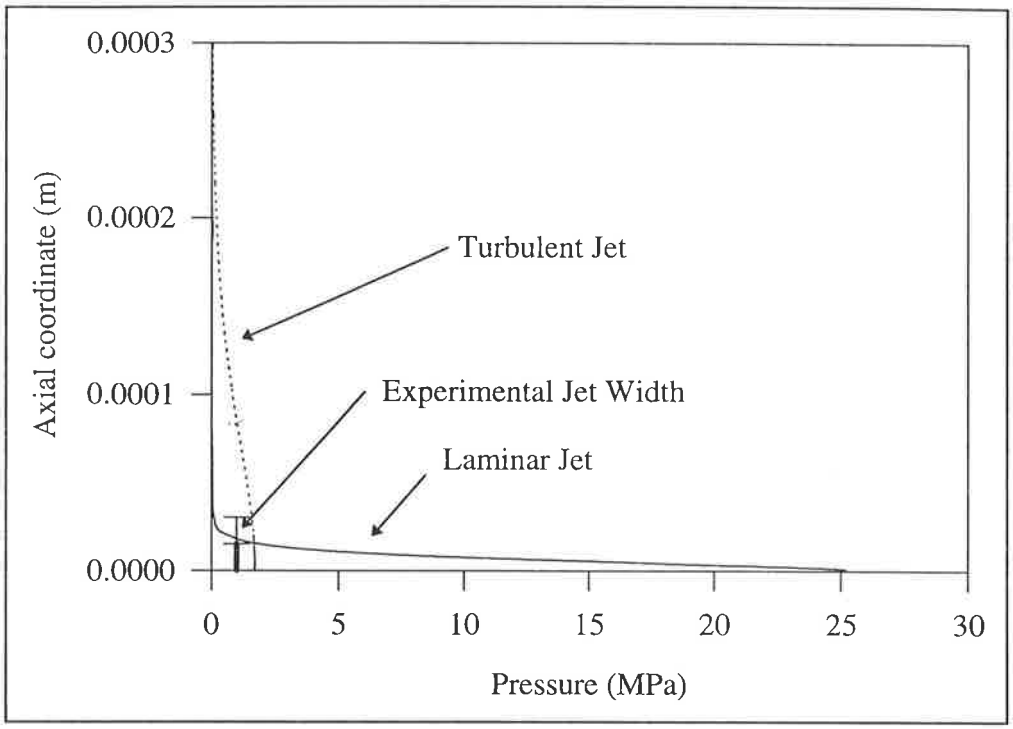

Figure 3.20: Comparison of calculated laminar and turbulent jet axial stagnation pressure profiles at the jet stagnation point, for an 11.0 mm diameter impact ring and an 8 μm valve gap.

Further Evidence for Laminar Jet

Data obtained for Baker's yeast disruption are plotted against operating pressure in Fig. 2.1. These data were obtained for a range of impact rings, giving a wide scatter in disruption at any given operating pressure. For example, at the rated homogenizer operating pressure of 56 MPa, disruption ranges from 75% with a 10 mm diameter impact ring to 15% with a 17 mm diameter impact ring. Keshavarz Moore *et al.* (1990) were able to explain the effect of impact distance and valve gap on disruption rate, for one operating pressure, using stagnation pressure calculated from Eq. (3.30). Although originally only demonstrated for a single operating pressure, it is assumed that the effect of pressure on cell-disruption rate was explained in Eq. (3.30) by the variation of valve gap with operating pressure. Using the experimentally determined empirical relationship between valve gap and operating pressure for the cell-disruption valve seat, the right hand side of Eq. (3.30) was calculated for the data of Fig. 2.1. There is no apparent correlation between the disruption efficiency and stagnation pressure proportionality of Eq. (3.30) in Fig. 3.21, indicating that Eq. (3.30) is not applicable for the calculation of impinging-jet stagnation pressure.

Disruption data were plotted against numerically-determined turbulent jet stagnation pressures, with the results shown in Fig. 3.22. Turbulent stagnation pressure does not adequately correlate cell-disruption efficiency.

Disruption data were plotted against laminar-impinging-jet stagnation pressure calculated numerically, with the results shown in Fig. 3.23. From Fig. 3.23, it appears that the laminar stagnation pressure provides a good correlator for cell disruption efficiency. Most of the variation in Fig. 3.23 occurs at low values of stagnation pressure. These disruption values correspond to high operating pressures and large impact distances. Under these conditions, it is expected that the total cell-disruption achieved (< 20%) occurs in the valve inlet region rather than in the stagnation region of the impinging jet. Hence the variation represents the range of non-impingement disruption that occurs in the valve inlet region before the cell suspension is stagnated at the impact ring.

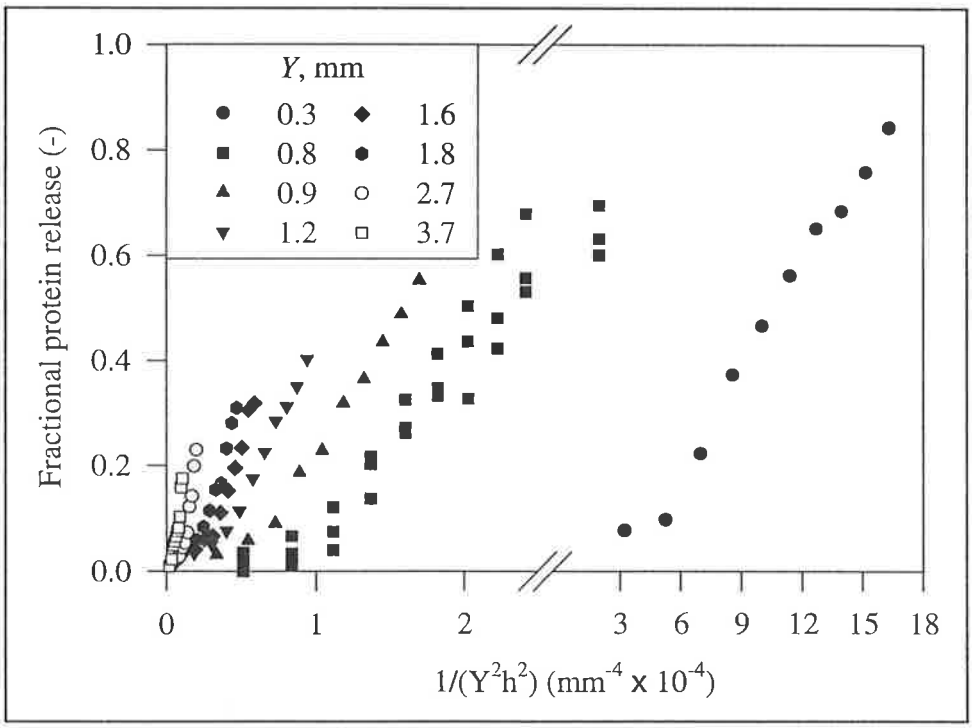

Figure 3.21: Dependence of Baker's yeast disruption efficiency on the stagnation pressure proportionality of Eq. (3.30) for a range of impact distances.

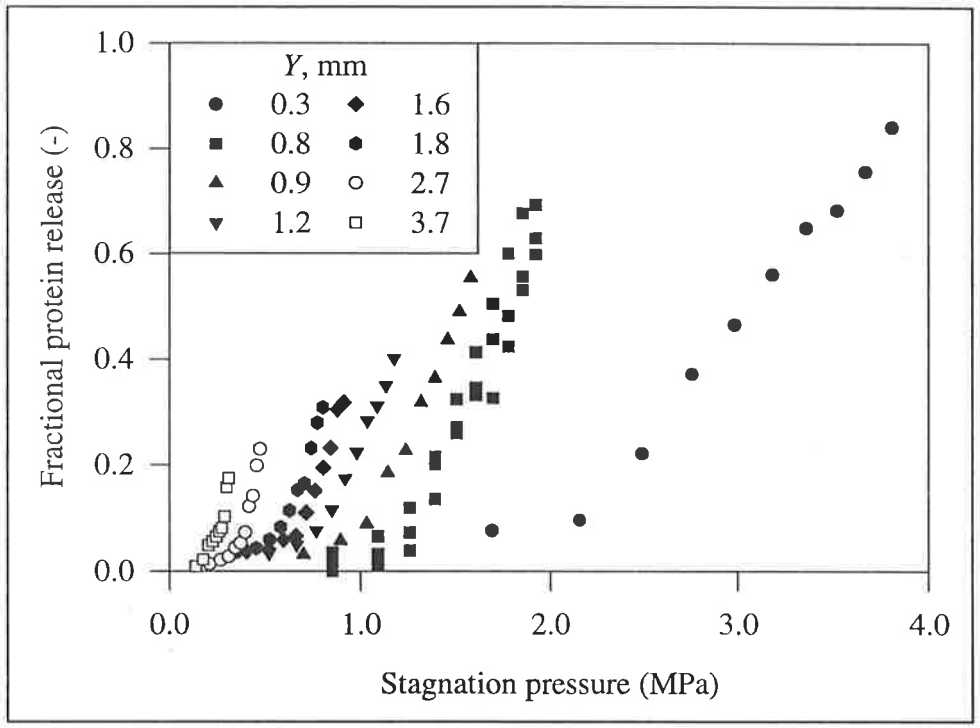

Figure 3.22: Dependence of Baker's yeast disruption efficiency on numerically determined turbulent jet stagnation pressure for a range of impact distances.

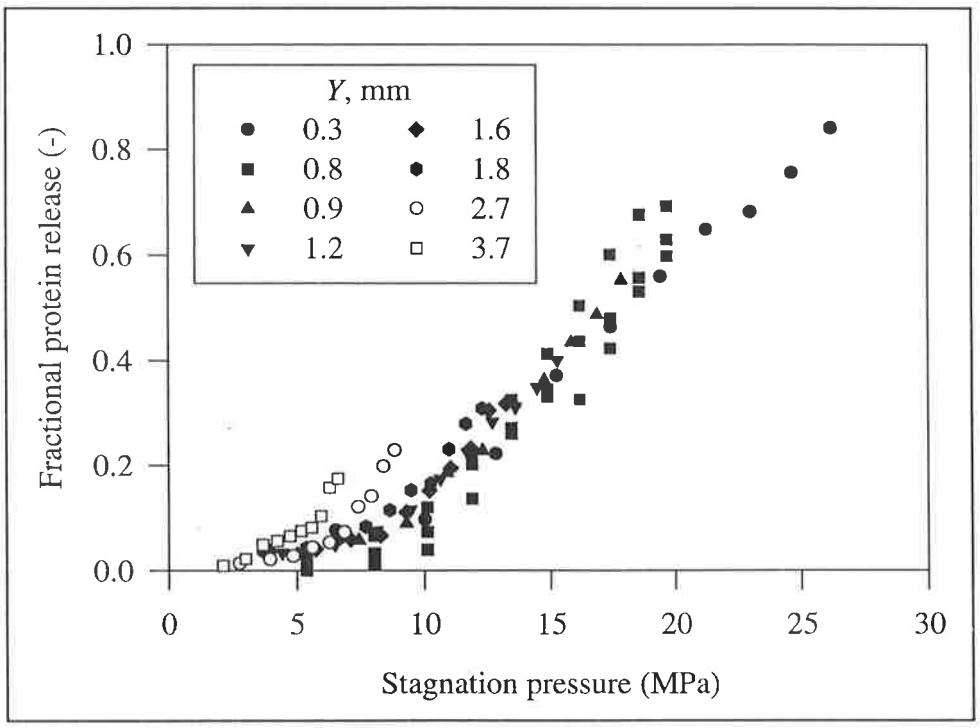

Figure 3.23: Dependence of Baker's yeast disruption efficiency on numerically determined laminar jet stagnation pressure for a range of impact distances.

Laminar jet pressure gradient

To quantify the effect of impact distance on pressure gradient for a laminar jet, the dependence of jet flow rate and stagnation pressure on impact distance are required in Eq. (3.54). Jet flow rate was determined by integrating the numerical axial velocity profile of the equivalent free radial jet, and its dependence on radius is described empirically by Eq. (3.55) for $0.0045 \leq r \leq 0.0085$.

$$\frac{Q(r)}{Q} = 115(r - 0.0045)^{0.73} + 1 \tag{3.55}$$

The maximum laminar jet stagnation pressure depends on valve gap and impact radius. In the absence of direct numerical simulation of the impinging jet stagnation pressure, a reasonable approximation is found by calculating stagnation pressure from the jet centreline velocity calculated by Eq. (3.48):

$$P_S \approx \frac{1}{2}\rho V_{\max}{}^2 \tag{3.56}$$

Substitution of Eqs (3.55) and (3.56) into Eq. (3.54) describes the dependence of laminar-jet stagnation-region pressure-gradient on impact radius and valve gap, with the length scale proportionality constant determined to be:

$$\beta_J = 0.9 \tag{3.57}$$

With the cell disruption valve seat and standard 11 mm impact ring, the maximum pressure-gradient in the impinging jet region approximately 1.5 times higher than the pressure-gradient in the valve inlet region.

3.4 Summary

Homogenizer fluid mechanics have been studied experimentally, analytically, and numerically. The homogenizer was divided into a "valve-inlet" and an "impinging-jet" region for analysis.

Experimentally-measured valve-gaps during homogenizer operation showed that homogenizer valve gap decreases with increased operating pressure. The measured dependence of valve gap on operating pressure was in excellent agreement with laminar and turbulent semi-analytical predictions.

Numerical simulation of flow within the valve-inlet shows that flow separation and cavitation do not occur under normal cell-disruption homogenizer operating conditions. The pressure gradient as fluid enters the valve gap is described by Eq. (3.25),

$$\frac{dP}{dy} = \frac{\rho Q^2}{8\beta_I \pi^2 r_i^2 h^3} \tag{3.25}$$

with values of the length scale proportionality constant β found to be 2.1 and 1.2 for the chamfered cell disruption and square edged valve seats respectively, and h determined by

$$h = 37 \times 10^{-6} \left(P \times 10^{-6} \right)^{-0.35} \tag{3.58}$$

for the cell disruption valve seat in an APV-Gaulin 15M homogenizer.

Comparison of simulated and measured stagnation region width revealed that the homogenizer's impinging jet is laminar. This conclusion was further supported by the correlation of disruption efficiency with laminar jet stagnation pressure over a wide range of operating pressures and impact distances. The pressure gradient in the stagnation region of the impinging jet is described by Eq. (3.54),

$$\frac{dP}{dx} = \frac{\sqrt{8} P_S^{1.5} \pi r}{Q(r) \sqrt{\rho} \beta_J} \tag{3.54}$$

with the length scale proportionality constant found to be 0.9. In the absence of numerical simulation results, the dependence of flow on impact ring radius for an APV-Gaulin 15M homogenizer is given by Eq. (3.55)

$$\frac{Q(r)}{Q} = 115(r - 0.0045)^{0.73} + 1 \tag{3.55}$$

where Q is flow rate and r is the stagnation radius. Stagnation pressure can be approximated by Eq. (3.56),

$$P_S \approx \frac{1}{2}\rho V_{\max}{}^2 \tag{3.56}$$

where

$$V_{\max} = \left[\frac{81}{3200}\frac{Q^4}{\pi^4 \nu h^2 r_e{}^2}\right]^{1/3}\left[y^3 - r_e{}^3 + \frac{3Qr_e h}{50\pi\nu}\right]^{-1/3} \tag{3.48}$$

In the following chapter, the effect of the flow fields (determined in this chapter) on cells is examined.

Chapter 4

Cell-Homogenizer Interaction

The physical process that is responsible for cell breakage, or the disruption mechanism, must be understood if an independent homogenizer stress distribution is to be determined. This physical process occurs as a result of the interaction between cells and the homogenizer. Proposed disruption mechanisms were briefly discussed in section 1.2.2, and are further discussed in section 4.2. Experimental data are often used to attempt to elucidate disruption mechanisms, and some relevant data were provided in chapter 2. However, a considerably more quantitative analysis is required, which must not only define the disruption mechanism, but also quantify the stresses it produces in cells.

In this chapter, previous attempts to define disruption mechanisms are reviewed, highlighting the need for further analysis. Numerical calculations are conducted to quantify the stresses that act to disrupt cells during homogenization. Results of this chapter are used in chapter 6 to define a homogenizer stress distribution and hence model and predict cell breakage during homogenization.

4.1 Introduction

It is the interaction between cells and the homogenizer (for example, the homogenizer-generated flow fields) that causes cell breakage. The manner in which the cells and homogenizer interact must be characterised and quantified if the stress applied to cells during homogenization is to be modelled. However, it is impossible to characterise these interactions directly from experiments, as it is not possible to view the processes that occur as a cell passes through a homogenizer valve assembly.

Because of this experimental difficulty, theoretical insights combined with numerical analysis provide a powerful tool to examine the interactions between cells and the homogenizer. In the most general case, the interaction could be examined directly. This would involve simulating the trajectory of cells as they pass through the homogenizer flow field (using flow fields determined by the methods of Chapter 3). At each position in the cell's trajectory, the forces that act on the cell would be evaluated, resulting in a complete force-time profile for the cell, including interactions it may have with solid boundaries. Trajectory simulations such as these are often conducted for rigid particles (for example, Clift *et al.*, 1978). If the particle is significantly smaller than the dimensions of the flow, the equations of motion for the particle can be defined and trajectory calculations are relatively straightforward. In this type of straightforward case, trajectory simulations can be carried out independently of flow simulation.

However, a cell in a homogenizer is a considerably more complex case. The cell is large compared to flow dimensions (section 4.4) and the cells may be deformable within the flow field. A complete problem formulation would need to include the effects of fluid flow on motion and deformation of the cell, together with the effect of the cell on the flow field. It would also require a knowledge of the material properties of the cell wall, to determine the cell's response to fluid forces. If the problem formulation were sufficiently complex, it would provide an accurate representation of the actual processes that occur when a cell passes through a homogenizer valve. Whilst such a general formulation will accurately determine the interactions between cells and the homogenizer that cause cell breakage, it is unlikely to be achieved in the near future. Firstly, in such a general form, a numerical problem that is likely to be intractable with present computational power will result (Zhou and Pozrikidis, 1995). Secondly, critical information regarding the mechanical properties

of cell walls is not presently available. Thus, cell-homogenizer interactions can only be determined with such a general approach when both of these constraints can be removed.

An alternative approach has been to consider the key physical phenomena or "mechanisms" that are likely to effect cell breakage. These phenomena can be examined in isolation and used to describe experimental observations during homogenization. Obviously, this approach relies on selection of the correct disruption mechanism, as support for any given mechanism can generally only be obtained indirectly (for example dependence of maximum stable cell diameter on homogenizer pressure). The degree of quantitative analysis that has been conducted is directly related to the complexity of the chosen mechanism. For example, it is difficult to quantitatively model cavitation effects on cells, and only qualitative predictions about changes in cavitation conditions can be made. In comparison, the deformation and breakup of liquid drops in viscous planar shear flows has been extensively examined and can be accurately predicted. Another limit to the degree of quantitative analysis that can be conducted is related to the amount of information that is available regarding the flow conditions in the homogenizer (for example velocities, pressures, strain rates). A quantitative analysis is also limited by the incomplete knowledge of cell-wall mechanical properties.

In this thesis, the latter approach of considering a disruption mechanism is utilised. This requires the information provided on homogenizer fluid mechanics in Chapter 3. After reviewing the mechanisms that have been proposed to effect disruption is section 4.2, the most physically-plausible of these mechanisms are chosen for further evaluation. Numerical simulations are conducted to provide quantitative estimates of the influence of homogenizer variables on cells. The results of this chapter are subsequently used in chapter 6 to define a homogenizer stress distribution.

4.2 Proposed Mechanisms

Initial work into the mechanism of homogenization investigated the disruption of fat globules, with particular emphasis on the homogenization of dairy products. Although the mechanism of cell disruption is reported to be different from that of fat droplet dispersion (Pandolfe, 1992), it is still relevant to review the extensive list of mechanisms that have been proposed for fat globule disruption. Likely mechanisms for cell disruption are selected, and then analysed in further detail.

Fat Globule Disruption

The range of theories that have been proposed for the high-pressure homogenization of emulsions include (Mulder and Walstra, 1974):

1. crushing of droplets on boundary walls of the valve as they are squeezed into the valve gap,
2. explosive decompression of droplets after being compressed at high pressure and then passing to regions of low pressure,
3. acceleration of droplets at the entry and exit to the valve gap,
4. collisions between droplets,
5. impact of droplets with boundary walls near changes in the flow direction,
6. shearing stresses in regions with high shear gradients,
7. Wittig mechanism (high shear in convergent flow followed by turbulence),
8. oscillations of the homogenizer valve that cause resonant oscillations and hence disruption of the droplets,
9. pressure differences at the surface of the droplet due to turbulence, and
10. pressure differences at the surface of the droplet due to the implosion of nearby cavitation bubbles.

Theory 1 has been discounted, as fat droplets are usually considerably smaller than the valve gap. Theory 2 is disregarded, as fat droplets are not considered to be compressible. Theory 3 is an analogy to the breakup of, for example, large raindrops, and assumes relative velocity differences between fat globules and the surrounding fluid phase. In this form it is rejected, and is distinguished from Theory 6 or 7 which consider accelerated flow that can lead to shearing forces. Theory 4 is rejected on the basis that droplets are not hard and brittle. Theory 5 is rejected as fat droplets are not denser than the suspending fluid,

and will not leave flow streamlines to interact with, *e.g.*, the impact ring. Theory 7 and 8 have also found little support.

The most likely mechanisms responsible for fat droplet disruption are thought to be shear (Theory 6), turbulence (Theory 9) or cavtitation (Theory 10) (Walstra, 1993). However, the following studies show that although these theories explain experimental observations, there is still some degree of uncertainty.

Phipps (1971, 1974b) dismissed cavitation and turbulence as disruption mechanisms, as effective homogenization could be achieved under conditions of laminar and turbulent flow and also with or without cavitation. Phipps (1974b) also demonstrated that disruption is completed close to the valve-seat inlet-boundary. This observation ruled out Couette-type shear flow between the valve and seat as being responsible for droplet dispersion, and led Phipps to conclude that extensional or plane hyperbolic shear (as fluid accelerates into the valve gap) is the main cause of droplet disruption. However, Kurzhals (1977) demonstrates that extensional viscous shear forces are probably not high enough to effect droplet disruption, and concluded that cavitation is likely to be the primary cause of droplet dispersion. Loo *et al.* (1950; 1953) have also argued that cavitation is a likely cause of droplet dispersion.

The turbulence theory suggests that the energy dissipated during the homogenization process generates intense turbulence with its associated energy dissipating turbulent eddies (Mulder and Walstra, 1974). For turbulent eddies which are approximately the same size or smaller than the droplets, turbulent pressure fluctuations at the surface of the droplet will lead to disruption. The dependence of the volume/surface average diameter of the droplets on the turbulent kinetic energy dissipation rate in a turbulent flow is given by:

$$d_{vs} = k_8 \left(\frac{\gamma}{P} \right)^{3/5} \varepsilon^{-2/5} \tag{4.1}$$

This energy density can be approximately related to the homogenizer operating pressure (Mulder and Walstra, 1974) and provides an excellent explanation of the effect of homogenizer operating pressure on average droplet diameter.

From this discussion, it would seem that these last three physical phenomena: cavitation, turbulence, and shear flow may be able to effect fat droplet dispersion during

homogenization, with the dominant mechanism depending on homogenizer valve design and operating conditions.

Cell Disruption

The ten theories for fat globule disruption presented above can also be discussed in the context of cell disruption.

Theory 3 and 8 can both be rejected for the same reasons that they are rejected for fat droplet disruption, and Theory 7 can be considered as a variation of Theory 6.

Theory 1: Kesharvarz Moore *et al.* (1990) have suggested that the distortion of cells by the valve itself (which are of similar dimensions as the valve gap) may significantly contribute to the disruption rate. However, the disruption rate for cells passing through an orifice (even without an impact effect) shows little dependence on flow rate and hence valve gap (Brookman, 1975), indicating that this effect is not usually likely to be important.

Theory 2: As with fat droplets, cells are not considered to be compressible, but decompression is able to disrupt cells if they are first mixed with a gas (see explosive decompression, section 1.1.2). However, Bavouzet *et al.* (1995) report that pressure release by itself is not able to effect the disruption of microorganisms, indicating that this is not likely to be an important mechanism.

Theory 4 and 5: Engler (1979) has suggested that cell disruption may result from abrasion of cells as they collide with one another or with a solid surface, and Middelberg *et al.* (1992a) have developed a homogenizer stress distribution function for *E. coli* based on impact of cylinders with a solid surface. These mechanisms are also useful in explaining the impact effect that is observed experimentally (section 1.2.2). However, they alone cannot explain the disruption occurring during homogenization, as high rates of disruption may be achieved, particularly for *E. coli*, even without impact effects (Chapter 2).

Theory 6: Couette shear stresses have been dismissed as being responsible for cell disruption (Engler, 1979). However, plane hyperbolic shear stresses have been implicated as the primary cause of cell disruption (Ayazi Shamlou *et al.*, 1995), and are able to predict that disruption occurs in both the valve inlet and impinging jet regions (Phipps, 1971; Ayazi Shamlou *et al.*, 1995).

Theory 9: Doulah *et al.* (1975) have developed a model for cell disruption which assumes that cell breakage occurs due to turbulence. Analysis of the jet in the homogenizer used in this study suggests that it is laminar rather than turbulent. This does not discount turbulence as a mechanism for cell disruption, as turbulent flow conditions may exist in other homogenizer designs or under different operating conditions. For a homogenizer that produces a turbulent jet, the maximum turbulent kinetic energy dissipation rates are found in the jet's mixing region (see Fig. 3.19). As discussed in section 3.3.5, the efficiency of homogenization with a turbulent jet would not show any dependence on impact distance, as the maximum turbulent kinetic energy dissipation rates are independent of impact distance. However, such a dependence is seen experimentally.

Theory 10: Cavitation has been shown to effect cell disruption in purpose-built apparatus (Save *et al.*, 1994). However, the results of Chapter 3 suggest that the commonly-used cell-disruption valve assembly does not cavitate under normal operating conditions. Also, valves that are likely to cavitate (*e.g.* square valve: see Fig. 3.11) do not appear to perform any better than valves that do not cavitate (see Fig 2.5). In addition, disruption during cavitation has been found to be extremely concentration dependent (Save *et al.*, 1994), which does not agree with experiments conducted in homogenizers (section 1.2.2).

Likely Mechanisms

From this discussion, the likely mechanisms for cell disruption during homogenization include turbulence, cell-cell and cell-solid impacts, and shear flow. As turbulence is not likely to be an important mechanism in the homogenizer examined in this thesis, it is not given further consideration. The remaining two mechanisms, which may be classed as cell-fluid and cell-solid interactions, are analysed in greater depth in sections 4.3 and 4.4 respectively.

4.3 Cell-Fluid Interactions

Ayazi Shamlou *et al.* (1995) have asserted that viscous shear stresses are responsible for cell breakage during homogenization. By assuming that the cell suspension has a Trouton ratio of 1000, it was predicted that a viscous force of 540 μN is exerted on a typical cell during homogenization. This is greater than the measured compressive force of 40 - 90 μN required to break yeast cells (Roberts *et al.*, 1994). However, the assumption that a cell suspension's Trouton ratio is 1000 is questionable. Whilst the Trouton ratio may exceed several thousand for non-Newtonian fluids such as polymer melts, it is only 3 for a Newtonian fluid. A dilute aqueous suspension of cells, often used in homogenizer studies, is likely to be very nearly Newtonian, and hence will not have a large Trouton ratio. If a more realistic Trouton ratio of 3 is assumed, viscous forces of less than 2 μN would be expected. This force is more than an order of magnitude lower than measured compressive forces required to break cells, and is thus likely to be too low to cause cell breakage.

Hence, it would appear that viscous shear forces do not provide a satisfactory explanation of the mechanism of cell disruption. However, planar shear is still a plausible candidate for the disruption mechanism. As discussed by Ayazi Shamlou *et al.* (1995), it occurs in both the valve inlet and impinging jet region, and is able to qualitatively explain the effect of homogenizer operating pressure and impact distance. Thus, the limitation in the analysis of Ayazi Shamlou *et al.* (1995) may not be the choice of planar shear, but the choice of a viscous mechanism. Also, rather than using viscous droplet deformation as an analogy for the cell, it is more correct to consider a cell as a "capsule", which may be defined as a particle consisting of a liquid interior surrounded by a thin membrane.

Numerous studies have considered stationary capsules in creeping shear flows (Barthes-Biesel and Rallison, 1981; Li *et al.*, 1988; Pozrikidis, 1990; Chang and Olbricht, 1993; Zhou and Pozrikidis, 1995). A comprehensive work has determined the motion and deformation of a capsule as it passes through a constriction in the limiting case of creeping flow (Leyrat-Maurin and Barthes-Biesel, 1994). However, the effect of inertial rather than viscous flows on capsules has not been considered. Studies determining the effect of finite Reynolds number flows on the deformation of drops in simple shear flows (Sheth and Pozrikidis, 1995) and bubbles in straining flows (Ryskin and Leal, 1984; Kang and Leal, 1987; 1989) have highlighted the importance of inertial effects at finite Reynolds number in drop and bubble deformation.

For cells in a homogenizer, this thesis is concerned with the case where the cell moves with the fluid, and experiences a high velocity and strain rate simultaneously. No previous studies have addressed this configuration. This problem is addressed in this section. Specifically, the tensions or stresses that are generated in a cell wall as it passes through a homogenizer valve are required. This thesis concentrates on the case of a spherical cell (applicable for, for example, *S. cerevisae*), but also addresses non-spherical cells.

4.3.1 Problem Formulation - Spherical Cell

As stated above, this section considers the tensions that are produced in a cell as it moves within a homogenizer's flow field. The flow field is a combination of a steady uniform flow and a straining flow. For simplicity, a fully axisymmetric configuration is considered. Although the valve of the homogenizer of interest in this thesis has an approximately plane symmetric rather than axisymmetric constriction, comparison with an axisymmetric case will still represent the salient features of plane symmetric convergence. Effects of the constriction boundary walls are effectively neglected by considering a cell that is small compared to the extent of the unbounded flow field's domain. Although this is not true in practice, this simplification does not influence the final results.

To remove feedback between the fluid-cell interactions, a limiting case of the general problem of a cell passing through a homogenizer is considered. Firstly, it is assumed that either the cell wall's elastic modulus is sufficiently high or the fluid's strain rate sufficiently low that the cell will not significantly deform from spherical. A sufficiently small deformation will not affect the flow field around the cell, and will not significantly alter the distribution or magnitude of tensions within the cell wall. This first assumption avoids the need to solve for the interactions between fluid flow and cell deformation. Secondly, it is assumed that the densities of the cell and fluid are sufficiently close that the cell will move at the same velocity as the flow field at its centre of mass. This is likely to be true even in the case of the small but significant density difference that does exist, as the drag on the cell will rapidly increase if the cell leads or lags the fluid, thus reducing the relative motion between the cell and fluid. This second assumption avoids the need to solve for either the cell motion or the interactions between the fluid and cell motion.

With the assumptions outlined above, the problem reduces to calculation of the instantaneous tensions within the cell wall. Analysis of the resulting tensions is required to investigate, for example, the possibility of failure events within the cell wall. In a simple uniaxial tension test, a specimen will fail when some critical failure tension is exceeded. However, in a membrane with biaxial tensions, a combination of each of the two tensions will define the critical failure tension. A commonly used method to calculate the critical failure conditions is based on the "shear strain energy per unit volume" in the test specimen (von Mises criterion (Ward and Hadley, 1993)). The critical failure tension for a von Mises failure criterion is expressed as:

$$T_{VM}{}^2 = T_A{}^2 + T_H{}^2 - T_A.T_H \tag{4.2}$$

which assumes material failure properties are the same in tension and compression. However, in many cases materials have higher failure stresses in compression, and Eq. (4.2) may not always be applicable. In such cases, more information regarding the failure properties of the material is required. For the present study, Eq. (4.2) is assumed to provide an adequate failure criterion.

Concordant with the above simplification, the tensions within the cell wall were determined by firstly solving for the external flow field around the spherical cell, and subsequently calculating the membrane tensions from a force balance. These two steps are now outlined in more detail.

External Flow Field

The external flow field around the cell is that of a straining flow around a moving, rigid sphere. Numerical simulations of straining flow around a rigid stationary sphere have been conducted (Magnaudet *et al.*, 1995) to improve knowledge of forces acting on a sphere in accelerating flows at finite Reynolds numbers. The present study also provides numerical simulations of straining flow around a rigid but moving sphere, and makes the following assumptions in formulation of the numerical model:

- the flow field far from the cell is defined by the combination of a uniform and an axisymmetric straining flow,
- the cell is not significantly deformed by the flow and remains spherical,
- the cell is moving at the same velocity as the flow field at its centre of mass,
- flow around the cell is laminar and axisymmetric, with no slip at the wall,

- flow is incompressible and isothermal, and
- gravity effects are not considered in the calculations.

The defining two-dimensional computational domain for this situation is shown schematically in Fig. 4.1.

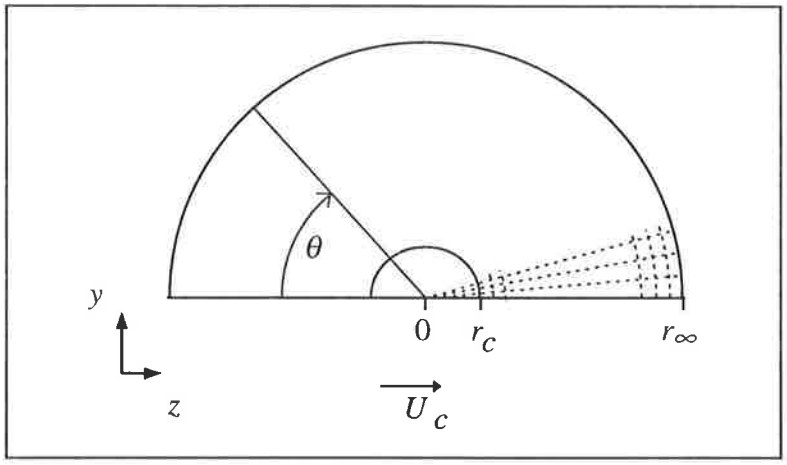

Figure 4.1: Representation of coordinate system used to represent external flow around spherical cell.

Governing Equations

The fundamental partial differential equations for laminar flow are the conservation equations for mass and momentum and can be written in tensor notation as follows:

$$\frac{\partial U_i}{\partial x_i} = 0 \tag{4.3}$$

and

$$U_j \frac{\partial U_i}{\partial x_j} = -\frac{1}{\rho}\frac{\partial P}{\partial x_i} + \frac{\partial}{\partial x_j}\left(\nu \frac{\partial U_i}{\partial x_j}\right) \tag{4.4}$$

Boundary Conditions

With the stated assumptions, the associated boundary conditions are:

1. On the cell surface
   - $W = U_c$ (4.5)
   - $V = 0$ (4.6)
2. Along the symmetry axis
   - $\frac{dW}{dy} = 0$ (4.7)
   - $V = 0$ (4.8)
3. At the upper domain boundary ($r_\infty = 20r_c$, $0° \leq \theta \leq 178°$)
   - $W = U_c + \alpha.z$ (4.9)
   - $V = -\frac{\alpha.y}{2}$ (4.10)
4. At the domain outlet ($r_\infty = 20r_c$, $178° \leq \theta \leq 180°$)
   - P = fixed (4.11)

Solution Procedure

The governing equations (Eqs 4.3 and 4.4) were solved subject to the conditions of Eqs (4.5) to (4.11) using a commercially-available finite-volume fluid-dynamics code (PHOENICS 2.1 CHAM, Wimbledon, London, UK). The spherical coordinate system (Fig. 1) was emulated using a rotated body fitting coordinate (BFC) grid. A grid with a total of 90 cells on the cell surface and 75 cells between the cell surface and outer boundary was chosen. The radial grid was clustered to give greatest refinement near the cell surface.

These numerical results were used to provide shear stress and pressure profiles on the cell surface. The pressure on the cell surface was approximated as the pressure in the centre of the finite volume cell closest to the surface. The shear stress was calculated as:

$$\tau = \mu.\frac{\Delta U}{\Delta x} \tag{4.12}$$

where ΔU is the difference in velocity between the cell surface and the parallel velocity at the nearest cell side, and Δx is the radial width of the cell nearest to the cell wall.

Cell Wall Tensions

A schematic representation of the cell is shown in Fig. 4.2 to define the principal membrane tensions.

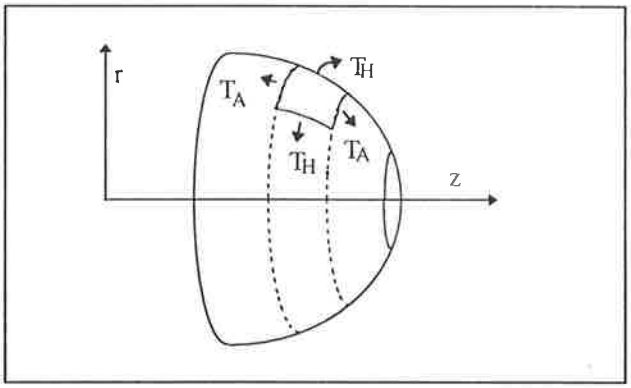

Figure 4.2: Representation of axisymmetric membrane with principal tensions T_A and T_H in the axial and hoop directions respectively.

Equations for the determination of these principal tensions in an axially-loaded axisymmetric shell have been formulated by Timoshenko and Woinowsky-Krieger (1959). The axial tension was determined by conducting a force balance on a portion of the shell,

$$T_A(\theta) = -\frac{R(\theta)}{2.\pi.r_c.\sin^2\theta} \tag{4.13}$$

where $R(\theta)$ is the resultant of the total load on the portion of the shell to θ.

$$R(\theta) = 2.\pi.{r_c}^2 \int_0^{\theta} \sin\theta\left(\cos\theta\left[P_e(\theta) - P_i(\theta)\right] + \sin\theta.\left[\tau_e(\theta) - \tau_i(\theta)\right]\right).d\theta \tag{4.14}$$

The hoop tension was determined by conducting a force balance on a small element of the shell.

$$T_H(\theta) = Z(\theta).r_c - T_A(\theta) \tag{4.15}$$

where $Z(\theta)$ is the net load acting perpendicular to the small element of the membrane.

$$Z(\theta) = P_i(\theta) - P_e(\theta) \tag{4.16}$$

Equations (4.13) to (4.16) allow calculation of axial and hoop tensions in the cell wall using the internal and external pressure and shear stress profiles. The external pressure and shear stress profiles were determined from the external flow field. The fluid within the cell is assumed to move at the same velocity as the cell in the absence of cell deformations, and hence internal shear stresses are not present. The fluid within the cell does contain a pressure gradient (as a result of the cell's acceleration with the external flow). This pressure gradient is calculated from Eq. (4.17),

$$\frac{dP}{dz} = -\rho_c . a \tag{4.17}$$

where the acceleration of the cell is determined from Newton's law, given as Eq. (4.18),

$$a = \frac{F_z}{m} = \frac{F_z}{\frac{4}{3}.\pi.r_c{}^3.\rho_c} \tag{4.18}$$

with the force acting on the cell exerted by the external flow field. This force is calculated by integrating the normal and tangential forces acting on the cell surface (Bird *et al.*, 1960),

$$F_z = 2.\pi.r_c{}^2 \int_0^{\pi} \sin\theta\left(\cos\theta . P_e(\theta) + \sin\theta . \tau_e(\theta)\right) d\theta \tag{4.19}$$

The internal pressure acting on the cell wall is thus determined from the internal pressure as a function of position (θ) by integration of Eq. (4.17).

$$P_i(\theta) = \int_0^{\theta} \frac{dP}{dz} dz = \rho_c . a . r_c \left(1 - \cos(\pi - \theta)\right) + P_{i0} \tag{4.20}$$

However, the minimum pressure within the cell's internal fluid, P_{i0}, is initially unknown. The minimum internal pressure is determined by minimising the total strain energy within the cell wall. The simplest (and most reasonable) approximation of membrane mechanical behaviour is to assume that the membrane has a linear stress-strain relationship and obeys the generalised Hooke's law. The generalised Hooke's law has a strain energy function given by Eq. (20).

$$w = \frac{Et}{2\left(1 - \nu^2\right)} \left\{ \varepsilon_A{}^2 + \varepsilon_H{}^2 + 2\nu\varepsilon_A\varepsilon_H \right\} \tag{4.21}$$

For the limiting case of low strains ($\varepsilon << 1$) in an incompressible membrane,

$$\varepsilon_A \approx \frac{1}{Et}\left(T_A - \nu T_H\right) \tag{4.22}$$

$$\varepsilon_H \approx \frac{1}{Et}\left(T_H - \nu T_A\right) \tag{4.23}$$

and Poisson's ratio (ν) is 0.5. Substitution of Eqs (4.22) and (4.23) into the strain energy function of Eq. (4.21) gives Eq. (4.24).

$$2wEt = T_A{}^2 + T_H{}^2 - T_A T_H \tag{4.24}$$

Total membrane strain energy, W, is determined by integrating strain energy over the membrane.

$$WEt = \int_0^{\pi} \left(T_A{}^2 + T_H{}^2 - T_A T_H\right) \pi r^2 \sin\theta . d\theta \tag{4.25}$$

The total membrane strain energy (Eq. (4.25)) depends on membrane tensions and hence internal pressure profile and the minimum internal pressure. The minimum internal pressure, P_{i0} in Eq. (4.20), is thus determined by minimising the total membrane strain energy as calculated by Eq. (4.25).

Dimensional Analysis

From the analysis presented above, it is apparent that the maximum cell-wall tension will depend on the following parameters:

$$T_{VM} = \Phi\left(U_c, r_c, \rho_f, \rho_c, \alpha, \mu\right) \tag{4.26}$$

There are thus seven independent parameters with three basic unit dimensions; [M], [L] and [T]. According to dimensional analysis theory, a minimum of four independent dimensionless parameters are required. The convenient and logical choice for these parameters are a Reynolds number (Re), Weber number (We), acceleration number (Ac) and density ratio (Π_ρ):

$$\mathrm{Re} = \frac{2.\rho_f . \alpha . r_c{}^2}{\mu} \tag{4.27}$$

$$We = \frac{2.\rho_f.\alpha^2.r_c^3}{T_{VM}} \tag{4.28}$$

$$Ac = \frac{\alpha.r_c}{U_c} \tag{4.29}$$

$$\Pi_\rho = \frac{\rho_c}{\rho_f} \tag{4.30}$$

These dimensionless groups are consistent with those used by Ryskin and Leal (1984) in studies of bubble deformation and Magnaudet *et al.* (1995) in studies on accelerated flow past rigid spheres. The widely studied case of a stationary cell in a straining Stoke's flow represents the limiting case of Ac = ∞ and Re << 1.

Typical values of the variables for a yeast cell in a commercial homogenizer system are determined as follows:

- Yeast cell diameter ranges from approximately 2 to 12 μm

  $\Rightarrow r_c = 1 \times 10^{-6}$ to 6×10^{-6} m (4.31)

- Cells are suspended in water at room temperature

  $\Rightarrow \rho_f = 1 \times 10^{-3}$ kg m^{-3} (4.32)

  $\Rightarrow \mu = 1 \times 10^{-3}$ Pa s (4.33)

- Typical yeast cell density is in the order of 1100 kg m^{-3}

  $\Rightarrow \rho_c = 1.1 \times 10^{3}$ kg m^{-3} (4.34)

- Homogenizer operating pressure ranges from approximately 7 to 70 MPa. Chapter 3 provides parameters relevant for a homogenizer system. The mean fluid velocity in the valve inlet is given by

  $$W = \frac{Q}{2\pi r_i h} \tag{4.35}$$

  and the strain rate is given by Eq. (4.36),

  $$\alpha = \frac{Q}{4\beta\pi r_v h_v^2} \tag{4.36}$$

  where the valve gap, h, is determined as a function of homogenizer operating pressure (see Table 3.1). Using Eqs (4.35) and (4.36) and typical values for a cell-disruption homogenizer valve (chapter 3: $Q = 4.6 \times 10^{-5}$ m^3 s^{-1}; $\beta_l = 2.1$; $r_i = 0.00385$ m), typical

velocities (assuming the cell moves at the same velocity as the fluid at its centre of mass) and strain rates are as follows:

$$U_c = 100 \text{ m s}^{-1} \text{ at 7 MPa to } 230 \text{ m s}^{-1} \text{ at 70 MPa} \quad (4.37)$$

$$\alpha = 1.3 \times 10^6 \text{ s}^{-1} \text{ at 7 MPa to } 6.5 \times 10^6 \text{ s}^{-1} \text{ at 70 MPa} \quad (4.38)$$

Based on the above values, we consider:

$$2.5 \leq Re \leq 490 \quad (4.39)$$

$$0.012 \leq Ac \leq 0.175 \quad (4.40)$$

$$\Pi_\rho = 1.1 \quad (4.41)$$

However, for a specific homogenizer system, α and U_c are not independent, but are connected by homogenizer operating pressure. For a given homogenizer operating pressure, maximum values of α and U_c are fixed, and hence Acceleration number (Eq. (4.29)) can be defined in terms of Reynolds number for a homogenizer valve.

$$Ac = \sqrt{\frac{\pi \mu r_i}{2\beta_l \rho_f Q}} \sqrt{\text{Re}} \quad (4.42)$$

For the cell disruption valve assembly considered here, with relevant values given in chapter 3, Eq. (4.42) reduces to:

$$\text{Ac} = 7.906 \times 10^{-3} \text{ Re}^{0.5} \quad (4.43)$$

This constrains the range of acceleration numbers possible in a high-pressure homogenizer and effectively defines a feasible operating line.

Model Verification (Stationary Sphere)

The numerical code was verified by comparing results with published data for flow past a single stationary sphere in uniform and straining flow (Table 4.1). Comparisons are made with data taken from Magnaudet *et al.* (1995) for the separation angle and total drag coefficient. Results agree to within approximately 2%. Excellent comparisons were also observed with pressure profiles at the sphere surface (results not shown).

Table 4.1: Drag coefficient and separation angle of a stationary rigid sphere in steady and straining flows.

Re	*Ac*	Drag coefficient		Separation angle	
		literature*	here	literature*	here
100	0	1.092	1.104	128	127
200	0	0.765	0.778	116	117
300	0	0.645	0.675	111	111
100	0.1	1.655	1.639	147	145
200	0.1	1.304	1.314	136	133
300	0.1	1.189	1.185	128	129

* values taken from Magnaudet *et al.* (1995).

4.3.2 Results - Moving Spherical Cells

Calculations were conducted for moving cells in axisymmetric straining flow. Figure 4.3 shows velocity vectors and pressure profiles for the case of Re = 160 and Ac = 0.1. The free stream velocity increases significantly from left to right as the pressure decreases, due to the imposed straining-flow boundary conditions. The greatest local relative velocity difference between the cell and surrounding fluid occurs at $\theta = 0°$, where the cell is moving significantly faster than the surrounding fluid. This results in a reduced pressure on the upstream side of the cell (in the region $0° \leq \theta \leq 80°$). Similarly, a region with higher pressure against the cell than in the surrounding fluid is formed on the downstream side of the cell. Over the complete range of conditions examined, no flow separation was found to occur on the cell. This is due to the favourable velocity gradient downstream of the cell and the fact that the cell is moving with the fluid. With this high velocity gradient and the absence of separation, the assumption of laminar flow conditions is likely to be a good approximation over the range of Reynolds numbers examined.

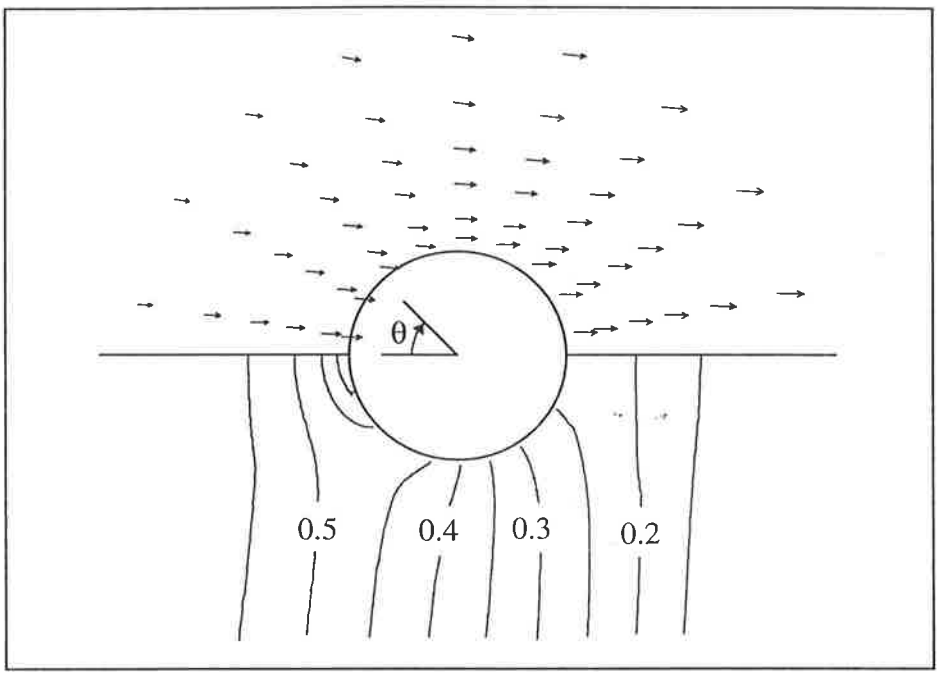

Figure 4.3: Velocity field and pressure contours around a capsule in straining flow (Re = 160, Ac = 0.1). Pressure normalised using ρU_c^2.

Calculation of the external drag force (Eq. (4.19)) acting on the cell confirms the initial assumption that the cell will move with the same velocity as the fluid at its centre of mass. The calculated cell acceleration (Eq. (4.18)) was found to be within 10% of the fluid acceleration at the cell's centre of mass. With the cell accelerating at nearly the same rate as the suspending fluid, it will not tend to significantly lead or lag the fluid.

Figure 4.4 shows the external pressure profile, the tangential stress acting at the cell wall, the normal pressure difference at the cell wall, and the internal pressure profile within the cell. With the high Reynolds number of 160 for the example in Fig. 4.4, normal pressure differences are much greater than tangential shear stresses at the membrane. Membrane tensions are likely to be dominated by these (predominantly inertial) pressure differences, rather than by viscous shear stresses.

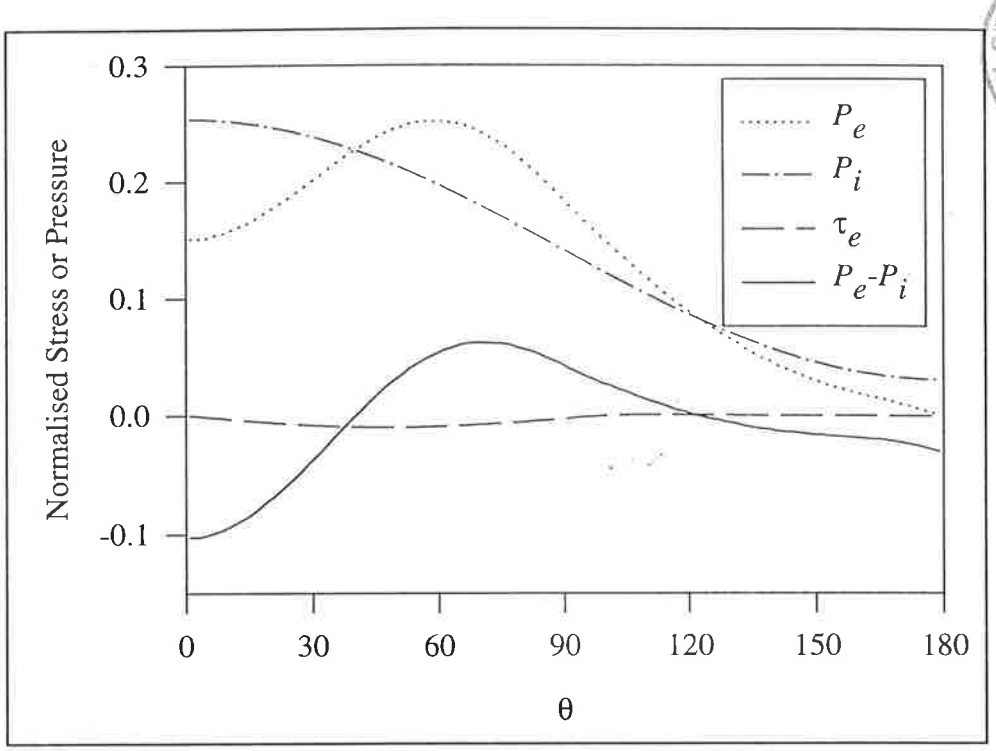

Figure 4.4: Pressure and shear-stress profiles (normalised using ρU_c^2) at capsule membrane surface (Re = 160, Ac = 0.1).

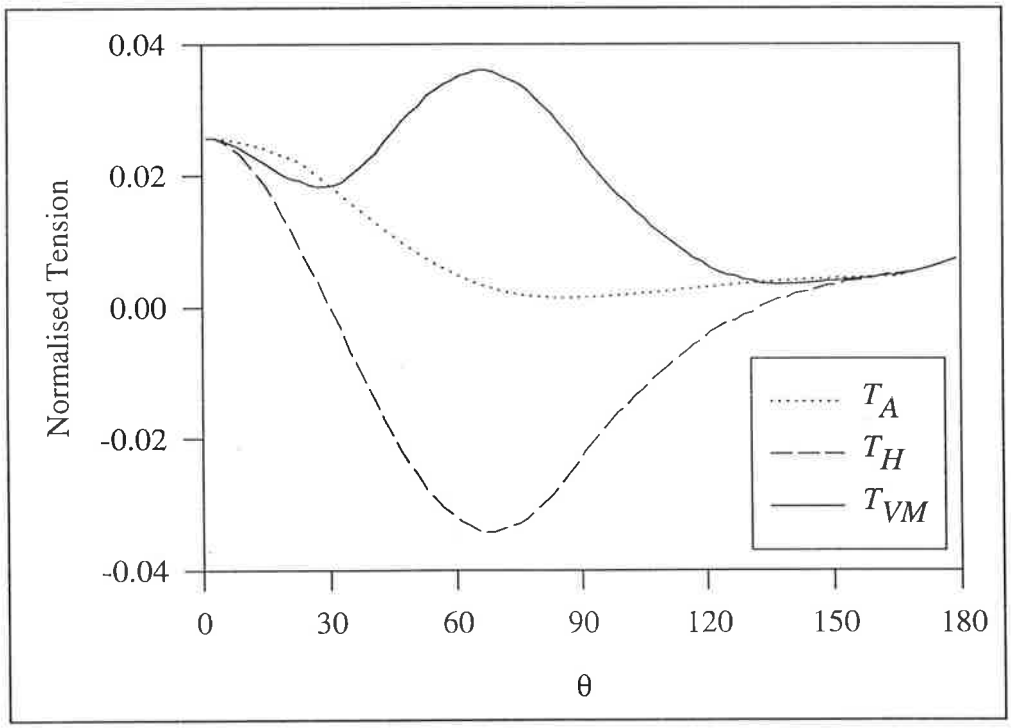

Figure 4.5: Axial, hoop and von Mises tensions in capsule membrane (Re = 160, Ac = 0.1).

Figure 4.5 shows the calculated axial and hoop tensions in the cell wall for the pressure and shear stress profiles shown in Fig. 4.4. Figure 4.5 also shows the distribution of von Mises tension within the cell wall (Eq. 4.2). The maximum von Mises tension occurs at $\theta \approx 67°$, where the hoop tension is negative (in compression). Qualitatively, the observation of compressive hoop tensions in the equatorial region is also described in the results of Leyrat-Maurin and Barthes-Biesel (1994) for a capsule passing through a constriction in Stoke's flow.

A critical* Weber number is calculated using the maximum von Mises tension in the cell wall. Results are summarised for a range of Reynolds and Acceleration numbers in Fig. 4.6. For Reynolds numbers greater than about 100, Weber number is almost independent of Reynolds number, indicating that membrane tensions are dominated by inertial rather than viscous forces. For Reynolds numbers less than about 50, Weber number shows a dependence on Reynolds number indicating that viscous effects do contribute to membrane tensions in this region.

However, the range of acceleration numbers possible in a high-pressure homogenizer is constrained and effectively defined by a feasible operating line, as discussed above. By choosing a Reynolds number, Eq. (4.43) defines the corresponding Acceleration number on the operating line. The Weber number on the homogenizer operating line was then be found for these Reynolds-Acceleration number pairs. The dependence of this Weber number on Reynolds number is given in Fig. 4.7, and was described by Eq. (4.44).

$$We = 9.0 \times 10^{-3}\,\mathrm{Re}^{0.68} \tag{4.44}$$

The general effect of Acceleration number on the capsule Weber number is not reflected in Eq. (4.44), as Eq. (4.44) is only applicable for the feasible homogenizer operating line (Eq. (4.43)).

* It is important to note that the critical Weber number defined here is calculated from the maximum cell-wall tension as the cell passes through a flow field. This maximum cell-wall tension is not to be confused with the ultimate cell-wall tension (a cell-wall property) calculated in chapter 5).

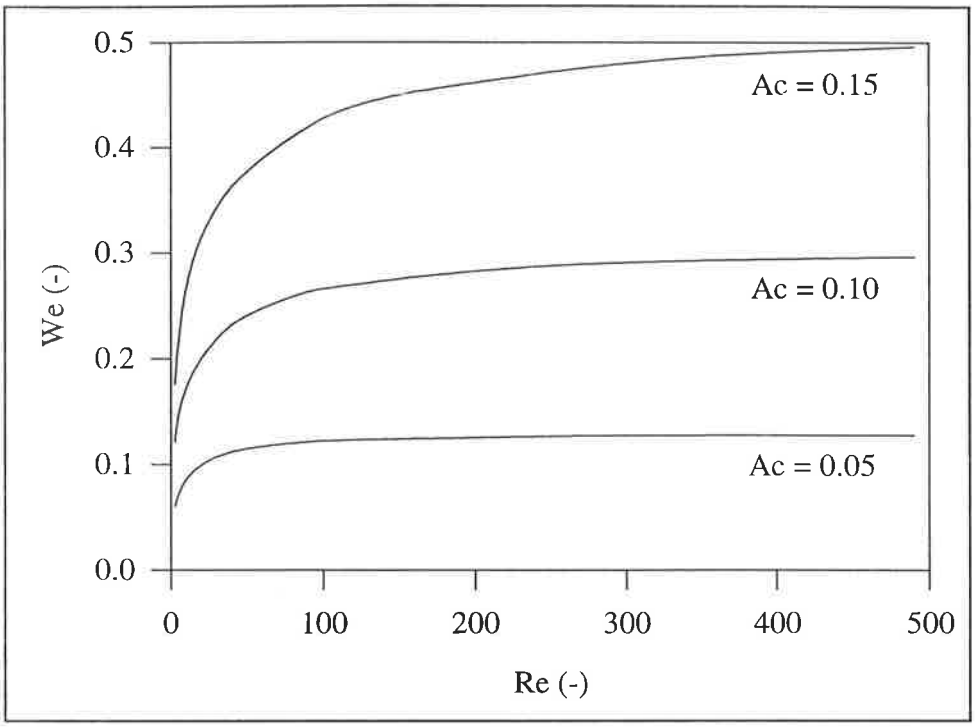

Figure 4.6: Dependence of critical Weber number on Reynolds and Acceleration numbers.

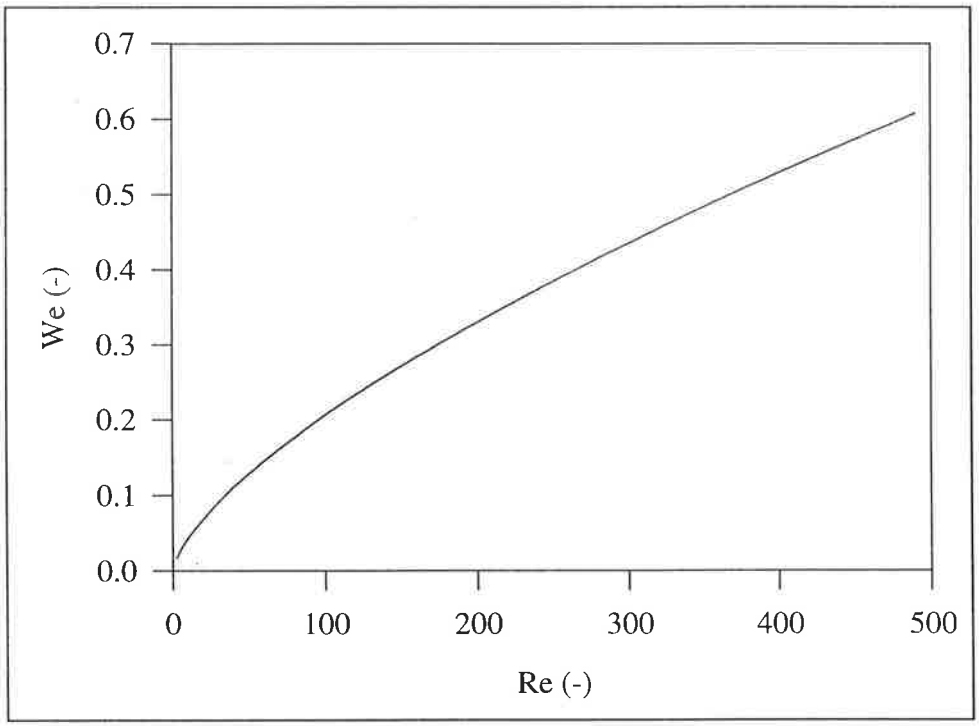

Figure 4.7: Dependence of critical Weber number on the Reynolds number of the feasible homogenizer operating line.

To highlight how important inertia is in determining the tensions within a cell wall, consider the practical example of a 6 μm cell in a homogenizer valve with a 56 MPa operating pressure by applying the above relationships. This cell has Re = 100 and Ac = 0.075. At this Reynolds number, tensions are dominated by inertial rather than viscous forces (see Fig. 4.6). From Eq. (4.44), We = 0.206 and hence the maximum tension in the cell wall will be in the order of 8 N m^{-1}. This corresponds to an applied force of approximately 150 μN, and exceeds the measured compressive forces of 40 to 90 μN required to break yeast cells (Roberts *et al.*, 1994). Also, it is approximately two orders of magnitude higher than the corresponding viscous force acting to disrupt a cell that was calculated in section 4.3. It is interesting to note that this cell experiences an acceleration of $10^8 \times g$, and thus it is not surprising that it is unlikely to survive its passage through a homogenizer.

Fig. 4.8 provides a plot depicting the effect of operating pressure and cell diameter on the maximum tension generated within the cell wall (valve inlet region only). Eqs (4.35) and (4.36) are used to calculate velocity and strain rate from operating pressure (and hence valve gap, Table 3.1). Reynolds number (Eq. (4.27)) is then used to calculate the Weber number for the homogenizer operating line (Eq. (4.44)) and hence maximum wall tension. In Fig. 4.8, it is apparent that the cell tension increases with operating pressure and cell diameter, in agreement with the observations that disruption increases with operating pressure, and that large cells are easier to disrupt than small cells.

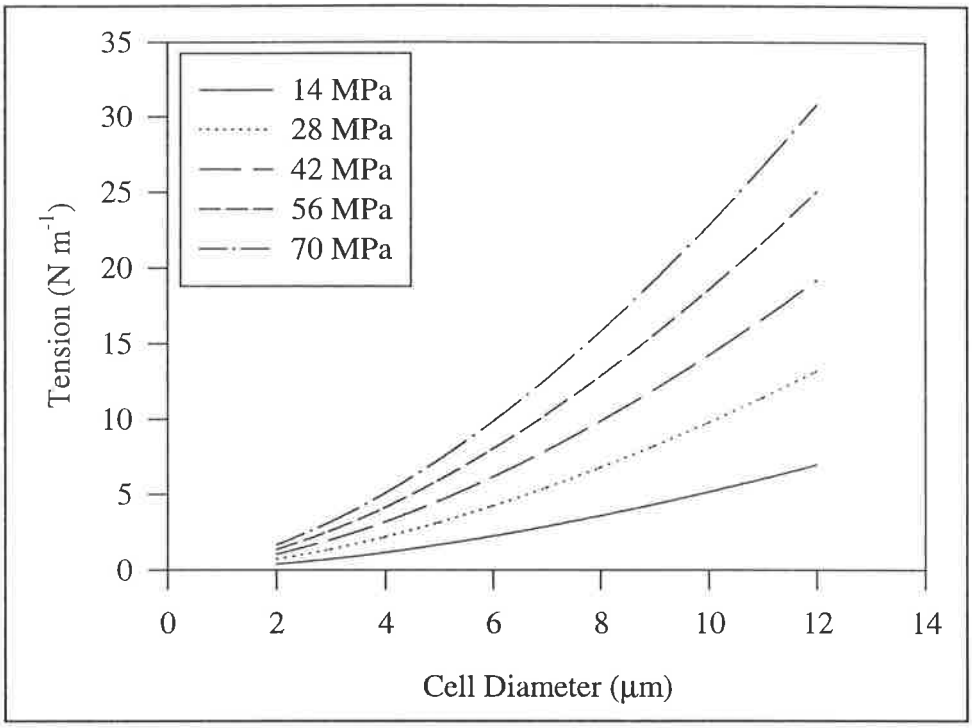

Figure 4.8: Effect of operating pressure and cell diameter on the maximum tension produced within a spherical cell.

However, beyond the generalisations that are made in the last two paragraphs, it is not possible to predict how cells will actually respond to these applied tensions or the actual disruption levels that will be achieved. To make some assessment of their likely behaviour and disruption probability, the mechanical properties of the cell wall are required. These mechanical properties are addressed in the following chapter.

The analysis of this section used positive strain rates, and hence is directly applicable for the valve inlet region of a homogenizer valve. In the impinging jet region, fluid decelerates, and hence strain rates are negative. However, to a first approximation, wall tensions will be qualitatively and quantitatively similar if the strain rate is positive or negative, making the results applicable to both the valve inlet and impinging jet regions.

Effect of Cell Deformation

The assumption that a cell remains spherical during passage through a homogenizer and may be compared to a rigid spherical capsule must be considered further given that the cell wall will be in varying degrees of tension. Yeast cell walls are known to be highly deformable (Levin, 1978). As they pass through the homogenizer valve, they are likely to elongate, although the extent of elongation will be influenced by the cell-wall properties at

the high strain rates and short residence time within the converging flow in a homogenizer valve. However, the deformation of a cell does not negate the conclusions of this study. Tensions or deformations produced in the cell-wall from inertial effects are still likely to be approximately two orders of magnitude greater than viscous forces for a typical cell and typical homogenizer operating conditions, and are a probable cause of cell breakage.

Redefinition of Dimensionless Groups

The Reynolds number of Eq. (4.27) and the Weber number of Eq. (4.28) were chosen to be consistent with previous studies. These numbers are derived with the basis that the inertial force acting on the capsule is defined by the maximum relative velocity difference between the capsule and the surrounding fluid.

$$F_{inertial} = \rho U^2 = \rho\left(\alpha r_c\right)^2 \tag{4.45}$$

However, this is only correct for a stationary object. In the case examined here, where the cell moves with the fluid and inertial forces are significant, it would be more appropriate to consider the inertial force to be based on the difference between the squared capsule and fluid velocities (Eq. (4.46)).

$$F_{inertial} = \rho \Delta U^2 \tag{4.46}$$

$$= \rho\left(U_c{}^2 - \left\{U_c - \alpha r_c\right\}^2\right) \tag{4.47}$$

$$= 2\rho U_c \alpha r_c - \rho \alpha^2 r_c{}^2 \tag{4.48}$$

This modified inertial force term then defines new Reynolds and Weber numbers as follows:

$$\mathrm{Re}' = \frac{2\rho}{\mu}\left(2U_c r_c - \alpha r_c{}^2\right) \tag{4.49}$$

$$We' = \frac{4\rho U_c \alpha r_c{}^2 - 2\rho \alpha^2 r_c{}^3}{T} \tag{4.50}$$

The data of Fig. 4.6 are replotted as Fig. 4.9 using the modified Reynolds and Weber numbers of Eqs (4.49) and (4.50) respectively. Using these modified dimensionless groups, the effect of acceleration number on results is reduced, as both strain rate (α) and velocity (U_c) are already included in the modified groups. The modified Weber number is

almost independent of the modified Reynolds number and attains a constant value of approximately 5.0 ± 0.5 over the limited range of Ac included in Fig. 4.9.

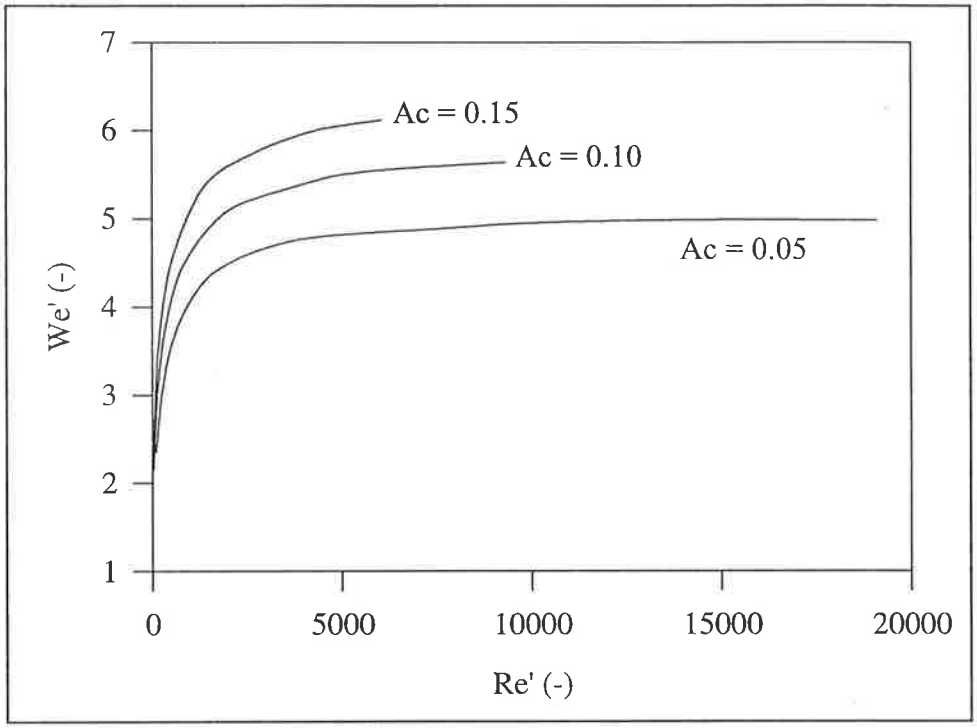

Figure 4.9: Dependence of modified Critical Weber number on modified Reynolds number and Acceleration number.

On the feasible homogeniser operating line defined by Eq. (4.43), Ac is less than one. Thus, U_c is greater than αr_c. For $U_c >> \alpha r_c$, the second term on the left-hand side of the modified Weber number of Eq. (4.49) is much less than the first term, and hence the modified Weber number simplifies as follows:

$$We' \approx We'' = \rho U_c \alpha \left(\frac{4 r_c^2}{T} \right) \tag{4.51}$$

This simplified Weber number contains the grouping $\rho U_c \alpha$, which is the pressure gradient in the fluid at the centre of mass of the cell. Hence, for a given cell, the wall tension will depend on the pressure gradient in the homogenizer valve. This suggests that a reasonable correlation between pressure gradient and disruption efficiency should be observed if cell disruption does occur as a result of inertial forces in the homogenizer valve. Fig. 3.23 revealed that impingement region cell disruption correlated well with laminar jet stagnation pressure. Substitution of Eq. (3.55) into Eq. (3.54) suggests that stagnation region pressure gradient is directly related to stagnation pressure alone and shows almost no dependence on

impact distance (other than the effect that impact distance has on stagnation pressure). Fig. 2.5 shows the effect of valve seat geometry on disruption efficiency (in the absence of impingement effects). The data of Fig. 2.5 are replotted in Fig. 4.10, using pressure gradient (rather than operating pressure) as the independent variable. This pressure gradient is calculated from Eq. (3.54) and the parameter values in Table 3.1.

Figure 4.10 reveals that disruption shows a strong dependence on pressure gradient in the valve region. Much of the variation evident in the plot of protein release versus pressure (Fig. 2.5) is removed, indicating that pressure gradient is a better independent parameter than operating pressure. Significant scatter remains at higher pressure gradients; this scatter can be attributed to experimental error in the measurement of valve gaps, as pressure gradient is inversely proportional to valve gap cubed and measured gaps have an error of approximately 10% (section 3.2.5). Small amounts of wear that occur on the square edged seats (and effectively creates a small chamfer) may also act to reduce pressure gradients in the inlet region.

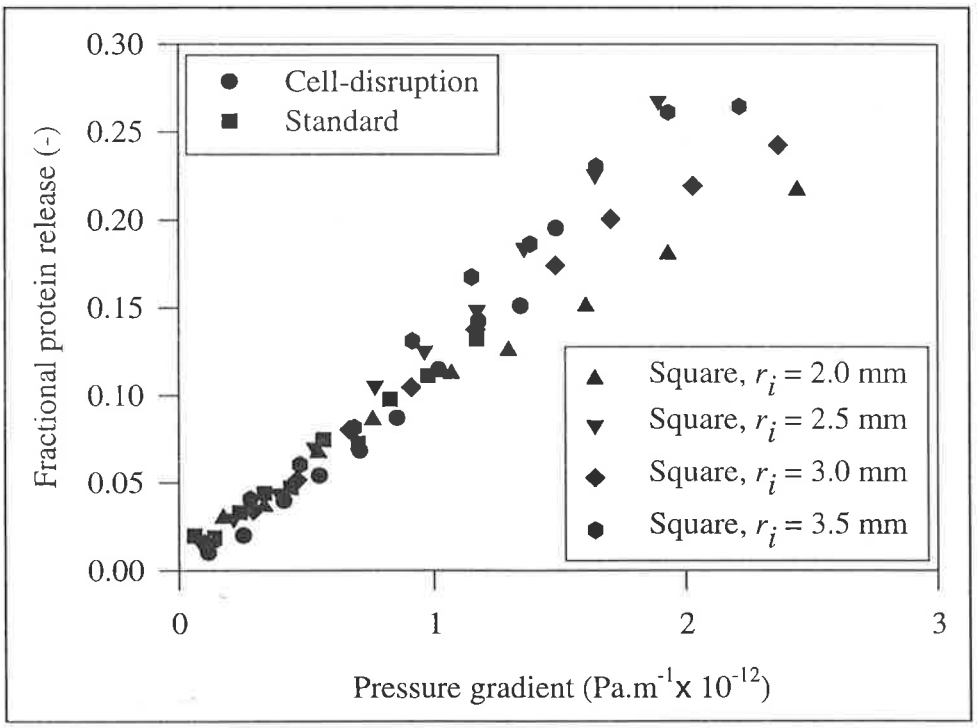

Figure 4.10: Dependence of fractional protein release in the valve region on pressure gradient (Eq. (3.54)) for chamfered and square edged valve seats over a range of operating pressures.

4.3.3 Non-spherical Cells

The shape of many biological cells is far from spherical. *Escherichia coli* are rod shaped. Budding yeast cells can almost be considered as two attached spheres. An in-depth analysis of the tensions that will be generated in non-spherical cells is beyond the scope of this study. However, some generalisations and qualitative effects are briefly discussed.

For a spherical cell, cell orientation during homogenization is not an important variable. Cell-wall properties, and cell-wall tensions generated during homogenization do not depend on the cell's orientation.

However, for non-spherical cells, cell-orientation during homogenization will be important for two reasons:

1. Cell-wall properties may be anisotropic. For a rod shaped cell, hoop tensions in the cylindrical sidewalls of the cell are twice the axial tensions in the cylindrical sidewalls under normal turgor conditions (Koch, 1988). This inherent tension-anisotropy results in anisotropic cell-wall properties.

2. The maximum cell-wall tensions that are produced during homogenization will depend on cell orientation. The maximum cell-wall tension will be determined by the largest dimension of the cell that is aligned with the flow direction. Hence, the maximum cell-wall tension will be much greater if a non-spherical cell is aligned with the flow direction rather than perpendicular to it.

Because of these two factors, the maximum cell-wall tensions produced in non-spherical cells during homogenization will depend on the cell's orientation. A population of cells experiencing the same flow conditions will not all experience the same maximum cell-wall tension due their different orientations within the flow field.

4.4 Cell-solid Interactions

Cell-solid interactions include the squeezing of cells between the valve and seat as they pass through the valve, the collision of cells with the impact ring in the stagnation region of the impinging jet and the impact of cells with one another during their passage through the homogenizer valve. Section 4.2 suggests that squeezing of cells is not likely to cause cell breakage, whilst the latter two processes have been suggested to be responsible for cell breakage during high-pressure homogenization (Engler, 1979).

Whilst the Microfluidizer (section 1.2.1) has been reported to achieve increased disruption efficiency with increased cell concentration (Sauer *et al.*, 1989), most studies report either no effect of cell concentration or decreased disruption with increased cell concentration (section 1.2.2). Thus, it would seem that cell-cell interactions are probably not highly significant and can be disregarded. However, the possibility of cell-solid interaction, particularly at the homogenizer impact ring of a Manton-Gaulin type homogenizer, requires further investigation. Even though flow acceleration is able to predict disruption in both the valve inlet and impinging jet region, it does not rule out cell-solid interaction in the impinging jet region. This section aims to firstly determine if cell-solid collision is likely to occur, and secondly, to determine if collisions are sufficiently potent to result in cell disruption.

Cell-solid Collision

Sommerfeld (1992) has stated that

> "There is too little experimental information for wall-collision-dominated particulate two-phase flows to allow a detailed modeling of a particle-wall collision and subsequently realistic numerical simulations"

and lists some of the most important of a large number of parameters that affect a particle-wall collision. In spite of the difficulty in conducting numerical simulations of particle-wall collisions, investigators have used simplifying assumptions to provide qualitative insights into particle-wall collision processes for spherical particles in a stagnation region.

Hasegawa and Tamura (1988) consider the collision of particles in the stagnation region of a plane jet, and define the critical conditions under which particle-wall collisions will begin to occur. Particle motion was considered to be governed by particle inertia and viscous

drag alone, and simulations were conducted to determine the effect of jet angle and Stoke's number on the type of collision, collision probability and other related parameters. Drew (1974) has also examined the conditions under which particle-wall collisions will occur in a stagnation region, and considered the interactions between particle inertia, fluid drag and stagnation region pressure gradient.

Unfortunately, the approach of determining particle trajectories using equations of motion for the particle that include drag, pressure gradient and other relevant terms (for example, added mass and history) is only applicable if a particle is small compared to the scale of velocity fluctuations in the fluid (Clift *et al.*, 1978). One criterion to determine if a particle is small compared to velocity variations is:

$$\frac{d^2}{\nu} \cdot \frac{du_x}{dx} << 1 \tag{4.52}$$

For typical cell diameters and homogenizer strain rates, the left hand side of Eq. (4.52) is the range of 10^0 to 10^2. This is clearly outside of the region of applicability. The situation is also complicated by the possible deformation of the cell along its trajectory.

As such, the particular problem of cell-solid interaction would be best approached by simulating the flow field, cell motion and cell deformation simultaneously. However, this approach is fraught with the intractibilities that are outlined in section 4.1. As these intractibilities preclude a realistic simulation of the cell-solid interaction, a simple analysis of the problem is presented here.

The simple analysis assumes that cells travel at the same velocity as the fluid at their centre of mass, consistent with the analysis of cell-fluid interactions. This assumption is justified by the relatively small density difference between the cell and suspending fluid. Hence, it is assumed that the fluid streamlines are a reasonable approximation of the cell trajectory. This behaviour is shown schematically in Fig. 4.11, illustrating that a cell-solid collision will occur provided the cell's centre of mass is initially within one cell radius of the jet's plane of symmetry. Thus, the probability of cell collision is approximately equal to the ratio of the cell diameter to the impinging jet's effective half width (this effective half width is approximately equal to half of the valve gap, and does not include the increase in jet width from fluid entrainment). This means that whilst nearly all cells greater than 5 μm

in diameter will contact the impact ring, less than 20% of 1 μm cells will contact the impact ring in the situation considered in Fig. 4.11.

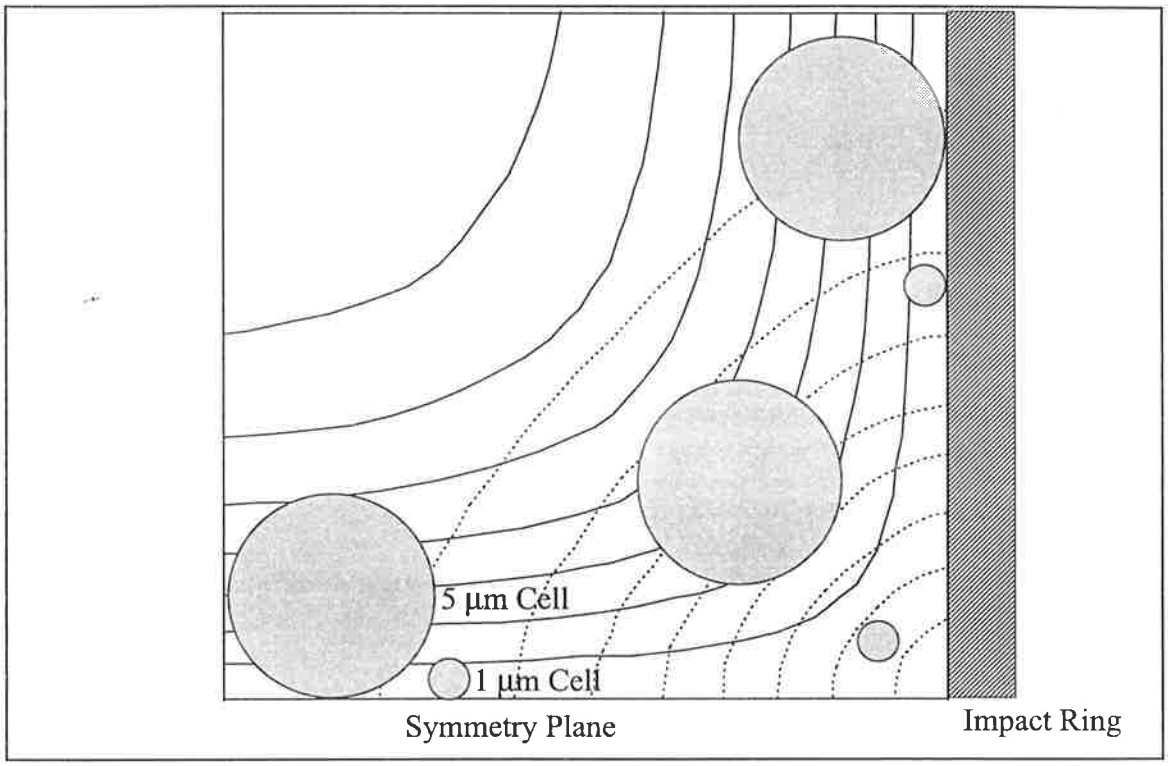

Figure 4.11: Schematic diagram showing 5 μm (large) and 1 μm (small) cell in stagnation region of homogenizer impinging jet (9 μm valve gap, 11 mm impact ring) at critical conditions for cell-solid collision to occur (picture to scale).

Collision Intensity

Collision of the cell with the impact ring alone is not a sufficient criterion to determine if cell breakage will occur. The likelihood of cell breakage will be dependent on its impact velocity, which will determine the energy that is available to deform and hence rupture the cell, and the cell's contact angle, which will determine the loss of energy on contact. Values of the cell's velocity at contact and the angle of contact are given in Table 4.2, assuming that cells follow fluid streamlines. The values in Table 4.2 are obtained for a 9 μm valve gap (56 MPa operating pressure) and the standard 11 mm diameter impact ring. It is apparent from Table 4.2 that the contact velocity increases with cell size. This is due to increased distance from the impact ring of the cell's centre of mass, and hence its higher normal velocity component. The collision velocity decreases as the contact angle increases, as the tangential component of the collision velocity is reduced. However, for

particularly large cells, impact velocity decreases as angle decreases, due to significant decreases in the normal velocity of cells at large axial distances.

Table 4.2: Collision velocity and collision angle of cells in the impact region of a homogenizer impinging jet (9 μm valve gap and 11 mm diameter impact ring).

Cell Diameter	Collision Velocity ($m\ s^{-1}$)		
(μm)	$\theta = 20°$	$\theta = 45°$	$\theta = 90°$
1	38	19	14
2	67	38	28
4	93	64	52
6	99	80	74
8	96	87	93
10	88	87	109

Empirical studies have examined particle velocities before and after impact, to determine the loss of momentum that occurs on impact (Grant and Tabakoff, 1975). The energy loss is transferred to both the particle and wall, and may result in erosive wear of the wall or particle attrition. Grant and Tabakoff (1975) have presented experimental results for the restitution ratio of quartz sand impacting on an aluminium alloy target. These results are summarised in Table 4.3.

Table 4.3: Restitution ratio for 200 μm quartz sand impacting onto 2024 aluminium alloy at 75 $m\ s^{-1}$ (Grant and Tabakoff, 1975).

Angle	mean	standard deviation
20°	0.697	0.1503
45°	0.550	0.1445
90°	0.210	0.0655

The impact of a biological cell into a ceramic impact ring is considerably different to the impacting of sand onto an aluminium alloy. Regardless, it is assumed that the values in Table 4.3 are representative of a cell-solid impact, particularly with regard to qualitative effect of collision angle and the large scatter (standard deviation) in the results. It is also assumed that all of the kinetic energy loss is to the colliding cell. Although these assumptions are questionable, using them provides qualitative estimates that are likely to be of correct magnitude but will probably contain systematic error.

The kinetic energy loss to the cell during impact is calculated from the following equation:

$$KE_J = \frac{1}{12}\pi\rho d^3 U^2\left(1-\varepsilon^2\right) \tag{4.53}$$

The kinetic-energy-loss of the cell, calculated from the collision velocities in Table 4.2 and the restitution ratios Table 4.3 is shown in Fig. 4.12. The kinetic-energy-loss of the cell during collision increases rapidly with cell size, and is almost independent of collision angle. For cells smaller than 5 μm, this increase in kinetic-energy-loss is due to increased diameter and collision velocity (Eq. (4.53)), whilst for cells larger than 5 μm, most of the increase is due to cell diameter alone. The question remains as to whether this kinetic energy loss is sufficient to cause cell breakage. Assuming a 6 μm cell with a 100 μN bursting force (Roberts *et al.*, 1994), the approximate work required to break the cell is 2.6 $\times 10^{-10}$ J. This is of similar order to the mean kinetic energy loss of 4.5 $\times 10^{-10}$ J for a 6 μm cell in Fig. 4.12. This simple analysis thus provides support to conclude that cells may collide with the homogenizer impact ring with sufficient energy to effect cell disruption. However, further information regarding the work required to disrupt a cell is required if a more accurate quantitative analysis is to be conducted. In addition to the kinetic energy loss that the cell experiences when contacting the impact ring, the forces exerted on the cell as it is accelerated with the suspending fluid (after being slowed down at the impact ring) may also contribute to cell breakage.

The kinetic energy loss (for a 45° collision angle) is described empirically by Eq. (4.54).

$$\overline{KE}(d) = 1.69\times 10^9 d^{3.61} \tag{4.54}$$

However, the kinetic energy loss does not take a fixed value, as the restitution ratio has a large standard deviation (Table 4.3). For a 45° collision angle, the standard deviation of the cell's kinetic energy loss is:

$$\sigma_{KE}(d) = 0.24\overline{KE}(d) \tag{4.55}$$

and is shown graphically in Fig. 4.13.

The actual kinetic energy lost by a given cell is thus expected to vary randomly about a mean value that is dependent primarily on the cell's size.

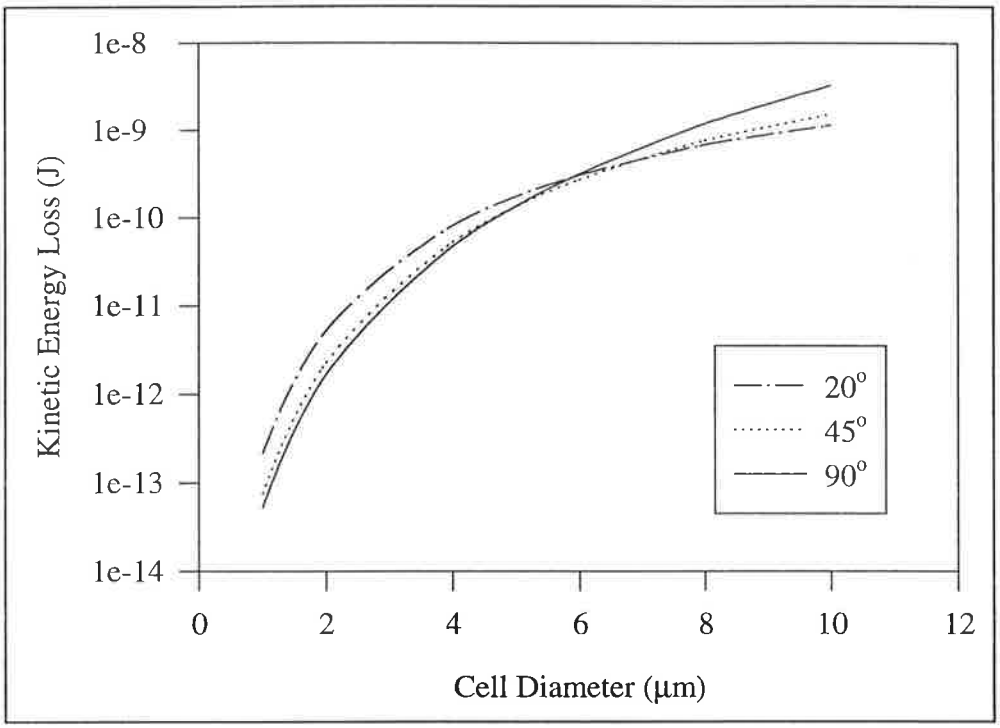

Figure 4.12: The dependence of cell kinetic energy loss during collision with the impact ring on cell size and collision angle.

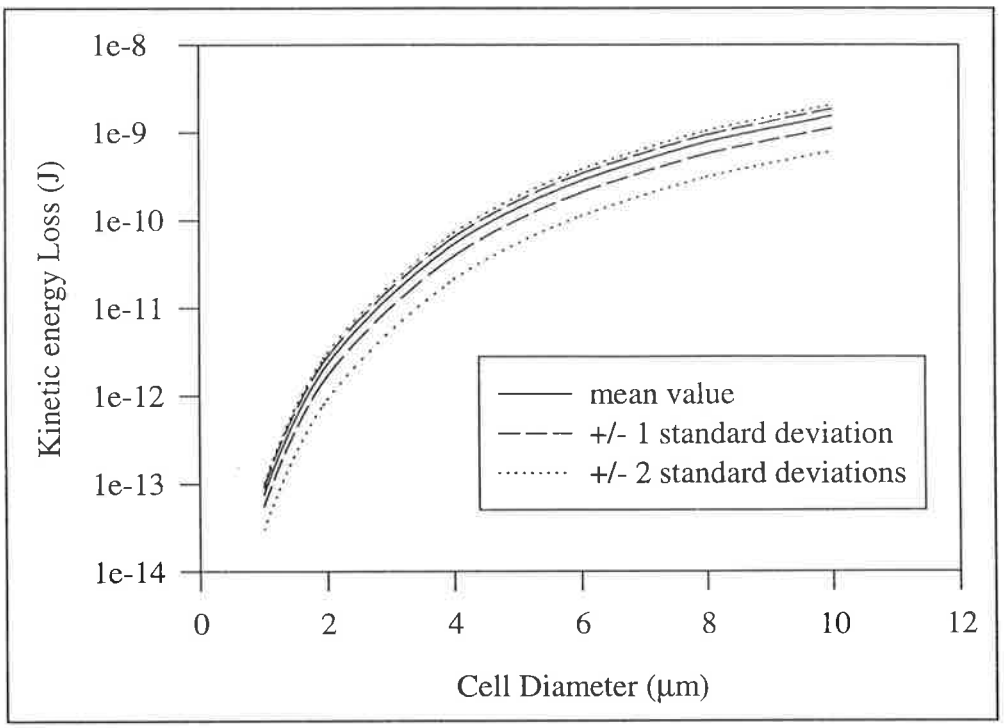

figure 4.13: Distribution of kinetic energy loss from cell with 45° collision angle.

4.5 Summary

The physical processes that cause cell breakage in a homogenizer must be understood and characterised if a homogenizer stress distribution is to be determined. A review of the physical processes that may cause cell disruption suggested that turbulence, cell-solid interaction, and converging flow may result in cell breakage. Two of these mechanisms are likely to be significant in a Manton-Gaulin homogenizer (converging flow and cell-solid interaction) and were chosen for further investigation.

Hyperbolic shear conditions occur in the valve-inlet region and in the stagnation region of the homogenizer's impinging-jet. A numerical analysis of the tensions that are generated in a spherical cell as it interacts with these regions of hyperbolic shear was conducted. Tensions produced in the cell wall were found to be dominated by inertial forces, and are of the correct order to effect cell breakage. The dependence of the maximum wall tension on cell size and homogenizer operating conditions was described by the following relationship,

$$We = 9.0 \times 10^{-3}\,\mathrm{Re}^{0.68} \tag{4.44}$$

with the Weber and Reynolds numbers defined by Eqs (4.28) and (4.27), respectively. Maximum cell-wall tension increases with cell diameter and homogenizer operating pressure, in agreement with experimental observations of cell-disruption efficiency.

In the homogenizer's impinging-jet, cell collision with the impact ring is also likely to be a significant cause of cell disruption. The probability of a cell collision increases with the size of cell, and the kinetic energy loss of a colliding cell (with an APV-Gaulin 15M homogenizer, cell disruption valve assembly, and 56 MPa operating pressure) is described by,

$$\overline{KE}(d) = 1.69 \times 10^{9} d^{3.61} \tag{4.54}$$

with a standard deviation of $0.24\overline{KE}(d)$. Again, cell-disruption probability is expected to increase with cell size and homogenizer operating pressure, in agreement with experimental observations.

Chapter 5

Mechanical Properties of Yeast

The cell strength distribution of microorganisms is an important factor in the disruption process. In this chapter, the mechanical properties of *Saccharomyces cerevisiae* are investigated. *Saccharomyces cerevisiae* was chosen due to its suitability for direct mechanical characterisation. Firstly, the structure of the cell wall of *S. cerevisiae* is presented. Experimental techniques that are available to characterise the mechanical properties of biological cell walls are then reviewed. A micromanipulation technique is used to measure the bursting strength of individual yeast cells, and modeling is used to derive ultimate celi-wall tensions. Ultimate cell-wall tension, total work-to-failure, and cell size distributions are presented for two cultures of *S. cerevisiae*.

5.1 *Saccharomyces cerevisiae* cell wall

The cell cytoplasm of *Saccharomyces cerevisiae* is encased in a lipid bilayer (the plasma membrane). A periplasm separates the plasma membrane and the cell wall proper. The yeast cell wall itself is a multifunctional organelle that determines cell shape, affords cell protection, metabolises non-permeable substrates, and controls nutrient uptake (Fleet, 1991; Ruiz-Herrera, 1992). Without the cell wall, the cell would be unprotected from environmental changes and would lyse due to osmotic differences with the surrounding medium. To appreciate the mechanical strength of the yeast cell wall, and the factors that contribute to that strength, it is necessary to know something of the chemistry and architecture of the yeast cell wall.

Chemical Composition

The chemical composition of the yeast cell wall is relatively simple, with polysaccharides accounting for 80-90% of the cell wall and small amounts of protein and lipid making up the balance. Glucans and mannans are the main polysaccharides, and a small amount of *N*-acetylglucosamine is also present. In total, the cell wall constitutes approximately 15 - 25% of the dry cell weight.

The reported glucan content of the cell wall ranges from 30 - 60% (Fleet, 1991). This glucan is differentiated into three groups, based on solubilities (Table 5.1). These are an alkali-insoluble acetic acid-insoluble β-(1→3)-glucan, an alkali-insoluble acetic acid-soluble and predominantly β-(1→6)-glucan, and an alkali-soluble β-(1→3)-glucan. The wall content and important structural properties of these glucans are given in Table 5.1.

Table 5.1: Properties of cell-wall glucans in *Saccharomyces cerevisiae* (Fleet, 1991).

	Linkage type (%)				wall content
Glucan	β-(1→3)-	β-(1→6)-	Branch	DP[a]	(% w/w)
Alkali/acid-insoluble	95	-	3	1500	35
β-(1→6)-	5	65	14	140	5
Alkali soluble	80-85	8-12	3-4	1500	20

[a]Degree of polymerisation

Mannan comprises 25 - 50% of the cell wall. As mannan is found covalently linked to most of the wall protein, it is more correctly called mannoprotein (about 90% mannose, 10% protein). About 10% of the mannose is linked to serine and threonine residues as

short oligosaccharides. The remaining 90% of the mannose is linked to asparagine through a double *N*-acetylglucosamine unit. This polysaccharide may be differentiated into a core region, composed of 12-15 mannose and two *N*-acetylglucosamine units, and a branched outer chain of about 250 mannose units. About 70 of these units form a backbone of mannose residues in α-(1→6)- linkage attached to mannobiose, mannotriose and mannotetraose side chains composed of mannose residues in α-(1→2)- and, to a lesser degree, α-(1→3)- linkage (Fleet, 1991). These mannoproteins have an average molecular weight of 450 kDa (Klis, 1994). Mannoproteins can be integral structural components of the cell wall, but are also present as enzymes and sexual agglutination factors.

Most of the *N*-acetylglucosamine (1 - 2% of the cell wall) is found as chitin (β-(1→4)-linked) in the bud-scar zone. A small amount (< 10% of total) is also found uniformly dispersed within the lateral walls (Cid *et al.*, 1995, Mol and Wessels, 1987).

Architecture

The yeast cell wall is in the form of a bilayered structure (Klis, 1994) and is approximately 70 nm thick (Brady *et al.*, 1994). The outer layer is fibrillar or brush like, with the fibrils perpendicular to the cell surface (Tokunaga *et al.*, 1986). This layer is composed of structural mannoproteins, that are crosslinked to each other by S-S or thioester bonds and hydrophobic interactions (Zlotnik *et al.*, 1984). Although this layer is not thought to contribute to the mechanical integrity of the cell wall, it is probably responsible for cell wall porosity and protects the wall from various macromolecules (Zlotnik *et al.*, 1984). Mannoprotein is also found near the inner layer of the cell wall as periplasmic proteins.

The inner layer of the cell wall is composed primarily of glucans. The alkali soluble fraction is found as an amorphous layer closest to the mannoprotein layer, and is covalently linked to the mannoprotein in the outer layer of the cell wall (Zlotnik *et al.*, 1984). The main structural component of the wall is likely to be the alkali- and acetic acid-insoluble glucan, that is found as densely interwoven microfibrils on the inner surface of the cell wall (Kopecká *et al.*, 1974). These microfibrils form a fine net about 7.5 - 10 nm thick with meshes about 20 - 60 nm wide (Kreger and Kopecká, 1975). A small amount of *N*-acetylglucosamine polymer (100 monomer units) is covalently linked to the alkali-insoluble glucan, and keeps it insoluble (Mol and Wessels, 1987; Kollár *et al.*, 1995).

However, it must be conceded that this structure is, in part, only tentative, and is still the subject of active research. A current understanding of the distribution and interconnections between the cell wall polysaccharides as outlined above is shown schematically in Fig. 5.1 (Cid *et al.*, 1995).

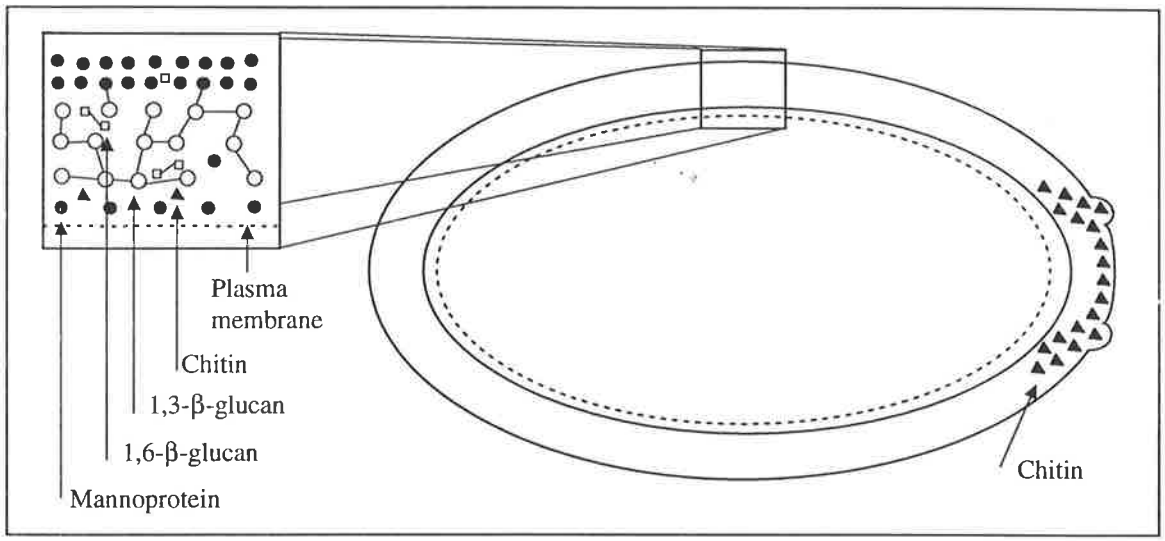

Figure 5.1: Model of the cell wall structure of *Saccharomyces cerevisiae* (Cid *et al.*, 1995)

Mechanical Properties

The main function of the yeast cell wall's structural glucans is to maintain the turgor pressure within the cell. By analogy with a spherical pressure vessel, the stress in the yeast cell wall can be calculated as (Gere and Timoshenko, 1987):

$$\sigma = \frac{P r}{2 t} \tag{5.1}$$

Assuming a 1.33 MPa turgor pressure (Levin *et al.*, 1978) and 70 nm wall thickness (Brady *et al.*, 1994) the tensile stress in the cell wall is in the order of 25 MPa for a 6 μm diameter cell. In addition to maintaining this tensile stress, the cell wall must also be able to readily stretch not only during the growth of a cell, but also to respond to changes in the cell's osmotic environment (Levin *et al.*, 1978).

The investigation of the mechanical properties of biological materials lies in the field of "biomechanics" (*e.g.*, Gordon, 1980). However, very few studies have attempted to characterise the mechanical properties of the yeast cell compared to the mechanical analysis of other biological materials (Ruiz-Herrera, 1992). In spite of this deficiency,

connections between the known cell-wall architecture and likely cell-wall mechanical properties are discussed here by making comparisons between the yeast cell wall and other materials with similar structures. Also, progress has been made in measuring mechanical properties of yeast cell walls (section 5.2).

The structural component of the yeast cell wall has been compared to reinforced concrete (Harold, 1990) and other man-made fibrous composites (Ruiz-Herrera, 1992). Perhaps the most physically-meaningful analogy for the structural glucans in the yeast cell wall is that of a non-woven, cross-linked fabric, as proposed by Koch (1988) for the bacterial sacculus. Mechanical properties of these bonded fibre fabrics are discussed by Hearle (Hearle, 1980; Hearle *et al.*, 1969). In such a fabric, cross links stiffen the structure and the individual fibres share the load. If the fabric is subjected to a tensile load, the fibres become straightened and aligned in the direction of extension. Ultimately, yield and failure of the specimen will occur due to the failure of individual bonds - either the breakage of fibres, the breakage of crosslinks, or the slipping of fibres past each other. Typically, individual fibres or crosslinks break when they are loaded beyond their tensile strength. The stress in the material is then redistributed among the remaining fibres. The slippage of chains is also a time dependent or viscoelastic process.

The experimental stress-strain curve of a typical bonded fibre fabric is provided by Hearle (1980). At low extensions, the fabric essentially behaves elastically. When a critical tension is reached, the material begins to yield. The tension is maintained, producing an almost horizontal stress-strain curve, as bonds break and stresses are redistributed amongst the remaining fibres. Ultimately, when no fibres are left to maintain the load, the specimen will fail. The part of the curve that is almost horizontal has virtually no shear modulus, which prevents the communication of strain between parts of the structure and prevents tearing (Gordon, 1980). This type of behaviour is in contrast to, for example, rubbers, which fail catastrophically at high loads (when chains become extended) due to crack propagation.

In addition to this non-reversible type of elastic tension, the glucan fibre network also has other methods of extending reversibly. The structure of the β-(1→3)-glucan fibrils in the wall is such that they are able to form a long twisted ribbon (Ballou, 1982) that is likely to be highly elastic. This allows the transfer of stresses between fibres that are not equally strained, and reduces the proportion of redundant fibres that would occur if the fibres were

inelastic. This elasticity is analogous to using elastic fibres (such as elastomeric polyurethanes) to produce a flexible fabric (that also supports tension) in the textile industry (Powell, 1994).

In addition to the intertwined glucan microfibril phase, the cell wall contains a matrix of amorphous glucans and mannoproteins. Although this matrix is not likely to be directly responsible for the wall's tensile strength, it is still likely to influence mechanical properties. In common with other fibrous composites, the matrix support protects fibres from direct chemical or mechanical attack, keeps fibres separated (to help to prevent fracture of the material), and allows for the transfer of stresses between fibres (Harris, 1980; Ruiz-Herrera, 1992). A simple approach to estimate the failure stress of a fibre-matrix composite material is to add the contributions of both the fibre and matrix to the final properties,

$$\sigma_c = \eta \sigma_f V_f + \sigma_m (1 - V_f) \tag{5.2}$$

where η is "the efficiency of fibre reinforcement" (Harris, 1980). For perfectly planar but randomly oriented fibres (such as a 2-D mesh in the cell wall) $\eta = 0.375$. Table 5.1 gives the volume fraction of fibres as 0.35. The tensile strength of a similar polysaccharide (cellulose) is 900 MPa (Harris, 1980). If the contribution of the matrix to the failure stress is assumed negligible, the cell wall failure stress calculated from Eq. (5.2) will be in the order of 120 MPa. However, this is only an approximate estimate as efficiency of fibre reinforcement will be increased by fibre alignment at high strains and also decreased by crosslinks that act to make some of the fibres redundant until surrounding fibres have failed.

5.2 Experimental Characterisation of Mechanical Properties

A biological cell may be considered as a particle consisting of a liquid interior surrounded by a thin membrane. The possible response of this membrane to applied stresses, or the mechanical properties of the cell wall, have been discussed in comparison with a bonded fibre fabric in the previous section. An ultimate failure stress has also been predicted, based on a simplistic analysis. However, experimental measurements of cell-wall mechanical properties are required if any meaningful analysis of cell disruption based on cell mechanical properties is to be attempted.

Experimental investigation of the mechanical properties of biological membranes began in the 1930's with the investigation of sea urchin eggs (Cole, 1932) and nucleated red blood cells (Norris, 1939). Methods of investigating mechanical properties include cell compression, stretching between two needles, micropipette aspiration and deflection of the surface by a rigid spherical particle (Hiramoto, 1970). When ultimate membrane failure properties are of interest, a technique that produces large membrane deformations is required. For such an application, compression between two flat surfaces is most suitable (Zhang *et al.*, 1992).

Essentially, the compression technique involves the squeezing of a single entity between two flat surfaces. It was first used by Cole (1932) to demonstrate the presence of an elastic membrane at the surface of a sea urchin egg. The compression technique has subsequently been used to examine mechanical properties of sea urchin eggs (Mitchison and Swann, 1954; Hiramoto, 1970; Yoneda, 1964), synthetic capsules (Chang and Olbricht, 1993; Zhang *et al.*, 1994; Liu, 1995), mammalian cells (Zhang *et al.*, 1992) and yeast cells (Roberts *et al.*, 1994; Srinorakutara *et al.*, 1995, 1996).

Compression of yeast cells has been conducted to determine the ultimate bursting force of the cells during compression and the dependence of that force on growth phase (Roberts *et al.*, 1994; Srinorakutara *et al.*, 1995), carbon source (Roberts *et al.*, 1994), and suspending medium osmolarity (Srinorakutara *et al.*, 1996). These studies provide a wealth of information on the variables that influence the compressive force required to burst yeast cells. However, more fundamental mechanical properties, *viz.* cell wall failure stresses (or

tensions), are required to characterise cell-breakage processes. These fundamental properties can be obtained from an analysis of compression experiments.

Measurement of the applied load and deformed cell shape during squeezing allows the distribution of membrane tensions to be calculated directly. Cole (1932) and Hiramoto (1964) have formulated the relevant equilibrium equations at the equator of the membrane. Hiramoto (1964) used this technique to determine tensions, internal pressures, and the elastic modulus of sea urchin eggs.

However, yeast and bacterial cells are small, with dimensions in the order of 1 μm. Optical diffraction makes it difficult to observe dimensions accurately in this size range. Thus, the deformed shape of the cell during squeezing cannot be accurately measured. An alternative approach is to assume an elastic behaviour for the membrane, and to then calculate the static cell shape and membrane tensions using the measured applied load and cell deformation.

The process of assuming an elastic behaviour is used in this thesis. Specifically, a force balance approach (Zhang *et al.*, 1992) is used to calculate cell wall tensions and is outlined in appendix A3. Equation (A3.5) provides the analytical relationship between applied compressive force, cell wall tension, original cell radius, and the squeezed cells contact and equatorial radii:

$$\frac{F}{Tr_s} = \frac{2\pi r_{eq} r_c^{\,2}}{r_s\left(r_{eq}^{\,2} - r_c^{\,2}\right)} \tag{5.3}$$

Calculation of F, r_s and deformation from micromanipulation results are outlined in section 5.3.1. The contact and equatorial radii are determined from the undeformed cell radius and cell deformation using Fig. 5.2 which is reproduced from Appendix A3. Equation (5.3) is then rearranged to calculate cell wall tension from these variables:

$$T = \frac{r_s\left(r_{eq}^{\,2} - r_c^{\,2}\right)}{2\pi r_{eq} r_c^{\,2}} \frac{F}{r_s} \tag{5.4}$$

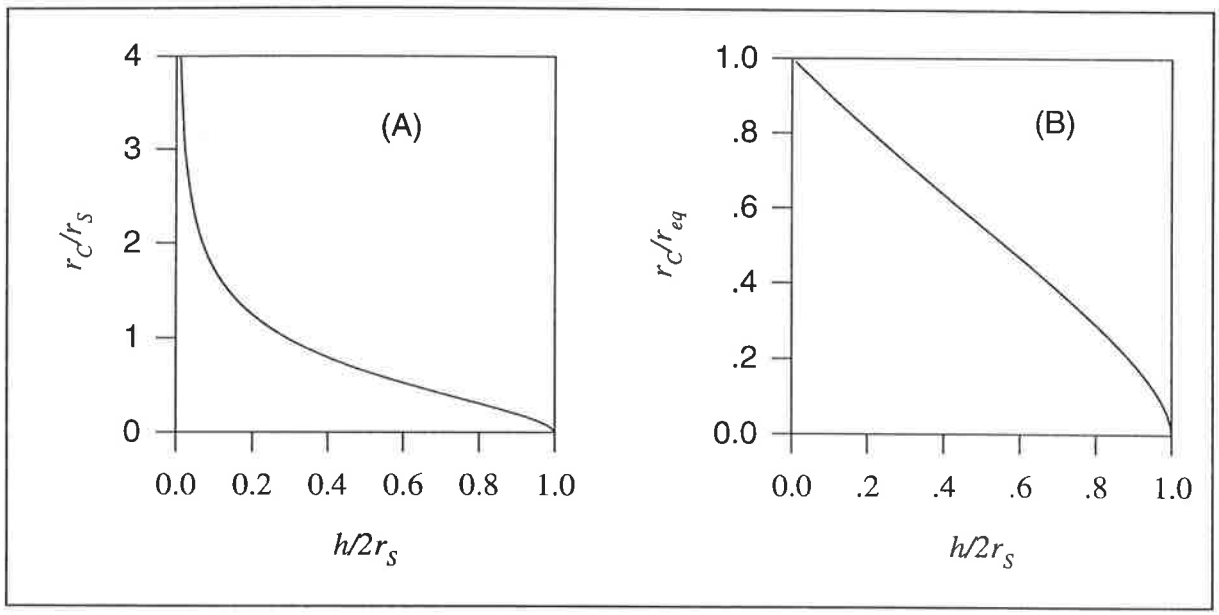

Figure 5.2: Numerical results that define the profile of the deformed cell during micromanipulation.

5.3 Materials and Methods

Cell mechanical properties were investigated using the compression technique. This investigation was achieved through the use of micromanipulation apparatus, developed specifically for the analysis of the mechanical properties of biological cells.

5.3.1 Micromanipulation

The micromanipulation apparatus used in this study (Fig. 5.3) is a modified version of an apparatus originally developed for squeezing single mammalian cells (Zhang *et al.*, 1991).

Apparatus

The two flat surfaces used to compress the cell consist of a fibre optic probe and a glass microscope probe. The flat end on the optic fibre probe was made by grinding 50 μm diameter optic fibres. Using polyurethane varnish, bundles of these fibres were glued tightly into a hole in a stainless steel block with finished surfaces. The fibres were then cut by a cleavage tool (Leetec, London, UK) to make preliminarily squared ends. These ends were polished by lapping films in finishes of 0.3 μm (Angula, Milton Keynes, UK). The polyurethane between the fibres and the block was dissolved using toluene. Fibres with flat, square ends were selected by visual inspection for use as probes.

The other end of the fibre optic probe was connected to the output tube of a force transducer (Model 406A, Cambridge Technology, Watertown, MA, USA) by low-melting-point paraffin wax. The force transducer itself was mounted onto a three-dimensional micromanipulator. The microscope slide that held the cell suspension was fixed to a metal stage, that was connected to a second micromanipulator. A hole in the centre of the metal stage allowed sample illumination and viewing from beneath.

During operation, cell suspension (20 μL) was put onto the microscope slide using a micropipette. Cells rapidly settled from the cell suspension to rest on the glass slide. The microscope was focussed on these cells. The fibre optic probe was manually lowered towards the slide, and stopped at a distance of approximately 10 - 15 μm above the slide's surface. The glass slide was micromanipulated to position an individual cell (chosen randomly) beneath the optic fibre's tip and the surface of the slide. The cell was squeezed

by starting automatic movement of the fibre optic probe towards the slide. After the cell had burst and the probe contacted the slide, the probe was stopped and manually raised from the slide surface. During this time, the force being imposed on the probe was measured by sampling the voltage signal from the force transducer using a PC 30-D data acquisition board (Amplicon Liveline, Brighton, East Sussex, UK) fitted to a personal computer. A sampling frequency of 100 Hz was used with a sampling time of 20 s. This was adequate to record the voltage output versus time for the deformation of the cell. From this voltage versus time history, the force versus distance history and hence the ultimate bursting force, bursting deformation, and cell diameter were determined, as discussed below.

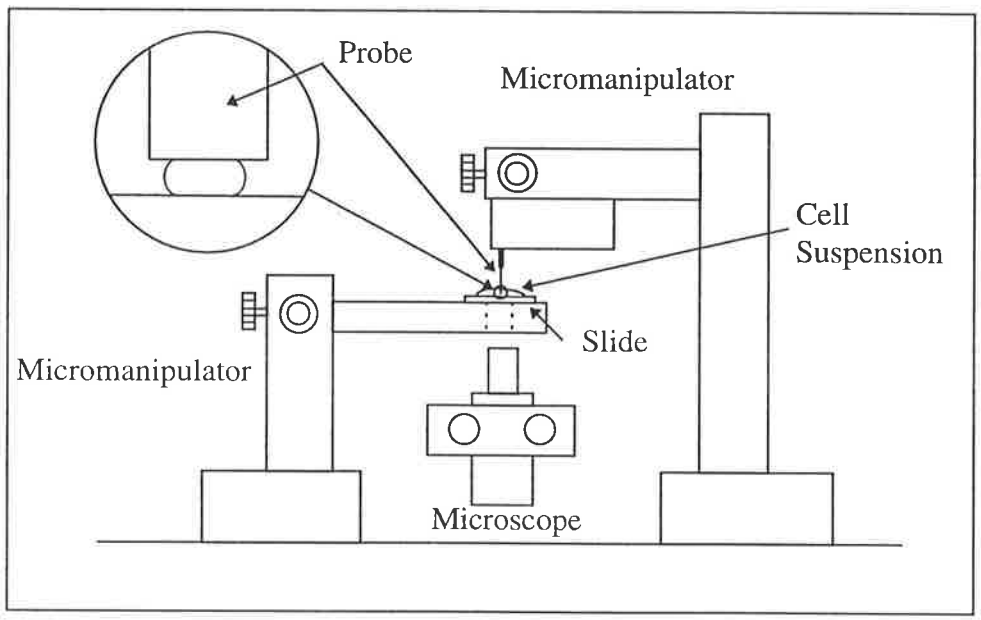

Figure 5.3: Schematic diagram of the micromanipulation apparatus.

Data Analysis

A typical curve describing the output voltage versus sampling time is shown in Fig. 5.4. To calculate the compressive force acting on the cell, the difference between the voltage output and the baseline voltage is multiplied by the transducer force-voltage proportionality:

$$F = K_{FT}\left(V(t) - V_{BL}\right) \tag{5.5}$$

If there is no resistive force acting on the probe, the distance travelled by the probe tip is equal to the product of time and the probe velocity.

$$x_{PT}(t) = K_{MM} t \tag{5.6}$$

However, when an applied force acts on the probe, the deflection of the force transducer beam acts to decrease the distance moved by the probe tip. The deformation of the beam is proportional to the applied load:

$$x_{MB}(F) = K_{MB} F \tag{5.7}$$

The position of the tip of the probe is thus determined by the distance the equivalent "free" probe moves, minus the deflection of the force transducer beam. Substitution of Eq. (5.5) into Eq. (5.7) gives the distance that the probe tip has moved:

$$x_{PT}(t) = K_{MM} t - K_{MB} K_{FT} (V(t) - V_{BL}) \tag{5.8}$$

The translation of the voltage-time data of Fig. 5.4 to force-distance data is shown in Fig. 5.5. The diameter of the cell is calculated from the distance the probe tip travels between contacting the cell and contacting the glass slide. This diameter can be obtained graphically in Fig. 5.5, or from Eq. (5.9):

$$d = K_{MM} (t_{SC} - t_{CC}) - K_{MB} K_{FT} (V_{CC} - V_{BL}) \tag{5.9}$$

The fractional deformation of the cell during compression is the distance of the probe tip from the glass slide divided by the cell's diameter, and is calculated as:

$$h / 2r_S = 1 - \left\{ K_{MM} (t_B - t_{CC}) - K_{MB} K_{FT} (V_B - V_{BL}) \right\} / d \tag{5.10}$$

These values of force (Eq. (5.5)), deformation (Eq. (5.10)) and undeformed cell diameter (Eq. (5.9)) are used to calculate cell wall tensions as outlined in section 5.2.

5.3.2 Yeast cells

The cells investigated in this study were commercially-available Baker's yeast cells (Fermipan instant yeast, Gist-brocades, Delft, The Netherlands). For experiment A, the yeast was resuspended in an isotonic buffer (ISOTON II, Coulter Electronics Ltd., Hertfordshire, UK) at a low cell concentration (1.4 g L^{-1} DW) and stored at 6°C for 24 h.

Cells were fixed (formaldehyde, 0.1% v/v) and warmed to room temperature prior to analysis. This protocol provided a reproducible suspension of late stationary phase cells.

Cells in early stationary phase were used for experiment B. These cells were grown in a complex yeast extract peptone glucose (YEPG) medium with the composition given in Table 5.2. Fermentation was conducted in a 5 L (4 L working volume) fermenter. Inoculation was conducted with 1 g L^{-1} of the Fermipan instant yeast (0.7 g L^{-1} DW). Culture pH was automatically controlled at 28°C. Air was supplied at 1 vvm. The fermentation broth was harvested after 12 h (10.2 g L^{-1} DW). After broth removal, cells were collected by centrifugation (Jouan C422 high-speed centrifuge, 2400g, 10 min) and resuspended in ISOTON II to give a final cell concentration of 1.4 g L^{-1} DW. Cells were fixed (formaldehyde, 0.1% v/v) to prevent further physiological changes prior to analysis.

Table 5.2: Composition of YEPG medium used for Experiment B.

Component	Concentration (g L^{-1})
Yeast extract	10
Bacteriological peptone	5
D-glucose	100
$(NH_4)_2SO_4$	1.2
NaCl	0.5
$CaCl_2.2H_2O$	0.1
MgCl2.6H2O	0.7
KH_2PO_4	1.0
$FeCl_3.6H_2O$	0.003

5.3.3 Size Analysis

The micromanipulation technique used in this study provided a measure of the size of individual cells examined. In addition, the size distribution of the cells was measured using a Coulter Multisizer II particle sizer (Coulter Electronics Ltd, Hertfordshire, UK) fitted with a 100 μm orifice tube. Cells were diluted with ISOTON II diluent prior to analysis (typically 1:1000) to maintain automatic coincidence correction below 10% as recommended by the manufacturer. Results were also corrected for diluent background noise.

5.4 Results and Discussion

Individual Cells

Raw output from the micromanipulator's force transducer for an individual cell from experiment A is shown in Fig. 5.4. Initially, the voltage increases once the probe contacts the cell (Fig. 5.4, point A). Voltage continues to increase until the cell breaks (Fig. 5.4, point B), and then decreases. The voltage then continues to rise when the probe contacts the glass slide.

The voltage output with time is used to calculate a force output with distance curve using Eqs (5.5) and (5.8). This translated data is shown in Fig. 5.5, and can used to obtain the cell's bursting force and bursting deformation. For the cell in Fig. 5.4, the cell bursting force is 102 μN, the cell diameter is 5.45 μm, and the cell bursting deformation is 0.69.

Force, deformation and original cell diameter were used to calculate the cell-wall tension. The data in Fig. 5.5 were used to calculate cell-wall tensions (Eq. 5.4), as shown in Fig. 5.6. At high closure displacements, when the cell is not highly deformed, the calculated tension has a high degree of error due to small uncertainties in the applied force and deformation. These errors are rapidly reduced as cell deformation proceeds. Initially, it appears that the cell wall is in constant tension, until a closure displacement of approximately 0.6. The tension then increases, before decreasing with time in what appears to be a slow, viscoelastic response. The cell-wall failure tension is considerably lower than the ultimate cell-wal tension as the cell deforms. Figure 5.6 is only one individual cell. Within the population of cells examined, there was a wide variation in behaviour. Significant variation in the shape of the tension - closure curve and the magnitude of the ultimate and bursting tension could be seen. Figure 5.7 shows the tension - closure for a second cell from experiment A, which shows a larger amount of tension relaxation in the wall before failure. Common features in the tension - closure curves for experiment A were constant tensions, a tension increase (near a closure displacement of 0.6) and a variable degree of tension relaxation prior to failure. The behaviour of cells from experiment B also showed these qualitative effects.

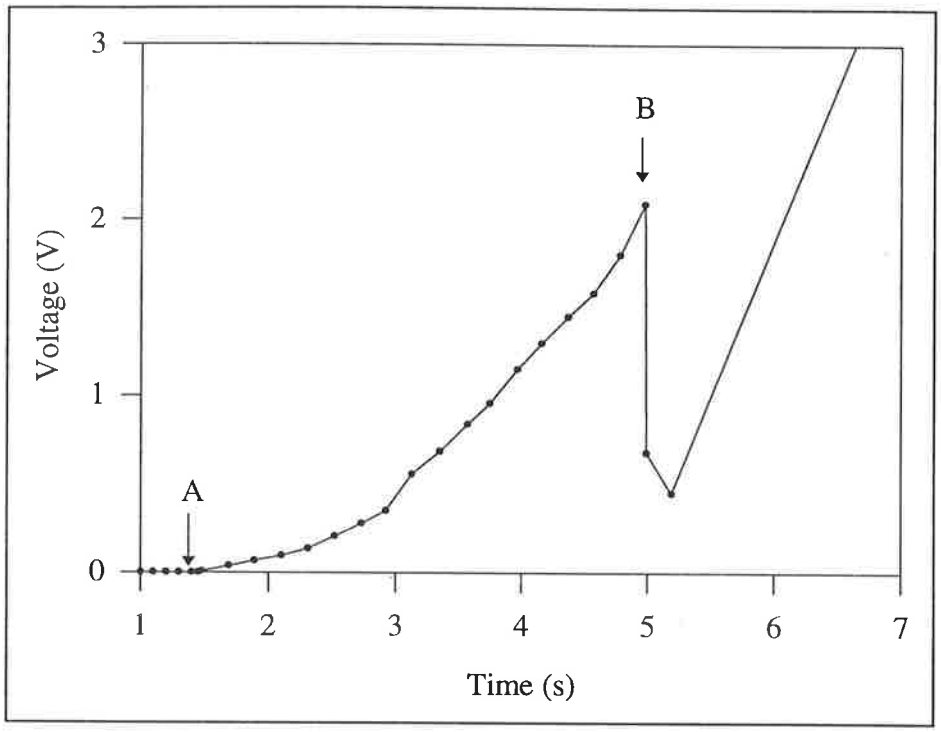

Figure 5.4: Voltage output with time from force transducer during micromanipulation of an individual yeast cell.

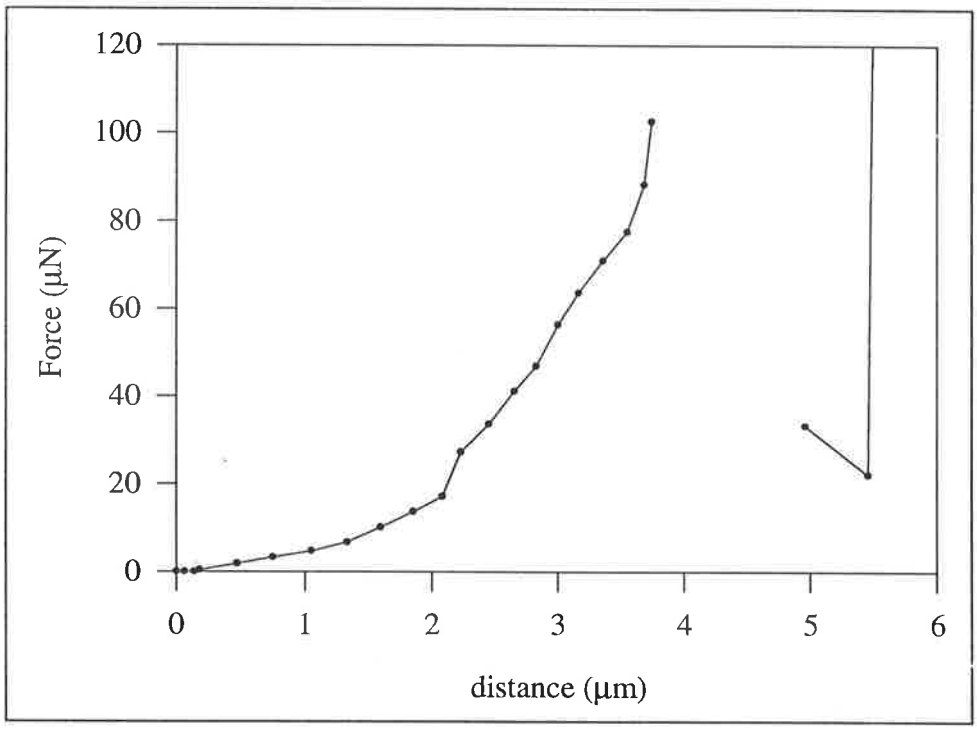

Figure 5.5: Applied force with distance travelled during micromanipulation of an individual yeast cell.

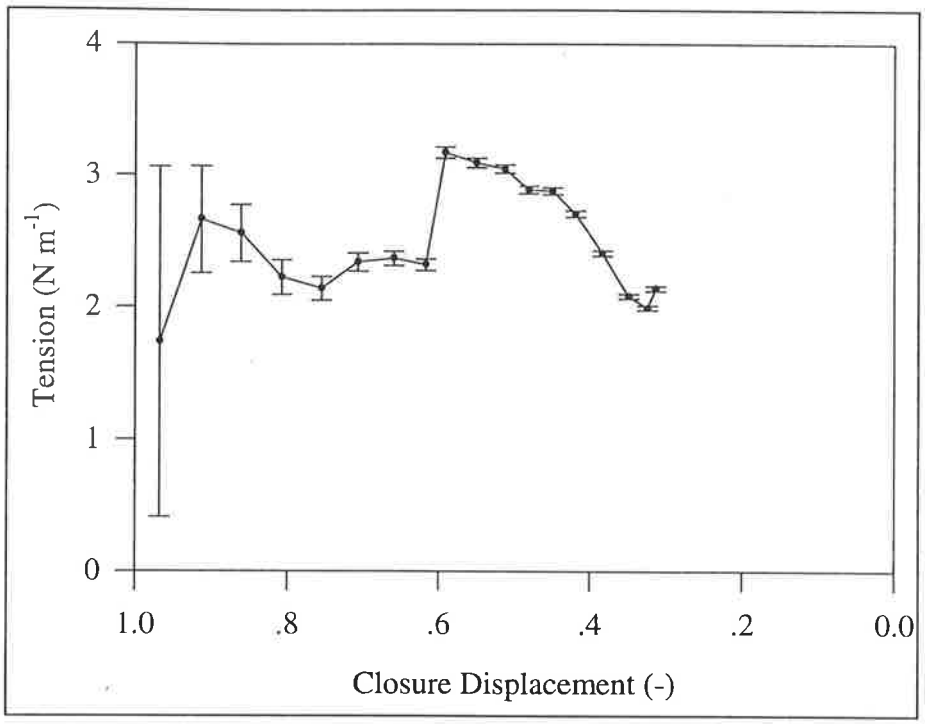

Figure 5.6: Cell wall tension with closure displacement during micromanipulation of an individual yeast cell (from Fig. 5.4).

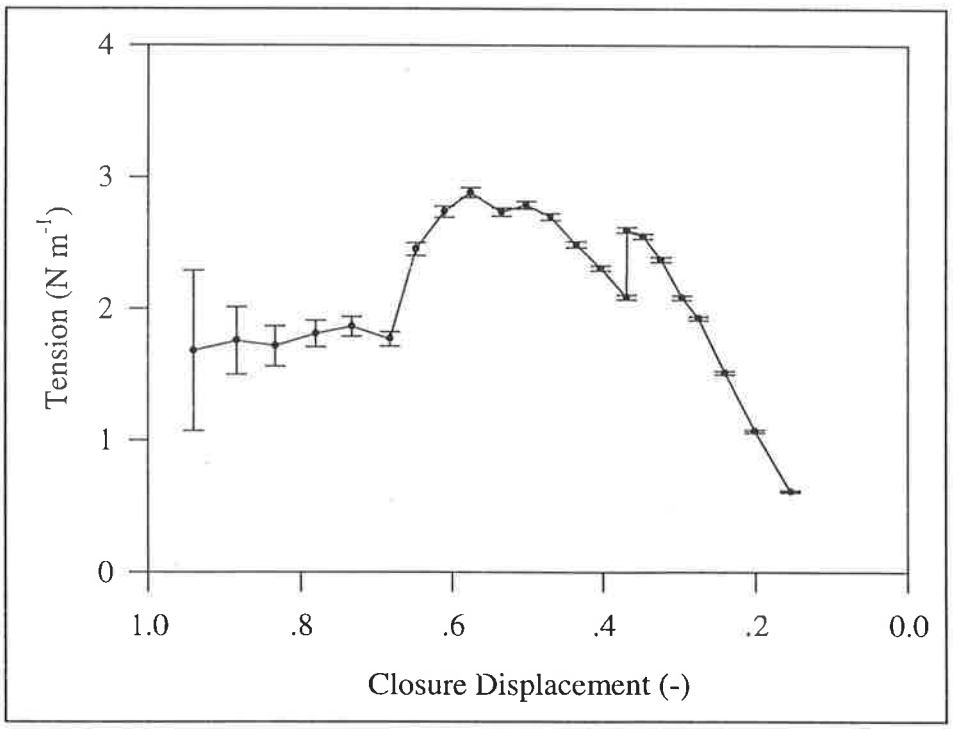

Figure 5.7: Cell wall tension with closure displacement during micromanipulation of an individual yeast cell.

Qualitatively, the tension-closure behaviour of the cell is consistent with the behaviour of a bonded fibre fabric. Initially, tension is constant as fibres are stretched reversibly. However, the tension must then increase before bonds are irreversibly broken. Ultimately, the sample either yields (suddenly through a tear) or tension relaxation occurs as the number of fibres available to support the load decreases until the wall fails.

In addition to the ultimate cell-wall tension, the total work-to-failure is likely to be important in, for example, the process of cell-solid collisions at the impact ring. The total work-to-failure is found by integrating the area under the force-distance curve. The total energy to failure for the cell shown in Fig. 5.5 is 1.0×10^{-10} J.

Cell Population

The dependence of cell bursting force on cell diameter for cells from experiments A and B are shown in Fig. 5.8. There is a large variation in the measured bursting force, over nearly an order of magnitude for both experiments. The scatter can be attributed primarily to biological variability rather than experimental error, as good bursting force measurement reproducibility has been demonstrated for cells from a synchronous culture of mammalian cells (Zhang *et al.*, 1991). In contrast with results reported for animal cells, there is no increase in bursting force with cell size. The mean bursting force for experiment A of 113 μN is considerably lower than the mean bursting force of 186 μN for experiment B. For both samples, the bursting deformation ranged from 40 to 90%, with a mean bursting deformation of 65%.

The dependence of ultimate cell-wall tension (the maximum tension during micromanipulation) on cell diameter is shown in Fig. 5.9. There is no significant correlation between ultimate cell wall tension and cell diameter. Cells from experiment B were considerably stronger than those from experiment A. The results in Fig. 5.9 can be compared with the ultimate wall stress estimate of Eq. (5.2) in section 5.1. The estimated failure stress of 120 MPa corresponds to a wall tension of 8.4 N m^{-1} for an assumed wall thickness of 70 nm. This is a remarkably close approximation to the upper ultimate cell-wall tension in Fig. 5.9.

The scatter seen in Fig. 5.9 may be due to either "between cell" or "within cell" variation. Between cell variation is attributable to the variations between cells within the population. Within cell variation represents the variation that occurs due to property variations within

the wall of an individual cell (for example inhomogeneities in cell wall thickness or chemical composition). Although it is probable that variation is due to both of these factors, it is assumed that most of the variation can be attributed to between cell variation.

To determine if the ultimate cell wall tension can be adequately described by a Gaussian distribution, the cumulative utimate cell wall tension is compared with a Gaussian distribution with the same mean and standard deviation as the cell population in Fig. 5.10. The mean and standard deviation of the ultimate tensions is given in Table 5.3. Figure 5.10 confirms that a Gaussian distribution provides an accurate representation of the ultimate cell wall tension distribution, although there is a slight skewness in the Gaussian distribution due to a relative small number of large ultimate cell-wall tension values.

Table 5.3: Mean and standard deviation of ultimate wall tensions during micromanipulation.

Experiment	Mean Tension (N m^{-1})	Standard deviation (N m^{-1})
A	3.4	1.3
B	5.4	1.7

The dependence of work-to-failure during micromanipulation is shown in Fig. 5.11. There is some dependence of total work on cell diameter, as cells larger than 9 μm required more energy to fail. For cells below 9 μm, there is almost no dependence of work-to-failure on cell diameter. Figure 5.12 confirms that a Gaussian distribution provides an adequate representation of the work-to-failure distribution. Again, the Gaussian distribution is skewed (at the upper end) due to a small but significant number of large work-to-failure values. The mean and standard deviation of work-to-failure (for cells below 9 μm) is given in Table 5.4.

Table 5.4: Mean and standard deviation of work-to-failure during micromanipulation (cells < 9 μm).

Experiment	Mean Work (J)	Standard deviation (J)
A	1.1×10^{-10}	0.7×10^{-10}
B	1.9×10^{-10}	0.7×10^{-10}

The observation that ultimate cell-wall tension is independent of cell size is not surprising, as fundamental cell wall properties would not be expected to exhibit strong dependence on cell size. The observation that bursting force and work-to-failure is independent of cell diameter is, however, surprising. This unexpected independence is probably due to the

large variation in properties that tends to overshadow any effects that might otherwise be observed if cells exhibited less biological variability.

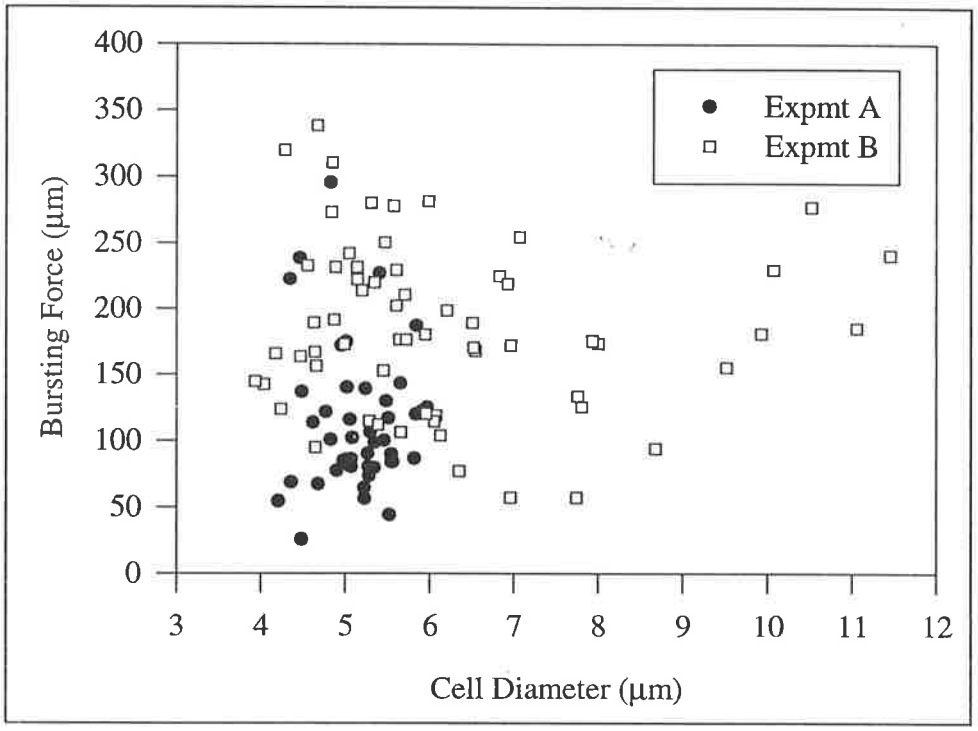

Figure 5.8: Dependence of cell bursting force on cell diameter.

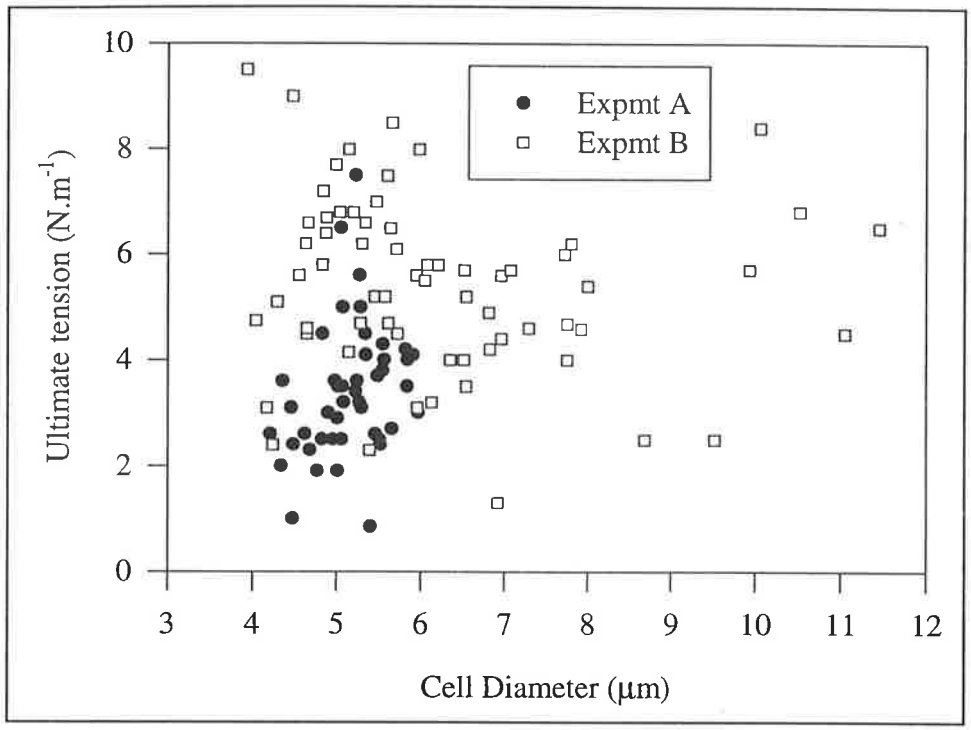

Figure 5.9: Dependence of ultimate cell wall tension on cell diameter.

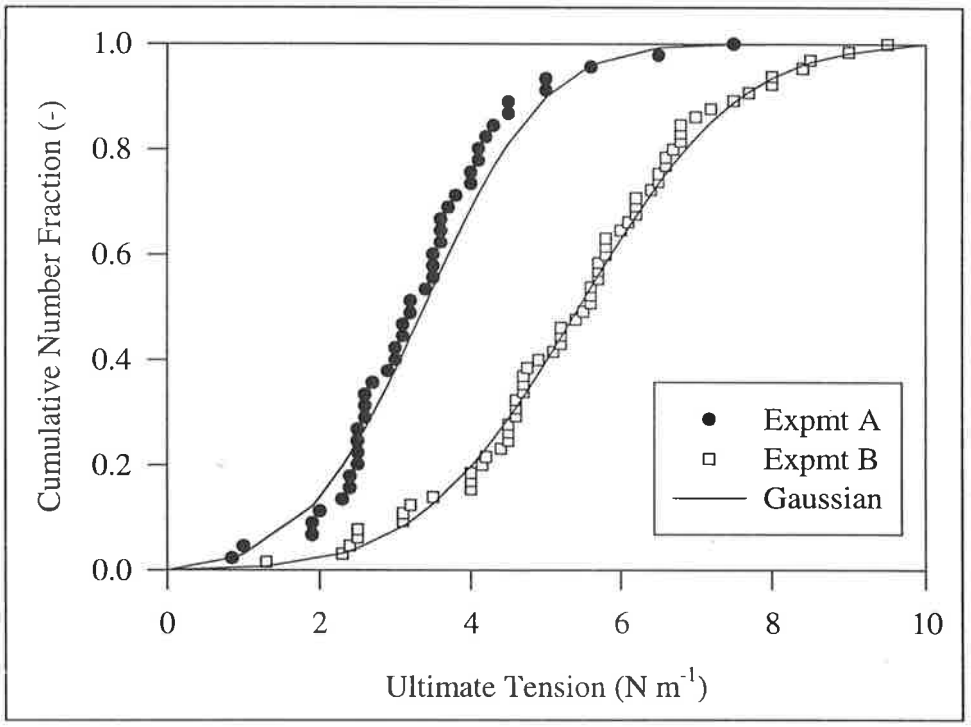

Figure 5.10: Comparison of cumulative ultimate cell wall tension with a cumulative Gaussian distribution with same mean and standard deviation as the cell population.

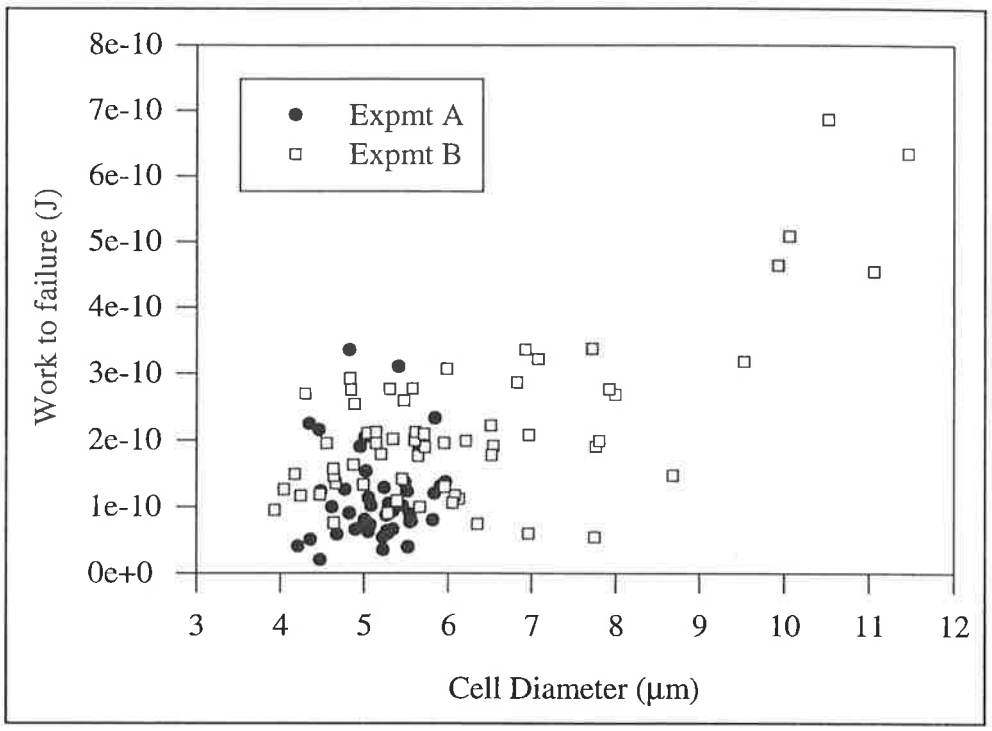

Figure 5.11: Dependence of work-to-failure during micromanipulation on cell diameter.

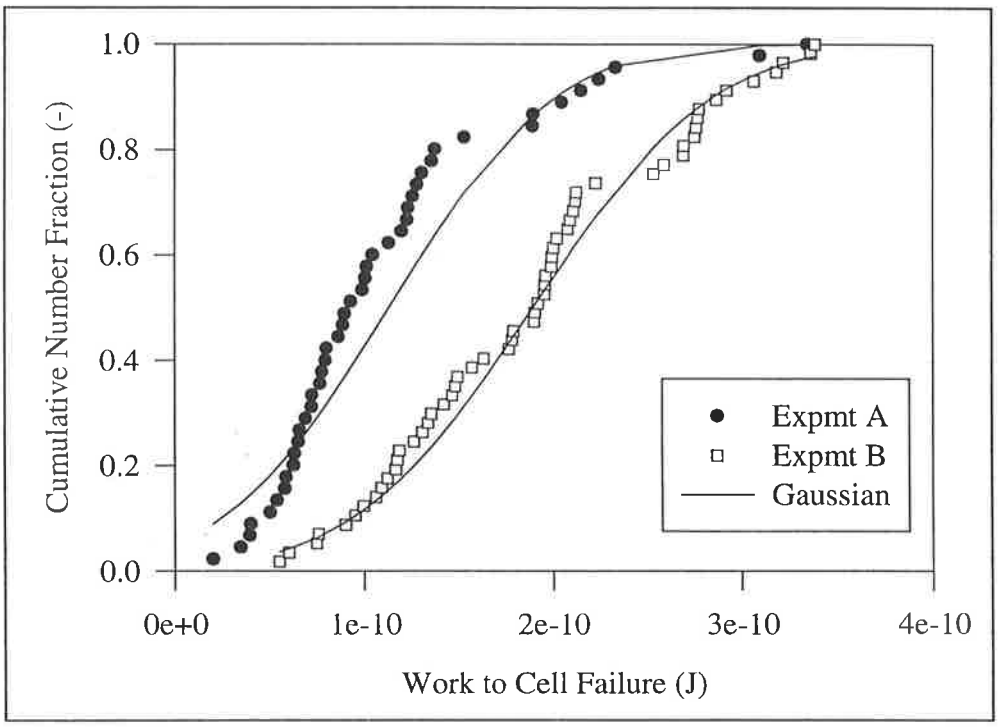

Figure 5.12: Comparison of cumulative work-to-failure with a cumulative Gaussian distribution having the same mean and standard deviation as the cell population (cells < 9 µm only).

Size Distributions

In addition to the cell-size distribution measurement provided by micromanipulation, independent size distributions were obtained using a Coulter Multisizer. Coulter Multisizer size distributions are shown in Fig. 5.13. In agreement with the micromanipulation results, cells from experiment B are larger than those from experiment A.

The Coulter Multisizer is expected to produce a more accurate cell size distribution than micromanipulation. Firstly, a larger number of cells are used to produce the size distribution (> 50000 compared to 50 - 100 for micromanipulation). Secondly, micromanipulation may be subject to some operator bias and may be more prone to sampling errors. Thirdly, the diameter calculated from micromanipulation analysis is the distance between the point where the probe touches the cell and the slide. This measure will have an associated error that increases as the deviation of the cell from spherical increases. Comparison of Coulter Multisizer and micromanipulation cumulative number size distributions in Fig 5.14 shows that cells smaller than approximately 4 μm in diameter are absent from micromanipulation analysis. However, as these small cells represent only a small fraction of the cell volume, it is not likely that this possible sampling error affects the conclusions of this study. Qualitative light microscopy revealed that cells from experiments A and B did not contain budding cells, and that cells were close to spherical. It was also seen that for the cells in experiment B, some cells were present as clumps of 3 - 12 cells. These clumps will be measured as a cell with a large equivalent diameter with the Coulter Multisizer. To break up these clumps, a feed cell suspension from experiment B was homogenized at a low operating pressure (2 MPa) at which no measurable protein release occurred. Although the cell clumps are barely noticeable at the upper end of the differential number size distribution (Fig. 5.15), they give a significantly different volume distribution (Fig. 5.16). As fractional protein release is dependent on cell volume, it is the volume distribution that is used for further analysis in the following chapter.

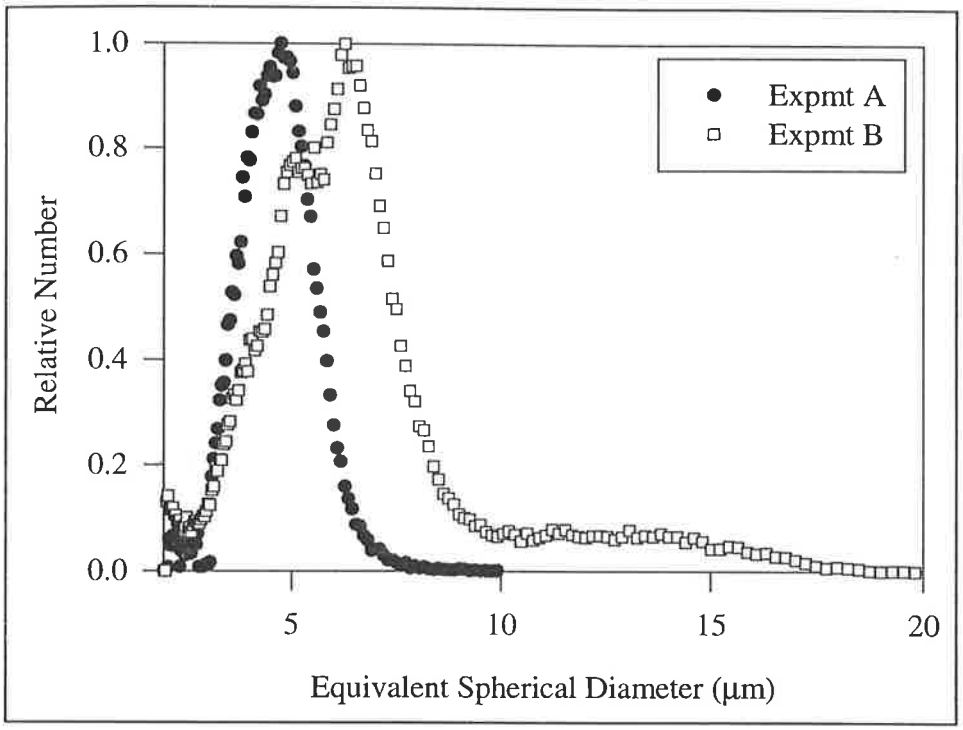

Figure 5.13: Coulter Multisizer size distribution of cells from experiments A and B.

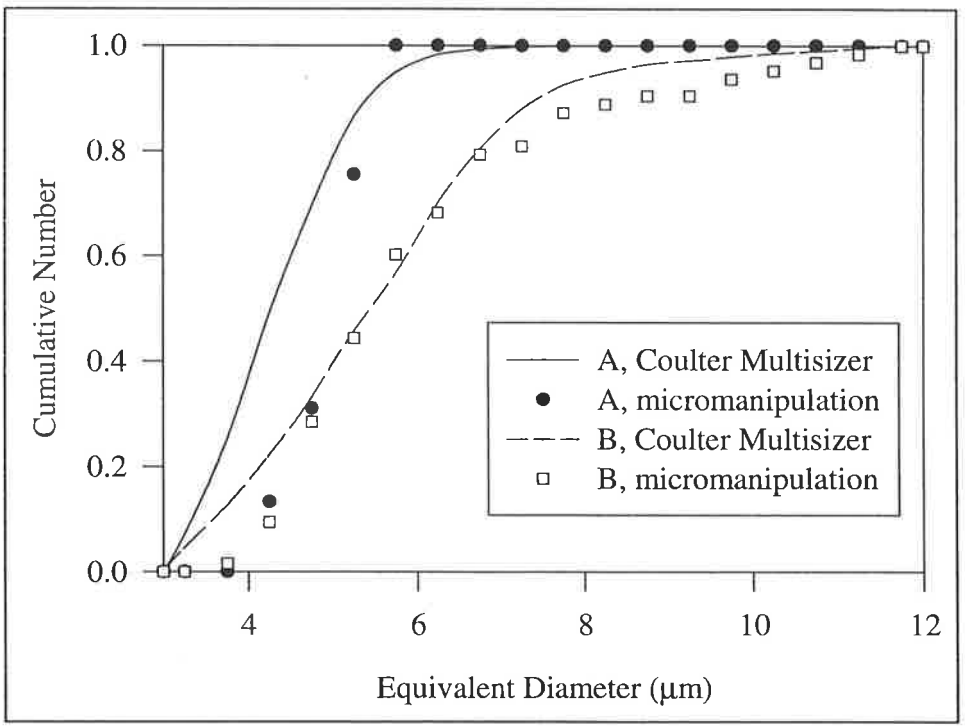

Figure 5.14: Comparison of Coulter Multisizer and micromanipulation size distributions.

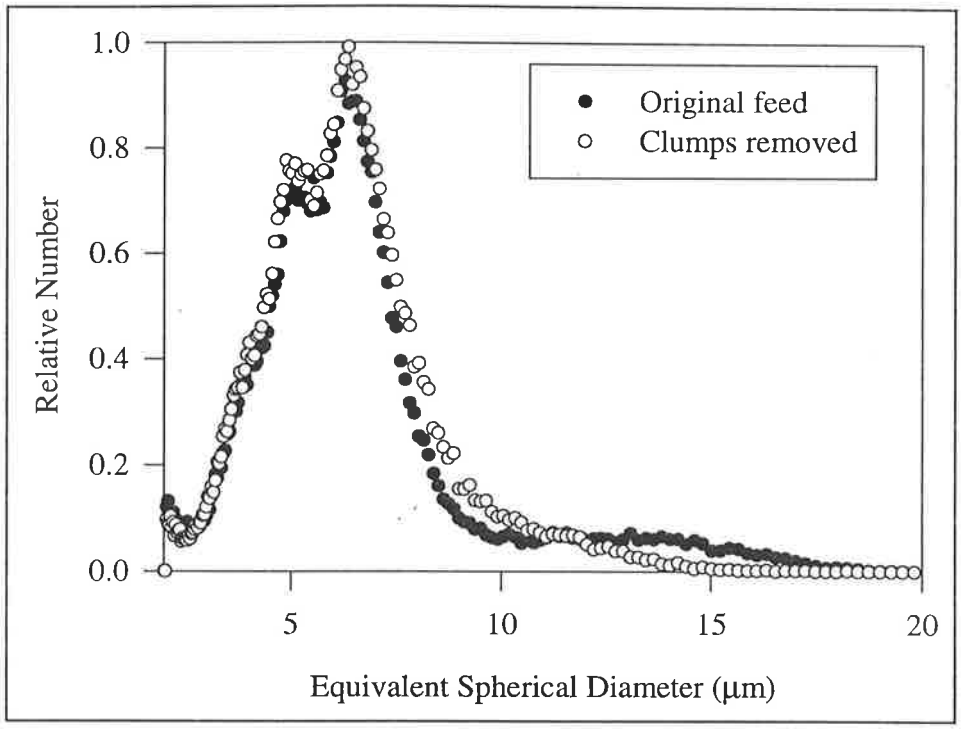

Figure 5.15: Comparison of number size distribution for cells from experiment B before and after cell clump breakup.

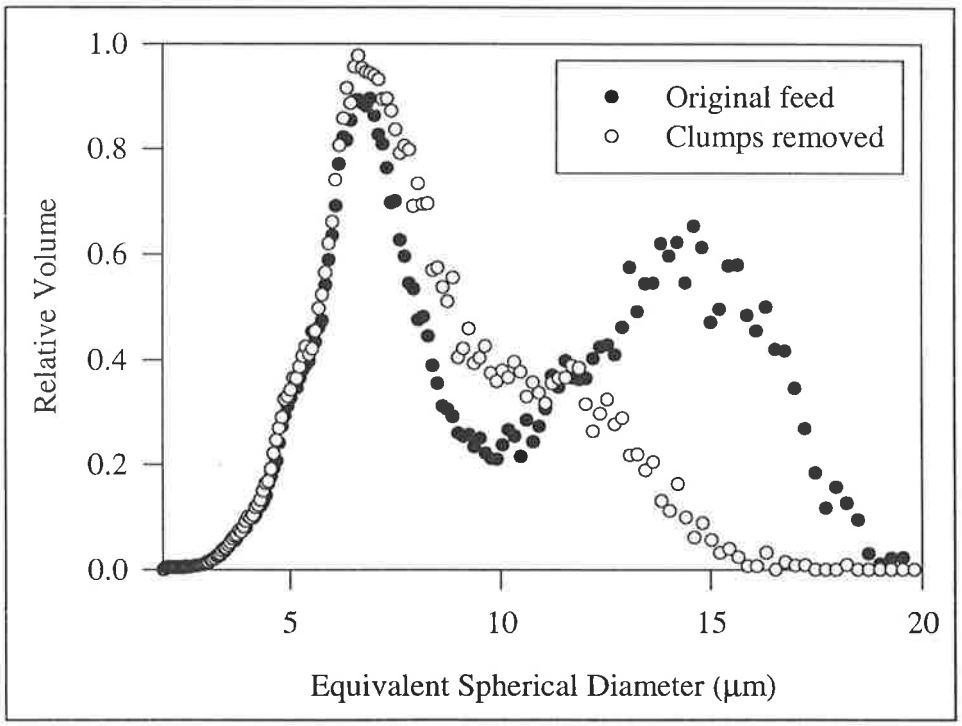

Figure 5.16: Comparison of volume size distribution for cells from experiment B before and after cell clump breakup.

5.5 Summary

Direct measurement of the strength distribution of cells is required to remove the inherent weaknesses in empirical cell-disruption models. In this chapter, a microoganism that is suitable for direct characterisation of mechanical properties, *S. cerevisiae*, was examined. Individual cells from two separate cultures were individually micromanipulated to cell burst. The micromanipulation results were then used to infer ultimate cell-wall tensions and work-to-failure. Ultimate cell-wall tensions and work-to-failure were found to be described by Gaussian distributions, with means and standard deviations given in Table 5.5.

Table 5.5: Mechanical properties of cells determined from micromanipulation experiments.

	Tension		Work-to-failure	
Experiment	Mean (N m^{-1})	SD* (N m^{-1})	Mean (J)	SD* (J)
A	3.4	1.3	1.1×10^{-10}	0.7×10^{-10}
B	5.4	1.7	1.9×10^{-10}	0.7×10^{-10}

* standard deviation

Chapter 6

Prediction and Modeling of Cell-Disruption Efficiency

This chapter uses the information provided in chapters 4 and 5 to characterise cell strength and homogenizer-stress distributions. Corrections are made to account for the dependence of cell-strength on the rate of applied stress. These independent distributions are then substituted into the wall-strength model to predict disruption efficiency. In addition to providing support for the approach used to determine the stress- and strength-distributions, the results also highlight areas where further investigation is required. Multiple disruption events are considered. A simplified approach to disruption modeling is also developed, that does not require direct characterisation of cell-culture properties.

6.1 Introduction

The wall-strength model for high-pressure homogenization was proposed with the following key considerations (Middelberg, 1992):

- The homogenizer applies a continuous distribution of stresses to a population of cells during homogenization. If the stress applied to a given cell exceeds its strength, disruption results. The form of this distribution is a characteristic of the system (*i.e.* homogenizer and valve), and is independent of the particular culture used.

- Disruption is opposed by the cell wall. This wall possesses "strength", which may be defined as an ability to resist an applied disruptive stress. A given population contains cells with a distribution of strengths, which is a population characteristic, and is independent of the applied stress distribution.

As highlighted by Middelberg (1992), the key requirement for the successful application of the wall strength model is a knowledge of approximate forms for the stress and strength distributions. In the original development of the wall-strength model, the particular functions were not known. Instead, logical forms for the stress and strength distributions were proposed, and parameter values were determined by regression to experimental disruption data. However, a key weakness of this approach is the resulting parameter interaction and redundancy as shown in appendix A1. This weakness prevents the distributions from being independent, and prevents extrapolation of model constants to new systems or organisms beyond those for which parameters have been determined.

The aim of this thesis is to determine independent stress and strength distributions for a homogenizer-microorganism system through an examination of the fundamental processes that occur during homogenization. Specifically, it is aimed to produce distributions that do not rely on an assumed functional form or empirical regression analysis for key parameters. The examination of homogenizer fluid mechanics in chapter 3 led to calculations of maximum cell-wall tensions produced during homogenization in chapter 4. Micromanipulation was used to characterise the wall-strength of populations of yeast cells in chapter 5. The results of these chapters are used to define independent stress- and strength-distributions in the wall-strength model and hence model and predict cell-disruption efficiency in this chapter.

Initially, single disruption events are examined. Disruption data obtained in parallel with the mechanical characterisation studies of chapter 5 are used to compare predicted and observed cell-disruption efficiencies. The first true *a priori* predictions of cell disruption efficiency are obtained in section 6.2 and do not rely in any way on regression to experimental data. However, it is apparent that a high degree of uncertainty exists in the parameters that describe the independently determined stress- and strength-distributions. Although the *a priori* parameters provide reasonable predictions of cell-disruption efficiency, the "true" value of the required parameters remains uncertain.

Multiple disruption events are subsequently analysed in section 6.3. Further work is required to accurately model such events, as process variations and cell-wall fatigue effects require better characterisation.

A simplified disruption model is also developed, that does not require independent characterisation of cell culture properties. It uses pressure gradient as the dependent variable, and is able to describe the effects of valve design and homogenizer operating conditions on cell-disruption efficiency.

6.2 Single Disruption Event

Initially, a single disruption event is analysed. A single disruption event implies that only one process of cell breakage occurs. By definition, this requires that only the valve-inlet region and one homogenizer pass are considered. Cell-disruption involving multiple homogenizer events (*viz.* multiple passes through valve-inlet region or valve-inlet and impinging-jet disruption) is considered in section 6.3.

6.2.1 Model Development

In the wall-strength model, the fraction of cells of a given strength that are broken is given by Eq. (6.1),

$$dD(S) = f_S(S) f_D(S) dS \tag{6.1}$$

and an expression for the total disruption of a cell population after one homogenizer pass is deduced by integration:

$$D = \int_0^\infty f_D(S) f_S(S) dS \tag{6.2}$$

To use Eq. (6.2) to predict disruption, the stress and strength distribution functions are required, and are now developed.

Homogenizer Stress Distribution Function

Section 4.3 analysed the tensions that are produced within the wall of a spherical cell as it passes through the homogenizer valve inlet region. Along the homogenizer's feasible operating line (cell-disruption valve seat), a critical Weber number was determined from the maximum cell-wall tension, and was given by Eq. (4.44).

$$We = 9.0 \times 10^{-3} \, \mathrm{Re}^{0.68} \tag{4.44}$$

Substituting the definition of Weber and Reynolds numbers into Eq. (4.44) and rearranging for the maximum cell-wall tension gives Eq. (6.3),

$$T(\alpha,d)=\frac{\rho\alpha^2 d^3}{3.6\times10^{-2}\left(\frac{\rho\alpha d^2}{2\mu}\right)^{0.68}} \tag{6.3}$$

where the strain is determined from Eq. (6.4) and parameter values are given in Table 6.1.

$$\alpha=\frac{Q}{4\beta\pi r_i h^2} \tag{6.4}$$

Table 6.1: Parameters used to calculate maximum cell-wall tension in the inlet region of a cell-disruption valve in an APV-Gaulin 15M homogenizer.

Parameter	Value
Q	4.6×10^{-5} m^3 s^{-1}
β_I	2.1
r_i	0.00385 m
h	37 P$^{-0.35}$ μm
ρ	1000 kg m^{-3}
μ	1×10^{-3} Pa s

Hence, the "tension-distribution" function, which defines the fraction of events with a tension $\geq T$, is defined as:

$$f_D(T)=\begin{cases}1 & \text{if } T\leq T(\alpha,d) \text{ from Eq.(6.3)}\\ 0 & \text{if } T>T(\alpha,d) \text{ from Eq.(6.3)}\end{cases} \tag{6.5}$$

In Eq. (6.3), tension (rather than stress) is the independent variable. The maximum cell-wall tension is dependent on the homogenizer operating conditions and cell size only. This tension-distribution is a unit step function, in contrast to the sigmoidal stress-distribution function developed for the original wall-strength model. However, the unit step tension-distribution function is an approximation, as not all cells will experience the same maximum cell-wall tension during homogenization. A distribution of maximum cell-wall tensions (and hence a sigmoidal tension-distribution) is due to process variations that may include:

- axial variations in the flow in the valve inlet,
- angular variations in the flow around the valve inlet,
- temporal flow variations as the valve opens and closes, and
- variations in cell orientation for non-spherical cells.

Potential temporal variations are examined in appendix A2, where it is concluded that their magnitude is highly uncertain. Nevertheless, a unit step tension-distribution function approximates a sigmoidal tension-distribution function and will only introduce minimal error for a single homogenizer pass.

Whilst the stress-distribution function in the original wall-strength model was only dependent on homogenizer operating pressure, Eq. (6.5) is dependent on cell size and homogenizer operating pressure. Inclusion of a cell property (cell diameter) in the tension-distribution function contradicts the original definition of the tension-distribution function as being dependent on homogenizer-system variables alone. As an alternative, a different variable could be sought (for instance, homogenizer strain-rate or pressure-gradient) and cell strength-distributions translated into "strain-rate" or "pressure-gradient" distributions (see section 6.4.2). However, this requires additional data translation, and will not provide the size distribution information that Eq. (6.21) does.

Equation (6.5) is an independently-determined homogenizer tension-distribution function applicable for homogenization. It does not rely in any way on the empirical regression of experimental cell-disruption data.

Cell Strength Distribution

Chapter 5 examined the mechanical properties of yeast cells, and in particular ultimate cell-wall tensions. The ultimate cell-wall tension-distribution was Gaussian (Eq. (6.6)). The mean and standard deviation for the two yeast cultures of chapter 5 were given in Table 5.3.

$$f_S(T) = \frac{1}{\sigma\sqrt{2\pi}} \exp\left[\frac{-(T-\overline{T})^2}{2\sigma^2}\right] \tag{6.6}$$

Table 5.3: Mean and standard deviation of ultimate cell-wall tensions.

Experiment	Mean Tension (N m^{-1})	Standard deviation (N m^{-1})
A	3.4	1.3
B	5.4	1.7

However, the strength of materials depends on the rate of the applied stress (as discussed in section 1.2.3). During micromanipulation the time from the probe initially contacting the cell up to cell failure is in the order of 10^0 seconds. During homogenization, the cell passes

through the homogenizer valve-inlet region with high strain rate in $\approx 10^{-7}$ seconds. This extreme difference in the rate of stress application between micromanipulation and homogenization will influence the ultimate cell-wall tension. Assuming that the properties of the cell-wall are controlled by a crosslinked glucan network (section 5.1), cell-wall failure will be governed by the process of chain scission (as opposed to the process of chain slippage, applicable for an uncross-linked polymer). This chain scission is governed by mechano-chemical reactions (Terselius *et al.*, 1986). A kinetic rate equation that describes the effect of applied stress on the time to failure is given as Eq. (6.7),

$$\tau_f = \tau_0 e^{\left(\frac{E_a - V\sigma}{RT}\right)} \tag{6.7}$$

where the activation volume is constant for a given material (Terselius *et al.*, 1986). Rearranging Eq. (6.7) for the effect of time to failure on failure stress gives:

$$V\sigma = E_a - RT\ln\left(\frac{\tau_f}{\tau_0}\right) \tag{6.8}$$

Hence, the ratio of homogenization to micromanipulation stress is given by:

$$\frac{\sigma_{HPH}}{\sigma_{MM}} = \frac{E_a - RT\ln\left(\frac{\tau_{f,HPH}}{\tau_0}\right)}{E_a - RT\ln\left(\frac{\tau_{f,MM}}{\tau_0}\right)} \tag{6.9}$$

Substitution of the values in Table 6.2 into Eq. (6.9) provides the following result:

$$\sigma_{HPH} = 1.8\sigma_{MM} \tag{6.10}$$

Table 6.2: Parameter values used in Eq. (6.9) to calculate the effect of loading rate on ultimate cell-wall tension.

Parameter	Value
E_a	120 kJ $gmol^{-1}$*
R	8.314 J $gmol^{-1}$ K^{-1}
T	293 K
$\tau_{f,HPH}$	10^{-7} s
$\tau_{f,MM}$	10^{0} s
τ_0	10^{-12} s*

* values given in Terselius *et al.*, 1986.

Other rate effects that are also applicable to the cell wall have been discussed by Bueche (1962). At low strain rates (such as during micromanipulation) individual fibres within a network can move slowly to rearrange themselves as the load is applied. Viscous forces are too low to be significant. At high strain rates (such as during homogenization) fibre velocities and hence viscous retarding forces will increase. If the viscous forces approach the fibres' failure force, the network is not easily stretched. Instead, brittle failure occurs at very low strains. This qualitative explanation justifies the assumption made in chapter 4 that cells remain spherical during passage through a homogenizer valve. In an unstretched cell-wall, bond density and hence ultimate cell-wall tensions will be higher than in a comparable stretched wall. Tension is inversely proportional to the wall stretch ratio and hence:

$$\frac{T_{HPH}}{T_{MM}} = \frac{1+\varepsilon_{MM}}{1+\varepsilon_{HPH}} \tag{6.11}$$

For the feed cells of chapter 5, cell failure occurred at an average cell deformation of 65%, corresponding to an equatorial hoop strain of approximately 0.4 (the ratio $r_{eq}/r_S - 1$) during micromanipulation. Assuming a low strain brittle-failure during homogenization ($\varepsilon_{HPH} \approx 0$), Eq. (6.11) evaluates to:

$$T_{HPH} = 1.4 T_{MM} \tag{6.12}$$

This increase in ultimate cell-wall tension is multiplicative with the mechano-chemical effect. Hence, the ultimate cell-wall tension during homogenization is:

$$T_{HPH} = 1.8 \times 1.4 T_{MM} = 2.5 T_{MM} \tag{6.13}$$

The ultimate cell-wall tensions measured during micromanipulation (Table 5.3) are translated to high-pressure homogenizer values using Eq. (6.13) and are given in Table 6.3.

Table 6.3: Mean and standard deviation of ultimate wall tensions translated to high-pressure homogenizer conditions.

Experiment	Mean Tension (N m^{-1})	Standard deviation (N m^{-1})
A	8.6	3.3
B	13.6	4.3

Equation (6.6) is an independently determined "cell-strength" distribution (the ultimate cell-wall tension distribution) applicable for homogenization. This distribution has been measured directly rather than inferred through regression to disruption data.

6.2.2 Disruption Model

From Eq. (6.1), the fraction of cells broken at a given tension is given by Eq. (6.14).

$$dD(T) = f_S(T) f_D(T) dT \tag{6.14}$$

This expression is dependent on both homogenizer operating pressure and cell diameter. Substitution of the tension-distribution of Eq. (6.5) into Eq. (6.14) gives

$$dD(T) = \begin{cases} 0 & \text{if } T > T(\alpha,d) \text{ from Eq.(6.3)} \\ f_S(T)dT & \text{if } T \le T(\alpha,d) \text{ from Eq.(6.3)} \end{cases} \tag{6.15}$$

Integration of Eq. (6.15) gives the total fraction of cells that will be broken.

$$D = \int_{T=0}^{T=\infty} dD(T) \tag{6.16}$$

With the step function stress-distribution function of Eq. (6.5), Eq. (6.16) evaluates to

$$D = \int_0^{T(\alpha,d)} f_S(T)dT = F_S\left(T(\alpha,d)\right) \tag{6.17}$$

where $F_S(T)$ is the cumulative fraction of cells of diameter d with ultimate cell-wall tension $\le T$ at an applied strain α. This is represented graphically in Fig. 6.1. The volume fraction of cells that are broken at a given cell diameter is then given as

$$dD(d) = F_S\left(T(\alpha,d)\right) f_V(d).dd \tag{6.18}$$

as $F_S(T)$ is the fraction of cells of size d that will disrupt as their ultimate tension is less than the maximum tension during homogenization. Integration gives total cell disruption:

$$D = \int_0^{d_{\max}} F_S\left(T(\alpha,d)\right) f_V(d) dd \tag{6.19}$$

This integration is most conveniently conducted using the size distributions provided by the Coulter Multisizer (*e.g.* Figure 5.16). Each "channel" of the multisizer provides the volume fraction of cells ($f_V(d)$) within a narrow size range ($d \pm \delta d$) enabling Eq. (6.19) to be evaluated by a summation over each of the Coulter Multisizer channels:

$$D = \sum_{i=1}^{n\,channels} F_S\left(T(\alpha, d_i)\right) f_V(d_i) \tag{6.20}$$

In addition to being able to calculate disruption efficiency, the homogenate cell-size distribution is readily calculated as

$$f_V(d)_{homogenate} = \left\{1 - F_S\left(T(\alpha, d)\right)\right\} f_V(d)_{feed} \tag{6.21}$$

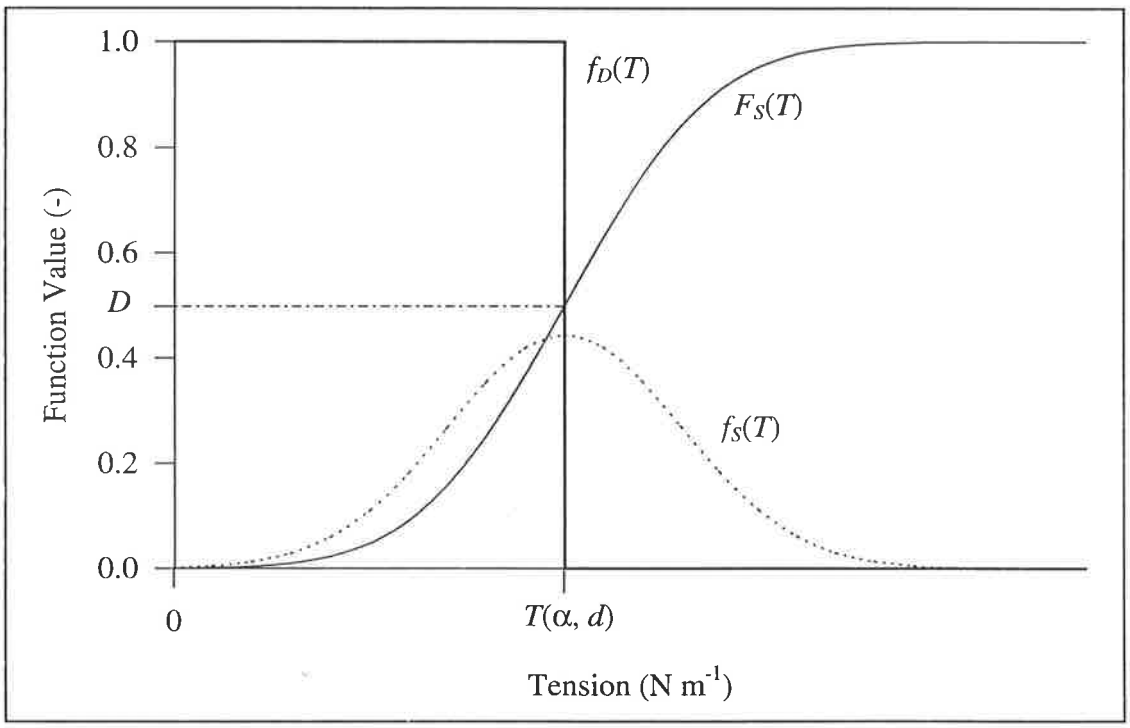

Figure 6.1: The combination of homogenizer-tension and cell-strength distributions which allows disruption to be calculated for cells of a given diameter.

6.2.3 Results

The modified wall-strength model, using the independently determined tension and strength distributions calculated in section 6.2.1, is used to predict cell disruption efficiency in this section. Predictions are made for the two yeast cultures described in section 5.3. Cell-disruption efficiency was measured in parallel with the mechanical properties determined in chapter 5, using an APV-Gaulin 15MR high-pressure homogenizer with a cell disruption valve assembly (section 2.1.2).

Parameter Values

Initially, a homogenizer operating pressure of 56 MPa was considered. From Table 6.1, the corresponding homogenizer valve gap was 9.0 μm. Homogenizer strain rate was calculated from Eq. 6.4 and was 5.54×10^6 s^{-1}. This value was then used in Eq. (6.3) to calculate the maximum* cell-wall tension generated in the homogenizer valve. The calculated dependence of maximum cell-wall tension on cell diameter is shown in Fig. 6.2. Figure 6.2 also shows the dependence of ultimate cell-wall tension on cell diameter (redrawn from Fig. 5.9 by recalculating ultimate cell-wall tensions (Eq. (6.13)). Figure 6.2 shows graphically that the maximum cell-wall tensions (generated during homogenization) are comparable to the ultimate cell-wall tensions. Figure 6.2 also provides a graphical interpretation of the homogenizer tension-distribution function of Eq. (6.5). If the maximum cell-wall tension (Eq. (6.3), solid line) exceeds the ultimate cell-wall tension (chapter 5, individual points), it is assumed that the cell will fail in the homogenizer. Hence, cells in Fig. 6.2 below the line of Eq. (6.3) will be broken during homogenization, as their ultimate cell-wall tension is below the maximum cell-wall tension generated within the homogenizer. Cells above the line of Eq. (6.3) will survive, as their ultimate cell-wall tension exceeds the maximum cellwall tension generated within the homogenizer. Also, as the maximum wall tension (Eq. (6.3)) increases with cell diameter, the probability of disruption is expected to increase with cell diameter.

* Maximum cell-wall tension refers to the tensions generated within the cell wall as it passes through the homogenizer valve (chapter 4) whilst ultimate cell-wall tensions are a measured mechanical property of the cell (chapter 5).

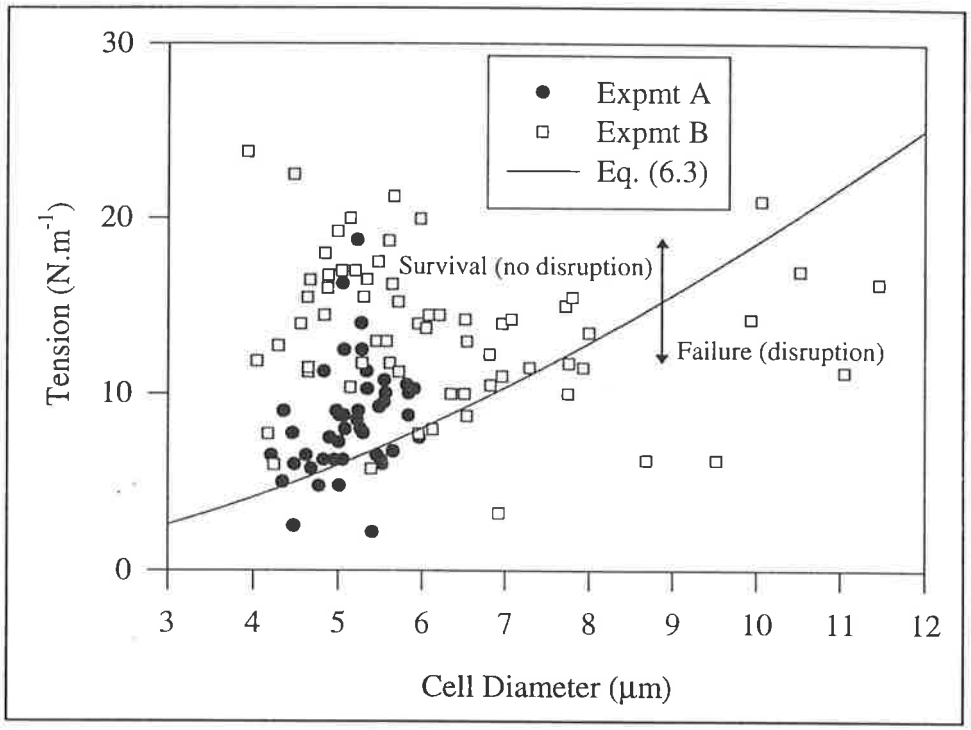

Figure 6.2: Dependence of maximum cell-wall tension (within homogenizer, 56 MPa) and ultimate cell-wall tension on cell diameter.

Cell Size Distributions

Equation 6.21 was used to calculate homogenate cell-size distributions from the original feed-cell size distributions. Homogenate size distributions after one homogenizer pass were also obtained experimentally. Observed and predicted size distributions are compared in Figs 6.3 and 6.4 for cells from experiments A and B, respectively.

The predictions shown in Figs 6.3 and 6.4 are in excellent qualitative and reasonable quantitative agreement with experimental observations. Eq. (6.21) accurately predicts that large cells are preferentially disrupted and hence removed from the size-distribution. However, there are some quantitative differences. Part of the difference for experiment B is attributed to cell clumps (e.g. above 9 μm) that dissociate into individual cells (3 - 8 μm). Measured homogenate size-distributions will also be convoluted with some cell-debris (at sizes < approximately 2 - 3 μm) or cell "ghosts" (ruptured cells where the cell wall remains in one piece) at larger sizes. These and other possible systematic errors are discussed further in section 6.2.4.

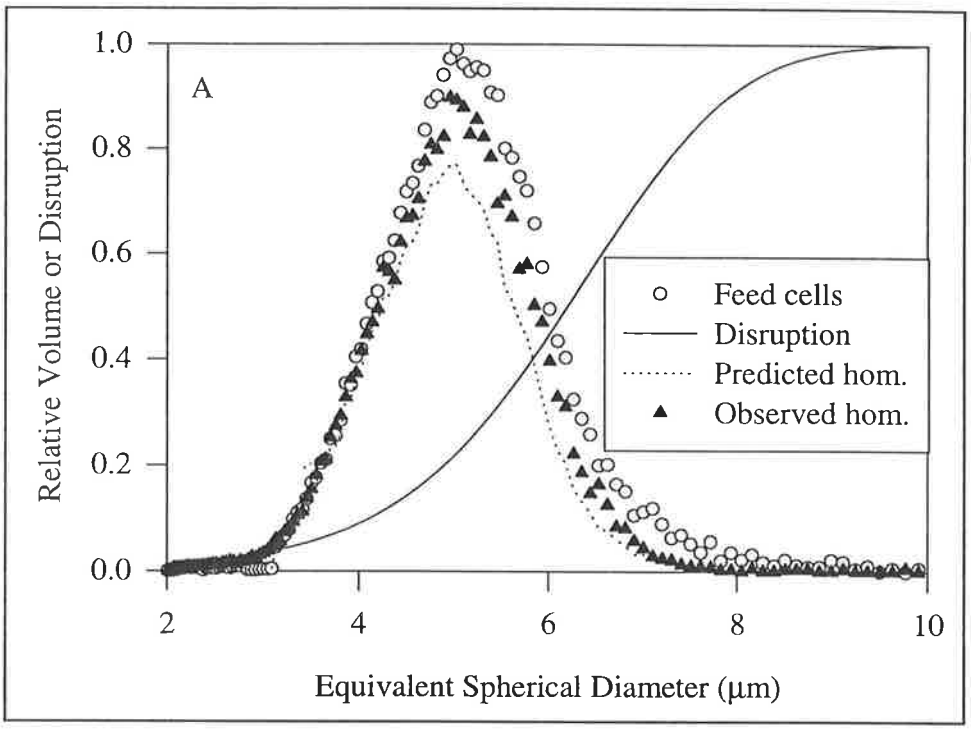

Figure 6.3: Comparison of feed-cell size distribution, dependence of predicted disruption efficiency on cell size (Eq. (6.17)), predicted homogenate cell size distribution (Eq. (6.21)) and observed homogenate cell-size distribution for cells from experiment A homogenized at 56 MPa.

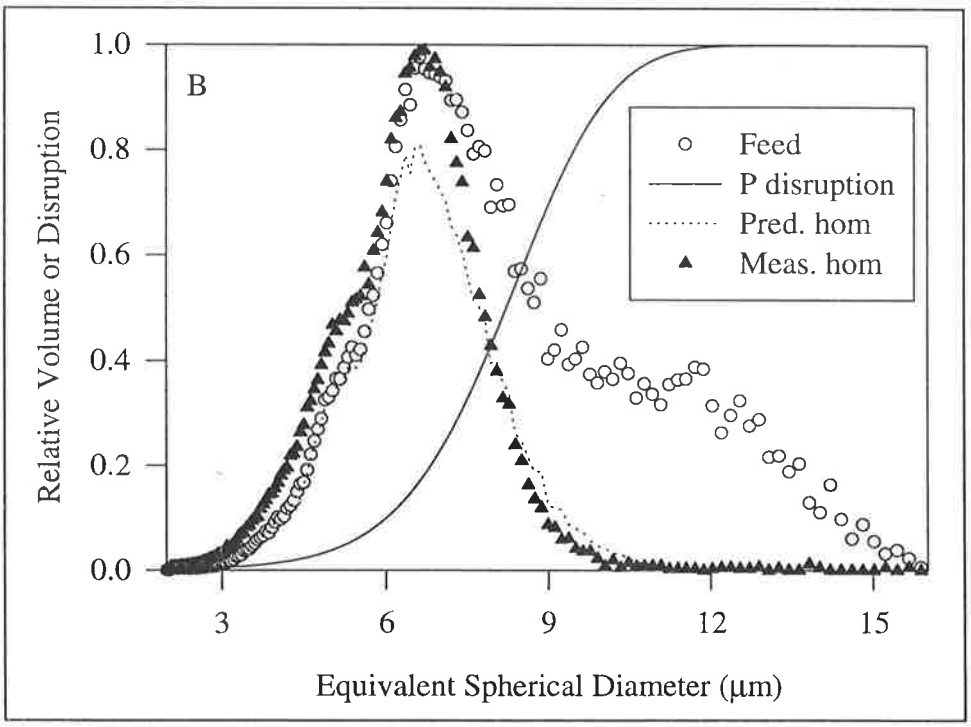

Figure 6.4: Comparison of feed-cell size distribution, dependence of predicted disruption efficiency on cell size (Eq. (6.17)), predicted homogenate cell-size distribution (Eq. (6.21)) and observed homogenate cell-size distribution for cells from experiment B homogenized at 56 MPa.

Cell Disruption Efficiency

Equation (6.20) was used to calculate disruption efficiency. Fractional protein release was calculated as 26% and 40% for experiments A and B respectively (56 MPa homogenizer pressure). This compares with fractional protein releases of 8% and 44% obtained experimentally. Whilst disruption efficiency is significantly over-predicted for experiment A, good prediction is observed for experiment B.

The dependence of disruption efficiency on homogenizer operating pressure was then calculated. This is shown in Fig. 6.5. Although cells from experiment A are weaker than those from experiment B (Table 6.3), it was predicted that they would be more resistant to disruption due to their smaller size. This is also seen in the experimental results (Fig 6.5).

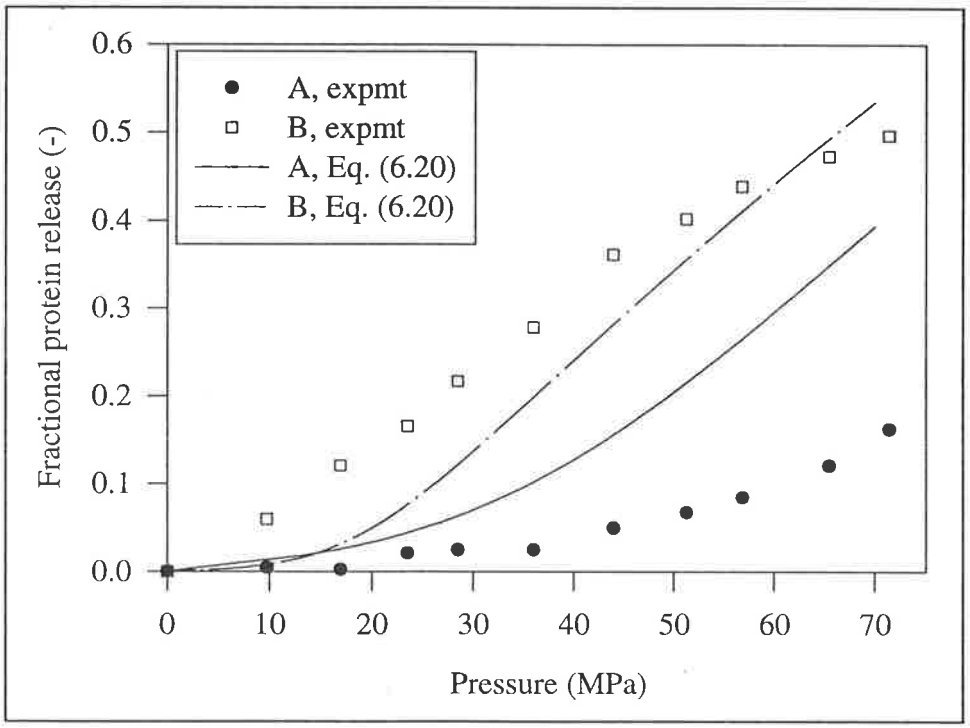

Figure 6.5: Comparison of predicted and observed dependence of cell disruption efficiency on homogenizer operating pressure.

The predictions in Fig. 6.5 correctly forecast the qualitative effects of cell size, homogenizer operating pressure, and cell-culture variability on cell disruption efficiency. Possible reasons for the quantitative errors in Fig. 6.5 are discussed further in the following section.

6.2.4 Discussion

It must be emphasised here that section 6.2.3 provides the firstly truly *a priori* predictions of cell disruption efficiency in a high-pressure disruption device. Unlike any previous disruption "predictions", these predictions do not rely in any way on the regression of any previous experimental disruption data, as they are based on an independent characterisation of the cell-strength distribution (using a micromanipulation technique), a primarily numerical study of the flow conditions within a homogenizer, and the interaction between cells and the flow field. However, the methods used to characterise the distributions and any systematic errors that they may include requires further discussion.

Limitations of the micromanipulation technique used to characterise the cell strength distributions are readily apparent. During micromanipulation, cells are squeezed in a relatively slow process until they burst. In comparison, cells are rapidly accelerated in a fluid flow field during homogenization. Hence, corrections are required to account for cell-wall thinning due to cell deformation, an increased stress required to initiate bond scission at high loading rates, and differences in the pattern of cell-wall tensions that are generated. The method that was used to generate the required correction factors inherently introduces many assumptions that are not readily proven:

- it used an assumed bond-scission activation energy. Although this activation energy was measured experimentally for similar materials, its application to the yeast cell is an unjustified (although highly plausible) approximation. Alternative activation energy values would alter the increase in stress required to initiate bond scission at high loading rates.

- it assumed that cells are not significantly deformed during the homogenization process. This assumption can be justified as at the rapid loading conditions in the homogenizer, the crosslinked, intertwined polymers in the cell wall will behave in a "glass-like" rather than "rubber-like" material. However, without further verification, this assumption must be viewed as a simplification of the actual process. If significant cell deformation does occur in practice, the tension distribution will be significantly altered.

- it assumed that the cross-linked glucan network in the cell wall controls the mechanical properties of the cells wall. Under the (relatively) slow loading conditions of micromanipulation, un-crosslinked chains will be free to slide past each other within

the wall structure and will not contribute to the mechanical strength of the cell wall. However, under the rapid loading conditions within the homogenizer, the viscous forces required to slide free chains past each other will exceed the chains' strength, and the free chains will then contribute to the wall's strength.

- it assumed that stress relaxation did not significantly reduce the ultimate tension measured during micromanipulation. If large numbers of chains are broken during the cell deformation process, then the actual ultimate tension for an unstretched cell-wall would be significantly greater as more intact chains would remain in the cell-wall.

- it assumed that the maximum and ultimate cell-wall tensions are able to be compared directly. However, the ultimate cell-wall tension is found under conditions of isotropic cell-wall tension, whilst the maximum cell-wall tension occurs under conditions of anisotropic tensions or shear stresses. Although a von Mises criterion was used to make valid comparisons, it introduces further assumptions of material behaviour that cannot readily be proven.

Possible limitations of the unit step tension distribution function have been discussed in section 6.3.3 (*viz.* effects of non-spherical cells and axial, angular or temporal variations). Although inclusion of these process variations (appendix A2) will make the tension-distribution function more sigmoidal in form, they will not significantly change the value of the median maximum cell-wall tension. A more important systematic error potentially arises from error in the measured homogenizer valve-gap. Figure 3.7 shows that there is significant error within these measured values. A reproducibility error of $\pm$ 1.5 μm corresponds to a valve-gap error of approximately 15% at high operating pressure (> 50 MPa). As valve inlet pressure gradient (Eq. (3.25)) is inversely proportional to valve gap cubed, this corresponds to a potential error of 40% in the maximum cell-wall tension.

The presence of these potential systematic errors implies that the predictions seen in Figs 6.3 to 6.5 could almost be fortuitous. The "true" numerical values used to describe the strength- and stress-distribution parameters may vary considerably from the "calculated" numerical values used in this thesis. Section 6.2.5 examines some potential errors in the cell-strength distribution. It assumes that the ultimate cell-wall tension distribution's mean and standard deviation are unknown, and determines best fit parameters through non-linear regression using the stress-distribution used in section 6.2.1. Regressed parameters are then compared with the measured values. To examine the additional potential errors

introduced by the stress-distribution, section 6.2.6 assumes that the dependence of homogenizer valve-gap on operating pressure is described by the laminar flow relationship of Eq. (3.2) rather than the measured dependence given in Table 3.1. Essentially, this represents a "worse-case" scenario, with the minimum potential valve-gap (and hence maximum pressure gradient) at a given operating pressure. Best-fit strength-distribution parameters are then determined by regression, and compared with measured values.

6.2.5 Regression for Strength-Distribution Parameters

As discussed in the previous section, the parameter values measured for the cell-strength distribution (mean and standard deviation) contain potential systematic errors, with their "true" values being different to those measured using micromanipulation. This section examines the possible magnitude of the systematic error in these strength-distribution parameters, assuming that the stress-distribution function given in section 6.2.1 is correct.

Disruption

Disruption in the valve inlet region was calculated as

$$D = \sum_{i=1}^{n\,channels} F_S\left(T(\alpha, d_i)\right) f_V\left(d_i\right) \tag{6.20}$$

where

$$F_S(T) = \int_0^T \frac{1}{\sigma\sqrt{2\pi}} \exp\left[-\frac{(T-\bar{T})^2}{2\sigma^2}\right] .dT \tag{6.22}$$

$$T(\alpha, d) = \frac{\rho\alpha^2 d^3}{3.6\times 10^{-2}\left(\frac{\rho\alpha d^2}{2\mu}\right)^{0.68}} \tag{6.3}$$

and $f_V(d)$ is the cell size distribution.

Model Regression

Disruption was calculated using Eq. (6.20). A spreadsheet package (Microsoft Excel for Windows 95) was used to perform a non-linear regression of the model to the experimental disruption data to determine the mean and standard deviation of the ultimate cell wall tension distribution ($\overline{T}$ and σ in Eq. (6.22)). A quasi-Newton search algorithm was used to determine the minimisation search direction to minimise the total sum squared error (SSE, Eq. (6.23)).

$$SSE = \sum_{i=1}^{n} \left(Experimental\ Disruption_i - Predicted\ Disruption_i \right)^2 \qquad (6.23)$$

The standard error in the regressed mean and standard deviation was calculated using 50 bootstrap replications with Monte Carlo sampling (Efron and Tibshirani, 1986).

Results

The results of the non-linear regression are summarised as Fig. 6.6 (comparing regressed and experimental disruption efficiency) and Table 6.4 (comparing regressed and measured strength-distribution parameters). The regressed cell disruption versus pressure dependence provides an exceptionally good description of the experimental disruption data, removing most of the quantitative error that exists with the predicted disruption values. Interestingly, the regressed mean ultimate cell-wall tensions for experiments A and B (Table 6.4) is very similar, in contrast to the large difference in the measured values. The regressed and measured mean ultimate cell-wall tensions for experiment B are very similar, although the regressed standard deviation is much larger. These differences are discussed further in section 6.2.7.

Table 6.4: Comparison of mean and standard deviation of ultimate wall tensions at high-pressure homogenizer conditions determined from non-linear regression of disruption data and measured through micromanipulation.

	Mean Tension (N m^{-1})		Standard deviation (N m^{-1})	
Experiment	Calculated	Regressed	Calculated	Regressed
A	8.6	12.6 ± 0.3	3.3	4.3 ± 0.2
B	13.6	14.4 ± 0.4	4.3	8.5 ± 0.5

* regressed values given as ± one standard deviation

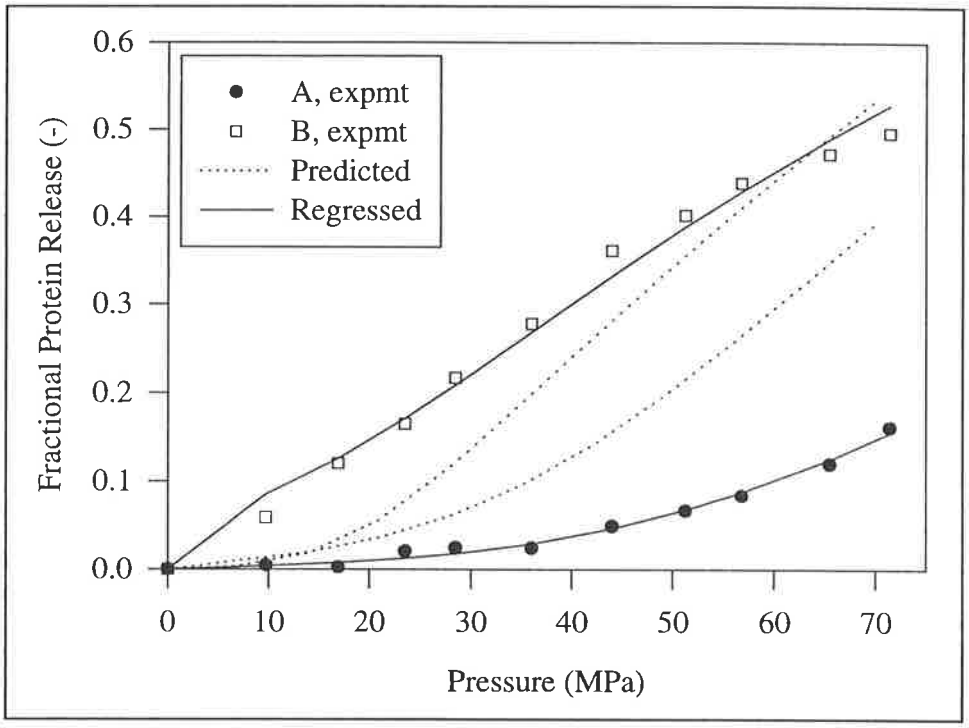

Figure 6.6: Comparison of regressed (Eq. (6.20), Table 6.1, Table 6.4), predicted and experimental disruption efficiency for experiments A and B.

6.2.7 Stress-Distribution Systematic Errors

As discussed in section 6.2.4, the stress-distribution function contains potential systematic errors. In particular, there is potentially a large error in the measured homogenizer valve gap. This section examines the possible magnitude of the systematic error in the stress-distribution function, and the changes in the strength-distribution function that are required to compensate for this error.

Disruption Calculation

As in section 6.2.5 above, disruption was calculated using Eq. (6.20), together with Eqs (6.22) and (6.3). Strain rate was calculated using Eq. (6.4)

$$\alpha = \frac{Q}{4\beta\pi r_i h^2} \tag{6.4}$$

and the parameter values in Table 6.1. However, the dependence of valve-gap on operating pressure was described using the laminar relationship of Eq. (3.2) rather than the measured dependence given in Table 3.1.

$$\Delta P_L = f_L \frac{\rho}{2}\left[\frac{Q}{2\pi r_i h}\right]^2 + \frac{6\mu Q}{\pi h^3}\ln\left[\frac{r_e}{r_i}\right] + \frac{54\rho}{70}\left[\frac{Q}{2\pi r_e h}\right]^2 \qquad (3.2)$$

Regression of the model (with modified dependence of valve-gap on homogenizer pressure) was conducted using the procedure given in section 6.2.6 to obtain the mean and standard deviation of the ultimate cell-wall tension distribution. The regressed dependence of disruption on operating pressure was almost identical to that seen in Fig. 6.6 (results not shown). The regressed means and standard deviations are given in Table 6.5. It is apparent that these regressed values are considerably different to both the measured values (section 6.2.1) and the values from the previous regression (section 6.2.6). This is a direct illustration of the redundancy in the wall-strength model: if one set of parameters changes, then others may change to compensate and provide an equally good description of the disruption data.

Table 6.5: Comparison of mean and standard deviation of ultimate cell-wall tensions at high-pressure homogenizer conditions determined from non-linear regression of disruption data.

	Mean Tension ($N\ m^{-1}$)		Standard deviation ($N\ m^{-1}$)	
	A	B	A	B
Calculated	8.6	13.6	3.3	4.3
Regressed (6.2.6)	12.6 ± 0.3	14.4 ± 0.4	4.3	8.5
Regressed (6.2.7)	19.6 ± 0.5	20.7 ± 0.6	7.6	14.9

Additional systematic errors within the stress-distribution (*e.g.*, the effect of cell-deformation in the homogenizer on the maximum cell-wall tension, and the use of a von Mises failure criterion to compare ultimate and maximum cell-wall tensions) also contribute to uncertainty in the stress-distribution and hence the strength distribution.

6.2.8 Further Discussion

The comparison of measured and regressed ultimate cell-wall tension distribution means and standard deviations in Table 6.5 highlights the sensitivity of the numerical values within the disruption model presented in this thesis. It is possible that errors within the stress- and strength-distributions compensate to provide the reasonable predictions shown in section 6.2.5, as changes in the stress-distribution are accompanied by significant changes in the strength-distribution as shown in Table 6.5. Although large uncertainties in

the true numerical values of the stress- and strength-distributions parameters (determined within this thesis) still remain, significant advances in the understanding of the disruption process have been made. Independent determination of the stress- and strength-distributions provides a mechanistic basis for the disruption process. The model parameters have direct physical meaning allowing them to be measured and also making extrapolation to different homogenizer systems applicable. Redundancy in the original formulation of the wall-strength model has been reduced to the uncertainty in the numerical values within the model. Potentially, the uncertainty could be reduced by further work, for example, by using a homogenizer with fixed orifice dimensions (such as the CSL disrupter in section 1.2.1) where more accurate calculations of fluid velocities and strain rates can be made.

It is highly significant that micromanipulation analysis showed that cells from experiment A had a lower mean ultimate cell-wall tension than cells from experiment B, whereas regression showed that both tensions were very similar (Table 6.4). An explanation for this observations is whilst both cell-walls were of similar thickness and contain similar glucan contents, experiment B's cell-wall glucan was more highly crosslinked than experiment A's. Micromanipulation reflected large differences between the ultimate cell-wall tensions, due to the difference in crosslinking. During homogenization, both crosslinked and uncrosslinked glucans contribute to ultimate cell-wall tension, and hence little difference between ultimate cell-wall tension was observed. Thus, whilst cell wall crosslinkage is important for the cell in its normal environment (to prevent cell lysis due to turgor pressure) and during slow deformation processes (micromanipulation) it is not the only contributor to cell strength during homogenization (as crosslinked and un-crosslinked cell-wall glucans will contribute to the mechanical strength). During homogenization, cell-wall thickness and chemical composition (*e.g.*, glucan content for yeast cells) will be the primary determinates of cell strength, with crosslinkage playing only a minor role.

Regression analysis found that cells from experiment B had a much larger standard deviation than the measured value. This large standard deviation may be due to a non-uniform cell population (*e.g.* a bimodal distribution). Whilst disruption is adequately modelled with a unimodal population with a large ultimate cell-wall tension variance, it would be more physically meaningful to model the cell population with a bimodal distribution (Middelberg (1992)).

Comparison of predicted and observed homogenate cell size-distributions provides excellent supporting evidence for the predictive modeling in this chapter. However, these homogenate distributions are convoluted by cell ghosts (cells with a ruptured wall that remains intact) and smaller pieces of cell debris that cannot be removed prior to size analysis. Alternative methods of obtaining a homogenate cell size distribution are available (*e.g.*, image analysis coupled with cell integrity staining). However, convolution is only significant at the lower end of the particle size-distribution, and electronic sensing zone particle size analysis (such as the Coulter Multisizer that was used in this thesis) is likely to be more reproducible. Cell clumps (experiment B, Fig. 5.16) present a more important cell sizing problem. These clumps will cause disruption efficiency to be over-predicted at low homogenizer pressures (due to an artificially high fraction of large cells in the measured cell size-distribution). Breakup of the clumps will add cells to the homogenate cell size-distribution that will convolute the distribution in the same way that cell debris does. Care must taken to ensure that accurate cell size-distributions are used, that do not contain cell clumps.

Measurement of the cells' equivalent spherical diameter was adequate for the cells used in this thesis as they were highly spherical. However, for non spherical cells such as *E. coli* rods or budding yeast cells, further information of cell dimensions and rather than simply their equivalent spherical diameters will be required to model the cell-disruption process.

6.3 Multiple Disruption Events

Multiple disruption events imply that the cell suspension is exposed to disruptive forces more than once. Reasons for cells being broken in multiple disruption events include the random distribution of disruptive forces, cell fatigue (*e.g.*, multiple homogenizer passes) or increased disruptive forces in subsequent disruption events (*e.g.*, valve inlet region followed by impinging jet disruption).

6.3.1 Modeling Multiple Disruption Events

The wall-strength model has been extended to allow prediction for multiple homogenizer passes (Middelberg, 1992). With a probability of disruption $f_D(S)$, then $1 - f_D(S)$ is the probability of surviving one homogenizer pass. Eq. (6.24) then gives the fraction of cells of strength S not disrupted, $d\phi(S)$.

$$d\phi(S) = 1 - dD(S) = \left[1 - f_D(S)\right] f_S(S) dS \tag{6.24}$$

The probability of surviving N homogenizer passes is $(1 - f_D(S))^N$. The fraction of cells of strength S surviving N homogenizer passes is given by Eq. (6.25).

$$d\phi(S) = \left[1 - f_D(S)\right]^N f_S(S) dS \tag{6.25}$$

Integration of Eq. (6.25) provides the total fraction of cells that are not disrupted in the homogenizer. Thus, the total disruption for N homogenizer passes is provided by Eq. (6.26).

$$D = 1 - \int_0^\infty \left[1 - f_D(S)\right]^N f_S(S) dS \tag{6.26}$$

Equation (6.26) reduces to Eq. (6.2) for one homogenizer pass (N = 1). If the stress-distribution is different for each disruptive event, Eq. (6.26) becomes

$$D = 1 - \int_0^\infty \left[1 - f_D(S)_1\right]\left[1 - f_D(S)_2\right] \ldots \left[1 - f_D(S)_N\right] f_S(S) dS \tag{6.27}$$

For multiple homogenizer passes through the homogenizer valve-inlet region at a fixed operating pressure, Eq. (6.26) is applicable. However, with a unit step stress-distribution function, Eq. (6.26) predicts that cell disruption will not increase with subsequent homogenizer passes. This prediction is, however, at variance with the majority of experimental observations (section 1.2.2). The inconsistency is due to simplifications in Eq. (6.26), including the neglect of process variations (appendix A2) and cell fatigue (appendix A4). When cell fatigue is important, the cell strength-distribution is not constant, but is dependent on the stress-history or previous disruption events:

$$f_S = f(S,N) \tag{6.28}$$

Equation (6.27) is still applicable for the calculation of the fraction of unbroken cells that will be disrupted in a given disruption event, by replacing the cell-strength distribution function with the stress-history-dependent cell-strength distribution:

$$D_N = \int_0^\infty f_D(S)_N f_S(S,N)dS \tag{6.29}$$

The total disruption after a single disruption event is the disruption efficiency of that event:

$$D(1) = D_1 = \int_0^\infty f_D(S)_1 f_S(S,1)dS \tag{6.30}$$

The fraction of cells that survive this disruption event is $(1 - D(1))$, and hence the increase in disruption after a second disruption event is:

$$D(2) - D(1) = (1 - D_1)D_2 \tag{6.31}$$

Extending Eq. (6.31) to N disruption events and rearranged to give the total disruption achieved after N disruption events gives:

$$\begin{aligned} D(N) &= D(N-1) + (1 - D(N-1))\int_0^\infty f_D(S)_N f_S(S,N)dS \\ &= \sum_{i=1}^{N} (1 - D(i-1))\int_0^\infty f_D(S)_i f_S(S,i)dS \end{aligned} \tag{6.32}$$

To apply Eq. (6.32), the stress-history-dependence of the cell-strength distribution is required. This requires a significant endeavour that is beyond the scope of this thesis. Specifically, further theoretical and/or experimental analysis is required. A theoretical

analysis would require investigation of a mechanistic cell wall model (with a representative cell-wall material such as a bonded-fibre-fabric) and the effects of repeated stress application on cell-wall properties.

However, for purely illustrative purposes, a contrived approach is used here to model the stress-history-dependent cell-strength distribution and hence multiple disruption events. By assuming that the cell strength distribution is independent of the number of homogenization events (Eq. (6.33)), Eq. (6.32) can be used to model multiple-disruption-event disruption-efficiency.

$$f_S(S,N) = f_S(S,0) \tag{6.33}$$

The following section (6.3.2) provides illustrative results multiple pass valve-inlet region disruption. Section 6.3.3 then considers combined valve-inlet and impinging-jet region cell-disruption. However, these sections are only intended to illustrate the modeling process, as further work is required to characterise the various process variations and the stress-history-dependence of the cell-strength distribution before accurate modeling can be conducted.

6.3.2 Multiple Pass Valve-Inlet Region Disruption

Single pass valve-inlet region cell-disruption was modelled in section 6.2. Multiple pass disruption is modelled using Eqs (6.20) and (6.32), which reduces to Eq. (6.34) with the assumed stress-history-dependence of the cell-strength distribution of Eq. (6.33).

$$D(N) = 1 - \sum_{i=1}^{n\,channels} \left\{1 - F_S\left(T(\alpha, d_i)\right)\right\}^N f_V(d_i) \tag{6.34}$$

Essentially, Eq. (6.34) assumes that disruption is first order for cells of a given diameter, with the disruption rate dependent on cell diameter. Figure 6.7 compares calculated multiple-pass disruption (Eq. (6.34), with the stress- and strength-distribution parameters of section 6.2.1), experimental results, and predicted disruption for a first-order disruption process. Although disruption efficiency for experiment A is significantly over-predicted, the qualitative observation that overall disruption is almost a first-order process is supported (due to the relatively narrow size-distribution). For experiment B, disruption

does not follow first-order kinetics, which is well predicted both qualitatively and quantitatively (due to the much wider size-distribution). It is concluded that cell-disruption processes will approach first-order kinetics for a "uniform" cell-population (*e.g.*, for cells with a narrow size distribution).

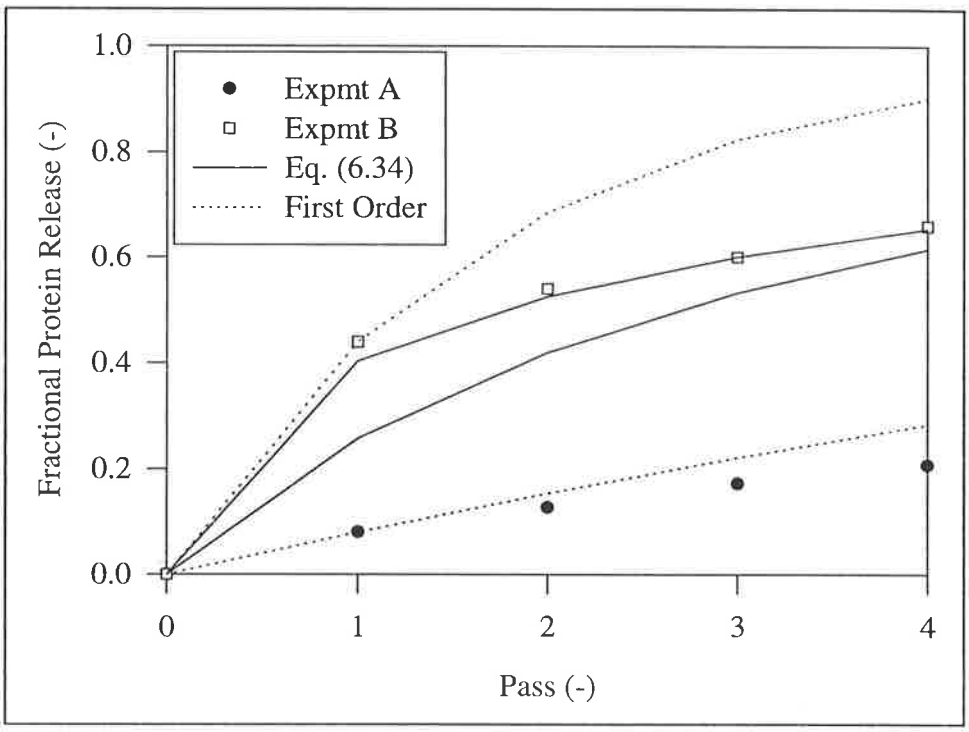

Figure 6.7: Comparison of predicted multiple pass disruption (Eq. (6.34)), observed multiple-pass disruption, and multiple pass disruption expected for a first-order process. Homogenizer operating pressure of 56 MPa.

6.3.3 Combined Valve-Inlet and Impinging-Jet Region Disruption

For the APV-Gaulin 15M high-pressure homogenizer fitted with the cell-disruption valve assembly, cell-disruption occurs in both the valve-inlet and impinging-jet regions (chapter 2). A single pass through this valve assembly represents two sequential disruption events: valve-inlet disruption followed by impinging-jet disruption. Equation 6.31 is rearranged to calculate the overall disruption efficiency after such a two-stage process:

$$D = D_I + (1 - D_I)D_J \tag{6.35}$$

Valve-inlet region cell-disruption was examined in section 6.2, and calculated using Eq. (6.20). The impinging jet region is considerably more complex to analyse and model than the valve-inlet region. In the valve-inlet region (particularly for the chamfered valve-inlet

on the cell-disruption valve-seat), there is almost plug-flow into the valve gap, with all cells experiencing the same velocity and strain-rate profile. This uniformity results in the unit-step stress-distribution function of Eq. (6.5) for spherical cells. However, in the impinging-jet region, the maximum strain rates and fluid velocities around the cell are not uniform. Figure 4.14 shows that cells close the jet's plane of symmetry will pass through regions of higher strain rates with longer residence times than cells at the outer edge of the jet. Cells are decelerated as they enter the stagnation region and accelerated again as they leave it. Also, large cells almost certainly collide with the impact ring, which may result in their breakage. Hence, a complete model for the impinging-jet region must consider the magnitude, distribution and interaction of stresses resulting from deceleration, possible collision, and subsequent acceleration.

To provide illustrative results, this section assumes that combined valve-inlet and impinging-jet cell-disruption occurs in only two disruption events: cell acceleration in the valve-inlet and cell collision in the impinging-jet. Although this does not accurately reflect the physical processes that occur during cell-disruption by jet-impingement, it illustrates modeling applicable to sequential disruption events of unequal magnitude.

Section 6.2.1 developed the stress and strength distribution formulations relevant to valve-inlet region cell-disruption. In this section, a similar procedure is followed to develop stress- and strength-distribution functions applicable to the cell-collision process.

Cell Collision Stress-Distribution Function

Cell collision was investigated in section 4.4 by considering the collision event as an energy process. If the kinetic-energy loss of the cell after collision was greater than the work to rupture the cell, it was assumed that cell would rupture. For a 56 MPa homogenizer operating pressure, the mean kinetic energy loss for a cell after collision was calculated as

$$\overline{KE}(d) = 1.69 \times 10^{9} d^{3.61} \tag{4.54}$$

with a standard deviation of

$$\sigma_{KE}(d) = 0.24 \overline{KE}(d) \tag{4.55}$$

Hence, the "kinetic-energy-distribution" function for the homogenizer is determined by integration of a Gaussian distribution.

$$f_D(KE) = 1 - \int_0^{KE} \frac{1}{\sigma_{KE}(d)\sqrt{2\pi}} \exp\left[-\frac{\left(KE - \overline{KE}(d)\right)^2}{2\sigma_{KE}(d)^2} \right] dKE \qquad (6.36)$$

As with the valve-inlet's tension-distribution function, the impinging jet's kinetic-energy-distribution function of Eq. (6.36) is dependent on cell diameter.

Cell Collision Strength-Distribution Function

The cell strength-distribution for cell collisions can be represented by a Gaussian distribution (Eq. (6.6)). Mean and standard deviation for the two cultures examined in chapter 5 is given in Table 5.4. Correction of the values in Table 5.4 is required to account for the difference in cell loading time in the homogenizer. It was assumed that only the mechano-chemical correction factor of Eq. (6.10) was required to translate the micromanipulation values to the high pressure homogenizer (as work to failure is a property of the whole cell, compared with tension, which is based on a unit length of cell-wall). Translated work values (using Eq. (6.10)) are given in Table 6.6.

$$f_S(KE) = \frac{1}{\sigma_{KE}\sqrt{2\pi}} \exp\left[\frac{-\left(KE - \overline{KE}\right)^2}{2\sigma_{KE}{}^2} \right] \qquad (6.37)$$

Table 6.6: Mean and standard deviation of work to cell failure from Table 5.4 translated to high pressure homogenizer conditions.

Experiment	Mean Work (J)	Standard deviation (J)
A	2.0×10^{-10}	1.3×10^{-10}
B	3.2×10^{-10}	1.3×10^{-10}

Illustrative Results

Disruption in the impinging jet region was calculated by Eq. (6.38),

$$D_J = \int_0^{d_{max}} f_V(d) \int_0^{\infty} f_D(KE).f_S(KE).dKE.dd \qquad (6.38)$$

with the kinetic-energy-distribution function of Eq. (6.36), cell strength-distribution function of Eq. (6.37), the cell size-distribution after valve-inlet disruption (Eq. (6.21)), and

an assumed stress-history-dependence of cell strength-distribution (Eq. (6.33)). Figure 6.8 shows the calculated cell size-distributions after valve-inlet and combined valve-inlet and impinging-jet disruption. Calculated impinging-jet disruption efficiency was 17%, resulting in an increase in total disruption from 26% (after the valve-inlet) to 38% (after the impinging-jet).

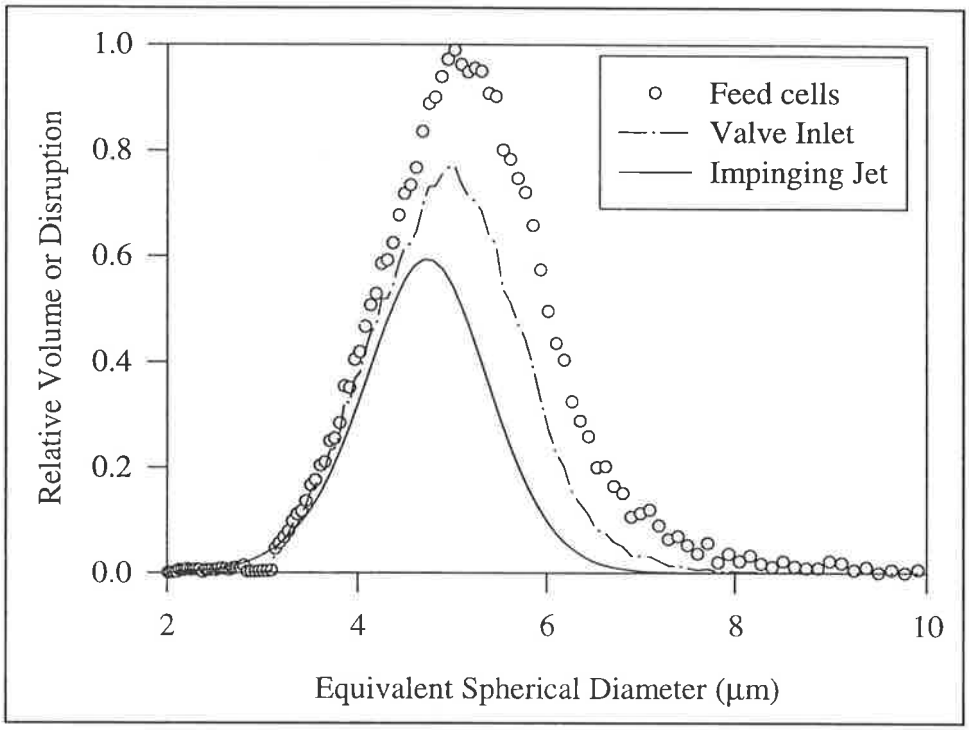

Figure 6.8: Comparison of feed cell-size distribution with predicted homogenate cell-size distributions after valve-inlet disruption and valve-inlet with impinging-jet disruption.

6.3.4 Multiple Pass Impinging-Jet Region Disruption

The results presented in Fig. 6.8 (for a single homogenizer pass with multiple disruption events) are purely illustrative rather than an accurate representation of the combined valve-inlet region and impinging-jet disruption processes. However, they demonstrate the approach required to model this complicated process. Further work is required to characterise the stress variations in the impinging-jet region and the stress-history-dependence of the cell strength-distribution before more accurate modeling can be provided for combined valve-inlet and impinging-jet disruption. This is particularly important for modeling of multiple pass disruption efficiency with an impinging jet.

6.4 Simplified Disruption Modeling

To predict or calculate cell disruption efficiency during high-pressure homogenization, the models developed in sections 6.2 and 6.3 require:

1. the cell strength-distribution, obtained from micromanipulation experiments,
2. the cell size-distribution, measured in this thesis with a Coulter Multisizer, and
3. the homogenizer stress-distribution, determined from an analysis of fluid mechanics within the cell-homogenizer system.

However, obtaining these three distributions is likely to be difficult in most practical situations. It is plausible to determine the homogenizer stress distribution function for any given homogenizer, and this information could ultimately be supplied directly by homogenizer manufacturers. Unfortunately, characterisation of the cell-strength distribution through micromanipulation is not likely to be readily available to a production facility. Even accurate measurement of the cell-size distribution may be difficult (or costly) to obtain. In this section, simplified models are presented that can be used in practice if cell size distribution and/or cell strength distribution cannot be measured directly.

6.4.1 Size Distribution Model

In the absence of a measured cell-strength distribution, but with a measured cell-size distribution, the wall strength model (with the independent homogenizer stress distribution of Eq. (6.5) and the cell strength distribution of Eq. (6.6)) is still applicable. The mean and standard deviation of the ultimate cell-wall tension distribution can then be determined by a non-linear regression analysis of disruption data. This approach was outlined in sections 6.2.6 and 6.2.7. Whilst regressing for the cell-strength distribution parameters prevents the model from being truly predictive, the model is still likely to be practically useful.

6.4.2 Pressure Gradient Model

In many situations, neither measured cell-strength nor cell-size distributions will be available. Such is the case for the disruption data presented in chapter 2. This makes application of the stress- and strength-distribution functions developed in this thesis impossible to apply. A simplified model that does not require cell-strength or cell-size distributions is required. Homogenizer operating pressure and impinging jet stagnation pressure have been used as correlating variables for cell-disruption (section 1.2.2). However, these variables are not able to simultaneously describe the effect of valve design and homogenizer operating variables on disruption efficiency. Pressure gradient is likely to be a suitable variable to describe valve-inlet and impinging-jet disruption (and hence the effects of valve design and homogenizer operating variables) and is used in this section.

Model Development

The dependence of disruption-efficiency on pressure-gradient is likely to follow a sigmoidal functional form. A suitable sigmoidal function is likely to be:

$$D = 1 - \exp\left\{-\left(\frac{\frac{dP}{dx}C}{A}\right)^{B}\right\} \tag{6.39}$$

where A and B are empirical constants. Equation (6.39) will apply to disruption in both the valve-inlet and impinging-jet regions. Parameter C is required to account for differences in mechanism and hence disruption-efficiency in these two regions. By making C unity in the valve-inlet region, the value of C in the impinging-jet region will depend on the microorganism being modelled. For example, for a given pressure gradient, yeast disruption efficiency is likely to higher in the impinging-jet than valve-inlet region, due to additional disruption caused by cell-solid collisions. By analogy with Eq. (6.6.35) the total disruption achieved after one homogenizer pass is:

$$D = \left[1 - \exp\left\{-\left(\frac{\frac{dP}{dx_I}}{A}\right)^{B}\right\}\right] + \left[\exp\left\{-\left(\frac{\frac{dP}{dx_I}}{A}\right)^{B}\right\}\right]\left[1 - \exp\left\{-\left(\frac{\frac{dP}{dx_J}C}{A}\right)^{B}\right\}\right] \tag{6.40}$$

Parameter C was determined from experimental results. The dependence of baker's yeast disruption efficiency (at 56 MPa) is shown in Fig. 6.9 (data from experiment A, chapter 2). Impinging jet region disruption efficiency is calculated by rearranging Eq. (6.35):

$$D_J = \frac{D - D_I}{1 - D_I} \tag{6.41}$$

Impinging jet disruption efficiency is equal to the valve inlet disruption efficiency when the impinging-jet pressure-gradient is approximately half of the valve-inlet pressure-gradient. Hence, parameter C in Eq. (6.40) is 2 for yeast. This value is greater than unity due to disruption occurring as yeast cells collide with the impact ring. Repeating this procedure for *E. coli*, parameter C in Eq. (6.40) is 0.5 (Fig. 6.9, data from experiment B1, chapter 2).

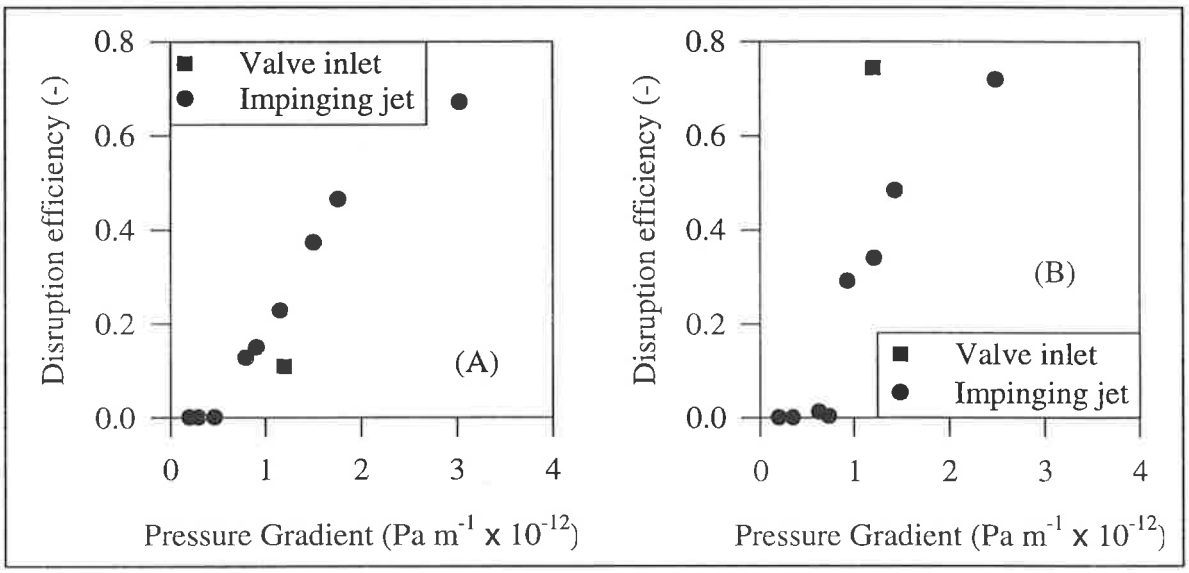

Figure 6.9: Dependence of impinging-jet disruption-efficiency for baker's yeast (A) and stationary *E. coli* (B) on impinging-jet pressure-gradient. Disruption efficiency in the valve-inlet, at the same operating pressure (56 MPa), is shown for comparison.

Model Results

A spreadsheet package (Microsoft Excel for Windows 95) was used to perform a non-linear regression of the model (Eq. (6.40)) to the experimental data. Regressed values for parameters A and B are given in Table 6.7. A parity plot, comparing regressed and experimental disruption for each of the four cultures examined is given in Fig. 6.10. Equation (6.40) is able to describe disruption variability due to both cell-culture and homogenizer system changes. Although it is an empirical model, the parameters A and B do have physical meaning. Parameter B is a measure of the spread in pressure-gradient

required to disrupt cells, and reflects the spread in cell-strength and cell-size distributions. Parameter A is a measure of the pressure-gradient required to achieve a given level of cell disruption, and reflects the average of the cell strength- and cell size-distributions. Parameter C accounts for differences in disruption mechanism in the valve-inlet and impinging-jet regions.

Table 6.7: Parameters in Eq. (6.40) to describe the effect of pressure-gradient on cell-disruption efficiency for four different cultures.

Culture (chapter 2)	A (Pa m^{-1} $\times 10^{-12}$)	B (–)
Baker's yeast	4.4	1.6
Brewer's yeast	2.2	1.9
Stationary *E. coli*	0.95	1.0
Growth Phase *E. coli*	0.37	1.1

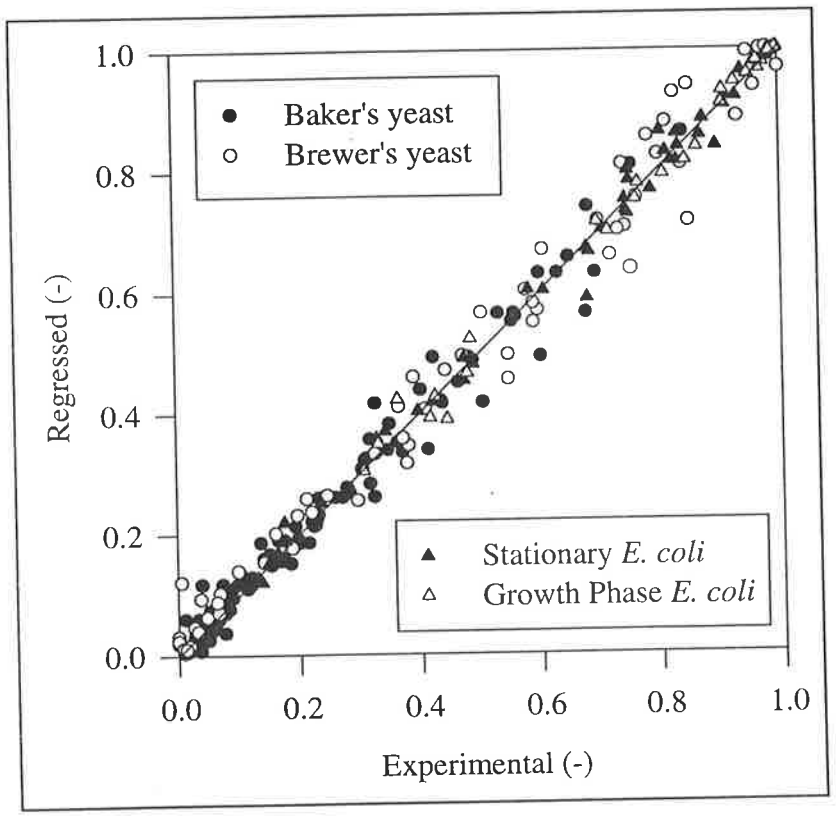

Figure 6.10: Parity plot comparing regressed and experimental disruption efficiency for yeast and *E. coli* cultures from chapter 2 regressed to Eq. (6.40) with parameters in Table 6.7.

6.5 Summary

In this chapter, the results of chapters 4 and 5 were used to formulate truly independent homogenizer-tension and cell-strengthdistributions. Disruption in the valve-inlet region was calculated as:

$$D = \sum_{i=1}^{n\,channels} F_S\left(T(\alpha, d_i)\right) f_V(d_i) \tag{6.20}$$

where

$$F_S(T) = \int_0^T \frac{1}{\sigma\sqrt{2\pi}} \exp\left[-\frac{(T-\bar{T})^2}{2\sigma^2}\right] dT \tag{6.22}$$

$$T(\alpha, d) = \frac{\rho\alpha^2 d^3}{3.6\times10^{-2}\left(\frac{\rho\alpha d^2}{2\mu}\right)^{0.68}} \tag{6.3}$$

$$\alpha = \frac{Q}{4\beta\pi r_i h^2} \tag{6.4}$$

and $f_V(d)$ is the cell size distribution. Parameter values for the cell-disruption valve-seat and an APV-Gaulin 15M homogenizer are given in Table 6.1. Measured cell-strength distribution parameters (corrected for homogenizer conditions) are given in Table 6.3.

Table 6.1: Parameter values used to calculate maximum cell-wall tension for the valve-inlet region of a cell-disruption valve-seat in an APV-Gaulin 15M homogenizer.

Parameter	Value
Q	4.6×10^{-5} m^3 s^{-1}
β_I	2.1
r_i	0.00385 m
h	37 P$^{-0.35}$ μm
ρ	1000 kg m^{-3}
μ	1×10^{-3} Pa s

Table 6.3: Mean and standard deviation of ultimate cell-wall tensions translated to high-pressure homogenizer conditions.

Experiment	Mean Tension (N m^{-1})	Standard deviation (N m^{-1})
A	8.6	3.3
B	13.6	4.3

Homogenate size distributions were calculated using Eq. (6.21).

$$f_V(d)_{homogenate} = \left\{1 - F_S\left(T(\alpha,d)\right)\right\} f_V(d)_{feed} \tag{6.21}$$

Cell disruption efficiency and homogenate cell-size distributions were calculated for the two cell cultures described in Table 6.3. These results provided the first truly *a priori* predictions of cell disruption efficiency in a homogenizer system that do not rely in any way on the regression of disruption data for model parameters.

Regression analysis showed that there is considerable uncertainty in the parameters used to calculate the cell-strength distribution (due to uncertainties in the extrapolation of micromanipulation results to high-pressure homogenization) and the homogenizer stress-distribution (due to uncertainty in the dependence of valve-gap on operating pressure).

Multiple disruption events were then considered. However, further work is required to characterise process variations and cell-wall fatigue effects that contribute to increased disruption after repeated homogenization events.

A simplified disruption model that avoids the need for experimental characterisation of the cell-size distribution and cell-strength distribution was developed. Disruption was correlated with valve-inlet and impinging-jet pressure gradients,

$$D = \left[1 - \exp\left\{-\left(\frac{\frac{dP}{dx}_I}{A}\right)^B\right\}\right] + \left[\exp\left\{-\left(\frac{\frac{dP}{dx}_I}{A}\right)^B\right\}\right]\left[1 - \exp\left\{-\left(\frac{\frac{dP}{dx}_J{}^C}{A}\right)^B\right\}\right] \tag{6.40}$$

where A and B are empirical constants for a given culture and C reflects different disruption mechanisms in the valve-inlet and impinging-jet regions. Parameter C was found to be 2 and 0.5 for yeast and *E. coli* cells, respectively.

Chapter 7

Summary Discussion

Recombinant DNA techniques have resulted in a rapid growth in the production of useful biochemicals within host microorganisms. The most widely used hosts for industrial application are *Escherichia coli* and *Saccharomyces cerevisiae*. These two organisms generally produce intracellular products, and require a cell disruption technique to release the product for subsequent concentration and purification.

One of the major factors influencing the choice of a cell-disruption technique is the aim to release the maximum amount of product at the lowest cost. This process of optimisation is best conducted mathematically, at the design stage of a process. To conduct a meaningful mathematical optimisation, sound mathematical models of process units are required. The mathematical models that have been developed for high-pressure homogenization thus far have key deficiencies. Kinetic rate models require empirical coefficients, which depend on properties of the feed cells and the homogenizer system in an undetermined fashion. Alternative models attempt to separate system and culture specific factors that affect disruption, and are developed with a mechanistic basis for the disruption process. These alternative models include the turbulence model (Eq. (1.5)), the extensional shear model (Eq. (1.8)) and the wall-strength model (Eq. (1.9)). Of these models, it is only the wall strength model that has been demonstrated for quantitative disruption modeling. In the development of the wall-strength model, Middelberg (1992) concluded that obtaining truly general expressions for the stress and strength distributions within the model was unrealistic and that approximate distributions would suffice. He also deemed that direct and independent measurement of the distributions was impractical, and resorted to empirical approximations. However, the use of empirical approximations resulted in a model that is over-specified and shows parameter redundancy. As a result, the empirical

functions are not truly independent, even though they are able to describe and even predict cell disruption efficiency for a specified homogenizer system and microorganism.

The aim of this thesis was to independently characterise homogenizer stress and cell strength distributions and to use these distributions to model cell breakage during homogenization. However, to determine these distributions, fundamental knowledge of the homogenization process is required. Specifically, this thesis aimed to determine:

- the nature of the stresses that cause cell breakage,
- the magnitude of these breakage stresses,
- the characteristics of the microorganism that resist disruption,
- the strength of microorganisms,
- the dependence of cell strength on the rate of applied stress,

and to use this information to characterise cell-strength and homogenizer-stress distributions, and hence model the cell disruption process.

It is apparent from a review of the literature and the experiments in chapter 2 that disruption occurs in two distinct regions of the homogenizer:

- Valve Inlet region
- Impinging Jet region

The relative importance of each region is dependent on both valve design and microorganism. Overall disruption efficiency increases as the impact ring diameter is decreased. The impact effect is more important for yeast than *E. coli*: with the standard cell disruption valve design, 80% of overall yeast disruption occurs at the impact ring, whilst for *E. coli*, only 20% of overall disruption occurs at the impact ring.

However, these observations do not define the actual stresses that cause cell breakage. To determine the nature of the stresses, a fundamental investigation of homogenizer fluid and particle mechanics was required. Chapter 3 examined fluid mechanics within the APV-Gaulin 15M homogenizer system. The homogenizer valve assembly was divided into two regions for analysis: the "valve inlet" region (where fluid is accelerated radially into and passes through the gap between the valve and seat) and the "impinging jet" region (where the fluid forms a radial jet that is subsequently stagnated at the impact ring).

Experimental measurements of homogenizer valve gap and pressure transients were obtained using a sensitive LVDT and a pressure transducer. The measured dependence of homogenizer valve gap on mean homogenizer pressure was described by Eq. (7.1) for the APV-Gaulin cell disruption valve seat,

$$h = 37 \times 10^{-6} \left(P \times 10^{-6} \right)^{-0.35} \tag{7.1}$$

and was in excellent agreement with semi-analytical laminar flow predictions. Numerical simulation of steady-state laminar flow within the valve inlet region was conducted using the PHOENICS finite-volume computational-fluid-dynamics code. Simulation revealed that no flow separation or cavitation occurred within the homogenizer valve gap under standard homogenizer operating conditions. Numerical results were also used to determine a length scale proportionality constant (β_I) which was used in Eq. (3.25) to calculate the effect of homogenizer operating conditions on the radial pressure gradient as the fluid accelerates into the valve gap.

$$\frac{dP}{dy} = \frac{\rho Q^2}{8\beta_I \pi^2 r_i^2 h^3} \tag{3.25}$$

For the chamfered cell disruption valve seat, the length scale proportionality constant was found to be 2.1.

Numerical simulation was also conducted for the homogenizer's impinging radial jet. Laminar and turbulent flow situations were conducted and compared. Experimental measurement of the stagnation region width of the impinging jet provided evidence that the impinging jet is laminar. Laminar flow was confirmed by the correlation of cell disruption efficiency with jet stagnation pressure: an excellent correlation was observed with laminar P_S, compared with the poor correlation observed with a turbulent P_S. Extreme pressure gradients were seen within the jet's stagnation region, and were described by Eq. (3.54).

$$\frac{dP}{dx} = \frac{\sqrt{8} P_S^{1.5} \pi r}{Q(r) \sqrt{\rho} \beta_J} \tag{3.54}$$

The impinging jet length scale proportionality constant (β_J) was found to be 0.9.

Chapter 4 surveyed proposed physical mechanisms (or the nature of the stresses that cause cell breakage). Plausible candidates were identified as turbulence, cell-solid interactions

and extensional flow fields. As chapter 3 had found that turbulence does not occur in the homogenizer system examined in this thesis, it was not given further consideration. The interaction between cells and fluid was examined for straining flow. After ruling out a viscous mechanism, simulations were conducted to calculate the tensions generated within a spherical cell's wall. Cell-wall tensions are produced by (predominantly inertial) pressure differences across the cell wall in the straining flow field, and, to a first approximation, are directly proportional to the pressure gradient within the straining flow field and the squared cell radius. The empirical dependence of a critical Weber number (calculated from maximum cell wall tension) on cell Reynolds number for a cell disruption valve seat was calculated as Eq. (4.44).

$$We = 9.0 \times 10^{-3} Re^{0.68} \tag{4.44}$$

Rearrangement of Eq. (4.44) gives the dependence of critical wall tensions on cell diameter and fluid strain rate:

$$T = \frac{\rho \alpha^2 d^3}{3.6 \times 10^{-2} \left(\frac{\rho \alpha d^2}{2\mu} \right)^{0.68}} \tag{6.3}$$

The interaction of cells within the homogenizer's impinging jet region was also examined in chapter 4. In addition to the straining flow described above, cell disruption was also found to be likely to occur due to direct collisions between cells and the impact ring. The collision effect is highly sensitive to cell size, with collision frequency and intensity increasing rapidly with cell diameter.

Equation (6.3) suggests that a primary characteristic of a microorganism that resists disruption in a straining flow field is some form of cell-wall tension. Chapter 5 presented an experimental investigation of the mechanical properties of yeast cells. Ultimate cell-wall tensions were calculated from the analysis of micromanipulation experiments. Micromanipulation involved the squeezing of individual cells between a fibre optic probe and glass microscope slide up to catastrophic cell-wall failure. Ultimate cell-wall tensions were calculated from measurement of the force applied to the cell and the degree of cell compression. These tensions were found to be normally distributed and independent of the cell diameter.

Ultimate cell-wall tensions determined by micromanipulation were applicable for the relatively slow loading and bursting conditions of the micromanipulation experiments. The micromanipulation ultimate cell-wall tensions were extrapolated to rapid loading conditions within the homogenizer by incorporating the mechano-chemical effect of loading rate on bond failure stress, and correcting for the decrease in microfibril density that occurs due to cell wall extension during micromanipulation. It was found that the ultimate cell wall tension under homogenizer conditions was 2.5 times greater than the ultimate cell-wall tension determined by micromanipulation.

With the dependence of ultimate cell-wall tension on cell size and fluid strain rate in the homogenizer (Eq. (6.3)) and the strength characterisation of cell populations, predictive modeling of disruption efficiency within the valve-inlet region was able to be conducted. The Gaussian cell strength-distribution was modelled using measured strength-distribution parameters determined by the translation of micromanipulation data given in Table 6.3:

$$f_S(T) = \frac{1}{\sigma_T \sqrt{2\pi}} \exp\left(-\frac{(T - \bar{T})}{2{\sigma_T}^2} \right) \tag{6.6}$$

Table 6.3: Mean and standard deviation of ultimate wall tensions translated to high-pressure homogenizer conditions.

Experiment	Mean Tension (N m^{-1})	Standard deviation (N m^{-1})
A	8.6	3.3
B	13.6	4.3

The dependence of maximum cell-wall tension on cell diameter and homogenizer strain rate suggested the following homogenizer tension-distribution function:

$$f_D(T) = \begin{cases} 1 & \text{if } T \le T(\alpha, d) \text{ from Eq.(6.3)} \\ 0 & \text{if } T > T(\alpha, d) \text{ from Eq.(6.3)} \end{cases} \tag{6.5}$$

As this tension distribution function is dependent on cell size, homogenate size distributions were calculated using Eq. (6.21).

$$f_V(d)_{homogenate} = \left\{ 1 - \int_0^{T(\alpha,d)} f_S(T).dT \right\} f_V(d)_{feed} \tag{6.21}$$

Total disruption achieved was calculated using the integral of Eq. (6.19):

$$D = \int_0^{d_{\max}} \int_0^{T(\alpha,d)} f_S(T).dT\, f_V(d).dd \tag{6.19}$$

which was represented as a discrete summation to facilitate the use of the discrete cell size distribution obtained from the Coulter Multisizer particle size analyser used in this thesis:

$$D = \sum_{i=1}^{n\,channels} f_V(d_i) \int_0^{T(\alpha,d_i)} f_S(T).dT \tag{6.20}$$

Single-pass disruption efficiency and homogenate cell size distributions predicted by Eq. (6.20) and Eq. (6.21), respectively, were found to be in excellent qualitative and accepatable quantitative agreement with experimental measurements of cell disruption efficiency. These results represent a significant advance in homogenizer modeling: they are the first true *a priori* predictions of disruption efficiency and homogenate cell size distributions that do not rely in any way on the regression analysis of previous experimental disruption efficiency data.

Equation (6.20) was then extended to multiple disruption events, including multiple valve-inlet region passes and combined valve-inlet and impinging-jet disruption. It was found that cell-fatigue and process variations are likely to be contributing factors in multiple pass disruption efficiency. Due to the lack of characterisation of cell-fatigue and the complex interactions between cell-fatigue and process variations, illustrative modeling only was provided for multiple disruption events.

A simplified disruption model was also developed that avoided the need for experimental characterisation of the cell size-distribution and the cell strength-distribution. If cell size-distribution data is available, it was shown that Eq. (6.20) can be used to describe disruption data in the valve inlet region by regressing for the unknown cell strength-distribution parameters. For situations where neither cell size- or cell strength-distributions are available, a pressure-gradient disruption model was developed,

$$D = \left[1 - \exp\left\{-\left(\frac{\frac{dP}{dx}_I}{A}\right)^B\right\}\right] + \left[\exp\left\{-\left(\frac{\frac{dP}{dx}_I}{A}\right)^B\right\}\right]\left[1 - \exp\left\{-\left(\frac{\frac{dP}{dx}_J{}^C}{A}\right)^B\right\}\right] \tag{6.40}$$

where A and B are empirical constants for a given culture and C is a parameter to reflect the different disruption mechanisms in the valve inlet and impinging jet regions. Parameter C was found to take approximate values of 2 and 0.5 for yeast and *E. coli* cells, respectively. Although Eq. (6.40) is essentially an empirical model, it is able to describe the effects of valve-seat and impact-ring design on cell disruption efficiency. Also, the empirical culture parameters (A and B) have physical meaning and may be related to the cell strength and cell size distributions used to predict or calculate disruption in Eq. (6.20).

The development of the fundamentally-based predictions of cell disruption efficiency presented in this thesis is highly significant, as it may be readily and accurately extrapolated from the conditions for which it has been originally demonstrated. As an example, it accurately predicts that qualitative effect of variables that influence cell disruption efficiency:

- As operating pressure increases, fluid strain rate and velocity increase in the valve inlet region, resulting in increased critical cell-wall tensions and increased disruption efficiency. Similarly, strain rate and collision frequency and intensity also increase in the impinging jet region.

- Knife-edged seats will perform better than standard seats as they result in reduced valve-gap (lower frictional losses) with increased valve inlet strain rates and impinging jet stagnation pressures. Also, decreased impact distance results in increased stagnation pressure and disruption efficiency. However, the impinging jet region will be more important for effecting the disruption of (large) yeast cells than (smaller) *E. coli* cells.

- Disruption efficiency will increase with the number of homogenizer passes, due to a combination of process variations and cell wall fatigue. However, disruption efficiency is likely to asymptote below 100% it the maximum stresses generated are not large enough to damage all of the cells within the population (this will be particularly important for small cells or cells with very strong cell walls).

- Suspension temperature is only likely to have minimal influence on valve inlet region disruption efficiency (slightly higher valve gap with increased viscosity and hence lower disruption efficiency). However, the impinging jet stagnation pressure is approximately inversely proportional to $\mu^{2/3}$ (Eq. (3.48)) and hence increasing temperature (decreasing μ) will increase disruption efficiency.

- The effect of flow rate is generally likely to be small, but will depend on valve design. As an example, the valve-inlet region pressure-gradient is calculated for two homogenizer valve-seat designs (cell-disruption and square-edged) for different flow rates (centred around the APV-Gaulin 15M homogenizers standard flow rate). Pressure gradient was calculated using Eq. (3.25), valve gap was calculated using Eq. (3.2) for laminar flow, constants used in these calculations are given in Table 7.1 and results are shown in Fig. 7.1. For the valve seat with low frictional losses (cell-disruption) there is almost no dependence of pressure-gradient on flow-rate, with pressure-gradient increasing as flow-rate decreases. For the square-edged seat, the opposite is observed, and pressure-gradient increases with flow-rate. From Fig. 7.1 it is apparent that slight increases or decreases in disruption efficiency as flow rate increases can be observed, depending on valve design and flow-rate. This is due to the interaction between pressure, frictional losses, and fluid velocity. For efficient valve designs (with low frictional losses) disruption efficiency is expected to show a slight decrease as flow rate through the valve assembly is increased. Similar trends are expected for impinging-jet pressure-gradients.

Table 7.1: Parameters used to calculate pressure gradients (using Eqs (3.25) and (3.2) shown in Fig. 7.1).

Parameter	Cell disruption	Square edged
r_i	0.00385 m	0.0025 m
r_e	0.00425 m	0.0045 m
β_l	2.1	1.2
ρ	1000 kg m^{-3}	1000 kg m^{-3}
μ	0.001 Pa s	0.001 Pa s
P	56 MPa	56 MPa

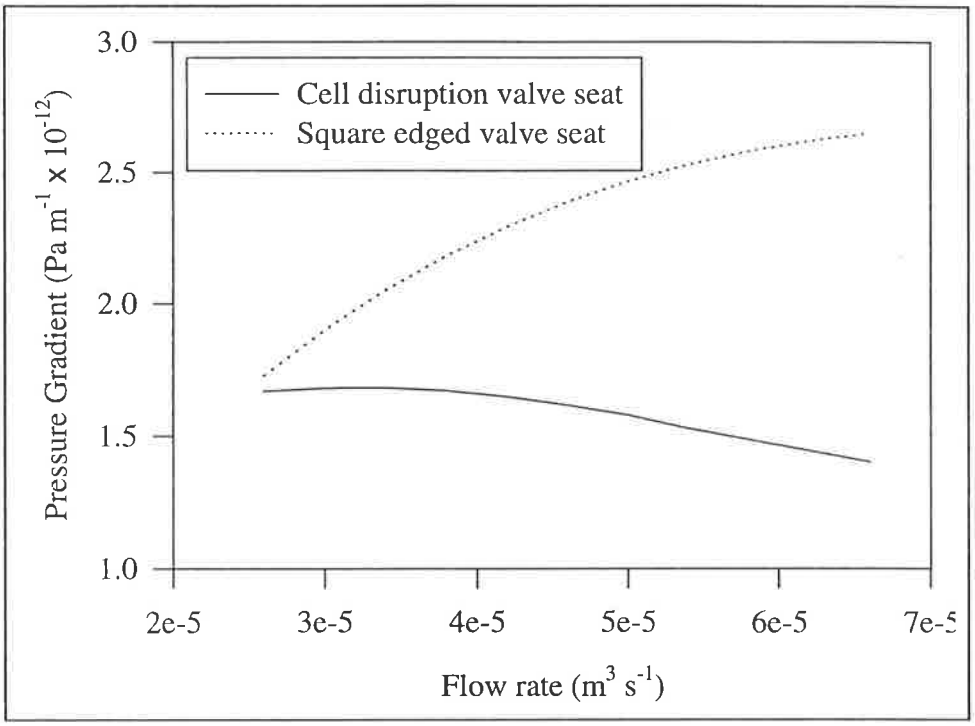

Figure 7.1: Dependence of valve-inlet region pressure-gradient on flow-rate for two valve seat designs.

- Microorganisms with thin cell walls will have lower failure tensions and hence be disrupted more easily than cells with thick walls, for equally sized cells. Thus, gram (-) bacteria are expected to be weaker than gram (+) bacteria. Rods will be more easily disrupted than cocci, due to their length. Similarly, large cells are more susceptible to disruption than small cells. Cells grown at high growth rates or in growth phase are both larger and have thinner walls than cells grown at low growth rates or in stationary phase, making them easier to disrupt.

These qualitative observations are all in agreement with observed experimental trends reviewed in section 1.2.2. Also, from the analysis in this thesis it is apparent that it will be extremely difficult to achieve complete cell disruption in a single homogenizer pass (as small, strong cells will require extremely harsh conditions to be disrupted). Single-pass disruption will always be more energy efficient than multiple pass disruption, unless cell fatigue is significantly more effective than for the cultures examined in this thesis.

The extrapolation of the predictions provided in this thesis can only be extended to new systems which are mechanistically similar to the system considered within this thesis. Further work is required to extrapolate the approach used in this thesis to new systems. The results of this thesis are limited to:

- spherical (yeast) cells. If non-spherical cells (such as *E. coli* rods or budding yeast cells) are to be modelled, the homogenizer tension distribution developed in chapter 4 must be modified to account for the effects of cell orientation on disruptive tensions and tension distributions. Also, if somewhat smaller cells are to be examined, the calculation of critical wall tensions in lower Reynolds number flows (where viscous shear stresses will be more effective than inertial pressure differences in effecting cell disruption) must be conducted.

- the valve inlet-region of an APV-Gaulin 15M homogenizer. If a different homogeniser system is used, that has different hydrodynamics (*e.g.* turbulent flow) then homogenizer stress distributions must be recalculated for the different hydrodynamics conditions. Only limited modeling of disruption efficiency in the impinging jet region was attempted, even though quantitative prediction was demonstrated.

- a single disruption event. Both cell fatigue and process variations contribute to the increase in disruption efficiency that occurs after multiple disruption events. Neither of these processes have been adequately characterised, and their complex interaction presents even further difficulties in the modeling of multiple disruption events.

The accuracy of the independently determined cell-strength and homogenizer-tension distribution is limited. In particular, the homogenizer-tension distribution is limited by the error in measured homogenizer valve gaps, which produces a potential error of as much as 40% in homogenizer pressure-gradients and maximum cell-wall tensions. The micromanipulation technique used to measure cell strength has various shortcomings which are predominantly related to difference in loading times between micromanipulation and homogenization.

In concluding, it is clear that the independent distributions developed in this thesis are capable of providing reasonable predictions of cell-disruption efficiency in a high-pressure homogenizer. These predictions are mechanistically based, and do not require any regression analysis of previous disruption data. Uncertainty in the accuracy of the parameters used to calculate disruption limits the accuracy of the predictions. In its present stage of development, there are still many limitations with the disruption model. These limitations may be removed through further work. Investigations that address some of the limitations and hence provide important areas for future research include:

- *Test applicability for a different homogenizer*

Ideally, this study would be repeated for a different homogenizer system, but with the same disruption mechanism. In particular, if a device with fixed orifice dimensions was used, some of the potential errors in the homogenizer tension distribution would be reduced.

- *Extend to different systems with different mechanisms*

In this thesis, only a limited analysis of the quantitative processes occurring in the impinging jet region was conducted. A more in-depth analysis of this region is warranted, particularly when considering the large disruption enhancements that can be achieved by including jet impinging in a homogenizer design. Also, homogenizer hydrodynamics and disruption processes may require investigation for different homogenizer systems where, for example, turbulence or cavitation produce significant amounts of cell breakage.

- *Extend to non-spherical cells*

This thesis was limited to the predictive modeling of spherical cells, with some empirical modeling of *E. coli* disruption efficiency. Given the importance of non-spherical cells such as *E. coli* rods in the production of recombinant proteins, characterisation of the tensions developed within the cell wall of non-spherical cells is an important extension to this work.

- *Characterise process variations*

Process variations contribute to multiple disruption event disruption efficiency and are difficult to accurately quantify. Further work would examine the magnitude of these variations, and also possibly how to reduce them to potentially increase disruption efficiency.

- *Improve measurement of cell wall strength*

The micromanipulation technique used to characterise the mechanical properties of the cell wall incorporates potential errors due to the need to extrapolate the micromanipulation results to much more rapid loading conditions. It is not likely to be feasible to develop an experimental technique that is able to replicate the rapid homogenizer loading conditions. An alternative approach would be to characterise the cell wall (*e.g.* as a bonded fibre fabric) and combine numerical simulation of the wall structure with micromanipulation analysis to provide a cell wall that can be extrapolated to rapid loading conditions with

more confidence. Such a model would also prove beneficial in the characterisation of the process of cell fatigue and its effect on cell-disruption efficiency.

- *Characterise process interactions*

This thesis examined only two cultures of yeast cells, and does not allow generalisations to be made regarding the effect of fermentation conditions on cell wall mechanical properties or the cell size distribution. Similarly, there are interactions between the homogenizer a downstream process units. Such interactions require further modelling of the effects of homogenizer variables on cell-debris size distributions in addition to the predictions of product release and homogenate cell-size distributions that the model in this thesis can provide.

Ultimately, simultaneous numerical simulation of cell and fluid velocity and deformation may be possible. However, this is not likely to be in the near future. Two advances must be made before this complex problem can be solved: computational power must increase, and the mechanical properties of cell walls must be further characterised under conditions of rapid loading and fatigue. Until such a simultaneous analysis is available, disruption modeling must use the "mechanism" approach used in this thesis to characterise the most significant variables that influence disruption efficiency.

Appendices

Appendix A1: Redundancy Analysis of the Wall Strength Model

The wall strength model for cell disruption efficiency was given as Eq. (1.9). With the empirical functions that were originally chosen to represent the cell stress and homogenizer stress distribution functions, the wall strength model becomes:

$$D = 1 - \int_0^{\infty} \left[1 - \frac{\left(mP^n\right)^d}{S^d + \left(mP^n\right)^d} \right]^N \frac{1}{\sigma\sqrt{2\pi}} \exp\left[-\frac{(S-\bar{S})^2}{2\sigma^2} \right] dS \qquad \text{(A1.1)}$$

If all of the five empirical constants in Eq. (A1.1) were determined simultaneously by non-linear regression, a large number of iterations was typically required to minimise the total sum squared error (author's observations). It appeared that the regression search algorithm was making significant changes in the empirical variables, whilst only slowly reducing the total model SSE. This intuitively suggests some over-specification or parameter redundancy within the model. To examine this possibility more rigorously, a formal redundancy analysis was undertaken.

Parameter redundancy in curve fitting has been discussed by Reich (1981) who states that:

> "Parameter redundancy arises when the proposed kinetic model is too detailed for the actual information content of the measurable data. Then an enormous set of totally different, but interdependent parameter values is able to explain the data, and parameter estimation becomes impossible."

And goes on to state that:

> "the defect has nothing to do with the question of whether or not the model is the correct one. It may be entirely correct and consistent with the data, and its descriptive or physico-chemical assumptions may be fully justified, and nevertheless it may produce redundancy to such an extent that even the decadic range of the

parameter values cannot be estimated from the data without further information. In a sens, one may even say that the better the model, the more refined its parameter structure, the more redundancy comes into play."

Analysing for Parameter Redundancy

the following procedure is taken from Reich (1981). Consider the case of a model function where dependent variable y is a function of independent variable x and a set of invariant but unknown parameters p:

$$y = f\left(x, p_1, p_2, \ldots, p_n\right) \tag{A1.2}$$

A measure of sensitivity of the model response for a set of c discrete data points is defined as:

$$M_{ij} = M_{ji} = \frac{1}{c}\sum_{k=1}^{c}\left[\frac{\partial f\left(x_k, p_1, p_2, \ldots, p_n\right)}{\partial p_i}\right]\left[\frac{\partial f\left(x_k, p_1, p_2, \ldots, p_n\right)}{\partial p_j}\right] \tag{A1.3}$$

This matrix $\boldsymbol{M}$ contains two types of information:

1. The *sensitivity* with respect to one parameter, collected as diagonal elements M_{ii}.
2. The cross-sensitivity with respect to two parameters varying together: the elements M_{ij}, $i \neq j$.

It is convenient to separate these components into two matrices by the transformation:

$$\boldsymbol{S}=\boldsymbol{D}^{-1}\boldsymbol{M}\boldsymbol{D}^{-1} \tag{A1.4}$$

where

$\boldsymbol{D}$ is a diagonal matrix, $D_{ii} = +\sqrt{M_{ii}}$, expressing sensitivity

$\boldsymbol{S}$ is a scaled matrix with unity in the diagonal, expressing redundancy

The symmetric matrix $\boldsymbol{S}$ has real positive eigenvalues. If one or more of these is vary close to zero, then there exist parameter directions along which model sensitivity will be practically zero. We call these directions redundant. A global measure of redundancy is

the determinant of S, *i.e.*, the product of eigenvalues, which is largely determined by the smallest of them.

Analysis of wall strength model

For single pass disruption with the wall strength model,

$$D = f\left(P, m, n, d, \sigma, \bar{S}\right) \tag{A1.5}$$

where P is the independent variable and parameters m, n, d, σ, and $\bar{S}$ are the invariant unknown parameters. Parameter values determined for the wall strength model by Middelberg (1992) are given in Table A1.1, and are used for the determination of sensitivity matrices.

Table A1.1: Wall-strength model parameters determined for E. coli homogenized with an APV-Gaulin 15M homogenizer.

Parameter	Value
m	12.6
n	0.393
d	7.85
σ	3.82
$\bar{S}$	30 - 50

Using values of the independent variable, pressure, of 10 to 70 MPa, and arbitrarily choosing a value for $\bar{S}$ of 50, matrix $\boldsymbol{M}$ becomes

$$\boldsymbol{M} = \begin{bmatrix} 9.519\cdot10^{-3} & 0.433 & 5.733\cdot10^{-4} & -1.838\cdot10^{-5} & -2.397\cdot10^{-3} \\ 0.433 & 19.894 & 0.034 & -3.275\cdot10^{-3} & -0.109 \\ 5.733\cdot10^{-4} & 0.034 & 3.927\cdot10^{-4} & -1.077\cdot10^{-4} & -1.362\cdot10^{-4} \\ -1.838\cdot10^{-5} & -3.275\cdot10^{-3} & -1.077\cdot10^{-4} & 3.218\cdot10^{-5} & 2.174\cdot10^{-6} \\ -2.397\cdot10^{-3} & -0.109 & -1.362\cdot10^{-4} & 2.174\cdot10^{-6} & 6.04\cdot10^{-4} \end{bmatrix} \tag{A1.6}$$

transformation gives matrices $\boldsymbol{D}$ and $\boldsymbol{S}$:

$$\boldsymbol{D} = \begin{bmatrix} 10.249 & 0 & 0 & 0 & 0 \\ 0 & 0.224 & 0 & 0 & 0 \\ 0 & 0 & 50.463 & 0 & 0 \\ 0 & 0 & 0 & 176.294 & 0 \\ 0 & 0 & 0 & 0 & 40.69 \end{bmatrix} \tag{A1.7}$$

$$\boldsymbol{S} = \begin{bmatrix} 1 & 0.995 & 0.297 & -0.033 & -1 \\ 0.995 & 1 & 0.388 & -0.129 & -0.993 \\ 0.297 & 0.388 & 1 & -0.958 & -0.28 \\ -0.033 & -0.129 & -0.958 & 1 & 0.016 \\ -1 & -0.993 & -0.28 & 0.016 & 1 \end{bmatrix} \tag{A1.8}$$

The eigenvalues of matrix $\boldsymbol{S}$ are 3.2, 1.8, 0.006, 6.3×10^{-14}, and 1.6×10^{-8} and the inverse determinant of matrix $\boldsymbol{S}$ is:

$$\frac{1}{|\boldsymbol{S}|} = 2.9 \times 10^{22} \tag{A1.9}$$

Such a high value for the inverse determinant indicates a high degree of parameter redundancy within the wall strength model. With three of the eigenvalues of matrix $\boldsymbol{S} << 1$, it seems that only two independent parameters are required to explain the experimental disruption data. This is not surprising, as the kinetic model of Hetherington *et al.* (Eq. (1.1)) only required two empirical parameters. Specifically, the interaction occurs between:

- m, n and $\overline{S}$
- d and σ

This can be interpreted as meaning that if the parameters in one of the wall strength model distributions (homogenizer stress or cell strength distribution) could be obtained independently, the number of invariant unknown parameters will be reduced and most of the redundancy will be removed.

In practice, the redundancy within the wall strength model means that effectively an infinite set of regressed parameter values could be found that describe the experimental data equally well. This prevents the regressed parameters from containing physical meaning (*e.g.* in terms of dimensional stress units) or from being extrapolated beyond the range of data used to determine those regressed parameters. Whilst redundancy is not a fault of the model as such, it does prevent meaningful model parameters from being determined by the regression of disruption data alone.

Appendix A2: Homogenizer Dynamics

This thesis is primarily concerned with the analysis and modeling of a high-pressure homogenizer at steady-state operating conditions. However, this steady-state assumption is simply a first approximation of the true homogenizer dynamics, as the APV-Gaulin 15MR-8TBA homogenizer used in this study has a single-piston positive-displacement pump, which results in the presence of pressure and flow transients during operation. The influence of these transients on measured and calculated homogenizer variables is examined in this appendix.

Pressure Variation of Flow Rate

An important characteristic of a high-pressure homogenizer is the dependence of homogenizer flow rate on operating pressure. The flow rate through the homogenizer used in this thesis was measured using water as an operating fluid with the results shown in Fig. A2.1.

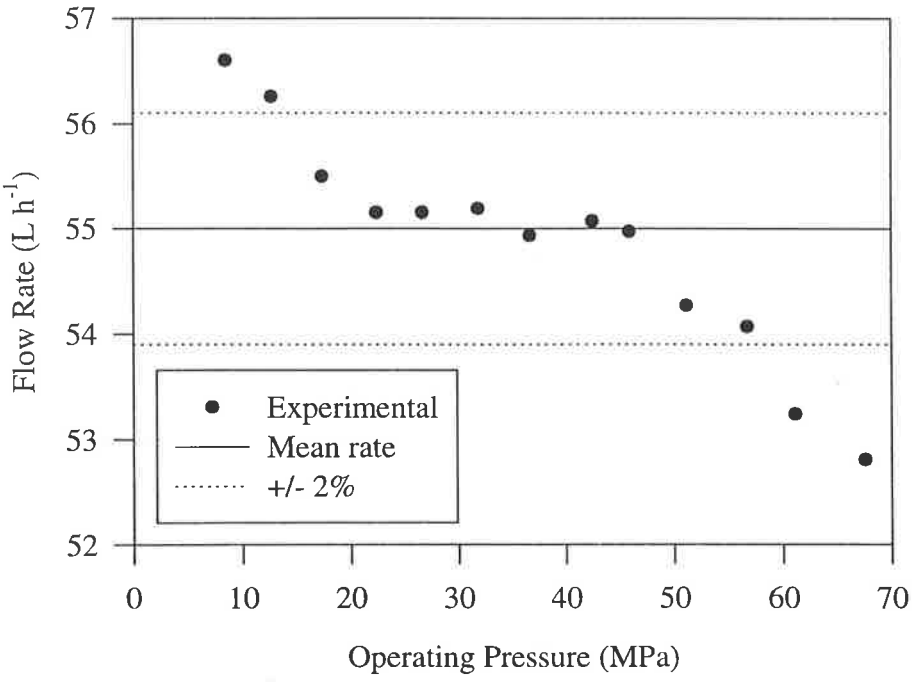

Figure A2.1: Dependence of homogenizer flow rate on operating pressure.

Figure A2.1 indicates that the homogenizer flow rate averages (and plateaus at) 55 L h^{-1} over most of the homogenizer's operating pressure range. However, flow rate is slightly higher at pressures below 20 MPa and decreases further above 50 MPa. This variation can be considered to be (relatively) minor, with the flow rate remaining constant to within approximately ± 2% over most of the operating pressure range.

Cycle Transients

The single piston positive displacement pump of the 15MR-8TBA homogenizer consists of a piston on a crank (Fig. A2.2).

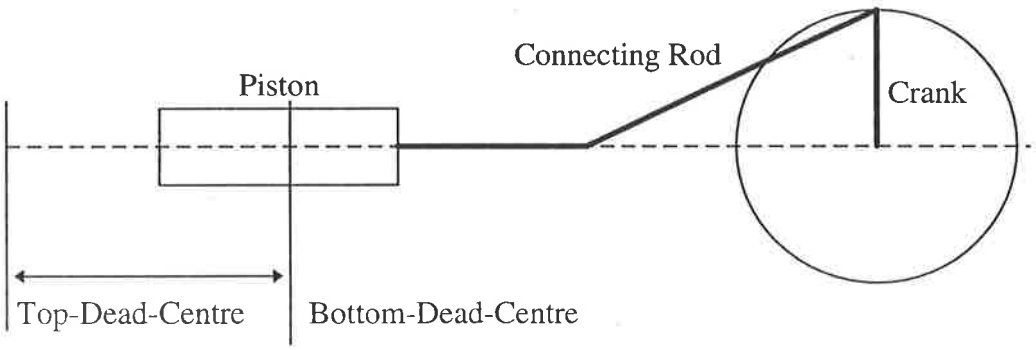

Figure A2.2: Schematic of piston and crank system in homogenizer drive.

The piston moves from bottom-dead-centre (BDC) to top-dead-centre (TDC) and back to BDC again for every revolution of the crank. The position of the piston from BDC is given by Eq. A2.1:

$$z(t) = B\{1+\cos(At)\} + C\left\{1-\sqrt{1+\left(\frac{\sin(At)}{C}\right)^2}\right\} \qquad \text{(A2.1)}$$

where A is the angular rotation rate of the crank (9.84 rad s^{-1}), B is the length of the crank (0.027 m) and C is the ratio of the connecting rod length to crank length (4.5). The instantaneous homogenizer flow rate is equal to the product of the piston velocity and the piston cross sectional area (0.000187 m^2):

$$Q(t) = z(t) * area \qquad \text{(A2.2)}$$

The calculated instantaneous flow rate is given in Fig. A2.3.

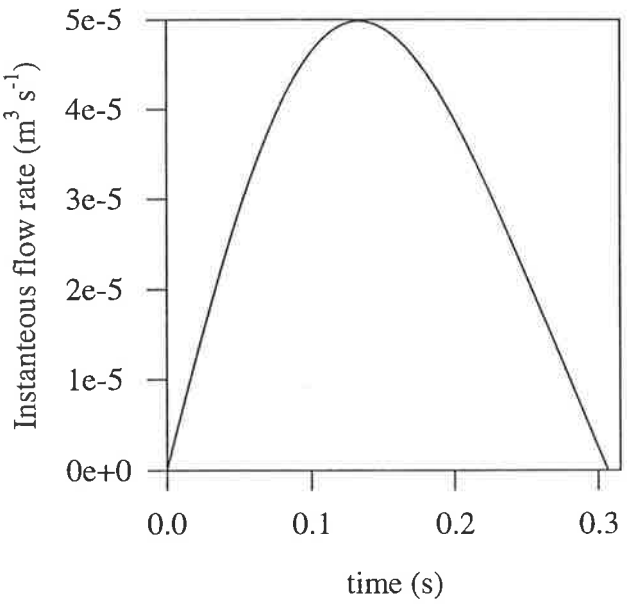

Figure A2.3: Dependence of instantaneous homogenizer flow rate on time.

The mean homogenizer flow rate of 4.6×10^{-5} m^3 s^{-1} (based on 55 L h^{-1}, valve open for 1/3 of stroke) is approximately 7% lower than the peak homogenizer flow rate (4.93×10^{-5} m^3 s^{-1}). Thus, homogenizer valve gap measured at the peak homogenizer flow rate is expected to be higher than the valve gap at the mean homogenizer flow rate. Valve gap is expected to be approximately proportional to the instantaneous flow rate (as total pressure drop is dominated by inertial rather than frictional losses). This is confirmed by comparison of instantaneous flow rate and valve gap measurements (Fig A2.4). As such, it is reasonable to correct valve gap measured at peak flow rate to a mean valve gap by using a factor of 0.93.

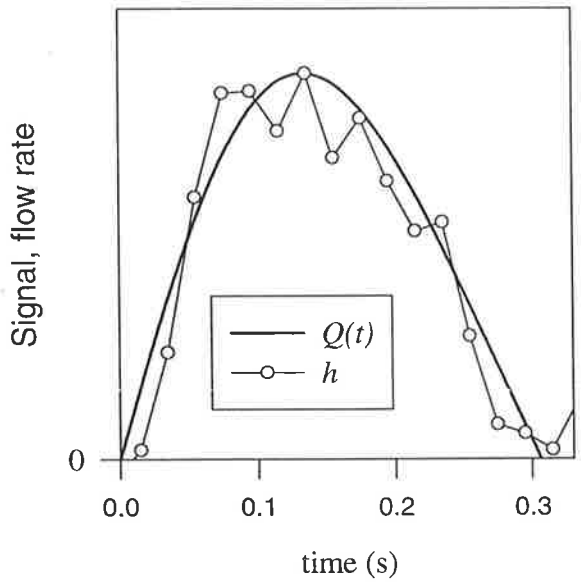

Figure A2.4: Comparison of instantaneous flow rate and valve gap for cell-disruption valve (66.1 MPa pressure drop).

Effect on Inlet Region Pressure Gradient

Figures A3.4, 3.5 and 3.6 show that operating pressure, flow rate and valve gap all show significant variation throughout the homogenizer's operational transient. The significance of these transients must be addressed, as the equations presented in chapters 3 and 4 of this thesis were developed for the "pseudo steady-state" homogenizer operating conditions defined above in this appendix. The net result of these variations is examined by determining the pressure gradient variation within the valve inlet region during a homogenizer piston cycle. Operating pressure and valve gap are measured experimentally with results shown in Figs 3.5 and 3.6. Flow rate through the valve assembly was calculated using Eqs A2.1 and A2.2 (*e.g.* Fig. A2.4). Pressure gradient was calculated using Eq. (3.25):

$$\frac{dP}{dy} = \frac{\rho Q^2}{8\beta_I \pi^2 r_i^2 h^3} \tag{3.25}$$

The total variation in pressure gradient is shown in Fig. A2.5 as a plot of cumulative volume fraction of homogenizer feed material experiencing a given pressure-gradient.

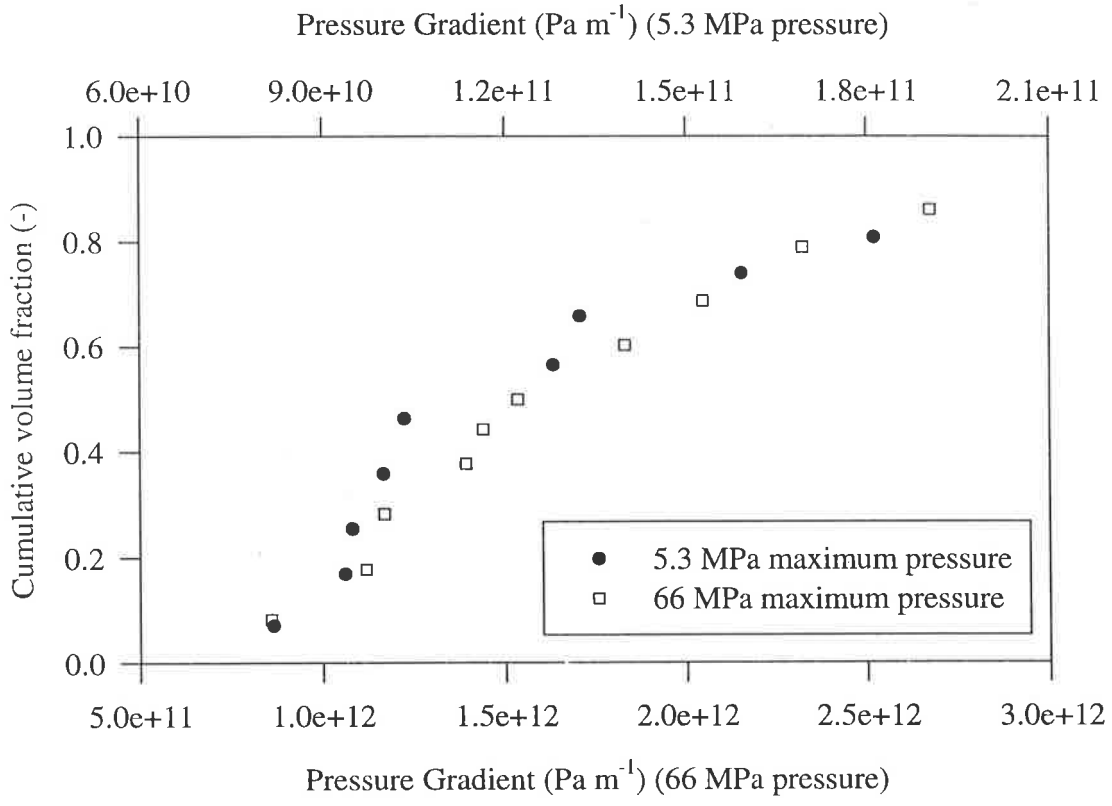

Figure A2.5: Variation of valve inlet pressure gradient within piston cycle.

Figure A2.5 indicates that within-cycle pressure gradient variation is highly significant. However, some of the variation within Fig. A2.5 will be due to experimental uncertainty (the error in measured valve gap) and numerical simplification (the calculated instantaneous flow rate from Eqs A2.1 and A2.2). Thus, whilst Fig. A2.5 indicates that pressure gradient varies by approximately ± 50% of the median value for 95% of the flow, variation is expected to considerably lower in practice. Figure 7.1 indicates that pressure gradient within the cell-disruption valve seat's inlet region is insensitive to flow rate variation. Substitution of Eq. 3.59 into Eq. 3.58 suggests that pressure gradient is approximately inversely proportional to the homogenizer operating pressure at a fixed flow rate. If pressure gradient variation is attributed entirely to pressure variation, then pressure gradient is only expected to vary by ± 5% from the median for 95% of the total flow. The order of magnitude difference between the variation estimated from pressure variability and that in Fig. A2.5 is due to the variation in measured homogenizer valve gap (see Figs 3.5 and 3.6). As it is uncertain how much of the measured homogenizer valve gap variation is due to experimental measurement error and how much is due to actual valve oscillations, it is uncertain how much pressure gradient variation (between the estimates of ± 5% and ± 50%) occurs during a typical piston cycle.

Appendix A3: Modeling Cell Compression

As highlighted in chapter 5, yeast and bacterial cells are small, with dimensions in the order of 1 μm, which causes optical diffraction that makes it difficult to observe size accurately. Thus, the deformed shape of the cell during squeezing cannot be accurately measured. An alternative approach to measuring deformed cell shapes is to assume an elastic behaviour for the membrane, and to then calculate the static cell shape and membrane tensions using the measured applied load and cell deformation.

The first example of the application of this approach is based on a membrane with uniform and isotropic tensions*. Yoneda (1964) demonstrated the application of this type of analysis with sea urchin eggs. Calculation of deformed cell properties using the isotropic membrane assumption was further examined by Evans and Skalak (1980) and subsequently used in the analysis of mammalian cells by Zhang *et al.* (1992).

Whilst the assumption of uniform and isotropic tension is likely to be appropriate for some situations, it is not likely to be valid in general. Lardner and Pujara (1980) defined an initial value problem, with the relevant ordinary differential equations to define the compression experiment. This analytical membrane model is able to determine the load-deformation, deformed profile, and distribution of tensions within the compressed cell. A choice of material model (linear elastic, Mooney-Rivlin) coupled with a best fit procedure allows the mechanical behaviour of the membrane to be defined.

A more general approach to examining the compression experiment is to use a finite-element analysis. As with the analytical membrane model, a particular membrane material model must be chosen, and the load-deformation, deformed cell profile, and tension distributions are calculated. In addition, the analysis can readily be formulated to include membrane bending moments, membrane inhomogeneity (*e.g.* varying wall thickness) or

* Isotropic tension implies that hoop and axial tensions are equal. Uniform tension implies that these tensions are independent of position on the cell. Constant tension implies that the tension is independent of the membrane's strain (a horizontal stress-strain curve).

non-axisymmetric cells. Examples of finite element analysis of the compression experiment includes the work of Pitt and Davis (1984) and Cheng (1987).

In this thesis, the compression technique is used to analyse the mechanical properties of yeast cells. The analytical membrane model or finite element analysis is likely to be the most useful approach when analysing experimental results to obtain parameters such as cell-wall failure tensions. Such an analysis is beyond the scope of this thesis. As an alternative, the simple force balance approach as used by Zhang *et al.* (1992) is used in this thesis. This approach is restrictive, as it assumes that the membrane is in a state of uniform and isotropic tension, which is unlikely to be a valid approximation in general. However, uniform isotropic tension should be a reasonable representation for cell compression if the cell wall behaves as a bonded fibre fabric (as discussed in section 5.2). The following analysis is provided by Zhang *et al.* (1992).

The geometry of a deformed cell during the compression experiment is shown schematically in Fig. A3.1. Initially, the work required to compress the cell is expended on membrane stretching, membrane bending, deformation of any cytoplasmic structures and volume compression of the cell (Yoneda, 1964). As compression proceeds, work will also be required to irreversibly break bonds within the cell wall. For a typical cell, it is most likely that membrane stretching is the significant contribution.

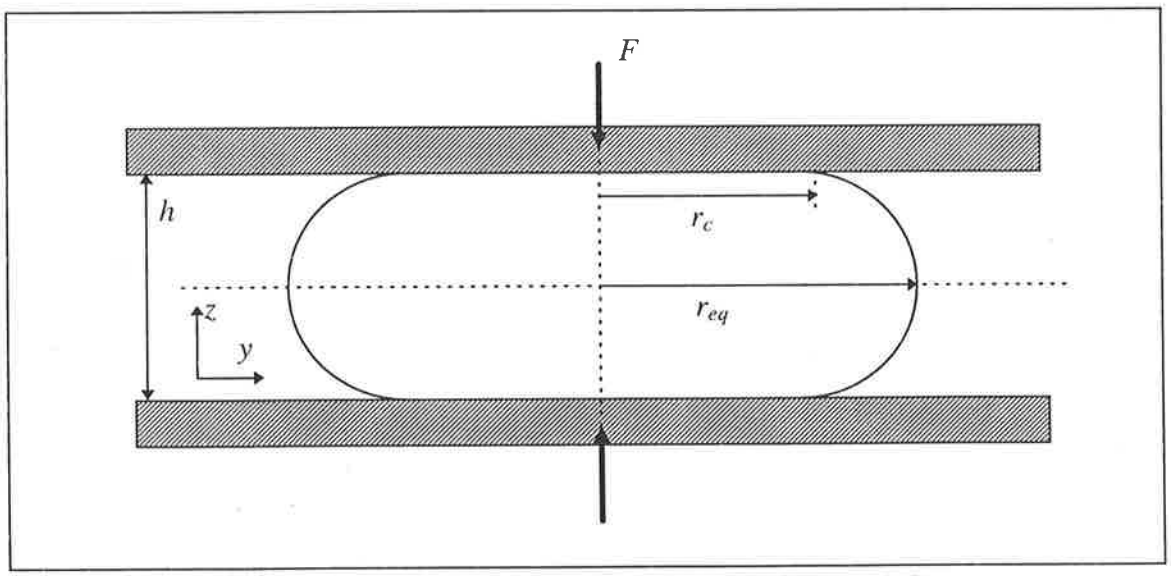

Figure A3.1: Cross section of a deformed, spherical cell between two parallel plates.

If the part of the cell wall that is not in contact with the two compressing plates is in uniform and isotropic tension, then the total membrane curvature (Eq. (A3.1)) is constant (Yoneda, 1964; Evans and Skalak, 1980).

$$\frac{1}{r_H}+\frac{1}{r_A}=constant \tag{A3.1}$$

From an axial force balance, the total force acting on the compressing plates is determined by the pressure difference across the cell wall and the contact area between the cell and plates (Eq. (A3.2)).

$$F=\Delta P\pi {r_c}^2 \tag{A3.2}$$

At the equator, a force balance gives:

$$2\pi r_{eq}T=\Delta P\pi\left({r_{eq}}^2-{r_c}^2\right) \tag{A3.3}$$

Eqs (A3.2 and (A3.3) may be combined to eliminate internal pressure:

$$F=\frac{2\pi r_{eq}{r_c}^2T}{{r_{eq}}^2-{r_c}^2} \tag{A3.4}$$

This is rearranged into dimensionless form:

$$\frac{F}{Tr_s}=\frac{2\pi r_{eq}{r_c}^2}{r_s\left({r_{eq}}^2-{r_c}^2\right)} \tag{A3.5}$$

From Eq. (A3.5), the isotropic membrane tension can be determined if the applied force, and contact and equatorial radii are known. The assumption of constant curvature (Eq. (A3.1)) gives the following equation to describe the shape of the curved portion of the deformed cell (Zhang *et al.*, 1992):

$$z=\frac{r_{eq}\left(z^2-{r_c}^2\right)}{{r_{eq}}^2-{r_c}^2}\sqrt{1+\left(\frac{dz}{dy}\right)^2} \tag{A3.6}$$

Eq. (A3.6) can be rearranged to give:

$$dy=\left[\frac{\left({r_{eq}}^2-{r_c}^2\right)^2z^2}{\left(z^2-{r_c}^2\right)^2{r_{eq}}^2}-1\right]^{-0.5}dz \tag{A3.7}$$

Thus, the distance between the two parallel surfaces can be calculated by integration of Eq. (A3.7):

$$\int_0^{h/2} dy = \frac{h}{2} = \int_{r_c}^{r_{eq}} \left[\frac{\left({r_{eq}}^2 - {r_c}^2\right)^2 z^2}{\left(z^2 - {r_c}^2\right)^2 {r_{eq}}^2} - 1 \right]^{-0.5} dz \qquad \text{(A3.8)}$$

The undeformed cell volume can readily be calculated. As the cell is considered to be incompressible, the undeformed and deformed cell volumes are equal:

$$\frac{4}{3}\pi {r_s}^3 = \int_{r_c}^{r_{eq}} \pi z^2 \left[\frac{\left({r_{eq}}^2 - {r_c}^2\right)^2 z^2}{\left(z^2 - {r_c}^2\right)^2 {r_{eq}}^2} - 1 \right]^{-0.5} dz \qquad \text{(A3.9)}$$

A solution to these equations is obtained as follows:

1. Select a value for r_{eq}
2. Select a value for r_c/r_{eq} and hence r_c
3. Use Eq. (A3.8) to calculate $h/2$, rearrange and solve Eq. (A3.9) for r_s
4. Calculate dimensionless variables $h/2r_s$, r_c/r_{eq}, r_c/r_s and F/Tr_s (Eq. (A3.5)).
5. Repeat 2 - 4 for a new values of r_c/r_{eq} until step 4 has been completed for a suitable range of r_c/r_{eq} values (eg 0.01 to 0.99).

Results from these equations were obtained numerically and are shown in Fig. A3.2

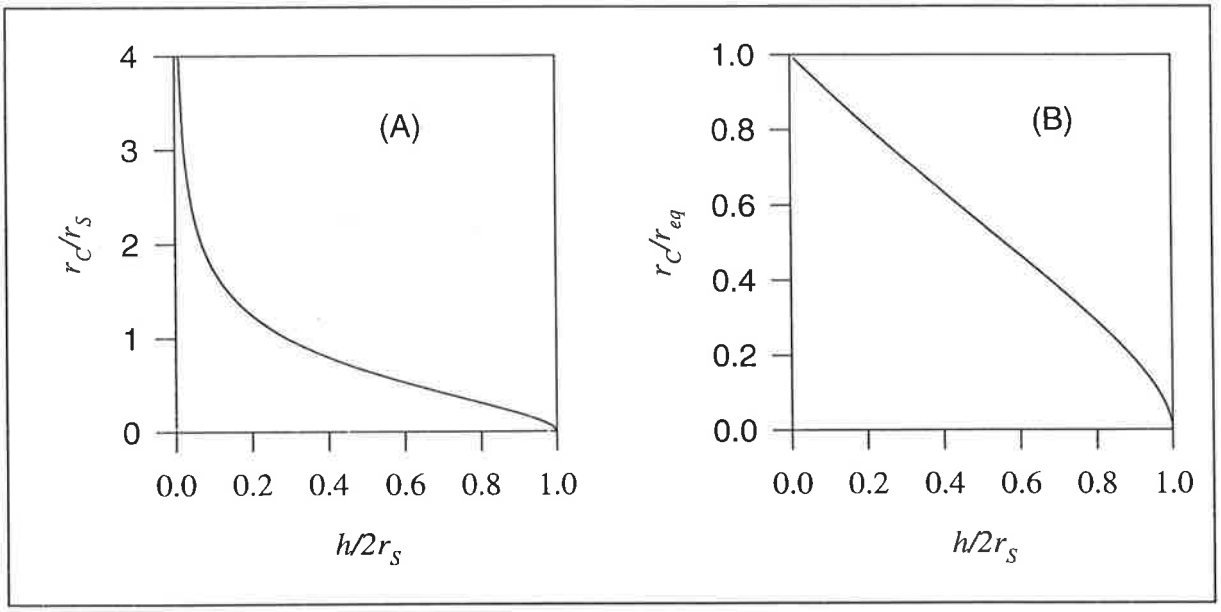

Figure A3.2: Numerical results that define the profile of the deformed cell during micromanipulation.

Appendix A4: Cell-Wall Fatigue

Using Eq. (6.26) to predict the effect of multiple disruption events on disruption efficiency with the independently-determined tension-distribution of Eq. (6.5) predicts that disruption will not increase after the first disruption event. However, this contradicts experimental observations. This contradiction is attributed to:

- process variations, and
- cell-wall fatigue.

Process variation has been examined in appendix A2, and although its magnitude is uncertain, it evidently occurs to some degree. The presence of cell-wall fatigue (*i.e.*, the weakening of the cell-wall during homogenization, such that the cell may be disrupted in subsequent homogenizer passes) is examined in this appendix.

Experimental Evidence Cell-Wall Fatigue

During micromanipulation of homogenate cells, it was apparent that "intact" cells in the homogenate were considerably more deformable than cells in the original feed. Some cells were apparently so deformable that they could not be burst beneath the micromanipulation probe, making collection of representative population data difficult. The difference in deformability to cell breakage was also confirmed statistically. Deformability increased from 65% for feed cells (experiments A and B) to 76% and 70% for experiments A and B respectively after one homogenizer pass through the valve-inlet region. A t-test confirmed that these differences were significant at a 1% significance level (Table A4.1).

Table A4.1: t-test for significant difference between deformability of feed and homogenate cells.

H_0: Feed and homogenate cell deformability is the same

H_A: Feed cell deformability is lower than homogenate cell deformability

Statistic	Experiment A	Experiment B
mean homogenate deformation	0.76	0.70
mean feed deformation	0.65	0.65
standard deviation, homogenate	0.098	0.091
standard deviation, feed	0.075	0.107
n homogenate	31	58
n feed	45	62
significance level	0.01	0.01
degrees of freedom	74	118
$t_{critical}$	2.38	2.37
t_0	5.3	2.8

As $t_0 > t_{critical}$ for experiments A and B, the original hypothesis is rejected.

Results were also obtained for homogenate cells from experiment B after 4 homogenizer passes. The average cell deformability to failure was found to be 79%. The observation that these homogenate cells are more deformable than the original feed cells provides direct evidence that cell-wall fatigue occurs during homogenization. Ultimate cell-wall tensions were then calculated using the procedure given in chapter 5, and are compared for feed and homogenate cells in Table A4.2.

Table A4.2: Comparison of mean and standard deviation of ultimate cell-wall tensions during micromanipulation for feed and homogenate cells.

Sample	Mean Tension (N m^{-1})	Standard deviation (N m^{-1})
A, feed	3.4	1.3
A, 1 pass × 56 MPa	2.6	0.7
B, feed	5.4	1.7
B, 1 pass × 56 MPa	5.0	1.8
B, 4 pass × 56 MPa	4.0	2.5

It is apparent from Table A4.2 that the mean ultimate cell-wall tension decreases significantly after homogenization. This does not, however, translate directly to weaker cells during homogenization. Results in Table A4.2 were translated to high-pressure homogenizer conditions using the mechano-chemical and failure strain corrections presented in section 6.2.1. Results are given in Table A4.3. Graphical results are also given for experiments A and B in Figs A4.1 and A4.2, respectively.

The marked increase in cell deformability to failure during micromanipulation provides strong evidence that cells suffer from fatigue effects during homogenization. Although

these cells are structurally sound, their ultimate tension is somewhat lower. This is likely to be due to the scission of a (possibly small, but still significant) fraction of bonds within the cell wall's glucan network. This compromised cell wall is still able to resist turgor pressure, but is more easily deformed (and deformed to a greater extent) during the micromanipulation process. If a fraction of cross links are broken, there will be more potential for cell wall extension through chain slippage, which will occur at lower tensions than chain scission (Table A4.2). The ultimate cell-wall tension during homogenization, however, will not necessarily have changed greatly, as the number of microfibrils to be broken may not be significantly lower at the rapid loading rates. Hence, from the combined evidence (tension distributions in Figs A4.1 and A4.2 and deformability changes in Tables A4.1 and A4.3) it is likely that cell-wall fatigue is a significant factor in the experimental observation that cell disruption increases with homogenizer passes. Further characterisation of the cell-wall fatigue process is required, particularly if multiple disruption events are to be accurately modelled.

Table A4.3: Comparison of mean and standard deviation of ultimate cell-wall tensions for feed and homogenate cells translated to high-pressure homogenizer conditions.

Sample	Failure deformation	Failure strain	Tension ($N\ m^{-1}$)	SD ($N\ m^{-1}$)
A, feed	0.65	0.4	8.6	3.3
A, 1 pass × 56 MPa	0.76	0.7	8.0	2.1
B, feed	0.65	0.4	13.6	4.3
B, 1 pass × 56 MPa	0.70	0.5	13.5	4.9
B, 4 pass × 56 MPa	0.79	0.8	13.0	8.1

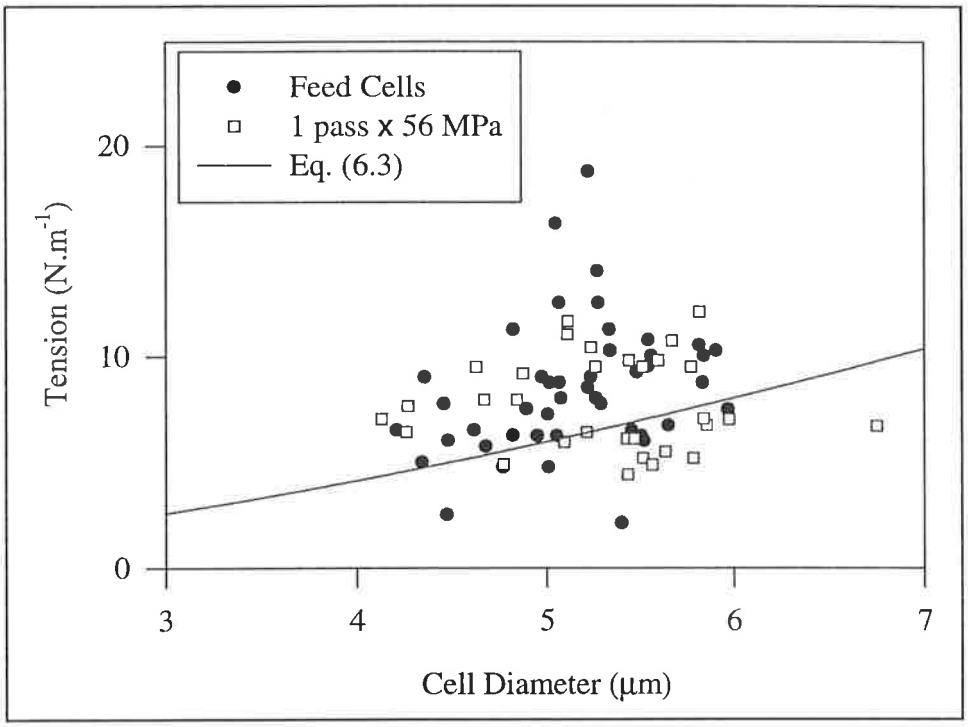

Figure A4.1: Dependence of cell wall failure tension and critical cell wall tension in homogenizer valve on cell diameter for feed and homogenate cells from experiment A.

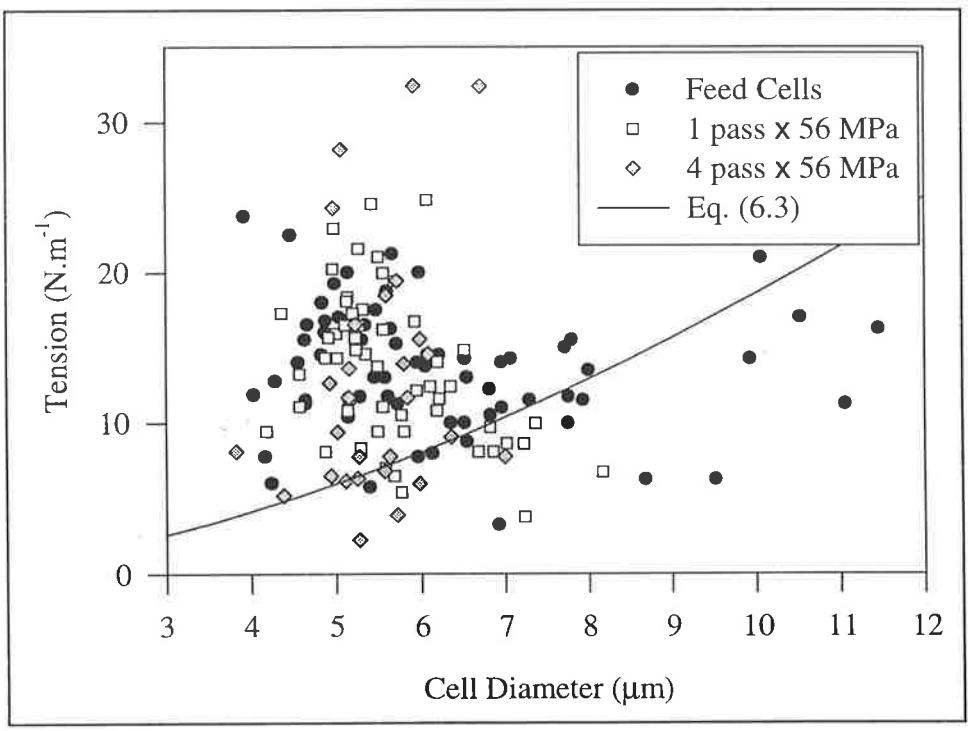

Figure A4.2: Dependence of cell wall failure tension and critical cell wall tension in homogenizer valve on cell diameter for feed and homogenate cells from experiment B.

Appendix B: Publications List

Publications related to this Thesis

Kleinig, A.R., Middelberg, A.P.J., Mashmoushy, H., Zhang, Z., and Thomas, C.R. 1997. Prediction of yeast cell-disruption efficiency during high-pressure homogenization. *Biotech. Bioeng.*, SUBMITTED.

Kleinig, A.R., and Middelberg, A.P.J., 1997. Membrane tensions in a spherical capsule moving with a converging flow. *AIChE J.* SUBMITTED.

Kleinig, A.R., and Middelberg, A.P.J., 1997. A numerical and experimental study of a homogenizer impinging jet. *AIChE J.* IN PRESS.

Kleinig, A.R., and Middelberg, A.P.J., 1996. The correlation of cell disruption with homogenizer valve pressure gradient determined by computational fluid dynamics. *Chem. Eng. Sci.*, **51**: 5103-5110.

Kleinig, A.R., O'Neill, B.K., and Middelberg, A.P.J., 1996. The effect of homogenizer impact distance on the disruption of *Escherichia coli*. *Biotechnol. Tech.*, **10**, 199-204.

Kleinig, A.R., Mashmoushy, H., Middelberg, A.P.J., Thomas, C.R. and Zhang, Z., 1996. Can we predict the breakage of yeast cells? CHEMECA '96, 24th Australian and New Zealand Chemical Engineering conference and exhibition, Sydney, Australia, Sept 1996, 4: 117-121.

Kleinig, A.R., Mashmoushy, H., Middelberg, A.P.J., Thomas, C.R. and Zhang, Z., 1996. Predicting the breakage of yeast cells during high-pressure homogenisation. Proceedings of 10th International biotechnology symposium, Sydney, Australia, Aug. 1996, p 134.

Kleinig, A.R., and Middelberg, A.P.J., 1996. Fluid Mechanics of a high-pressure homogenizer. The 1996 IChemE Research Event, Leeds, UK, April 1996, **1**, 109-111.

Kleinig, A.R., Ide, B.H., and Middelberg, A.P.J., 1995. High-pressure homogenizer valve mechanics. CHEMECA '95, 23rd Australasian Chemical Engineering Conference, Adelaide, Australia, September 1995, **3**, 50-55.

Kleinig, A.R., O'Neill, B.K., and Middelberg, A.P.J., 1995. High-pressure homogenizer impact distance affects the disruption of *Escherichia coli.* Proceedings of Fourth Pacific Rim Biotechnology Conference, Melbourne, Australia, February 1995, 266-267.

Kleinig, A.R., Middelberg, A.P.J., 1994. Disruption of Yeasts by High-Pressure Homogenisation. In *Better Living Through Innovative Biochemical Engineering (W.K. Teo, M.G.S Yap and S.K.W. Oh -eds)*, Proceedings of APBioChEC '94, Third Asia-Pacific Biochemical Engineering Conference, Singapore, June 1994, 384-386.

Publications not directly related to this Thesis

Kleinig, A.R., Mansell, C.J., Nguyen, Q.D., Badalyan, A., and Middelberg, A.P.J., 1995. Influence of broth dilution on the disruption of *Escherichia coli. Biotechnol. Tech.*, **9**, 759-762.

Smith, A.E., **Kleinig, A.R.**, and Middelberg, A.P.J., 1996. Disruption of *Saccharomyces cerevisiae* by combining enzymatic lysis and high-pressure homogenization. Proceedings of 10th International biotechnology symposium, Sydney, Australia, Aug. 1996, p 132.

Nomenclature

a	constant in Eq. (1.1) (–)
A	absorbance (–)
A	parameter in Eq. (6.40) (Pa m^{-1})
Ac	Acceleration number (–)
B	parameter in Eq. (6.40) (–)
C	parameter in Eq. (6.40) (–)
C_μ	k-ε turbulence model coefficient (–)
$C_{1\varepsilon}$	k-ε turbulence model coefficient (–)
$C_{2\varepsilon}$	k-ε turbulence model coefficient (–)
d	cell diameter (m)
d	deformed cell height (m)
d	parameter in Eq. (1.11) (–)
D	disruption (–)
Ea	activation energy (kJ $gmol^{-1}$)
f	inlet loss coefficient (–)
F	force (N)
$f_D(S)$	stress distribution function (Eq. (1.9)) (–)
$f_S(S)$	cell strength distribution function (Eq. (1.9)) (–)
$f_V(d)$	volume distribution function (–)
h	valve gap (m)
k	turbulent kinetic energy (m^2 s^{-2})
k_1	constant in Eq. (1.1) (MPa^{-a})
k_2	constant in Eq. (1.2) (–)
k_3	constant in Eq. (1.3) (–)
k_4	constant in Eq. (1.3) (–)
k_5	constant in Eq. (1.4) (MPa^{-a})
k_6	constant in Eq. (2.2) (MPa^{-a})
k_7	constant in Eq. (2.2) (–)
k_8	constant in Eq. (4.1) ($m^{12/5}$ $s^{-6/5}$)
K	proportionality constant

KE	kinetic energy (J)
l	virtual origin of jet (m)
L	cell length (μm)
L	length scale (m)
$\overline{L}$	mean cell length (μm)
m	experimental jet spreading rate (–)
m	parameter in Eq. (1.11) (–)
M	measure of jet strength (Eq. (3.44)) (–)
N	number of homogenizer passes (–)
n	parameter in Eq. (1.11) (–)
P	pressure (MPa, Pa)
P_k	stress production rate of turbulent kinetic energy ($m^2\ s^{-3}$)
Q	flow rate ($m^3\ s^{-1}$)
R	fractional protein release (–)
r	radius (m)
Re	Reynolds number (–)
S	stress (MPa, Pa)
S	cell strength (–)
$\overline{S}$	mean cell strength (–)
t	cell wall thickness (m)
t	time (s)
t	t-test statistic (–)
T	temperature (K)
T	tension ($N\ m^{-1}$)
U	velocity ($m\ s^{-1}$)
V	activation volume (Eq. (6.7)) (m^3)
V	radial velocity ($m\ s^{-1}$)
V	voltage (V)
V	volume fraction (–)
w	coordinate perpendicular to primary flow direction (m)
w	strain energy per unit volume ($J\ m^{-3}$)
W	radial velocity ($m\ s^{-1}$)
W	total membrane strain energy (J)
We	Weber number (–)
x	general coordinate (m)

X	peptidoglycan crosslinkage (–)
y	radial coordinate (m)
Y	impact distance (mm)
z	axial coordinate (m)
Z	normal load (N m^{-2})

Greek symbols

α	strain rate (s^{-1})
β	length scale proportionality coefficient (–)
γ	cell wall strength (N m^{-1})
γ	surface tension (N m^{-1})
δ	Kronecker delta
ε	rate of dissipation of turbulent kinetic energy (m^2 s^{-3})
ε	restitution ration (–)
ε	strain (–)
η	efficiency of fibre reinforcement (–)
θ	angular coordinate (rad)
μ	viscosity (Pa s)
ν	kinematic viscosity (m^2 s^{-1})
Π_ρ	density ratio (–)
ρ	density (kg m^{-3})
σ	standard deviation (various)
σ	stress (N m^{-2})
σ_ε	k-ε turbulence model coefficient (–)
σ_k	k-ε turbulence model coefficient (–)
τ	time to failure (s)
τ	shear stress (N m^{-2})

Subscripts

A	axial
B	cell burst
BL	base line
c	cell

c	composite
c	contact
CC	cell contact
e	exterior cell surface
e	valve exit
eq	equatorial
f	failure
f	feed
f	fibre
FT	force transducer
h	homogenate
H	hoop
HPH	high pressure homogenization
i	index variable
i	interior cell surface
i	valve inlet
I	valve inlet region
j	index variable
J	impinging jet region
L	laminar
m	matrix
max	maximum
MB	micromanipulator beam
MM	micromanipulation
PT	micromanipulation probe tip
S	stagnation
S	undeformed cell
SC	slide contact
T	turbulent
VM	von Mises
VS	volume surface average

References

Agerkvist, I. and Enfors, S.-O., 1990. Characterisation of *E. coli* cell disintegrates from bead mill and high pressure homogenizers. *Biotechnol. Bioeng.*, **36**, 1083-1089.

Ames, G. F.-L., Prody, C. and Kutsu, S., 1984. Simple, rapid, and quantitative release of periplasmic proteins by chloroform. *J. Bacteriol.*, **160**, 1181-1183.

Asenjo, J. A., Parrado, H. and Andrews, B. A., 1991. Rational design of purification processes for recombinant proteins. *Annals New York Acad. Sci.*, **646**, 334-356.

Augenstein, D. C., Thrasher, K., Sinskey, A. J. and Wang, D. I. C., 1974. Optimisation in the recovery of a labile intracellular enzyme. *Biotechnol. Bioeng.*, **16**, 1433-1447.

Ayazi Shamlou, P., Siddiqi, S. F., and Titchener-Hooker, N. J., 1995. A physical model of high-pressure disruption of bakers' yeast cells. *Chem. Eng. Sci.*, **50**, 1383-1391.

Bailey, J. E. and Ollis, D. F., 1986. Biochemical engineering fundamentals. McGraw-Hill Book Company, New York.

Baldwin, C. and Robinson, C. W., 1990. Disruption of *Saccharomyces cerevisiae* using enzymatic lysis combined with high-pressure homogenization. *Biotechnol. Tech.*, **4**, 329-334.

Baldwin, C. V. and Robinson, C. W., 1994. Enhanced disruption of *Candida utilis* using enzymatic pretreatment and high-pressure homogenization. *Biotechnol. Bioeng.*, 43, 46-56.

Ballou, C. E., 1982. Yeast cell wall and cell surface. *In The molecular biology of the yeast* Saccharomyces*: metabolism and gene expression*, Cold Spring Harbour Laboratory, New York, 335-360.

Barnacal, P. A., 1995. Biotechnology comes of age. In *Parmaceutical Manufacturing International 1995*, Sterling Publications Limited, London, 9-11.

Barthes-Biesel, D., and Rallison, J. M., 1981. The time-dependent deformation of a capsule freely suspended in a linear shear flow. *J. of Fluid Mechanics*, **113**, 251-267.

Bavouzet, J-M., Lafforgue-Delorme, C., Fonade, C., and Goma, G., 1995. The effect of an abrupt stepwise reduction in pressure on the integrity of the eukaryotic and prokaryotic cell envelope. *Enzyme Microb. Technol.*, **17**, 712-718.

Beltaos, S. and Rajaratnam, N., 1974. Impinging circular turbulent jets. *Proc. ASCE J. Hydraul. Div.*, **100**, 1313-1328.

Beltaos, S. and Rajaratnam. N., 1973. Plane turbulent impinging jets. *Journal of Hydraulic Research*, **11**, 29-59.

Belter, P. A., Cussler, E. L. and Hu, W.-S., 1988. Cell disruption. In *Bioseparations: Downstream Processing for Biotechnology*, John Wiley, New York, 77-98.

Bhaduri, S. and Demchick, P. H., 1983. Simple and rapid method for disruption of bacteria for protein studies. *Appl. Environ. Microb.*, **46**, 737-752.

Bird, R. B., Stewart, W. E., and Lightfoot, E. N., 1960. *Transport Phenomena*, John Wiley and Sons, New York, 58-59.

Brady, D., Stoll, A. D., Starke, L. and Duncan, J. R., 1994. Chemical and enzymatic extraction of heavy metal binding polymers form isolated cell walls of *Saccharomyces cerevisiae*. *Biotechnol. Bioeng.*, **44**, 297-302.

Brookman, J. S. G. and Davies, M., 1973. An extreme pressure pump for continuous cell disintegration. *Biotechnol. Bioeng.*, **15**, 693-705.

Brookman, J. S. G., 1974. Mechanism of cell disruption in a high pressure homogenizer. *Biotech. Bioeng.*, **16**, 371-383.

Brookman, J. S. G., 1975. Further studies on the mechanism of cell disruption be extreme pressure extrusion. *Biotechnol. Bioeng.*, **17**, 465-479.

Bueche, F., 1962. *Physical properties of polymers*, John Wiley and Sons, New York.

Büschelberger, H. G. and Loncin, M., 1989. Untersuchungen zum mechanischen Aufschluß von Mikroorganismen in Hochdruck-Homogenisatoren, *Chem. Ing. Tech.*, **61**, 420-421.

Büschelberger, H. G., 1987. Untersuchungen zum mechanischen Aufschluß von Mikroorganismen in Hochdruckhomogenisatoren. PhD Thesis, Universität Fredericiana Karlsruhe, Karlsruhe, Germany.

Champion, M. and Libby, P. A., 1994. Reynolds stress description of opposed and impinging turbulent jets. II. Axisymmetric jets impinging on nearby walls. *Phys. Fluids*, **6**, 1805-1819.

Chang, K. S., and Olbricht, W. L., 1993. Experimental studies of the deformation of a synthetic capsule in extensional flow. *J. of Fluid Mechanics*, 250, 587-608.

Chatterjee, A. and White, D., 1989. Radial entry flow of a Newtonian fluid. *J. Phys. D: Appl. Phys.*, **22**, 915-924.

Cheng, L. Y., 1987. Deformation analyses in cell and developmental biology. Part II - Mechanical experiments on cells. *J. Biomech. Eng.*, **109**, 18-24.

Cid, V. J., Duran, A., del Rey, F., Snyder, M. P., Nombela, C. and Sanchez, M., 1995. Molecular basis of cell integrity and morphogenesis in *Saccharomyces cerevisiae*. *Microbiol. Rev.*, **59**, 345-386.

Cleland, J. L. and Wang, D. I. C., 1993. *In vitro* Protein refolding. In *Biotechnology, vol 3: Bioprocessing*, G. Stephanopolous (Ed.), VCH, Weinheim, 527-555.

Clift, R., Grace, J. R. and Weber, M. E., 1978. *Bubbles, Drops and Particles*. Academic Press, New York.

Cohen, S. N., Chang, A. C. Y., Boyer, H. W. and Helling, R. B., 1973. Construction of biologically functional bacterial plasmids *in vitro*. *Proc. Natl. Acad. Sci. USA*, **70**, 3240-3244.

Cole, K. S., 1932. Surface forces of the Arbacia egg. *J. Cell. Comp. Biol.*, **1**, 1-9.

Collins, S., Attouche, C., Yau, C., Jones, M. and Lovitt, R., 1996. An investigation of the disruption of micro-organisms using a new type of cell homogeniser. Proceedings *1996 IChemE Research Event*, **1**, 52-54.

Collis, M. A., O'Neill, B. K. and Middelberg, A. P. J., 1995. Thermal deactivation affects disruption of *Escherichia coli*. *Biotechnol. Tech.*, **9**, 91-94.

Dean, C. R. and Ward, O. P., 1992. The use of EDTA or polymixin with lysozyme for the recovery of intracellular products from *Escherichia coli*. *Biotechnol. Tech.*, **6**, 133-138.

Deshpande, M. H. and Vaishnav, R. N., 1982. Submerged laminar jet impingement on a plane. *J. Fluid Mech.*, **114**, 213-236.

DeSmet, M. J., Kingma, J. and Witholt, B., 1978. The effect of toluene on the structure and permeability of the outer and cytoplasmic membranes of *Escherichia coli*. *Biochim. Biophys. Acta.*, **506**, 64-80.

Doulah, M. S., Hannond, T. H. and Brookman, J. S. G., 1975. A hydrodynamic mechanism for the disintegration of *Saccharomyces cerevisiae* in an industrial homogenizer. *Biotechnol. Bioeng.*, *17*, 845-858.

Drew, D. A., 1974. Low concentration two-phase flow near a stagnation point. *Phys. of Fluids*, **17**, 1688-1691.

Dunnill, P. and Lilly, M. D., 1975. Protein extraction and recovery from microbial cells. In *Single-Cell Protein II*, (Tannenbaum, S. R. and Wang, D. I. C., Eds), The MIT Press, Cambridge, MA, 179-207.

Efron, B. and Tibshirani, R., 1986. Bootstrap methods for standard errors, confidence intervals, and other measures of statistical accuracy. *Stat. Sci.*, **1**, 54-77.

Elison, B. and Webb, B. W., 1994. Local heat transfer to impinging liquid jets in the initially laminar, transitional and turbulent regimes. *Int. J. H&MT*, **37**, 1207-1216.

Engler, C. R. and Robinson, C. W., 1981. Disruption of *Candida utilis* cells in high pressure flow devices. *Biotechnol. Bioeng.*, **23**, 765-780.

Engler, C. R., 1979. Disruption of microorganisms in high pressure flow devices. PhD Thesis, University of Waterloo, Waterloo, Ontario, Canada.

Engler, C. R., 1985. Disruption of microbial cells. In *Comprehensive Biotechnology, Vol. 2*, M. Moo-Young, A. E. Humphrey and C. L. Cooney (Eds), Chap 20, Pergamon, Oxford, 305-324.

Evans, E. A. and Skalak, R., 1980. *Mechanics and thermodynamics of biomembranes*, CRC Press, Boca Raton.

Fish, N. M. and Lilly, M. D., 1984. The interactions between fermentation and protein recovery. *Bio/Technology*, **2**, 623-627.

Fleet, G. H., 1991. Cell walls. In *The Yeasts (Volume 4, Yeast organelles)*, Rose, A. H. and Harrison, J. S. (*Eds*), Academics Press Ltd., London, 199-277.

Flores, M. V., Voget, C. E. and Ertola, R. J. J., 1994. Permeabilization of yeat cells (*Kluyveromyces lactis*) with organic solvents. *Enzyme Microb. Tech.*, **16**, 340-346.

Follows, M., Hetherington, P. J., Dunnill, P. and Lilly, M. D., 1971. Release of enzymes from baker's yeast by disruption in an industrial homogenizer. *Biotechnol. Bioeng.*, **13**, 549-560.

Fraser, D., 1951. Bursting bacteria by release of gas pressure. *Nature*, **167**, 33-34.

Georgiou, G., 1995. Recombinant DNA technology. *TIBTECH*, **13**, 79-80.

Gere, J. M. and Timoshenko, S. P., 1987. *Mechanics of Materials*, Second SI edition, Van Nostrand Reinhold (International), Hong Kong.

Gordon, J. E., 1980. Biomechanics: the last stronghold of vitalism. In *The mechanical properties of biological materials*, symposia of the society for experimental biology, number XXXIV, Cambridge University Press, Cambridge, 1-12.

Grant, G. and Tabakoff, W., 1975. Erosion prediction in turbomachinery resulting from environmental solid particles. *J. Aircraft*, **12**, 471-478.

Gray, P. P., Dunnill, P. and Lilly, M. D., 1972. The continuous-flow isolation of enzymes. In *Proc. IV IFS: Ferment. Technol. Today*, (Terui, G., Ed.), 347-351.

Hacking, A. J., 1986. *Economic Aspects of Biotechnology*. Cambridge University Press, Cambridge.

Hahn, S. K., Chang, Y. K., Kium, B. S and Chang, H. N., 1994. Optimisation of microbial poly(3-hydroxybutyrate) recovery using dispersions of sodium hypochlorite solution and chloroform. *Biotechnol. Bioeng.*, **44**, 256-261.

Harlow, F. H., and Nakayama, P. I., 1968. Transport of turbulence energy decay rate. LA-3854, Los Alamos Science Lab., Univ. of California, USA.

Harold, F. M., 1990. To shape a cell: an inquiry into the causes of morphogenesis of microorganisms. *Microbiol. Rev.*, **54**, 381-431.

Harris, B., 1980. The mechanical behaviour of composite materials. In *The mechanical properties of biological materials*, symposia of the society for experimental biology, number XXXIV, Cambridge University Press, Cambridge, 37-74.

Harrison, S. T. L., 1990. The extraction and purification of poly-β-hydroxybutyrate from *Alcaligenes eutrophus*. PhD Thesis, University of Cambridge, Cambridge, UK.

Harrison, S. T. L., Chase, H. A. and Dennis, J. S., 1991b. The disruption of *Alcaligenes eutrophus* by high pressure homgoenisation: Key factors involved in the process. *Bioseparation*, **2**, 155-166.

Harrison, S. T. L., Dennis, J. S. and Chase, H. A., 1991a. Combined chemical and mechanical processes for the disruption of bacteria. *Bioseparation*, **2**, 95-105.

Hasegawa, E. and Tamura, M., 1988. On the collision between small particles and a plane wall in a jet. *JSME Int. J.*, **31(II)**, 22-29.

Hearle, J. W. S., 1980. The mechanics of dense fibre assemblies. In Mechanics of flexible fibre assemblies, Hearle, J. W. S., Thwaites, J. J. and Amirbayat, J. (*Eds*), Sijthoff & Noordhoff, Alphen aan den Rijn, The Netherlands, 1-34.

Hearle, J. W. S., Grosberg, P. and Backer, S., 1969. *Structural mechanics of fibres, yarns and fabrics*, Wiley-Interscience, New York.

Heskestad, G., 1976. Hot-wire measurements in a radial turbulent jet. *ASME J. Appl. Mech.*, **23**, 31-64.

Hetherington, P. J., Follows, M., Dunnill, P. and Lilly, M. D., 1971. Release of protein from baker's yeast (*Saccharomyces cerevisiae*) by disruption in an industrial homogeniser. *Trans. Instn. Chem. Engrs.*, **49**, 142-148.

Hettwer, D. and Wang, H., 1989. Protein release from *Escherichia coli* cells permeabilised with guanidine-HCl and Triton X100. *Biotechnol. Bioeng.*, **33**, 886-895.

Higgins, J. J., Lewis, D. J., Daly, W. H., Mosqueira, F. G., Dunnill, P. and Lilly, M. D., 1978. Investigation of the unit operations involved in the continuous flow isolation of β–galactosidase from *Escherichia coli*. *Biotechnol. Bioeng.*, **20**, 159-182.

Hiramoto, Y., 1970. Review article: Rheological properties of sea urchin eggs. *Biorheology*, **6**, 201-234.

Hopkins, T. R., 1991. Physical and Chemical cell disruption for the recovery of intracellular proteins. In *Purification and Analysis of Recombinant Proteins*, R Seetharam and S. K. Sharma (Eds), Chap. 3, Marcel Dekker, New York, 57-83.

Hughes, D. E., Wimpenny, J. W. T. and Lloyd, D., 1971. The disruption of microoganisms. In *Methods in Microbiology*, J. R. Norris and D. W. Ribbons (Eds), **5B**, Chap. 1, Academic, New York, 1-54.

Hull, A. S. and Middelberg, A. P. J., 1993. Evidence that septated *E. coli* disrupt preferentially during high-pressure homogenization. *Trans. I.Chem.E.*, **71(C)**, 264-266.

Hunter, J. B. and Asenjo, J. A., 1988. A structured mechanistic model of the kinetics of enzymatic lysis and disruption of yeast cells. *Biotech. Bioeng.*, **31**, 929-943.

Jackson, R. W. and DeMoss, J. A., 1975. Effects of toluene on *Escherichia coli*. *J. Bacteriol.*, **90**, 1420-1425.

Johnson, B. H. and Hecht, M. H., 1994. Recombinant proteins can be isolated from *E. coli* cells be repeated cycles of freezing and thawing. *Bio/Technology*, **12**, 1357-1360.

Jones, M. N., 1992. Surfactant interactions with biomembranes and proteins. *Chem. Soc. Rev.*, **21**, 127-136.

Kang, I. S., and Leal, L. G., 1987. Numerical solution of axisymmetric, unsteady free-boundary problems at finite Reynolds number. I. Finite difference scheme and its application to the deformation of a bubble in a uniaxial straining flow. *Physics of fluids*, **30**, 1929-1940.

Kang, I. S., and Leal, L. G., 1989. Numerical solution of axisymmetric, unsteady free-boundary problems at finite Reynolds number. II. Deformation of a bubble in a biaxial straining flow. *Physics of fluids A*, **1**: 644-660.

Katsui, N., Tsuchido, T., Hiramatsu, R., Fujikawa, S., Takano, M. and Shibasaki, I., 1982. Heat-induced blebbing and vesiculation of the outer membrane of *Escherichia coli*. *J. Bacteriol.*, **151**, 1523-1531.

Kawaguchi, T., 1971. Entrance loss for turbulent flow without swirl between parallel discs. *Bull. JSME.*, **14**, 355-363.

Kelemen, M. V. and Sharpe, J. E. E., 1979. Controlled cell disruption: a comparison of the forces required to disrupt different microorganisms. *J. Cell Sci.*, **35**, 431-441.

Keshavarz Moore, E., Hoare, M., and Dunnill, P., 1990. Disruption of baker's yeast in a high presure homogenizer: New evidence on mechanism. *Enzyme Microb. Technol.*, **12**, 764-770.

Keshavarz, E., Hoare, M. and Dunnill, P., 1987. Biochemical engineering aspects of cell disruption. In *Separations for Biotechnology*, M. S. Verrall and M. J. Hudson (Eds), Chap. 3, Ellis Horwood, Chichester, 62-79.

Khosrovi, B. and Gray, P. P., 1985. Products from recombinant DNA. In *Comprehensive Biotechnology*, Moo-Young, M., (Ed.), Pergamon Press, Oxford, Vol 3, 319-330.

Klis, F. M., 1994. Review: cell wall assembly in yeast. *Yeast*, **10**, 851-869.

Koch, A. L., 1988. Biophysics of bacterial walls viewed as stress-bearing fabric. *Microbiol. Rev.*, **52**, 337-353.

Kollár, R., Petráková, E., Ashwell, G., Robbins, P. W. and Cabib, E., 1995. Architecture of the yeast cell wall. The linkage between chitin and β(1→3)-glucan. *J. Biol. Chem.*, **270**, 1170-1178.

Kopecká, M., Phaff, H. J. and Fleet, G. H., 1974. Demonstration of a fibrillar component in the cell wall of the yeast Saccharomyces cerevisiae and its chemical nature. *J. Cell Biol.*, **62**, 66-76.

Kreger, D. R. and Kopecká, M., 1975. On the nature and formation of the fibrillar nets produced by protoplasts of *Saccharomyces cerevisiae* in liquid media: an electromicroscopic, X-ray diffraction and chemical study. *J. Gen. Microbiol.*, **92**, 207-220.

Kula, M.-R. and Schütte, H., 1987. Purification of proteins and the disruption of microbial cells. *Biotechnol. Prog.*, **3**, 31-42.

Kula, M.-R., Schütte, H., Vogels, G. and Frank, A., 1990. Cell disintegration and purification of intracellular proteins. *Food Biotechnol.*, **4**, 169-183.

Kurzhals, H.-A., 1977. Untersuchungen uber die physikalisch-technischen vorgange beim Homogenisieren von Milch in Hochdruck-Homogenisiermachinen. PhD Thesis, Technischen Universitat, Hannover, Germany.

Lardner, T. J. and Pujara, P., 1978. Compression of spherical cells. *Mech. Today.*, **5**, 161-176.

Laschefski, H., Braess, D., Haneke, H., and Mitra, N. K., 1994. Numerical investigations of radial jet reattachment flows. *Int. J. Num. Meth. Fluids.*, **18**, 629-646.

Law, H., and Masllyah, J. H., 1984, Mass transfer due to a confined laminar impinging axisymmetric jet. *Ind. Chem. Eng. Fundam.*, **23**, 446-454.

Leive, L., Shovlin, V. K. and Mergenhagen, S. E., 1968. Physical, chemical, and immunological properties of lipopolysaccharide released from *Escherichia coli* by ethylenediaminetetraacetate. *J. Biol. Chem.*, **243**, 6384-6391.

Levin, R. L., 1978. Water Permeability of Yeast Cells at Sub-Zero Temperatures. *J. Membrane Biol.*, **46**, 91-112.

Leyrat-Maurin, A. and Barthes-Biesel, D., 1994. Motion of a deformable capsule through a hyperbolic constriction. *J. of Fluid Mechanics*, **279**, 135-163.

Li, X. Z., Barthes-Biesel, D., and Helmy, A., 1988. Large deformations and burst of a capsule freely suspended in an elongational flow, *J. of Fluid Mechanics*, **187**, 179-196.

Lin, H.-M., Chan, E.-C., Chen, C. and Chen, L.-F., 1991. Disintegration of yeast cells by pressurized carbon dioxide. *Biotechnol. Prog.*, **7**, 201-204.

Lin, H.M., Yang, Z. and Chen, L.-F., 1992. An improved method for the disruption of cells with pressurized carbon dioxide. *Biotechnol. Prog.*, **8**, 165-166.

Liu, K.-K., 1995. The deformation of cellular entities. PhD Thesis, University of London, London.

Loo, C. C., and Carleton, W. M., 1953. Further studies of cavitation in the homogenization of milk products. *J. Dairy Sci.*, **36**, 64-75.

Loo, C. C., Slatter, W. L. and Powell, R. W., 1950. A study of the cavitation effect in the homogenization of dairy products. *J. Dairy Sci.*, **33**, 692-702.

Lubitz, W., Halfman, G. and Plapp, R., 1984. Lysis of *Escherichia coli* after infection with ϕX174 depends on the regulation of the cellular autolytic system. *J. Gen. Microbiol.*, **130**, 1079-1087.

Lutzer, R. G., Robinson, C. W. and Glick, B. R., 1994. Two-stage process for increasing cell disruption of E. coli for intracellular products recovery. In *Proceedings of the 6th European Congress on Biotechnology*, A. Alberghina, L. Fontali and P. Sensi (Eds), Elsevier Science, Amsterdam, 909-916.

Lux, F., 1932. Br. Patent Spec. 367063.

Madsen, F. S. and Ibsen, C. I., 1987. Cell disruption by means of high pressure. Dept. of Biotechnology, Engineering Academy of Denmark, Copenhagen.

Magnaudet, J., Rivero, M., and Fabre, J., 1995. Accelerated flows past a rigid sphere or a spherical bubble. Part 1. Steady straining flow. *J. of Fluid Mechanics*, **284**, 97-135.

Malin, M. R., 1989. Modeling the effects of lateral divergence in radially spreading turbulent jets. *Computers & Fluids*, **17**, 453-465.

McKillop, A. A., Dunkley, W. L., Brockmeyer, R. L. and Perry, R. L., 1955. The cavitation theory of homogenization. *J. Dairy Sci.*, **38**, 273-283.

McLean, E. A. and Schaschke, C. J., 1996. Disruption of yeast cells using high-pressure carbon dioxide. Proceedings *1996 IChemE Research Event*, **1**, 85-87.

Middelberg, A. P. J., 1992. A model for the disruption of *Escherichia coli* by high-pressure homogenization. PhD Thesis, University of Adelaide, Adelaide, Australia.

Middelberg, A. P. J., 1995. Process-scale disruption of microorganisms. *Biotech. Advances*, **13**, 591-551.

Middelberg, A. P. J., O'Neill, B. K., Bogle, I. D. L. and Snoswell, M. A., 1991. A novel technique for the measurement of disruption in high-pressure homogenization: studies on *E. coli* containing recombinant inclusion bodies. *Biotechnol. Bioeng.*, **38**, 363-370.

Middelberg, A. P. J., O'Neill, B. K., and Bogle, I. D. L., 1992a, A new model for the disruption of *Escherichia coli* by high-pressure homogenization. Part I. Model development and verification. *Trans. I.Chem.E.*, **70(C)**, 205-212.

Middelberg, A. P. J., O'Neill, B. K., Bogle, I. D. L., Gully, N. J., Rogers, A. H., and Thomas, C. J., 1992b, A new model for the disruption of *Escherichia coli* by high-pressure homogenization. Part II. A correlation for the effective cell strength. *Trans. I.Chem.E.*, **70(C)**, 213-218.

Milburn, P. T. and Dunnill, P., 1994. The release of virus-like particles from recombinant *Saccharomyces cerevisiae*: effect of freezing and thawing on homogenization and bead milling. *Biotechnol. Bioeng.*, **44**, 736-744.

Milner, H. W., Lawrence, N. S. and French, C. S., 1950. Colloidal dispersion of chloroplasm material. *Science*, **111**, 633-634.

Mitchison, J. M. and Swann, M. M., 1954. The mechanical properties of the cell surface. I. The cell elastimeter. *J. Exp. Biol.*, **31**, 443.

Mohaupt, U. H. and Burns, D. J., 1974. Machining unreinforced polymers with high-velocity water jets. *Experimental Mechanics*, **14**, 152.

Mol, P. C. and Wessels, J. G. H., 1987. Linkages between glucosaminoglycan and glucan determine alkali-insolubility of the glucan in wall so *Saccharomyces cerevisiae*. *FEMS Microbiol. Lett.*, **41**, 95-99.

Moller, P. S., 1963. Radial flow without swirl between parallel discs. *Aeronautical Quaterly*, **14**, 163-186.

Mossinghoff, G. J., 1993. Biotechnology medicines in development. In *The Biotechnology Report 1993/94*, Campden Publishing Ltd., London, 276-287.

Mulder, H. and Walstra, P., 1974. Homogenization. In *The milk fat globule: Emulsion science as applied to milk products and comparable foods*, The Universities Press, Belfast, 163-194.

Naglak, T. J., Hettwer, D. J. and Wang, H. Y., 1990. Chemical permeabilization of cells for intracellular product release. In *Separation Processes in Biotechnology*, J. A. Asenjo (Ed.), Marcel Dekker, New York, 177-205.

Nakayama, Y., 1964. Action of the fluid in the air-micrometer (3rd report, characteristics of double-disc nozzle No. 1, in the case of compressibility being ignored). *Bull. JSME.*, **7**, 698-707.

Neu, H. C. and Heppel, L. A., 1964. On the surface localisation of enzymes in *E. coli*. *Biochem. Biophys. Res. Comm.*, **17**, 215-219.

Norris, C. H., 1939. The tension at the surface, and other physical properties of the nucleated erythrocyte. *J. Cell. Comp. Physiol.*, **4**, 117.

Novella, I. S., Fargues, C. and Grévillot, G., 1994. Improvement of the extraction of penicillin acylase from *Escherichia coli* cells by a combined use of chemical methods. *Biotechnol. Bioeng.*, **44**, 379-382.

Pandolfe, W. D., 1982. Development of the new Gaulin Micro-Gap™ Homogenizing Valve. *J. Dairy Sci.*, **65**, 2035-2044.

Pandolfe, W. D., 1992. The cell disruption homogenizer. APV-Gaulin Technical Bulletin.

Patel, R. P., 1979. Some measurements in radial free jets. *AIAA J.*, **17**, 657-658.

Phipps, L. W., 1971. Mechanism of oil droplet fragmentation in high pressure homogenizers. *Nature*, **233**, 617-619.

Phipps, L. W., 1974a. Cavitation and separated flow in a simple homogenizing valve and their influence on the break-up of fat globules in milk. *J. Dairy Res.*, **41**, 1-8.

Phipps, L. W., 1974b. Some operating characteristics of a simple homogenizing poppet valve; pressure profiles and separation: zone of fat globule dispersion. *J. Dairy Res.*, **41**, 339-347.

Phipps, L. W., 1975. The fragmentation of oil drops in emulsions by a high-pressure homogenizer. *J. Phys. D: Appl. Phys.*, **8**, 448-462.

Pitt, R. E. and Davis, D. C., 1984. Finite element analysis of fluid-filled cell response to external loading. *Trans. ASAE.*, **27**, 1976-1983.

Pittroff, M. and Schubert, H., 1990. Mechanical disintegration of microbial cells by high pressure homogenisation and wet milling - comparative study of performance. In *DECHEMA biotechnology conferences*, VCH Verlagsgesellschaft, **4**, 1055-1059.

Pittroff, M., Wilk, M. and Schubert, H., 1992. Linearization of disintegration kinetic curves of microbial cells: studies on high-pressure homogenisation and wet milling. In *DECHEMA Biotechnology Conferences*, VCH Verlagsgesellschaft, **5**, 687-691.

Pittroff, M., Wilk, M. and Schubert, H., 1993. Auswahl und Optimierung mechanischer Zellaufschlußverfahren mit Hilfe eines zweiparametrigen kinetischen Ansatzes. *BioEngineering*, **9**, 12-18.

Powell, P. C., 1994. *Engineering with fibre-polymer laminates*, Chapman and Hall, London.

Pozrikidis, C., 1990. The axisymmetric deformation of a red blood cell in uniaxial straining Stokes flow. *J. of Fluid Mechanics*, **216**, 231-254.

Roberts, A. D., Zhang, Z., Young, T. W., and Thomas, C. R., 1994. Direct determination of the strength of brewing yeast cells using micromanipulation. Proceedings *1994 IChemE Res. Event*, 73-75.

Ruiz-Herrera, J., 1992. *Fungal cell walls: structure, synthesis and assembly*, CRC Press, Boca Raton.

Ryskin, G., and Leal, L. G., 1984. Numerical solution of free-boundary problems in fluid mechanics. Part 3. Bubble deformation in an axisymmetric straining flow. *J. of Fluid Mechanics*, **148**, 37-43.

Sauer, T., Robinson, C. W. and Glick, B. R., 1989. Disruption of native and recombinant Escherichia coli in a high-pressure homogenizer. *Biotechnol. Bioeng.*, **33**, 1330-1342.

Save, S. S., Pandit, A. B. and Joshi, J. B., 1994. Microbial cell disruption: role of cavitation. *Chem. Eng. J.*, **55**, B64-B72.

Schütte, M.-R. and Kula, H., 1993. Cell disruption and isolation of non-secreted products. In *Biotechnology, vol 3: Bioprocessing*, G. Stephanopolous (Ed.), VCH, Weinheim, 505-526.

Schwarz, W. H., 1963. The radial free jet. *Chem. Eng. Sci.*, **18**, 50-62.

Sheth, K. S., and Pozrikidis, C., 1995. Effects of inertia on the deformation of liquid drops in simple shear flow. *Computers & Fluids*, **24**, 101-119.

Shuler, M. L. and Kargi, F., 1992. Utilising genetically engineered organisms. In *Bioprocess Engineering: Basic Concepts*, P T R Prentice Hall, New Jersey, 395-430.

Siddiqi, S. F. and Titchener-Hooker, N. J., 1994. Simulation of changes occurring in the size distribution of cell debris during homogenization. Proceedings *1994 IChemE Research Event*, UCL, London. 192-194.

Siddiqi, S. F., Bulmer, M., Ayazi Shamlou, P. and Titchener-Hooker, N. J., 1995. The effect of fermentation conditions on yeast cell debris particle size distribution during high pressure homogenisation. *Bioprocess. Eng.*, **14**, 1-8.

Siddiqi, S. F., Titchener-Hooker, N. J. and Ayazi Shamlou, P., 1996. Simulation of particle size distribution changes occurring during high-pressure disruption of bakers' yeast. *Biotechnol. Bioeng.*, 50, 145-150.

Sommerfeld, M., 1992. Modelling of particle-wall collisions in confined gas-particle flows. *Int. J. Multiphase Flow*, **18**, 905-926.

Squire, H. B., 1955. Radial jets. In *50 Jahre Grenzschichtforschung*, Vieweg & Sons, Braunschweig, FRG, 47-54.

Srinorakutara, T., Zhang, Z. and Thomas, C. R., 1996. Osmolarity effect on yeast cell strength and cell size. Proceedings *1996 IChemE Res. Event*, 151-153.

Srinorakutara, T., Zhang, Z., and Thomas, C. R., 1995. Mechanical properties of yeast. CHEMECA '95, Proc. 23rd Australasian Chemical Engineering Conference, Adelaide, Australia, **3**, 45-49.

Tanaka, T. and Tanaka, E., 1976. Experimental investigation of a radial turbulent jet. *Bull. JSME.*, **19**, 792-799.

Tannenbaum, S. R. and Miller, A. A., 1967. Effect of cell fragmentation on nutritive value of *Bacillus megaterium* protein. *Nature*, **214**, 1261-1262.

Terselius, B., Gedde, U. W. and Jansson, J.-F., 1986. Mechano-chemical phenomena in polymers. In *Failure of Plastics*, Brostow, W. and Corneliussen, R. D. (Eds), Hanser Publishers, Munich, 273-286.

Timoshenko, S., and Woinowsky-Krieger, S., 1959. Deformation of shells without bending. In *Theory of Plates and Shells*, 2nd edition, McGraw-Hill Book Company, New York, 433-435.

Tokunaga, M., Kusamichi, M. and Koike, H., 1986. Ultrastructure of outermost layer of cell wall in *Candida albicans* observed by rapid-freezing technique. *J. Electron Microsc.*, **35**, 237-246.

Tsuchido, T., Katsui, N., Takeuchi, A., Takano, M. and Shibasaki, I., 1985. Destruction of the outer membrane permeability barrier of *Escherichia coli* by heat treatment. *Appl. Environ. Microbiol.*, **50**, 298-303.

Vogels, G. and Kula, M.-R., 1992. Combination of enzymatic and/or thermal pretreatment with mechanical cell disintegration. *Chem. Eng. Sci.*, **47**, 123-131.

Vosberg, H.-P. and Hoffmann-Berling, H., 1971. DNA synthesis in nucleotide-permeable *Escherichia coli* cells. *J. Mol. Biol.*, **58**, 739-753.

Walstra, P., 1993. Formation of emulsions. In *Encyclopedia of Emulsion Technology*, Becker, P. (Ed.), Marcel Dekker Inc., New York, chapter 2.

Ward, I. M., and Hadley, D. W., 1993. *An Introduction to the Mechanical Properties of Solid Polymers*, John Wiley & Sons, Chichester.

Watson, J. S., Cumming, R. H., Street, G. and Tuffnell, J. M., 1987. Release of intracellular protein by thermolysis. In *Separations for Biotechnology*, M. S. Verrall and M. J. Hudson (Eds), Ellis Horwood, London, 105-109.

White, M. D. and Marcus, D., 1988. Disruption of microorganisms. *Adv. Biotechnol. Process*, **8**, 51-96.

Whitworth, D. A., 1974. Hydrocarbon fermentation: protein and enzyme solubilisation from *C. lipolytica* using an industrial homogenizer. *Biotechnol. Bioeng.*, **16**, 1399-1406.

Wimpenny, J. W. T., 1967. Breakage of microorganisms. *Process Biochem.*, **2**, 41-44.

Witze, P. O. and Dwyer, H. A., 1976. The turbulent radial jet. *J. Fluid Mech.*, **75**, 401-417.

Wood, P. E., and Chen, C. P., 1985. Turbulence model predictions of the radial jet - a comparison of k-ε models. *Can. J. Chem. Eng.*, **63**, 177-182.

Yoneda, M., 1964. Tension at the surface of sea-urchin egg: a critical examination of Cole's experiment. *J. Exp. Biol.*, **41**, 893-906.

Zhang, Z., Ferenczi, M. A. and Thomas, C. R., 1992. A micromanipulation technique with a theoretical cell model for determining mechanical properties of single mammalian cells. *Chem. Eng. Sci.*, **47**, 1347-1354.

Zhang, Z., Ferenczi, M. A., Lush, A. C. and Thomas, C. R., 1991. A novel micromanipulation technique for measuring the bursting strength of single mammalian cells. *Appl. Microbiol. Biotechnol.*, **36**, 208-210.

Zhang, Z., Saunders, R. and Thomas, C. R., 1994. Micromanipulation measurements of the bursting strength of single microcapsules. Proceedings *1994 IChemE Res. Event*, 722-724.

Zhou. H., and Pozrikidis, C., 1995. Deformation of liquid capsules with incompressible interfaces in simple shear flow. *J. of Fluid Mechanics*, **283**, 175-200.

Zlotnik, H., Fernandez, M. P., Bowers, B. and Cabib, E., 1984. *Saccharomyces cerevisiae* Mannoproteins form an external cell wall layer than determines wall porosity. *J. Bacteriol.*, **159**, 1018-1026.